Scalars in Bubbly Turbulence

On Yu Dung

Scalars in bubbly turbulence

On Yu Dung

Thesis committee members:

Prof. Dr. Ir. R. G. H. Lammertink (chairman)	UT, Enschede
Prof. Dr. rer. nat. D. Lohse (promotor)	UT, Enschede
Prof. Dr. C. Sun (co-supervisor)	Tsinghua University
Dr. S. G. Huisman (co-supervisor)	UT, Enschede
Prof. Dr. Ir. G. Brem	UT, Enschede
Prof. Dr. R. Verzicco	UT, Enschede
Prof. Dr. Ir. A. W. Vreman	TUE, Eindhoven
Prof. Dr. V. Roig	Institut de Mécanique des Fluides de Toulouse

Dutch title: *Scalairen in turbulente stromingen met bellen*

Cover design: Wong Shing Kit. Inspired by and based on the design of Fig. 1 in Celani A., Vergassola M. 2001. Phys. Rev. Lett. **86**(3):424.

Scalars in bubbly turbulence

DISSERTATION

to obtain
the degree of doctor at the University of Twente,
on the authority of the rector magnificus,
Prof. Dr. Ir. A. Veldkamp,
on account of the decision of the graduation committee,
to be publicly defended
on Thursday the 15th of April 2021 at 16:45

by

On Yu Dung
Born on the 9th of October 1994
in Hong Kong, China

This dissertation has been approved by the supervisor:

Prof. Dr. rer. nat. Detlef Lohse

and the co-supervisors:

Prof. Dr. Chao Sun

Asst. Prof. Dr. Sander G. Huisman

To Onki and my family

Contents

1

Introduction

Turbulence is very common in nature. We see it when fluids, such as air and water, exhibiting irregular and unsteady motions. It ranges from the smoke emitted from a cigarette to the storms in the atmosphere.

Technically, turbulence can be regarded as a nonlinear system in a non-equilibrium state which has a large number of excitable degrees of freedoms, exhibiting spatiotemporal chaos [2]. Statistical descriptions are therefore needed. Practically, we can also find turbulence in industrial processes, such as chemical reactors. Chemical reactions may release heat. To enhance the mixing of heat and mass (the microparticles related to the reactions), gas bubbles are commonly injected to provide extra mechanical stirring.

Turbulence with bubbles, is one of the big classes of turbulence, called dispersed multiphase turbulence [3]. The *dispersed* phase are the 'particles' such as solid particles, droplets, or bubbles, being present in the *continuous* phase which is a liquid or gas. A complete physical understanding on the mixing of heat and mass in bubbly turbulence is lacking. In this thesis, we focus on the mixing of a scalar field (local temperature or concentration) in *inhomogeneous bubbly flows* and *turbulent bubbly flows*, which are more common in industry and in nature than the idealised situation of a *homogeneous bubbly flow* and are distinguished from *single-phase homogeneous turbulence*.

The subject of heat and mass transfer in a fluid is the study of the dynamics of a *scalar field* in a fluid having a *velocity field*.

Therefore, *mixing* of scalar(s), which is the process when 'a system evolves from ... a segregation of the constituents to ... their complete uniformity' [4], involves the transport by *convection* (or advection) by the velocity field and by *diffusion* due to the molecular diffusivity (see e.g. Ref. [5]), see Fig. 1.1a. The ratio of the convective transfer to molecular diffusive transfer can be quantified by a dimensionless number called the Péclet number $\mathrm{Pe} = u_0 L_\theta / \kappa$, where u_0 is the typical velocity at the largest scale, L_θ is the largest length scale at which the scalar is introduced, and κ is the molecular diffusivity of a scalar. For $\mathrm{Pe} \gg 1$, which is usually the case in turbulent flows, the scalar that is introduced at a large scale (e.g. a mean concentration gradient) will be twisted and stretched by the velocity field until the size of the structure of the scalar becomes small enough such that molecular diffusion dominates the mixing (see e.g. Ref. [4, 6]).

Thus, to understand the mixing processes in bubbly flows, we need to understand how the velocity field advects a scalar. This implies that the structure of the velocity field also needs to be understood. Tracing back further, we have to identify the liquid velocity agitation mechanisms for bubbly flows. A general mixing process for $\mathrm{Pe} \gg 1$ is summarised in Fig. 1.1b.

The liquid velocity agitation mechanisms in bubbly flows are mainly *bubble-induced turbulence* (BIA) with or without *shear-induced turbulence* (SIT) [7], which are briefly introduced as follows. For homogeneous bubbly flows, bubbles are freely rising, and the liquid agitation caused by the bubbles only is called BIA [7]. However, inhomogeneous bubbly flows and turbulent bubbly flows consist of more than just BIA. For turbulent bubbly flows, there is externally forced turbulence which can be created by, for example, an external pressure gradient. This externally forced turbulence, which is from the inherent instability and nonlinearity of the liquid flow due to high Reynolds number, is called SIT [7]. For single-phase homogeneous turbulence, the liquid agitation mechanism is SIT. For inhomogeneous bubbly flows, due to the inhomogeneity of the bubble distributions, a large-scale liquid mean flow is created due to buoyancy, similar to natural convection [7, 8]. This induced liquid mean flow likewise agitates the liquid by SIT. The liquid agitation mechanisms for homogeneous bubbly flows, inhomogeneous bubbly flows, turbulent bubbly flows, and single-phase homogeneous turbulence are summarised in Fig. 1.2 and will be discussed in more details in the later sections.

In this Introduction, as both the velocity field and the scalar field has to be considered, the field equations of the scalar and the velocity field are first introduced. Since usually bubbly turbulence has $\mathrm{Pe} \gg 1$ and for the mixing
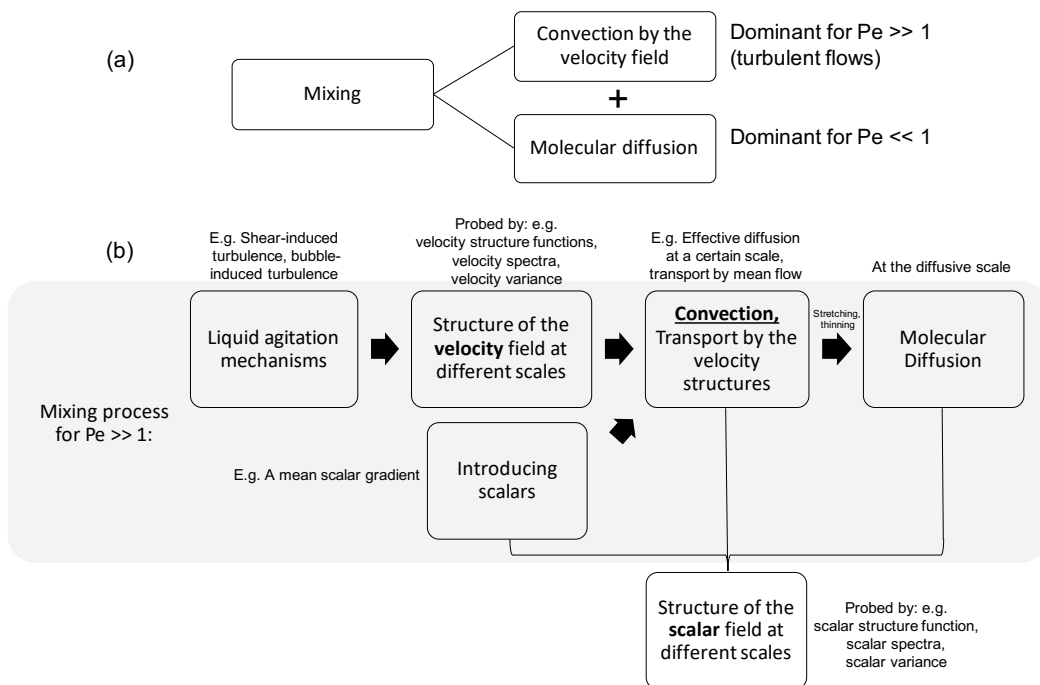
Figure 1.1: (a) Mixing consists of the convection by the velocity field and molecular diffusion. The Péclet number Pe $= u_0 L_\theta / \kappa$ measures the relative importance of convective transport as compared to the diffusive transport of the scalar, where u_0 is the typical velocity at the largest scale, L_θ is the largest length scale at which the scalar is introduced, and κ is the molecular diffusivity of the scalar. (b) A mixing process for Pe $\gg 1$.

process we need to understand the liquid velocity agitation first, we focus on reviewing each of the main agitation mechanisms, SIT and BIA, individually before introducing the interactions between them. They are manifested as single-phase homogeneous turbulence and homogeneous bubbly flows respectively. Next, we review the agitations and mixing in inhomogeneous bubbly flows and those in turbulent bubbly flows. Our review follows the general mixing process in Fig. 1.1b. For each of this section, the details of the liquid agitation mechanism(s) will be discussed. Then the structure of the velocity field at different scales are reviewed by considering the velocity structure
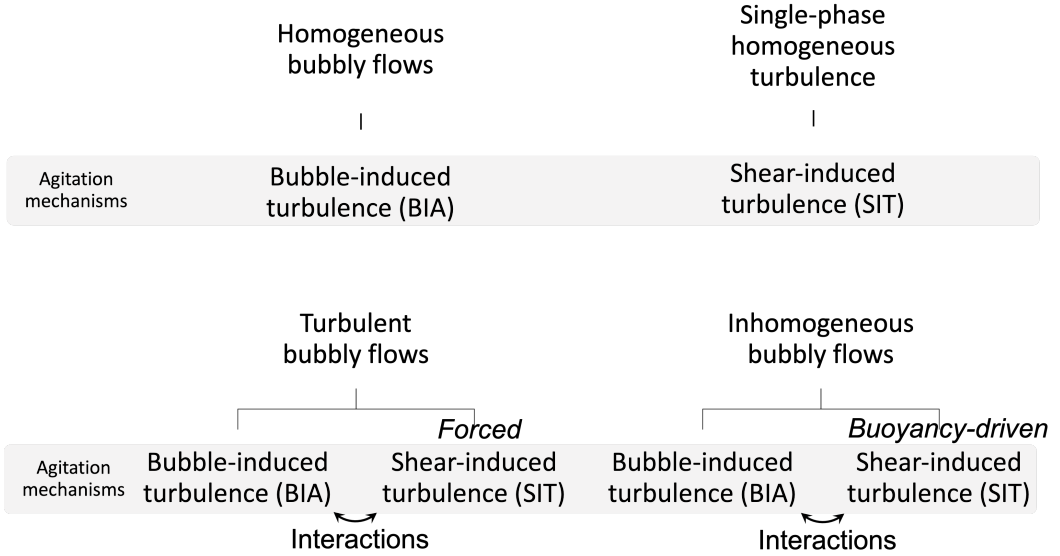
Figure 1.2: The liquid agitation mechanisms for homogeneous bubbly flows, inhomogeneous bubbly flows, turbulent bubbly flows and single-phase homogeneous turbulence. The shear-induced turbulence (SIT) is *forced* for the turbulent bubbly flows while it is *buoyancy-driven* for inhomogeneous bubbly flows.

function, velocity spectra, and the velocity variance (if applicable). After that, for each class of the turbulent flow, the overall mixing processes, due to the convection by the velocity field and the molecular diffusion, are discussed. Finally, as a result of the mixing, the structure of the scalar field are reviewed by using the scalar structure functions and the scalar spectra. From this review, we identify the unexplored research questions in which some of them will be discussed in this thesis.

1.1   Velocity field, scalar field, and statistical description

The velocity field $\mathbf{u}(\mathbf{x}, t)$ of the liquid phase, where $\mathbf{x}$ is the spatial coordinates and t is the time coordinate, is governed by the incompressible Navier-Stokes

equations and the continuity equation, which are given by

$$\frac{\partial}{\partial t}\mathbf{u} + \mathbf{u} \cdot \nabla \mathbf{u} = -\frac{1}{\rho}\nabla p + \nu \nabla^2 \mathbf{u} + \rho \mathbf{g} + \mathbf{f}, \qquad (1.1)$$

$$\nabla \cdot \mathbf{u} = 0 \qquad (1.2)$$

where $\mathbf{g}$ is the gravitational field which is assumed to be constant, ν is the kinematic viscosity of the liquid phase also assumed to be constant, ρ is the density of the liquid phase, and $\mathbf{f}$ is any possible forcing term depending on the physical conditions. The Navier-Stokes equations are nonlinear as can be seen from the inertial convective terms $\mathbf{u} \cdot \nabla \mathbf{u}$ on the L.H.S. of Eq. 1.1, which is also the source of the chaotic, irregular behaviour of the flows. Different boundary conditions and flow parameters lead to different flows. One important dimensionless parameter that govern the dynamics of the flow is the *Reynolds* number which compares the inertial forces to the viscous forces $\mathrm{Re} = u_0 L_u / \nu$, where u_0 and L_u are the velocity and the largest length scale of the velocity introduced, respectively. In particular, we focus at the case where $\mathrm{Re} \gg 1$. In this regime, the flow is *turbulent*.

We only consider *conserved* scalar field, i.e. no sources nor sinks locally. This means, for example, there are no local heat source from chemical reactions nor the conversion of any chemical species from one to another. Let $\theta(\mathbf{x}, t)$ be the scalar field. It satisfies the so-called advection-diffusion equation,

$$\frac{\partial}{\partial t}\theta + \mathbf{u} \cdot \nabla \theta = \kappa \nabla^2 \theta \qquad (1.3)$$

where κ is the molecular diffusivity of the scalar field in the liquid phase. which is assumed to be constant. Scalar fields include the temperature field, concentration field of microparticles or contaminant, etc. If the velocity field does not depend on θ, we called the scalar a *passive scalar*. In this thesis we mainly study the temperature field. Eq. 1.3 is different from the velocity field equation in the sense that it is a *linear* equation in θ if $\mathbf{u}$ does not depend on θ (i.e. θ is a *passive scalar*), meaning that, in this case, superposition principle holds and a mixing problem can be studied in the superposition of elementary structures such as lamellae [4]. Similar to the Reynolds number, there is also a dimensionless parameter that governs the dynamics of Eq. 1.3, which is the Péclet number $\mathrm{Pe} = u_0 L_\theta / \kappa$ that was defined before. It compares the inertial effect to the diffusive effect. Likewise, we consider the *convection-dominated* regime in which $\mathrm{Pe} \gg 1$.

In turbulent flows, as mentioned before, the velocity and the scalar field are both chaotic and irregular. Thus, in order to make predictions in turbulent

flows, we adopt a statistical description, i.e. to investigate the dynamics of *ensemble averages* of the physical quantities. We take ensemble averages of Eqs. 1.1 and 1.3 and decompose the fields into mean and fluctuations to investigate the dynamics of averaged quantities instead (which is called Reynolds decomposition, see e.g. Ref. [9]). Let $\mathbf{u} \equiv \langle\mathbf{u}\rangle + \mathbf{u}'$ and $\theta \equiv \langle\theta\rangle + \theta'$, where $\langle.\rangle$ denotes an ensemble average, and substitute them into Eqs. 1.2 and 1.3, then take ensemble averages on both sides, Eq. 1.3 becomes

$$\frac{\partial}{\partial t}\langle\theta\rangle + \langle\mathbf{u}\rangle\cdot\nabla\langle\theta\rangle = \kappa\nabla^2\langle\theta\rangle - \nabla\cdot\langle\mathbf{u}'\theta'\rangle, \qquad (1.4)$$

which is similar to the original scalar field equation but with an extra unknown $-\langle\mathbf{u}'\theta'\rangle$ which is known as the turbulent scalar flux [9]. The number of equations being less than the number of unknowns is known as a closure problem [9]. The mean scalar field distinguishes from the scalar field itself (Eq. 1.3) because of the turbulent fluctuations. In particular, in this thesis, we focus on bubbly turbulence and the previous results on the mixing of this subject are summarised in the later sections in the Introduction.

1.2 Shear-induced turbulence: single-phase homogeneous turbulence and the mixing

As discussed and shown in Fig. 1.1b, to understand the mixing process, we first need to understand the liquid agitation mechanism. As mentioned before, inhomogeneous bubbly flows and turbulent bubbly flows consists of shear-induced turbulence and bubble-induced turbulence, we first focus on the flows solely generated by SIT. Shear-induced turbulence (SIT) means the turbulence induced by the inherent instability and nonlinearity due to high Reynolds number in the liquid flow. Single-phase homogeneous turbulence is a manifestation of SIT. We introduce some important results on single-phase homogeneous turbulence without mean shear that help us to understand the thesis (see e.g. Refs. [2, 9–11]).

1.2.1 Relevant parameters

In practice, for example, one can generate a homogeneous turbulent flow by exerting external pressure gradient on a fluid, forcing it to pass through a grid in a wind tunnel or water channel, and we only consider the region away from the boundaries. This is called grid turbulence which is freely decaying [9].

We consider the fluctuations of velocity and temperature being introduced at the large scales say L_u and L_θ respectively. Due to the molecular viscosity and molecular diffusivity, such fluctuations will be dissipated at scales related the viscosity and diffusivity, namely at the scales η and η_θ respectively which are comparably small because of its molecular nature. Let u'_{rms} and T'_{rms} be the standard deviation of the velocity and temperature field respectively in a single-phase turbulent flow. Larger u'_{rms} and T'_{rms} means the velocity and temperature fluctuations are stronger. It is also convenient to define some intermediate scales between the largest scales L_u (or L_θ) and the smallest scale η (or η_θ) by using the curvature of the correlation functions of the velocity and scalar field at the zero lag position [9]. They are called Taylor-microscales λ_u and λ_θ, respectively for the velocity and scalar fields. The Reynolds and Péclet number based on the Taylor-microscales are commonly used when we consider unbounded turbulent flows such as grid-turbulence (freely decaying turbulent flow) [9], unlike the bounded ones that can use the domain size as the typical length scale. Together $(u_0, u'_{\mathrm{rms}}, T'_{\mathrm{rms}}, \eta, \eta_\theta, \lambda_u, \lambda_\theta, L_u, L_\theta)$ are the control parameters for a single-phase turbulent flow. By dimensional analysis, some dimensionless numbers can be formed to represent the physical system, namely $\mathrm{Re} = u_0 L_u / \nu$, $\mathrm{Pe} = u_0 L_\theta / \kappa$, $\mathrm{Re}_{\lambda_u} = u'_{\mathrm{rms}} \lambda_u / \nu$, $\mathrm{Pe}_{\lambda_u} = u'_{\mathrm{rms}} \lambda_u / \kappa$, $\mathrm{Pe}_{\lambda_\theta} = u'_{\mathrm{rms}} \lambda_\theta / \kappa$ [12] and the Prandtl number $\mathrm{Pr} = \nu / \kappa$. In particular, in room temperature, water has $\mathrm{Pr} \approx 7$, and air has $\mathrm{Pr} \approx 0.7$.

1.2.2 Structure of the velocity and scalar fields: scaling properties

As shown in Fig. 1.1b, a mixing process involves convection of a scalar by the velocity field at different scales, in which the structure of the velocity field at different scales are needed to be understood first. Such structure can be probed by the velocity structure functions. Similarly, as a result of the mixing, there is also a structure of the scalar field, which can also be captured by the scalar structure functions (see Fig. 1.1b). To mathematically describe the structure of turbulent flows at different scales, the velocity and temperature increments are used. The moments of the increments are called the structure functions, which are given by

$$\langle (\Delta_r u)^p \rangle \equiv \langle \{ [\mathbf{u}(\mathbf{r}, t) - \mathbf{u}(\mathbf{0}, t)] \cdot \mathbf{r}/r \}^p \rangle, \tag{1.5}$$

$$\langle (\Delta_r \theta)^p \rangle \equiv \langle [\theta(\mathbf{r}, t) - \theta(\mathbf{0}, t)]^p \rangle, \tag{1.6}$$

where p is the order of the structure function, $\mathbf{r}$ is the vector from the origin and $r = |\mathbf{r}|$. Thus $\langle (\Delta_r u)^p \rangle$ and $\langle (\Delta_r \theta)^p \rangle$ describes the statistical structure of

a turbulent flow at scale r. We note that the Fourier transforms of the second order structure functions $\langle(\Delta_r u)^2\rangle$ and $\langle(\Delta_r \theta)^2\rangle$ are the spectra of the velocity and scalar fluctuations, namely $E_u(k,t)$ and $E_\theta(k,t)$ respectively.

The Kolmogorov-Obukhov-Corrsin (KOC) theory [13–15] predicts that when the Reynolds number ($\mathrm{Re} = u_0 L_u/\nu$) and the Péclet number ($\mathrm{Pe} = u_0 L_\theta/\kappa$) are much larger than unity, there is a separation of scales such that there is a range for a length scale l, $\eta_u \ll l \ll L_u$ and $\max[\eta, \eta_\theta] \ll l \ll \min[L_u, L_\theta]$ that emerges, in which the molecular diffusivity (κ) and viscosity (ν) are not important. The two ranges are called *inertial* and *inertial-convective* subranges respectively. In the inertial and inertial-convective subranges, KOC theory [13–15] predicts the power-law scalings for $\langle(\Delta_r u)^2\rangle$ and $\langle(\Delta_r\theta)^2\rangle$ (or equivalently $E_u(k,t)$ and $E_\theta(k,t)$), which are given by

$$\langle(\Delta_r u)^2\rangle \propto r^{2/3}, \quad \eta \ll r \ll L_u \tag{1.7}$$

$$E_u(k) \propto k^{-5/3}, \quad k_{L_u} \ll k \ll k_\eta \tag{1.8}$$

and

$$\langle(\Delta_r \theta)^2\rangle \propto r^{2/3}, \quad \max[\eta, \eta_\theta] \ll r \ll \min[L_u, L_\theta] \tag{1.9}$$

$$E_\theta(k) \propto k^{-5/3}, \quad \max[k_{L_u}, k_{L_\theta}] \ll k \ll \min[k_\eta, k_{\eta_\theta}] \tag{1.10}$$

where k is the wavenumber and the subscripts for k denotes the wavenumber that corresponds to the length scale (e.g. $k_{L_u} = 2\pi/L_u$). The above derivation can be achieved by pure dimensional analysis on $E_u(k)$ and $E_\theta(k)$ in the inertial and inertial-convective subranges, in which the only relevant parameters are the wavenumber k and the dissipation rates of the velocity fluctuation (ϵ) and of the temperature fluctuations (ϵ_θ) since ν and κ are neglected [13–15].

1.2.3 Mixing in homogeneous turbulence without mean shear

For a complete mixing process, as shown in Fig. 1.1b, after discussing the structure of the velocity field in homogeneous turbulence, we proceed to discuss how a scalar is being convected in such velocity structure. We follow the treatment used in the literature [10, 11] by considering the large Pe regime, which is usually the case in turbulence, and the scalar θ is passive such as passive contaminants. Then, we can approximate θ is materially conserved and follows the velocity field before the molecular diffusion takes place. There are two famous problems such as single-particle dispersion (Taylor problem) and two-particle dispersion (Richardson problem) [2, 10, 16]. Here we only

focus on the Taylor problem. For the Taylor problem, the concept of *turbulent diffusion* and *effective diffusivity* will be introduced. The modeling of the effective diffusivity is essential to understand the mixing mechanisms in bubbly flows and it also contributes to the scalar fluctuations that will be discussed in Chapter 5. We note that the mixing process can be very different for flows with mean shear which we shall not consider in this section, see e.g. Refs. [2, 4, 10, 17].

Taylor dispersion and effective diffusivity

Let $\mathbf{X}(t)$ be the position of an infinitesimal fluid parcel or a passive contaminant. The Taylor problem asks for the root-mean-square distance $\langle \mathbf{X}^2 \rangle$ that a single particle migrates in a turbulent flow in a time t [18], which is equivalent to finding the size of a cloud of a passive dye being continuously injected at a fixed point in a turbulent flow [10]. The formulation of a fluid mechanical problem by following the trajectories of the fluid particles is the *Lagrangian* formulation. Let T_L be the Lagrangian integral time scale (i.e. the time scale after which the velocity of the fluid particle becomes uncorrelated) of the turbulent flow and $u'_{0,\mathrm{rms}}$ be the velocity standard deviation for the single-phase turbulent flow. In homogeneous isotropic turbulence, it is derived that [10,18]

$$\sqrt{\langle \mathbf{X}^2 \rangle} \approx u'_{0,\mathrm{rms}} t, \qquad \text{for } t \ll T_L, \tag{1.11}$$

$$\sqrt{\langle \mathbf{X}^2 \rangle} \approx \sqrt{2 u'^2_{0,\mathrm{rms}} T_L} \, t^{1/2}, \qquad \text{for } t \gg T_L, \tag{1.12}$$

meaning that the fluid particle or passive contaminant on average moved by a distance that is proportional to $t^{1/2}$ for large times [10]. The results for pair dispersion for different time scales are also reviewed in Ref. [16]. This result is typical for Brownian motion, and also typical for a solution of the diffusion equation (i.e. Eq. 1.3 without the advective terms at L.H.S.) [10], which leads to the name 'diffusion limit' for Eq. 1.12 [11]. Therefore, in the long time limit, we can also interpret results in Eq. 1.12 that the large-scale transport can be modelled as 'large-scale Brownian motion'. In this thesis, we focus on the dispersion in the long time limit.

Now we go back to the *Eulerian* description (physical quantities as a function of spatial coordinates), the dynamic equation of $\langle \theta \rangle$ in Eq. 1.4 can be turned into a diffusion equation if one uses the notion of *turbulent diffusivity*. Turbulent diffusivity, for temperature, may be thought as considering 'lumps' of fluid, moving in a turbulent flow, that exchange heat, which is an analogue of

molecules exchanging their kinetic energy. It is defined as [10]

$$-\langle \mathbf{u}'\theta' \rangle \equiv \kappa_t \nabla \langle \theta \rangle \quad \text{(isotropy assumed)}, \tag{1.13}$$

in which κ_t is a constant here because of homogeneous and statistically stationary turbulence. Then, Eq. 1.4 becomes,

$$\frac{\partial}{\partial t}\langle \theta \rangle = (\kappa + \kappa_t)\nabla^2 \langle \theta \rangle, \tag{1.14}$$

where we have imposed $\langle \mathbf{u} \rangle = \mathbf{0}$ in our problem of interest (which can be also achieved by changing our reference frame to be co-moving with the mean flow). We note that typically $\kappa_t \gg \kappa$ in turbulent flows [2, 10, 19]. For an instantaneous point source at the origin (not continuous injection [1]), Eq. 1.14 has a well-known solution in a Gaussian shape, which is given by

$$\langle \theta \rangle \ \propto \frac{1}{t^{3/2}} \exp\left[-\frac{r^2}{4(\kappa + \kappa_t)t} \right], \tag{1.15}$$

i.e. the size of a cloud of a passive dye increases roughly with $\sqrt{2(\kappa + \kappa_t)}t^{1/2}$ in an isotropic and homogeneous turbulence [10, 17], in which the time dependence coincides with Eq. 1.12 [10, 11]. Now we combine the results from the Lagrangian view and that from the Eulerian view. The turbulent dispersion for the Taylor problem in homogeneous isotropic turbulence is a *diffusive process* with an *effective diffusivity* $\kappa_{\text{eff}} \equiv \kappa + \kappa_t \approx \kappa_t$. Comparing the time dependence of the size of a cloud of passive dye with Eq. 1.12, we found that

$$\kappa_t \approx \kappa_{\text{eff}} = u'^2_{0,\text{rms}}T_L. \tag{1.16}$$

If one uses the Prandtl mixing length hypothesis, we can also write,

$$\kappa_t \equiv u'_{0,\text{rms}}l_m. \tag{1.17}$$

which defines the mixing length l_m [10]. l_m may be thought as the average size of the large eddies [10].

An important note for the effective diffusivity is that it can only be applied at the scale larger than the *coarse-grained* scale, since we have 'averaged' the 'eddies' at the smaller scale [11]. For Eqs. 1.16 and 1.17, the coarse-grained scale is the decorrelation time (Lagrangian integral time scale T_L) and the average size of the large eddies (e.g. the correlation length).

---

[1]The continuous injection case with a mean flow can be derived by integrating the point source solution since Eq. 1.3 is linear for passive scalar [2, 17].

Eddy diffusivity for anisotropic flows

For bubbly flows, the velocity statistics are anisotropic, as we will discuss in the next sections. In general, for anisotropic, non-homogeneous turbulence and non-statistically stationary turbulence, $\langle \mathbf{u}'\theta' \rangle$ depends on space and time and the turbulent diffusivity by definition is a second order tensor [20],

$$-\langle u_i'\theta' \rangle = \kappa_{t,ij}(\mathbf{x},t)\frac{\partial\langle\theta\rangle}{\partial x_j}. \tag{1.18}$$

Short conclusion

To conclude this subsection, we have used the Taylor problem to introduce the notion of turbulent diffusion and effective diffusivity, which can be mathematically modelled using Eqs. 1.16 or 1.17. These concepts and models are also used and extended in bubbly flows in order to understand the mixing mechanisms in bubbly flows at scales larger than the decorrelation scale, which will be discussed in the next section.

1.3 Bubble-induced agitations: homogeneous bubbly flows and the mixing

We refer to Fig. 1.1b for a general mixing process for Pe ≫ 1, in which the liquid agitation mechanism first need to be discussed. The liquid velocity fluctuations agitated by the rising bubbles only are called *bubble-induced agitations* (BIA), and homogeneous bubbly flows only has BIA as the liquid agitation mechanism [7]. Most of the results for the agitations and mixing in homogeneous bubbly flows are summarised in detail in Ref. [7]. The name 'pseudo-turbulence' is also used for indicating the turbulence induced by bubbles only [21].

1.3.1 Relevant parameters

Due to buoyancy, a bubble rises in a denser liquid. Let V_r be the bubble relative rise velocity, d be the bubble diameter and γ be the surface tension at the bubble-liquid interface. For bubble dynamics, two relevant dimensionless parameters are the bubble Reynolds number $\mathrm{Re}_{\mathrm{bub}} = V_r d/\nu$ and the Weber number that compares the inertial forces to the surface tension $\mathrm{We} = \rho V_r^2 d/\gamma$ [7]. Just like a flow around a sphere, $\mathrm{Re}_{\mathrm{bub}}$ has to be high enough in order to

generate a wake behind a bubble. The larger the Weber number, the smaller the effect of surface tension, and the bubbles are easier to deform. We restrict ourselves to the parameter regime $10 \leq \mathrm{Re}_{\mathrm{bub}} \leq 1000$ and $1 \leq \mathrm{We} \leq 4$ such that the wakes are strong enough, bubbles are deformed and exhibit ellipsoidal shapes. We also call the bubbly flows in this regime as *high-Reynolds bubbly flows*. Such parameter regime produces the $E_u(k) \propto k^{-3}$ scaling [7] as we will introduce in this section.

For a swarm of rising bubbles, an obvious control parameter is the gas volume fraction α. Therefore the relevant dimensionless parameters are $(\alpha, \mathrm{Re}_{\mathrm{bub}}, \mathrm{We})$. Note that V_r cannot be controlled directly and it is often measured after the creation of the bubbly flow. Therefore, strictly speaking, $\mathrm{Re}_{\mathrm{bub}}$ and We) are not control parameters but are the responses that characterise the system.

1.3.2   Agitation mechanisms

For each fast-rising bubble, the viscous boundary layer at the bubble-air interface transfers momentum to the carrier liquid, thereby producing liquid agitations. It is found that the fluctuations due to BIA have two parts. One is the agitation localized at the wake behind the bubbles which is dominant in confined bubbly flows because turbulence is suppressed [22]. The agitation at the vicinity of the bubbles are called *spatial fluctuations* [7] because the rising bubbles have insignificant clustering and randomly distributed in space, albeit there is a weak, long range ($\leq 20d$) vertical clustering [7,23]. Another agitation mechanism is the delocalized fluctuations that spread over the space due to the collective instability of the wakes (wake-wake interactions) because of high $\mathrm{Re}_{\mathrm{bub}}$ [7,24]. Since the delocalized fluctuations are from the flow instabilities, they are called *temporal fluctuations* [7,24]. The temporal fluctuations due to the collective instability of wake-wake interaction occurs in three-dimensional bubbly flows but are suppressed in confined bubbly flows [7]. The agitation mechanisms for BIA is summarised in Fig. 1.3, see page 21.

1.3.3   Structure of the velocity field: scaling properties

Next, we review the structure of the velocity field in homogeneous bubbly flows, which are generated by BIA. This helps one to understand how a scalar is advected by these structures.

Velocity fluctuation spectra

We note that this subsection on the spectral scalings can also be applied to Sec. 1.5.2 for the spectral scalings of the velocity fluctuations in turbulent bubbly flows. For more details on the spectra in turbulent bubbly flows, we refer to Sec. 1.5.2.

A notable scaling in the wavenumber spectra $E_u(k)$ or frequency spectra $\mathcal{P}_u(f)$ at a fixed spatial coordinate of the velocity fluctuations in high-Reynolds bubbly flows is given by

$$E_u(k) \propto k^{-3}, \quad \mathcal{P}_u(f) \propto f^{-3} \tag{1.19}$$

which are observed to be robust for the parameter regime $10 \leq \mathrm{Re_{bub}} \leq 1000$, $1 \leq \mathrm{We} \leq 4$ and $\alpha > 0$ [7] and the presence of wakes behind the bubbles is necessary in order to observe the -3 scaling [7, 25]. Note that $\mathcal{P}_u(f)$ can be transformed into $E(k)$ if there is a fast, unidirectional mean flow or a fast moving probe that measures velocity such that Taylor frozen-flow hypothesis can be applied [9]. The scaling is first experimentally observed in a high-Reynolds bubbly flow with incident turbulence in Ref. [21] and they argued that the -3 scaling is attributed to the balance between the viscous dissipation and the production of the velocity fluctuation production due to the rising bubbles in spectral space. Mathematically, one can derive the dynamic equation of a velocity spectrum $E_u(k, t)$ from the incompressible Navier-Stokes equation (Eqs. 1.1 and 1.2) (see e.g. Refs. [2, 9]),

$$\frac{\partial}{\partial t} E_u(k, t) + 2\nu k^2 E_u(k, t) = T_u(k, t) + \Pi_u(k, t), \tag{1.20}$$

where $T_u(k, t)$ is the local net spectral transfer and $\Pi_u(k, t)$ is the spectral production. In bubbly flows, there are BIA that contribute to $\Pi_u(k, t)$. In a statistical steady state, the time derivative is zero. We assume $\Pi_u = \Pi_u(\epsilon, k)$, where ϵ is the viscous energy dissipation rate, which may be justified if the production due to the bubbles are all dissipated by viscosity at a rate of ϵ. Then, by dimensional analysis, $\Pi_u \propto \epsilon k^{-1}$, If we further neglect T_u, of which the time scale is argued to be slow as compared to the other terms in Eq. 1.20 [21], rearranging terms in Eq. 1.20 (see Ref. [7, 21]),

$$2\nu k^2 E_u(k) \propto \epsilon k^{-1} \tag{1.21}$$

which implies

$$E_u(k) \propto k^{-3}. \tag{1.22}$$

Apart from the above derivation of the start of the -3 scaling, we note that it is also shown experimentally by using array of spheres [26] and numerically by using Large Eddy Simulations (LES) [24] that the two contributions from BIA, namely spatial fluctuations (due to the spatially random distribution of the dispersed phase) and temporal fluctuations (due to collective instability of wake-wake interactions which spread over the space), can individually lead to the -3 scaling [7, 24, 26].

The characteristic scale of the -3 scaling

A definite determination of the characteristic scale of the -3 scaling is lacking [7]. However, a candidate is proposed and roughly coincides with the onset scale of the -3 scaling.

As reviewed by Ref. [7], in the wavenumber space, a good candidate is given by [7, 27]

$$\lambda_{\text{bub}} \equiv d/C_D \tag{1.23}$$

where C_D is the drag coefficient of the bubbles, since it was 'found to be related to the length of the bubble wake' [7, 28]. The drag coefficient is the ratio $C_D = 2F_D/(\rho V_r^2 A_{bub})$, where F_D is the drag force acting on the bubble and A_{bub} is the cross-sectional area of the bubble normal to the rising direction [29]. Intuitively, the larger the drag force, the more momentum is transported to the liquid from the viscous boundary layer of the bubble-liquid interface in the form of a wake behind the bubble.

In the frequency space, the onset frequency can be extended by considering the frequency scale

$$f_{\text{bub}} \equiv \frac{V_r}{\lambda_{\text{bub}}} = C_D \frac{V_r}{d}, \tag{1.24}$$

which roughly indicates the onset frequency of the f^{-3} scaling [30].

Velocity structure functions

The velocity structure functions were investigated in a bubble column which is at the transition from homogeneous to heterogeneous case and at heterogeneous case [31]. However, the authors in Ref. [31] do not check the scaling of the structure functions. For turbulent bubbly flows [32], see Sec. 1.5.2 for the discussion.

1.3.4 Scalings of the velocity standard deviation

In homogeneous bubbly flows, when α increases, the bubble-induced agitation is stronger because there are more bubbles producing agitations per unit volume. Therefore we expect the velocity fluctuation increases with α. As there are wakes behind the bubbles which are not rotationally symmetric, the statistical isotropy is broken and we expect the velocity fluctuations to be *anisotropic*. Let u'_x and u'_z be the horizontal and vertical velocity fluctuations. It is found out that

$$\langle u_x'^2 \rangle^{1/2} = \gamma_x V_0 \alpha^{0.4}, \tag{1.25}$$
$$\langle u_z'^2 \rangle^{1/2} = \gamma_z V_0 \alpha^{0.4}, \tag{1.26}$$

where V_0 is the rise velocity of a isolated bubble, γ_x and γ_z are constants [27], and many studies confirm that $\gamma_z > \gamma_x$ [7]. The scalings in Eqs. 1.25 and 1.26 are due to the combination of the spatial and temporal fluctuations in bubbly flows [24]. Such scaling properties are useful because these are the kinematics of the mixing of a scalar which are used, for example, for estimating the effective diffusivity (Eqs. 1.16 and 1.17) in bubbly flows.

1.3.5 Mixing due bubble-induced agitation

With the knowledge of the structure of the velocity field, we may now discuss how a scalar is advected by such velocity structure. For homogeneous bubbly flows, since there are only BIA, we only need to consider the mixing due to BIA. As there are two agitation mechanisms in BIA, we may expect there are also two mixing mechanisms correspondingly in BIA. Indeed, BIA involves also two mixing mechanisms, namely the capture-release mechanism which describes a scalar entrained in a wake behind a bubble and then released [33, 34] and the liquid agitations from the collective instability in the liquid phase due to wake-wake interactions that spread over space [7, 24].

The dominant mixing mechanism is different for confined bubbly flows and three-dimensional bubbly flows. In a confined bubbly flow, the turbulence is suppressed and the velocity disturbance only comes from the wakes localised at the bubbles and the direct interactions between them [7, 22], implying that only the capture-release mechanism is present in a confined bubbly flow [33, 34]. This capture-release mechanism, however, is found to be not a pure diffusive process [33, 34].

For three-dimensional homogeneous bubbly flows, the mixing process was found to be dominated by the mixing due to the fluctuations from wake-

wake interaction and it was found to be well-described by a diffusive process [35]. The release of a cloud of passively advected, low-diffusive dye in a three-dimensional homogeneous bubbly flows was experimentally studied in Ref. [35]. They find that the concentration field of the dye follows a superposition of Gaussian profiles in which the size for each superposed point source increases as $t^{1/2}$ (Eq. 1.15) [35]. The superposition holds because of the linearity of Eq. 1.3 for passive scalar [2, 17]. The spreading is faster in the vertical direction [35]. This implies that the mixing of three dimensional BIA is an anisotropic, regular diffusive process [35]. The dispersion in the turbulence generated by BIA is dominant over the convection due to capture-release mechanism [35], in which the agitation is the collective instability of the wake-wake interaction that spreads over space [7, 24]. The effective diffusivity model in Eq. 1.16 for bubbly flows combines the knowledge of the scalings of velocity fluctuations from BIA (Eqs. 1.25 and 1.26) and the identification of the decorrelation time scales in BIA [35]. Two regimes for α are identified in Ref. [35]. For low α, since the turbulence is homogeneous, the correlation time scale is the Lagrangian integral time scale T_L which can be approximated by the ratio between the Eulerian integral length scale Λ and the velocity standard deviation $u'_{i,\mathrm{rms}}$, i.e. $T_L = \Lambda/u'_{i,\mathrm{rms}}$ [35, 36]. Substituting the scalings of the velocity fluctuations (i.e. $u'_{i,\mathrm{rms}} \propto \alpha^{0.4}$ from Eqs. 1.25 and 1.26) into Eq. 1.16, we have the horizontal (D_x^{low}) and vertical (D_z^{low}) effective diffusivity

$$D_x^{\mathrm{low}} = k_l u'_{x,\mathrm{rms}} \Lambda \propto \gamma_x \alpha^{0.4} \sim \alpha^{0.5}, \tag{1.27}$$

$$D_z^{\mathrm{low}} = k_l u'_{z,\mathrm{rms}} \Lambda \propto \gamma_z \alpha^{0.4} \sim \alpha^{0.5}, \tag{1.28}$$

where k_l is a constant of order one, the experimentally found Eulerian integral length scale is constant over α and the approximation of the scaling $\alpha^{0.5}$ is rough [35]. For higher α, the successive bubble passage time $T_{2b} = 2d/(3\chi^{2/3}\alpha V_r) \propto \alpha^{-1}$, where χ is the mean aspect ratio of the bubbles, becomes smaller and can be lower than T_L [35]. The fluid parcel is interrupted by the successive passage of bubbles and the decorrelation time scale becomes T_{2b} instead, implying that, by replacing T_L by T_{2b} in Eq. 1.16 and substituting $u'_{i,\mathrm{rms}} \propto \alpha^{0.4}$ from Eq. 1.25 and 1.26, we have the horizontal (D_x^{high}) and vertical (D_z^{high}) effective diffusivity:

$$D_x^{\mathrm{high}} = k_h u'^2_{x,\mathrm{rms}} T_{2b} \propto \gamma_x \alpha^{-0.1}, \tag{1.29}$$

$$D_z^{\mathrm{high}} = k_h u'^2_{z,\mathrm{rms}} T_{2b} \propto \gamma_z \alpha^{-0.1}, \tag{1.30}$$

where k_h is a constant of order one. This theoretical prediction suggests that the effective diffusivity has a very weak dependence on α which agrees with the

experimental results that the effective diffusivity is approximately constant for high α [35].

There is an application of the above modeling to another mixing problem in bubbly flows. We use the effective diffusivity of temperature in homogeneous bubbly flows to explain the scaling of the dimensionless heat transfer, Nusselt number (Nu), as a function of α in a vertical convection setup [37], see also Fig. 2.1 on page 35 but consider the case of homogeneous bubbly flows. We mention this work because Chapter 2 in this thesis extends this work to inhomogeneous bubbly flows to study the interactions of different mixing mechanisms. From the definition of the Nusselt number, it is the total heat flux averaged over an area and over time normalised by the heat flux for the conduction case [38]. The heat flux is composed of the convective heat flux and molecular heat flux [2],

$$\text{Nu} = \frac{\langle u_i T \rangle_{A,t} - \kappa \langle \partial T / \partial x_i \rangle_{A,t}}{\kappa \Delta T / L}, \tag{1.31}$$

where T is the temperature, the x_i denotes the horizontal direction, $\langle . \rangle_{A,t}$ denotes average over time and over a cross-sectional area parallel to the vertical walls, and ΔT is the temperature difference between the two vertical walls. Nu is conserved for different distances from the vertical walls, therefore it can be also defined as the area and time averaged heat flux at the wall divided by the heat flux for the conduction case (see Eq. 2.2 in page 33). Experimentally, it is found that $\text{Nu} \propto \alpha^{0.45 \pm 0.025}$ for $0\% < \alpha < 5\%$ for homogeneous bubbly flows [37].

Now we explain the empirical scaling relation theoretically with the eddy diffusivity model in homogeneous bubbly flows [37]. First, Nu is dominated by the convective heat flux $\langle u_i T \rangle_{A,t}$ in turbulent flows when it is away from the walls, implying that $\text{Nu} \propto \langle u_i T \rangle_{A,t}$ at the bulk. Second, since the mean horizontal velocity is zero in the experiments of Ref. [37], $\text{Nu} \propto \langle u_i T \rangle_{A,t} = \langle u_i' T \rangle_{A,t} = \langle u_i' T' \rangle_{A,t}$, where $T = T' + \langle T \rangle$ and $\langle u_i' \langle T \rangle \rangle_{A,t} = 0$. Third, we assume the ensemble average is the same as the average over a vertical cross-section area and time, i.e. assuming the turbulent heat flux does not change vertically in the bulk in homogeneous bubbly flows: $\langle u_i' T' \rangle_{A,t} \approx \langle u_i' T' \rangle$, implying $\text{Nu} \propto \langle u_i' T' \rangle$. Furthermore, we apply the definition of eddy diffusivity D_{ii} in i-direction (Eq. 1.18), approximate it to be dominant over the molecular diffusivity and assume the scaling relation of the effective diffusivity $D_{ii} \propto \alpha^{0.4}$ for low diffusive dye in homogeneous bubbly flows for low α (Eqs. 1.27 and 1.28) is also valid for

---

[2]Similar to the definition of the Nusselt number in Rayleigh-Bénard convection [39]

the temperature mixing in homogeneous bubbly flows[3]. Combining the above approximations and assumptions, we have the theoretical scaling relation [37],

$$\mathrm{Nu} \propto \langle u_i T \rangle_{A,t} \approx \langle u_i' T' \rangle \approx -D_{ii} \frac{\partial \langle T \rangle}{\partial x_i} \propto \alpha^{0.4}, \qquad (1.32)$$

which is close to the experimental scaling relation $\mathrm{Nu} \propto \alpha^{0.45 \pm 0.025}$ for $0\% < \alpha < 5\%$ [37]. This suggested that the mixing in homogeneous bubbly flows superposed in a vertical convection setup is a diffusive process [37] as opposed to the single-phase vertical convection case that there is a large-scale circulation induced by density difference due to buoyancy [37]. We note that in Chapter 2, by using the same setup as Ref. [37], we extend our study of heat transfer to inhomogeneous bubbly flows.

We emphasize again that the original Taylor problem that introduced the effective diffusivity in Sec. 1.2.3 is applied to homogeneous and isotropic turbulence but the essence of the use of the effective diffusivity is to consider the typical velocity fluctuation and the time when the velocity of a fluid particle decorrelates, which in this sense can be generalized. Furthermore, in other statistically homogeneous flows, if the profile of the scalar field can be described by a superposition of point source solutions to the diffusion equation (i.e. the solution of Gaussian shape of which the size evolves in $\sqrt{t}$, see Eq. 1.15), then the mixing process is a diffusive process. Because of these reasons, the concept of effective diffusivity and the diffusion process can be applied to homogeneous bubbly flows even though the flows are anisotropic and have different decorrelation times.

To conclude, we discussed that BIA has two mixing mechanisms, namely the capture-release mechanism and the turbulent diffusion in which the turbulence is generated by the collective instability of the wake-wake interaction that spreads over space [7, 24]. The latter mechanism is a dominant mixing mechanism in three-dimensional bubbly flows, which causes dispersion in turbulence [35]. Therefore, the mixing process can be described as a diffusive process by modelling the effective diffusivity extending Eq. 1.16 in which the velocity fluctuations follows $u_{i,\mathrm{rms}}' \propto \alpha^{0.4}$ and the decorrelation time scale being the Lagrangian integral time scale for low α and being the average time for successive bubble passages T_{2b} [35].

---

[3]It is noted in Ref. [37] that, in general, the effective diffusivity depends on the Péclet number [40]. The Péclet number for the temperature is different from that for the low diffusive dye in the same flow conditions because their molecular diffusivities are different.

1.3.6 Structure of the scalar field: scaling properties

As a result of the mixing of the scalar field due to the convection of the velocity field and the molecular diffusion, there is a structure of the scalar field at different scales. For high-Reynolds bubbly flows, the study of scalar spectra is limited. In a confined bubbly thin cell, the scalar spectral scaling $\mathcal{P}_\theta \propto f^{-3}$ is observed by using fluorescent dye as the passive scalar [41]. They also found that the onset frequency of f^{-3} scaling is roughly V_r/d.

$$\mathcal{P}_\theta(f) \propto f^{-3} \qquad \text{(confined bubbly flows)}. \tag{1.33}$$

This coincides with the -3 scaling in the frequency spectra in confined bubbly flows [22]. For the -3 scaling in the velocity spectra, it is argued that the random disturbances from the bubbles can lead to the -3 scaling [42]. Extending this to passive scalar in confined bubbly flows, it is argued that the -3 scaling in scalar frequency spectra is a result of the mixing of the dye due to capture-transport-release because of the wakes of the bubbles (discussed in Sec. 1.3.5) [41].

For three-dimensional bubbly flows, as discussed in the previous section, the dominant mixing mechanism in BIA is the turbulent diffusion through the turbulence generated by the delocalised fluctuations due to wake-wake interactions that spread over space. It is then of interest whether this will also lead to a -3 scaling. In a three-dimensional vertical convection setup, the scalar spectra are measured with freely rising high-Reynolds bubbles but the frequencies related the -3 scaling of the energy spectra in bubble-induced agitations are not resolved [37]. Therefore whether -3 scaling will also be observed for scalar spectra in homogeneous bubbly flows is subject to future research.

For turbulent bubbly flows, the spectral scaling of the scalar field will be studied in Chapter 4.

1.4 Agitation and mixing in inhomogeneous bubbly flows

Mixing in inhomogeneous bubbly flows is one of the focus in this thesis (Chapter 2). After the previous two sections discussing separately SIT and BIA, we now briefly describe how the two agitation mechanisms emerge in inhomogeneous bubbly flows, and then discuss the corresponding mixing mechanisms.

1.4.1   Agitation mechanisms

To understand the mixing mechanisms, we need to understand the liquid agitation mechanisms first, see Fig. 1.1b. If a bubbly flow is inhomogeneous, a mean liquid flow can be induced because of the inhomogeneity of the buoyancy force in space due to non-uniform gas volume fraction, similar to natural convection [7, 8]. In this case, there will be agitations caused by the nonlinearity of the mean liquid flow (the Reynolds number being large) as discussed in the SIT section (Sec. 1.2), though the turbulence induced by this induced mean liquid flow can be inhomogeneous and anisotropic. We recall that the velocity fluctuations induced by the inherent nonlinearity of the mean liquid flow are called SIT in Ref. [7], though it is possible to have no mean shear layer in the flow for SIT (but there are small-scale velocity gradients). The turbulence in the liquid phase in turn will affect the dispersed phase, implying there are interactions between BIA and SIT [7]. In addition, if the induced mean flow has a large-scale mean velocity gradient (a mean shear layer), there is further production of velocity fluctuations [9]. As such a large-scale circulation or even a shear layer can be formed because of the inhomogeneity of the bubbles [7, 43–45]. Such case is investigated in Chapter 2 in this thesis.

1.4.2   Mixing mechanisms

For a general high-Reynolds bubbly flow without external forced turbulence, the mixing mechanisms can be summarised as the mixing due to BIA, SIT and buoyancy-driven large-scale circulation [43–45]. The agitation and mixing mechanisms for freely rising high-Reynolds bubbly flows are summarised in Fig. 1.3 in page 21.

As discussed in the agitation section, there are BIA and SIT. The scale of BIA is *at most* at the scale λ_{bub} (Eq. 1.23) we mentioned for the onset scale of k^{-3} scaling and the scale SIT is at most the integral-scale of the SIT. When there is a mean flow induced by the inhomogeneity of bubble distributions such as large-scale circulation, the length and time scale for this circulation can be much larger than the BIA and SIT.

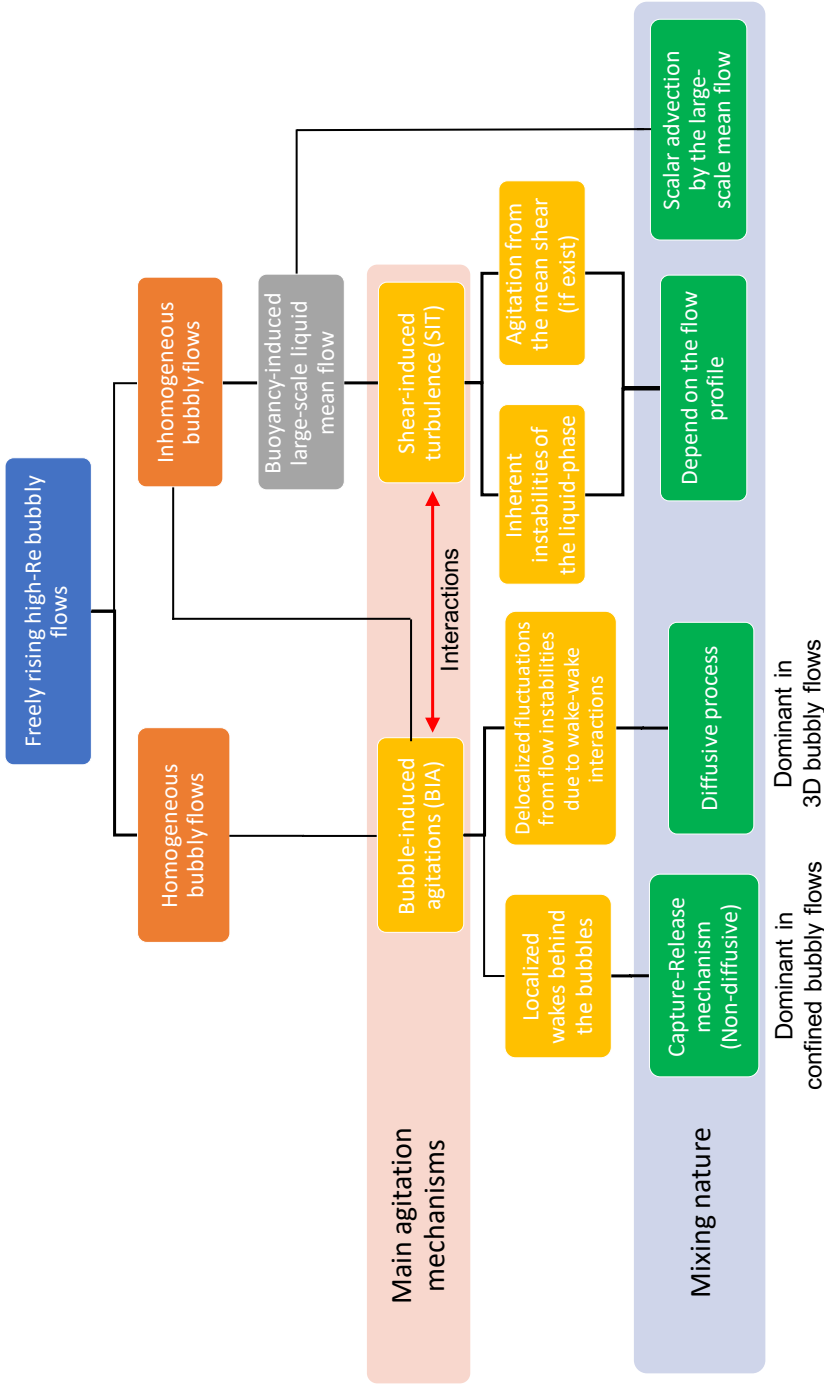Figure 1.3: The agitation and mixing mechanisms of freely rising high-Reynolds bubbly flows. The boxes with brown, yellow and green colors represent two different scenarios in a freely rising high Re-bubbly flow, the liquid agitation mechanisms and the mixing nature of the corresponding agitation mechanisms, respectively. See the main text in the Introduction for the explanations and the references therein.

As also shown in Fig. 1.1b, the structure of the velocity field at these scales are relevant to the advection of a scalar. As an example, the mixing mechanisms in a low-sheared inhomogeneous bubbly flow were decomposed into the advection due to the large-scale recirculation and the diffusion due to BIA [44]. They approximated the corresponding mixing time by using the advection velocity and effective diffusivities due to BIA (Eqs. 1.27 and 1.28) respectively, and compared them with the experimental mixing time [44]. It was found that with the aid of large-scale circulation, the mixing time was significantly reduced [44]. When SIT is also present and there is a mean shear layer, the eddy diffusivity due to SIT, for example by using the turbulent Schmidt number to relate the eddy diffusivity to the eddy viscosity of the velocity field, also needs to be taken into account [43, 44].

Therefore, in general, there are three mixing mechanisms in freely rising high-Reynolds bubbly flows, namely BIA, SIT and the large-scale circulation induced by bubbles inhomogeneity [7, 43–45]. This general situation will be encountered in Chapter 2.

A summary of the mixing processes for inhomogeneous bubbly flows can be found in Fig. 1.3, see page 21.

1.5 Agitation and mixing in homogeneous turbulent bubbly flows without mean shear

Apart from inhomogeneous bubbly flows that experience the interaction between BIA and SIT, turbulent bubbly flows also experience such interaction. The mixing in turbulent bubbly flows is also a focus in this thesis (Chapter 3–5). Turbulent bubbly flows are high-Reynolds bubbly flows *with incident turbulence* or externally forced turbulence. This can be produced in a grid-turbulence that has a mean flow with bubbles rising in it. To simplify the problem, we only consider homogeneous turbulent bubbly flows without mean shear, which is also the case in Chapter 3–5 when we consider the region away from the boundaries.

1.5.1 Agitation mechanisms and the relevant parameters

There are two agitation mechanisms in homogeneous turbulent bubbly flows, namely BIA and SIT that stems from the nonlinearity from the externally forced mean flow (incident turbulence) [7]. Although the name SIT contains the word 'shear', we restrict ourselves to the case *without* large-scale mean

shear of the flow because there are extra agitations produced by the mean shear [9], though certainly there are small-scale velocity gradients near the bubbles or in the liquid. Moreover, to distinguish the SIT for inhomogeneous bubbly flows that are purely induced by buoyancy, the SIT in turbulent bubbly flows are forced externally (e.g. by external pressure gradient) in addition to the modification due to the interaction with BIA. Therefore, the parameters used for single-phase homogeneous turbulence without mean shear (Sec. 1.2) are also applicable, though they may not be independent with the main parameter, the bubblance parameter, in turbulent bubbly flows (see below).

The bubblance parameter

To compare the effect from the two agitations, the bubblance parameter b, which is the ratio of the energy of the velocity fluctuations injected by the rising bubbles to that from the incident turbulence, was introduced, [21, 30, 32, 46],

$$b = \frac{V_r^2 \alpha}{u'^2_{0,\mathrm{rms}}} \qquad (1.34)$$

where $u'_{0,rms}$ is the velocity standard deviation when there are no bubbles in the flow, and the numerical prefactor is set to be unity because there are still discussions on the exact fluctuating energy injected by the bubbles [21, 27, 30, 47]. For $b = 0$, it is the case when no bubbles are injected (single-phase turbulence, discussed Sec. 1.2) or there are no relative flow against the bubbles. For $b = \infty$, it can be case when $u'^2_{0,\mathrm{rms}} = 0$, which are high-Reynolds bubbly flows without incident turbulence as discussed in Sec. 1.3 (or with the name 'pseudo-turbulence' [21]). In between $b = 0$ and $b = \infty$ are the cases where the two contributions are present and possibly interacting with each other.

Finally, likewise, we still restrict to the parameter regime as discussed in Sec. 1.3 in which the wakes of the bubbles are present for $b \neq 0$.

1.5.2   Structure of the velocity field: scaling properties

To understand the mixing mechanisms in turbulent bubbly flows, the knowledge of the structure of the velocity field is needed.

Velocity fluctuation spectra

From the previous two sections on the structure of the velocity field in homogeneous turbulence and homogeneous bubbly flows, there are two spectral

scalings, namely $k^{-5/3}$ in the inertial range and k^{-3} in the bubble-induced subrange. One may wonder whether the two scalings coexist when the above two subranges are separated.

The discussion for the spectral scalings of the velocity field for high-Reynolds bubbly flows (Sec. 1.3.3) are applicable to this section. In this subsection, we include also the results from turbulent bubbly flows.

Fixed point velocity measurements are performed in a swarm of high-Reynolds bubbles rising within incident turbulence in Ref. [30, 46]. They both show that the energy frequency spectra exhibit $f^{-5/3}$ scaling and then followed by f^{-3} scaling when $b > 0$ [30, 46]. We summarise the results of Ref. [30] in mathematical forms, which are given by

$$\begin{cases} \mathcal{P}_u(f) \sim f^{-5/3}, & 1/T_L < f \lesssim f_c \\ \mathcal{P}_u(f) \sim f^{-3}, & f \gtrsim C_D V_r/d, \end{cases} \tag{1.35}$$

where $f_c = 0.14 V_r/d$. In the velocity frequency spectra in Ref. [30], there is a 'bump' just before the f^{-3} scaling subrange when b is large enough, indicating a strong energy injection from that frequency. There are three candidates of the 'bump' frequency, which are summarised in Ref. [30]. The three candidates, all proportional to V_r/d, are:

$$f_c \equiv \frac{0.14 V_r}{d}, \qquad f_v \equiv \frac{\text{St} V_r}{d}, \qquad f_b \equiv \frac{V_r}{2\pi d}, \tag{1.36}$$

where f_c was first discovered in Ref. [24] which indicated the frequency of the energy peak due to collective instability of bubbles in a Navier-Stokes simulation in which the bubbles were modelled by fixed momentum sources, f_v is the vortex shedding frequency with the corresponding Strouhal number St, and f_b was proposed in Ref. [46], which stated that f_b is a 'frequency that is representative of the bubbles' [46].

Velocity structure functions

To the author's knowledge the only work which investigates the velocity structure functions in turbulent bubbly flows is Ref [32]. In Ref. [32], the Kolmogorov -5/3 scaling law (Eq. 1.8) is observed but -3 scaling is not observed. There are also no scalings observed for the velocity structure functions [32].

In this Introduction, we only focus on the scaling properties of bubbly flows in which a -3 scaling is observed. Therefore, since the energy spectra does not exhibit -3 scaling in Ref. [32], it is not clear whether the corresponding results on the velocity structure functions are relevant in our considerations.

1.5.3 Scalings of the velocity standard deviation

As mentioned, the main parameter for homogeneous turbulent bubbly flows is the bubblance parameter b. The empirical scaling of vertical velocity fluctuations $u'_{z,\mathrm{rms}}$ as a function of b was experimentally found in Ref. [30] while the scaling for the horizontal velocity fluctuation $u'_{x,\mathrm{rms}}$ for the same flow conditions as Ref. [30] was reported in Ref. [48]. They are given by [30, 48],

$$\begin{cases} u'_{x,\mathrm{rms}} \propto u'_{0,\mathrm{rms}} b^{0.25} \\ u'_{z,\mathrm{rms}} \propto u'_{0,\mathrm{rms}} b^{0.4} \end{cases} , \quad 0 < b < b_c, \tag{1.37}$$

$$\begin{cases} u'_{x,\mathrm{rms}} \propto u'_{0,\mathrm{rms}} b^{1.0} \\ u'_{z,\mathrm{rms}} \propto u'_{0,\mathrm{rms}} b^{1.3} \end{cases} , \quad b > b_c, \tag{1.38}$$

where $b_c \approx 0.7$. The exponents are different for different directions meaning that the agitation is anisotropic. We note that it is unclear whether the value of b_c is universal constant but the main observation here is that there are two regimes of the velocity fluctuations in turbulent bubbly flows (which are also related to the structure of primary and secondary wakes of the bubbles, see Ref. [30]).

1.5.4 Mixing mechanisms

Since BIA and SIT are both present in homogeneous turbulent bubbly flows, the mixing mechanism involves the combination of the two agitations. The mixing in three-dimensional BIA and homogeneous turbulence without mean shear can both be described by a diffusion process (discussed in Sec. 1.2.3 and 1.3.5). By investigating the spread of a continuous point source of dye in a homogeneous turbulent bubbly flow without mean shear, it was found that the spreading of a low-diffusive dye in such flow is also a *diffusive process* [48]. They modelled the effective diffusivity D_{xx} in the horizontal direction by considering the low α and high α regime [48]. The crossover α_c occurs when the time scale of successive passage of the bubbles $T_{2b} = \frac{d}{\chi^{2/3}V_r\alpha}$ is similar to the integral time scale T_L of the incident turbulent flow, which is given by [48]

$$\alpha_c = \frac{d}{\chi^{2/3}V_rT_L}. \tag{1.39}$$

The dimensionless diffusion coefficient $D_{xx}/(T_{2b}gd)$ was found to be an increasing function of α/α_c [48],

$$\frac{D_{xx}}{T_{2b}gd} = f\left(\frac{\alpha}{\alpha_c}\right) \tag{1.40}$$

and the transition of the two regimes occurred at $\alpha/\alpha_c \approx 3$ after which the increase is at a steeper rate [48].

The main message here is that, D_{xx} is not a monotonic function of α since Eq. 1.40 shows that it is the *normalised* effective diffusivity that increases with α/α_c and that T_{2b} and α_c also depends on α. For example, D_{xx} is found to decrease with α when the incident turbulent intensity is high in Ref. [48]. This is different from the effective diffusivity in homogeneous bubbly flows (Eqs. 1.27 to 1.30) which either increases with α or has a weak dependence of α.

1.5.5   Structure of the scalar field: scaling properties

As a result of the mixing due to the convection of the velocity field and the molecular diffusion, there is also a structure of the scalar field in a turbulent bubbly flow.

Similar to the scalar spectra for confined bubbly flows, the first question is whether the -3 scaling also exist in turbulent bubbly flows. If it exists, the second question will be whether the -5/3 scaling and the -3 scaling (if exist) can coexist also in the scalar spectra, just like the velocity fluctuation spectra in turbulent bubbly flows (Eq. 1.35).

To the best of the author's knowledge, previously there are no studies on the scaling properties of scalar fluctuations in turbulent bubbly flows. In Chapter 4, we will explore the scaling properties of the scalar spectra while Chapter 5 will investigate the scaling properties on the scalar structure functions.

1.6   Summary of the scaling relations for bubbly flows

Table 1.1 in page 29 summarised the scaling relations for homogeneous bubbly flows, single-phase homogeneous turbulence without mean shear and homogeneous turbulent bubbly flows without mean shear.

Open Questions

From the summary above, we find some open questions that remain to be answer in order to improve our understanding of the scalar mixing in bubbly turbulence.

- How do the three mixing mechanisms (BIA, SIT and large-scale buoyancy-driven circulation) in inhomogeneous bubbly flows affect the scalar transfer?
- What are the effects of the rising bubbles on the spectral scalings of the scalar fluctuations?
- How do the bubbles affect the integral statistics such as scalar variance and the PDFs of the scalar fluctuations in turbulent bubbly flows?
- What are the scaling properties for the scalar structure functions in turbulent bubbly flows?

A guide through the thesis

From the summary above, there are three mixing mechanisms in a general freely rising high Reynolds bubbly flow, namely bubble-induced turbulence (BIA), shear-induced turbulence (SIT) and buoyancy-driven large-scale circulation. The interactions between these three mechanisms are not clear. Therefore, Chapter 2 focuses on inhomogeneous bubbly flows in which the three mixing mechanisms manifest at the same time. This is achieved by studying the heat transfer from one vertical hot wall to another cold wall in a rectangular bubble column with millimetric bubbles injected from half of the injection section (near the hot or near the cold wall). The relative strength of the three mixing mechanisms can be controlled by the gas volume fraction. After that, in order to study the combined effect of forced turbulence and bubble-induced agitations on the mixing of a scalar, the Twente Mass and Heat Transfer Tunnel (TMHT) is built (Chapter 3). It will be demonstrated that temperature and mass transfer measurements in turbulent bubbly flows are possible in a controlled manner. With this setup, we are able to produce a turbulent bubbly thermal mixing layer in which the temperature fluctuations are induced in a turbulent bubbly flow. The temperature fluctuation spectra are calculated and the spectral properties are revealed in Chapter 4. In Chapter 5, we investigate the effect of bubbles on the integral statistics such as temperature variance and the probability density functions of temperature

fluctuations in a turbulent bubbly thermal mixing layer. Finally the small-scale statistics such as the scaling properties of the temperature structure functions will be investigated in the second part of Chapter 5.

	Homogeneous bubbly flows	Homogeneous turbulence without mean shear	Homogeneous turbulent bubbly flows without mean shear
Main parameters	Re_{bub}, We, α [7]	Re_{λ_u}, $\mathrm{Pe}_{\lambda_{(u,\theta)}}$ [12]	$b = \alpha V_r^2/u_0'^2$ [21,30,32,46]
Velocity fluctuation scaling	$u_i = \gamma_i V_0 \alpha^{0.4}$, for $\gamma_z > \gamma_x$ [7,27]	/	$u'_{(x,z),\mathrm{rms}} \propto u'_{0,\mathrm{rms}} b^{(0.25,0.4)}$ for low $b > 0$; $u'_{(x,z),\mathrm{rms}} \propto u'_{0,\mathrm{rms}} b^{(1.0,1.3)}$ for high $b > 0$ [30]
Velocity spectral scaling	$E_u(k) \propto k^{-3}$, for $k \gtrsim C_D/d$ [7]	$E_u(k) \propto k^{-5/3}$, for $k_{L_u} \ll k \ll k_\eta$ [13]	$f^{-5/3}$ for $1/T_L < f \lesssim 0.14 V_r/d$, f^{-3} for $f \gtrsim C_D V_r/d$ [30]
Velocity structure function	Studied in the bubbly column which is at the transition from homogeneous to heterogeneous case and at heterogeneous case but the scaling was not checked [31].	$\langle(\Delta_r u)^2\rangle \propto r^{2/3}$, for $\eta \ll r \ll L_u$ [13]	Studied in Ref. [32] but it does not observe k^{-3} scaling in their energy spectra [32]
Scalar spectral scaling	$\mathcal{P}_\theta(f) \propto f^{-3}$, for $f \gtrsim V_r/d$ (2D bubbly flow) [41]	$E_\theta(k) \propto k^{-5/3}$, $\max[k_{L_u}, k_{L_\theta}] \ll k \ll \min[k_\eta, k_{\eta_\theta}]$ [14,15]	see Chapter 4
Scalar structure function	Not studied	$\langle(\Delta_r\theta)^2\rangle \propto r^{2/3}$, $\max[\eta, \eta_\theta] \ll r \ll \min[L_u, L_\theta]$ [14,15]	see Chapter 5
Mixing process	Diffusive process (three-dimensional flows) $D_i = k_l u'_{i,\mathrm{rms}}\Lambda$ for low α $D_i = k_h u'^2_{i,\mathrm{rms}} T_{2b}$ for high α [35]	Diffusive process, effective diffusivity $\kappa_{\mathrm{eff}} = u'^2_{0,\mathrm{rms}} T_L$ [18]	Diffusive process $\frac{D_{xx}}{T_{2b}gd} = f\left(\frac{\alpha}{\alpha_c}\right)$, where f is an increasing function and the increase becomes steeper for $\alpha \gtrsim \alpha_c$ [48]

Table 1.1: Summary of the present findings on three classes of turbulent flows: homogeneous bubbly flows, homogeneous turbulence without mean shear and homogeneous turbulent bubbly flows without mean shear. The definitions of the notations refer to the main text of the Introduction.

It's time for Science!

Sander G. Huisman

2

Heat transport in inhomogeneous bubbly flow without incident turbulence [1]

Abstract

In this work we study the heat transport in inhomogeneous bubbly flow. The experiments were performed in a rectangular bubble column heated from one side wall and cooled from the other, with millimetric bubbles introduced through one half of the injection section (close to the hot wall or close to the cold wall). We characterise the global heat transport while varying two parameters: the gas volume fraction $\alpha = 0.4\% - 5.1\%$, and the Rayleigh number $Ra_H = 4 \times 10^9 - 2.2 \times 10^{10}$. As captured by imaging and characterised using Laser Doppler Anemometry (LDA), different flow regimes occur with increasing gas flow rates. In the generated inhomogeneous bubbly flow there are three main contributions to the mixing: (*i*) transport by the buoyancy driven recirculation, (*ii*) bubble induced turbulence (BIT) and (*iii*) shear-induced turbulence (SIT). The strength of these contributions and their interplay depends on the gas volume fraction which is reflected in the measured heat

transport enhancement. We compare our results with the findings for heat transport in homogeneous bubbly flow from Gvozdić *et al.* (2018) [37]. We find that for the lower gas volume fractions ($\alpha < 4\%$), inhomogeneous bubbly injection results in better heat transport due to induced large-scale circulation. In contrast, for $\alpha > 4\%$, when the contribution of SIT becomes stronger, but so does the competition between all three contributions, the homogeneous injection is more efficient.

2.1 Introduction

Injection of bubbles in a continuous liquid phase is widely used to enhance mixing without any additional mechanical parts. As a result, bubbly flows enhance heat and mass transfer and can therefore be found in various industrial processes such as synthesis of fuels and basic chemicals, emulsification, coating, fermentation, etc. In particular, to understand the effect of bubbles on heat transport, a variety of flow configurations have been used in previous works. These studies can be broadly classified based on (*i*) the nature of forcing of the liquid, i.e. natural convection (liquid is purely driven by buoyancy) [49, 50]r forced convection (liquid is driven by both buoyancy and an imposed pressure gradient or shear) [51–54]; and (*ii*) based on the size of the injected bubbles, i.e. sub-millimetric bubbles [49, 50, 55] to millimetric bubbles [56, 57].

Owing to the high complexity of the physical mechanism behind the bubble induced heat transfer enhancement, a systematic approach has to be taken when studying this phenomenon. Starting from a relatively simple case: bubbly flow in water combined with natural convection, Kitagawa *et al.* (2013) [55] studied the effect of bubble size on the heat transfer. They found that micro-bubbles (mean bubble diameter $d_{bub} = 0.04$ mm) which form large bubble swarms close to the wall with significant wall normal motion, induce higher heat transfer enhancement as compared to sub-millimeter-bubbles ($d_{bub} = 0.5$ mm), which have weak wakes and low bubble number density.

In our previous work [37] we studied heat transfer combined with natural convection with injection of millimetric bubbles in water which due to their strong wake enhance the heat transport even more. Those experiments were performed in a rectangular bubble column heated from one side and cooled from the other in order to understand the influence of homogeneously injected millimetric bubbles on the overall heat transport. The primary advantage with such a setup is that the dynamics of homogeneous bubbly flows has been adequately characterised and studied in the past [23, 27, 58, 59] and the flow without bubbles resembles the classical vertical natural convection system [60–66]. The strength of the thermal driving of the fluid in such a system is characterised by the Rayleigh number which is the dimensionless temperature difference:

$$Ra_H = \frac{g\beta(\overline{T_h} - \overline{T_c})H^3}{\nu\kappa};$$

(2.1)

and the dimensionless heat transfer rate, the Nusselt number:

$$\overline{Nu} = \frac{Q/A}{\chi\,(\overline{T_h} - \overline{T_c})/L},$$

(2.2)

where Q is the measured power supplied to the heaters, $\overline{T_h}$ and $\overline{T_c}$ are the mean temperatures (over space and time) of the hot wall and cold wall, respectively, L is the length of the setup, A is the surface area of the sidewall, β is the thermal expansion coefficient, g the gravitational acceleration, κ the thermal diffusivity, and χ the thermal conductivity of water. Gvozdić *et al.* [37] found that homogeneous injection of bubbles in vertical natural convection can lead to a 20 times enhancement of the heat transfer compared to the corresponding flow with no bubbles. It was found that for $Ra_H = 4.0 \times 10^9 - 2.2 \times 10^{10}$ and a gas volume fraction of $\alpha = 0.5\% - 5\%$ the Nusselt number remained nearly constant for increasing Ra_H. Furthermore, Gvozdić *et al.* (2018) [37] found good agreement for the scaling of an effective diffusivity D with the gas volume fraction α with the results of mixing of a passive scalar in a homogeneous bubbly flow [35], i.e. roughly $D \propto \alpha^{1/2}$, which implies that the bubble-induced mixing is controlling the heat transfer.

With a goal to further enhance bubble induced heat transport in vertical natural convection, in this study we explore the influence of inhomogeneous bubble injection on the overall heat transfer. Previous studies have shown that inhomogeneous gas injection induces mean liquid circulations (large-scale coherent rolls) in bubbles columns [43, 44]. It is also known from classical Rayleigh-Bénard convection that aiding formation of the coherent structures can enhance heat transfer [39, 67]. In this work, we take advantage of both these phenomena and use the large-scale circulation generated by inhomogeneous bubble injection in a vertical natural convection setup to further enhance heat transport as compared to the case of homogeneous injection of bubbles. We use the same experimental setup as in Gvozdić *et al.* (2018) [37], while we inject the bubbles through one half of the injection section, either close to the hot wall or close to the cold wall (see Figure 2.1). We characterise the global heat transfer while varying two parameters: the gas volume fraction $\alpha = 0.4\% - 5.1\%$, and the Rayleigh number $Ra_H = 4 \times 10^9 - 2.2 \times 10^{10}$. We compare findings on global heat transfer for the cases of homogeneous bubble injection, injection close to the hot wall, and injection close to the cold wall. We further demonstrate the difference in the dynamics between lower gas volume fraction case ($\alpha = 0.4\%$) and higher gas volume fraction case ($\alpha = 3.9\%$) by performing velocity profile measurements along the length of the setup at mid-height.

The paper is organised as follows. In section 2, we discuss the experimental set-up and the different flow configurations studied. Results on the liquid flow characterisation and on the global heat transfer enhancement are detailed in
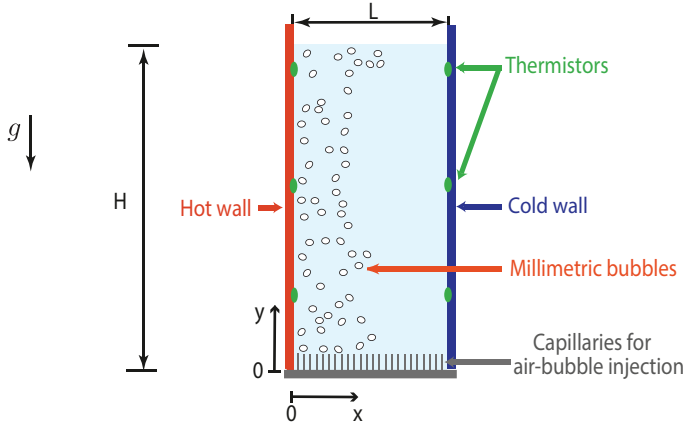
Figure 2.1: Rectangular bubbly column heated from one sidewall and cooled from the other ($H = 600$ mm, $L = 230$ mm). Bubbles are injected either close to the hot wall or close to the cold wall, through 90 capillaries (out of 180 in total) placed at the bottom of the setup (inner diameter 0.21 mm).

section 3 while concluding remarks are given in section 4.

2.2 Experimental setup and instrumentation

2.2.1 Experimental setup

In figure 2.1, we show a schematic of the experimental setup. The apparatus consists of a rectangular bubble column, where the two main sidewalls of the setup (600×230 mm^2) are made of 1 cm thick glass and the two (heated resp. cooled) sidewalls (600×60 mm^2) of 1.3 cm thick brass. Heating is provided via Joule heaters placed on the brass sidewall, while cooling of the opposite brass wall is performed using a circulating water bath. The temperature of these walls is monitored using thermistors. Millimetric bubbles are injected through 90 out of the total 180 capillaries at the bottom of the setup, either close to the hot wall or close to the cold wall.

The global gas volume fraction is modulated between 0.4% to 5.1% by varying the inlet gas flow rate. Global gas volume fraction was estimated as an average elevation of the liquid at the top of the setup, which is measured by processing images captured using a Nikon D850 camera. We find that different flow regimes develop with increasing inlet gas flow rate. Movies capturing
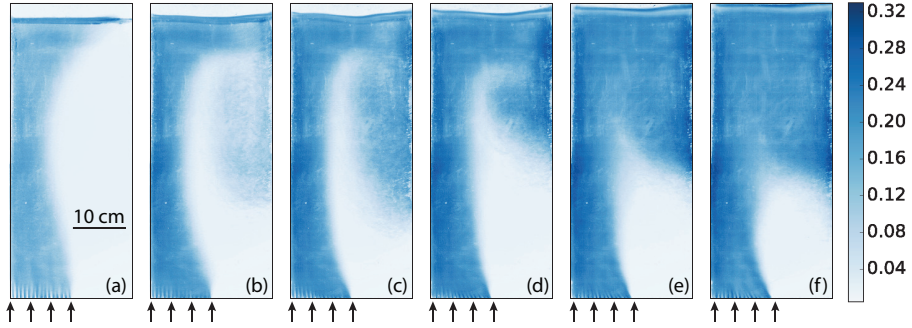
Figure 2.2: Visualisation of preferential concentration of bubbles for each gas volume fraction: (a) $\alpha = 0.4\%$, (b) $\alpha = 0.9\%$, (c) $\alpha = 1.4\%$, (d) $\alpha = 2.3\%$, (e) $\alpha = 3.9\%$, (f) $\alpha = 5.1\%$; arrows mark the gas injection. Colour corresponds to $\sigma/\langle\sigma_{bg}\rangle$, that is the standard deviation of each pixel intensity σ normalised by $\langle\sigma_{bg}\rangle$ the mean of the standard deviation of pixel intensity for a background image taken without the bubble injection.

these regimes can be found in the Supplementary material [45]. In order to visualise the preferential concentration of the bubbles in figure 2.2 we show the normalised standard deviation of each pixel in the movie frame converted to grayscale over around 1500 frames. For low global gas volume fractions (around 0.4%) we visually observe that the bubbles rise without migrating to the opposite side (see Figure 2.2(a)), while the bubble stream bends due to liquid recirculation caused by the pressure gradient between the two halves of the setup, as it was previously observed by [68]. For a global gas volume fraction of approximately 1%, the bubbles start migrating to the opposite side (see Figure 2.2(b)), inducing a weak bubble circulation loop on the opposite half of the setup. This recirculation loop does not interfere with the main bubble stream. At an even higher gas volume fraction of around 2.3%, a significant part of the bubble stream passes to the other half of the setup, and strongly interacts with the main bubble stream (see Figure 2.2(d)). The migrating bubbles form an unstable loop, which gets partially trapped by the main bubble stream and carried to the top of the setup. With increasing gas flow rate, the amount of bubbles passing from the injection side to the opposite half of the setup increases, as does the instability of the main bubble stream. These regimes have significant influence on the heat transfer, which will be addressed later in section 2.3.1.
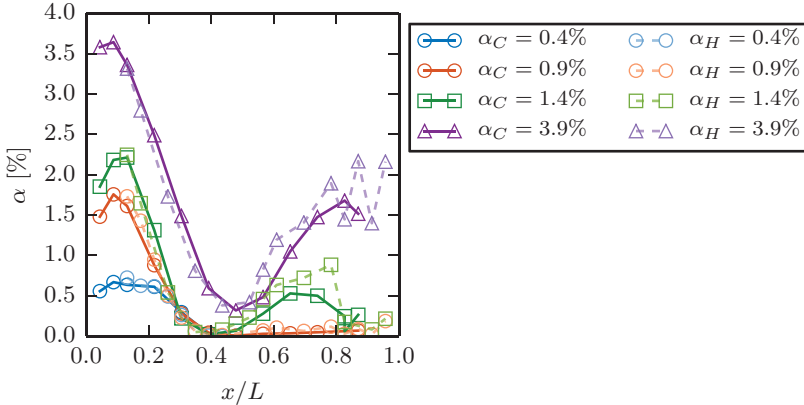
Figure 2.3: Gas volume fraction profiles at the mid-height for injection close to the hot wall α_H and injection close to the cold wall α_C (cold wall profiles are mirrored around $x/L = 0.5$ for the comparison).

2.2.2 Instrumentation for the gas phase characterisation

In order to characterise the gas phase, we first perform a scan of the local gas volume fraction using a single optical fibre probe (for working principle see [69]). We perform measurements only at half-width of the column because the capilaries for bubble injection are arranged in 6 rows and 30 columns, and the width of the column is only 6 cm. In figure 2.3, we plot the local gas volume fraction measured at half-height $y/H = 0.5$, versus the normalised length for both hot-wall and cold-wall injection. We find that the profiles of the gas volume fraction do not differ significantly for the cases where the bubbles are injected close to the hot wall or close to the cold wall.

The bubble diameter and bubble velocity were measured at half height using an in-house dual optical probe, which consists of two optical fibres placed one above the another. The bubble velocity is given as $V_{bub} = \delta/\Delta t$, where $\delta = 4$ mm is the vertical distance between the fibre tips and Δt is the time interval between which one bubble successively pierces each fibre. The diameter is estimated from the time during which the leading probe is in the gas phase. To ensure precise measurements of the bubble diameter and velocity, we perform measurements only in the injection stream. On the opposite side of the injection stream, bubbles move downwards which makes their accurate detection with a downward facing probe impossible. Bubble diameter mea-
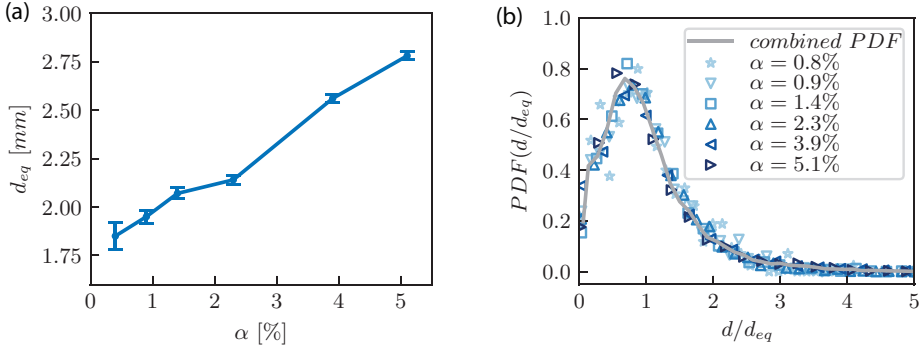
Figure 2.4: (a) Mean bubble diameter d_{eq} for different gas volume fractions α, the error-bar presents the standard error of the mean bubble diameter. (b) Probability density function (PDF) of the normalised bubble diameter. The symbols present the PDF for each gas volume fraction, while the line presents a PDF calculated using data points for all studied gas volume fractions.

surements indicate an expected increasing trend with increasing gas volume fraction (see Figure 2.4 (a)), while the distribution of the normalised bubble diameter remains nearly the same for all the gas volume fractions with a standard deviation of 0.7 (see Figure 2.4 (b)). The bubble velocity is in the range $V_{bub} = 0.5 \pm 0.02$ m/s for the given gas volume fraction span. The bubble rising velocity in the injection leg of the setup is nearly constant as it can be expressed as $V_{bub} = U + V_r$, and the mean rising liquid velocity U increases (see Section 2.3.2) while the relative velocity V_r decreases with increasing gas volume fraction [27], thus compensating each other.

2.2.3 Instrumentation for the liquid phase velocity measurements

The vertical and the horizontal component of the liquid phase velocity are measured by means of Laser Doppler Anemometry (LDA) in backscatter mode. The flow is seeded with polyamid seeding particles (diameter 5 μm, density 1050 kg/m^3). The LDA system used consists of DopplerPower DPSS (Diode Pumped Solid State) laser and a Dantec burst spectrum analyser (BSA). It has been shown previously that the LDA in backscatter mode measures predominantly the liquid velocity [70–72]. Therefore, no post-processing was performed on the data. Measurements of 30 minutes were performed for each

$Ra_H \times 10^{-9}$	4.0	5.3	6.8	9.1	12.3	16.5	22.4	30.2
$\Delta T \; [K]$	2	2.6	3.3	4.3	5.6	7.2	9.3	11.3

Table 2.1: Operating values of ΔT at different Ra_H

measurement point with a data rate of $\mathcal{O}(100)$ Hz.

2.2.4 Instrumentation for the heat flux measurements

In order to characterise the global heat transport, namely to obtain $\overline{Nu}$ and Ra_H, we measured the hot and cold wall temperatures (the control parameters), and the heat input to the system (the response parameters). Accordingly, resistances of the thermistors placed on the hot and cold walls and the heat power input were read out every 4.2 seconds using a digital multimeter (Keysight 34970A). Operating temperatures for each Rayleigh number are given in table 2.1. The heat losses were estimated to be in the range of 3% to 7% by calculating convective heat transport rate from all outer surfaces of the setup if they are at 25 °C and by measuring the power needed to maintain the temperature of the bulk constant ($T_{bulk} = 25$ °C) over 4 hours. More details on the temperature control of the setup and measurements of the global heat flux are provided in [37]. The experimental data was acquired after a steady state was achieved in which the mean wall temperatures fluctuated less that ± 0.5 K. Time averaging of the instantaneous supplied heating power was then performed over a period of 3 hours.

2.3 Results

2.3.1 Global heat transfer enhancement

We now analyse the heat transport in the presence of an inhomogeneous bubble swarm for gas volume fraction α ranging from 0.4% to 5.1% and the Rayleigh number ranging from 4×10^9 to 2.2×10^{10}. Experiments performed in a previous study showed that in the single-phase case Nusselt increases with Ra_H as $\overline{Nu} \propto Ra_H{}^{0.33}$, while in the case of homogeneous bubble injection $\overline{Nu}$ remains nearly constant with increasing Ra_H [37]. In figure 2.5, along with the results previously obtained for the cases of single-phase flow and homogeneous bubble injection, we plot the Nusselt number versus Ra_H for inhomogeneous injection. Similarly to the results for the homogeneous bubble injection, we
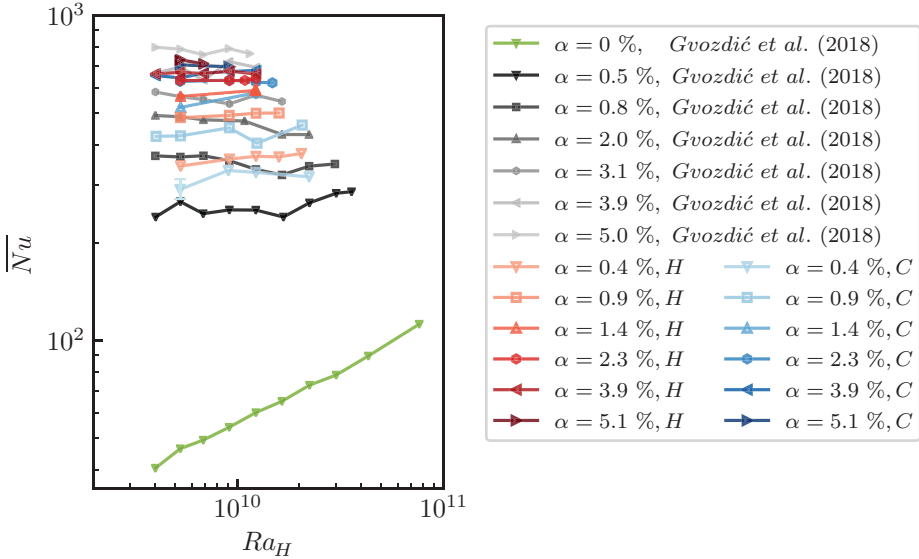
Figure 2.5: Dependence of the Nusselt number $\overline{Nu}$ on the Rayleigh number Ra_H for different gas volume fractions. Green data presents the single-phase case from [37], black data the homogeneously injected bubbles from [37], red data the injection of bubbles close to the hot wall (H) and blue data injection close to the cold wall (C).

find that $\overline{Nu}$ remains independent of Ra_H and is an order of magnitude higher when compared to the single-phase case even if the bubbles are injected only through one half of the bubble injection section.

Although Nusselt is not a function of Rayleigh in both cases, the heat transport enhancement mechanisms in case of inhomogeneous injection is different than the one present in case of homogeneously injected bubbles where $\overline{Nu} \propto \alpha^{0.45\pm0.025}$. While in the case of a homogeneous bubble injection the mixing mechanism limiting the heat transport is bubble induced turbulence (BIT) [37], the large-scale circulation of the liquid phase induced by inhomogeneous bubble injection leads to the occurrence of a shear layer between the fluid region injected with bubbles and its opposite side. Therefore, in the case of inhomogeneous bubble injection there are additional contributions to the mixing: the shear-induced turbulence (SIT) and mixing by large-scale liquid circulation. Given the difference in the fundamental mixing mechanisms for homogeneous injection and inhomogeneous injections, one can expect a dif-
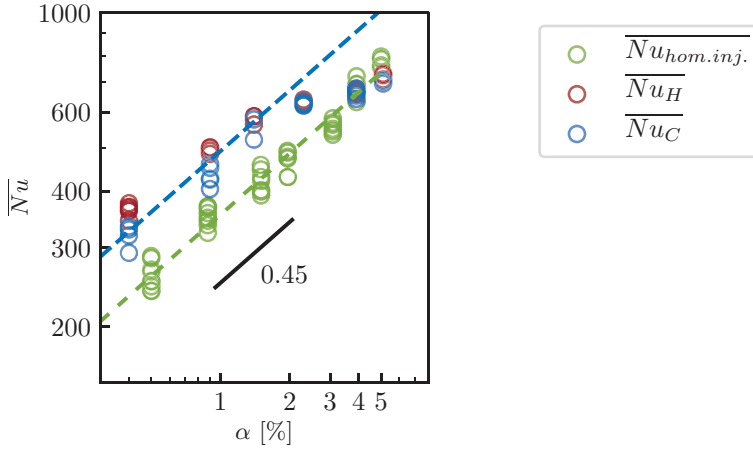
Figure 2.6: Nusselt number $\overline{Nu}$ as a function of the gas volume fraction α, subscripts: C - injection close to the cold wall; H - injection close to the hot wall, *hom. inj.* - homogeneous bubble injection. Hollow symbols show all the experimental measurements, and lines present the $\overline{Nu} \propto \alpha^{0.45}$ scaling. The crossover from strong enhancement by the inhomogeneous bubble injection for low α towards no enhancement for high α is clearly seen.

ference in the scaling of the Nusselt number with α. Indeed, for gas volume fractions $\alpha \geq 1.4\%$ $\overline{Nu}$ does not follow the same trend with gas volume fraction as in the case of homogeneous injection, it seems to be less affected by changing α (see Figure 2.6). However, for low gas volume fractions the scaling exponent of $\overline{Nu}$ with α for inhomogeneous injection agrees well with homogeneous injection, though with an increased prefactor. If we calculate the exact scaling exponent for inhomogeneous injection for gas volume fraction $\alpha \leq 1.4\%$, for hot wall injection we get 0.37 ± 0.03, for cold wall it is 0.41 ± 0.08. These exponents are comparable to the one for homogeneous injection. It should be however taken into account that better precision of the exact scaling exponent would be obtained if the number of data points at low gas volume fractions would be greater, since in the present work only 3 gas volume fractions are available. The small observed difference in the exact scaling exponent between hot wall injection and cold wall injection will be addressed later.

In order to understand the observed trend of Nusselt with increasing α, we plot the ratio of Nusselt number for inhomogeneous injection to the corresponding Nusselt for the homogeneous injection for the same gas volume fraction
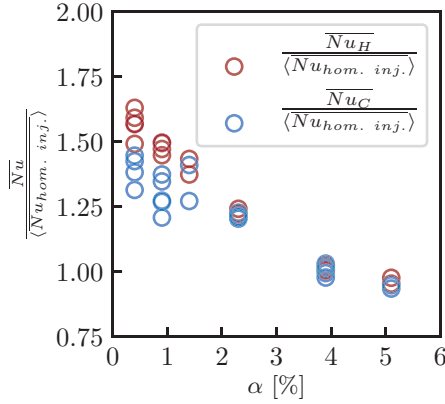
Figure 2.7: The ratio of Nusselt for the inhomogeneous bubble injection and Nusselt for homogeneous injection as a function of the gas volume fraction.

in figure 2.7. The results indicate that the heat transfer enhancement (as compared to the homogeneous bubble injection) decreases with increasing gas volume fraction. Studies focused on characterisation of the mixing in similar inhomogeneous bubbly flow have shown that (i) in case of $\alpha < 3.5\%$ the mixing is enhanced using inhomogeneous injection [43] [44], (ii) for $\alpha < 3\%$ in the case of inhomogeneous bubbly flow where the buoyancy driven flow generates shear-induced turbulence involving wide range of scales from the from the size of the column to bubble diameter, the mixing time evolves as $\alpha^{-0.5}$ [43]. Our results for low gas volume fraction agree well with these findings. On the other hand, at higher gas volume fractions the observed trend is changed. Possible cause of decreased heat transport enhancement at higher gas volume fractions is that the interacting mixing mechanisms might deteriorate one another, resulting in inhomogeneous bubble injection to be less effective that the homogeneous one for $\alpha > 4\%$.

We now compare the global heat transfer for injection close to the hot wall and injection close to the cold wall. From figures 2.5 and 2.6 we find that there is almost no distinction between hot wall injection and cold wall injection for the same gas volume fraction for higher α. The difference is more prominent for low gas volume fractions as compared to high gas volume fractions; namely, up to a critical value of the gas volume fraction $\alpha < 1.4\%$ the Nusselt number for hot wall injection is slightly higher than the one for cold wall injection. One possible reason for the observed difference in the Nusselt number could be the

different interaction between the rising bubbles and the falling cold boundary layer or rising hot boundary layer, namely the co-current flow of bubbles with the thermal boundary layer might perturb the boundary layer more than the counter-current flow. However, we suspect that this is not the actual cause of the difference between hot wall injection and cold wall injection for two reasons: (*i*) We do not see the difference between the different injection sides for higher gas volume fractions and (*ii*) the Nusselt number does not depend on the Rayleigh number, meaning that it is very likely that the perturbation of the boundary layers by the bubbles rising next to the wall is very strong even for the lowest gas volume fractions so that the boundary layers do not react back on the bubbles.

On the other hand, the main distinction between the $\alpha = 0.4\%$ and $\alpha = 0.9\%$ cases and the cases with $\alpha \geq 1.4\%$ is that at low gas volume fraction the boundary layer on the side opposite to the bubble injection is not mixed by bubbles because almost no bubbles migrate to the other half of the setup, while at high α both boundary layers are mixed by bubbles. Therefore the liquid (with almost no bubbles) flowing in the same direction as the cold boundary layer is more effective in transferring heat that the liquid flowing in the direction opposite to the movement of the hot boundary layer. Finally, the observed differences in heat transport if the bubbles are injected close to the hot wall or close to the cold wall at $\alpha \geq 1.4\%$ are of the same order of magnitude as the variation of the Nusselt number for a constant gas volume fractions over the studied range of Ra_H, but are reproducible by repeating the measurements. We also note that difference in the mixing mechanism close to the non-injection wall seems to be the cause of different exact scaling exponents of $\overline{Nu}$ with α observed for $\alpha \leq 1.4\%$ for hot and cold wall injection.

2.3.2   Local liquid velocity measurements

Liquid velocity measurements are performed by means of LDA with the goal of understanding the dynamics of the system and how it is affected by different bubble injection sides, heating, and different gas volume fractions, in order to relate it to our global heat transfer findings.

In the previous section we have seen that $\overline{Nu}$ is slightly higher for hot wall injection when compared to cold wall injection for lower gas volume fractions. In order to examine this further we performed velocity measurements at half height of the setup in the direction normal to the heated and cooled walls for the case of lowest studied gas volume fraction $\alpha = 0.4\%$. In figures 2.8, we show the vertical and horizontal liquid velocity profiles for both hot-wall and
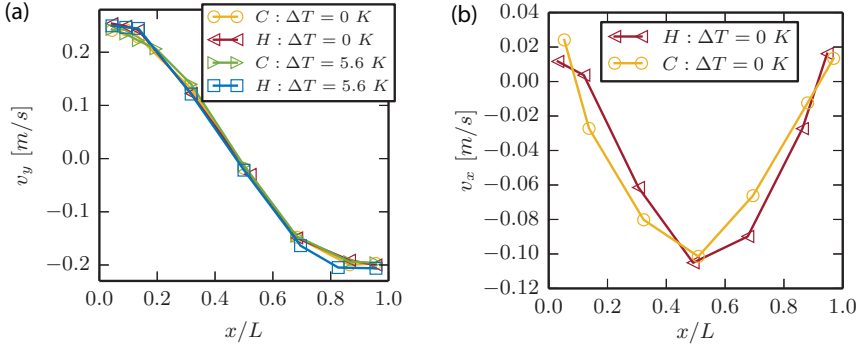
Figure 2.8: (a) Vertical velocity (v_y) profiles for a gas volume fraction $\alpha = 0.4\%$, for different injection sides and different imposed wall temperature differences, (b) Horizontal velocity (v_x) profiles for gas volume fraction $\alpha = 0.4\%$, for different injection sides without the heating.

cold-wall injections without the heating (cold side injection measurements are mirrored around $x/L = 0.5$). The vertical velocity profile shows a high positive value at the injection side which is of the same order of magnitude as the bubble rising velocity, while the horizontal velocity is always negative indicating that the injected side is entraining the fluid from the opposite side. These findings are in agreement with the results of Roig *et al.* (1998) [68] who studied a turbulent bubbly mixing layer, which was produced by applying different inlet conditions of liquid velocity and gas volume fraction in two halves of a vertical square water channel. They found that even a very low difference between the gas volume fraction in the two halves of the setup induces strong acceleration of the fluid on the injection side of the mixing layer and a bending of the flow. Figure 2.8 (a) also shows the vertical velocity profiles for different injection sides with the heating ($\Delta T = 5.6$ K). Results shown in figure 2.8 (a) indicate that heating and the side of injection do not have a significant influence on the mean velocity profiles. These findings do not comply with the ones for the global heat transfer possibly because the interaction of boundary layers with the co-current or counter-current bulk can only be captured by measuring velocity even closer to the heated and cooled wall, which is not possible due to strong reflections of the laser beam.

Since $\overline{Nu}$ depends strongly on the gas volume fraction but not on Ra_H we now look into the influence of gas volume fraction on the measured velocity profiles. In figure 2.9, we show the vertical and horizontal velocity profiles at
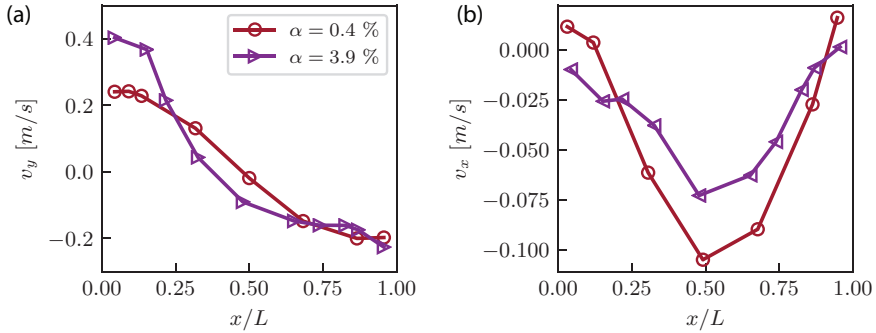
Figure 2.9: Vertical velocity (v_y) and horizontal velocity (v_x) profiles for different gas volume fractions without the heating. The gas injection is performed at $x/L \leq 0.5$.

half height for gas volume fractions of $\alpha = 0.4\%$ and $\alpha = 3.9\%$. The horizontal velocity profiles are slightly higher in the centre of the setup for $\alpha = 0.4\%$. This most likely occurs due to the presence of the bubbles on the side opposite to the injection side for $\alpha = 3.9\%$, which leads to lower gradient of gas volume fraction at mid height for $\alpha = 3.9\%$ and lower driving for horizontal motion. Based on the profiles of the mean liquid velocity in the vertical direction a mean liquid rising velocity in the injection side of the setup U can be estimated by averaging the velocity along the length of rising liquid layer. This way we find that the mean velocity for $\alpha = 0.4\%$ is 0.16 m/s and for $\alpha = 3.9\%$ is 0.25 m/s. The mean velocity in the case $\alpha = 0.4\%$ is comparable to the one observed in previous studies on mixing in inhomogeneous bubbly flows (where $U = \mathcal{O}(10)$ cm) [43, 44], which further justifies the direct comparison between the global heat transport results and findings from these studies.

2.4 Summary

An experimental study on heat transport in inhomogeneous bubbly flow has been conducted. The experiments were performed in a rectangular bubble column heated from one side and cooled from the other, where the millimetric bubbles were injected through one half of the injection section, either close to the cold wall or close to the hot wall (see figure 2.1). Two parameters were varied: the gas volume fraction (from 0.4% to 5.1%) and the Rayleigh number (from 4×10^9 to 2.2×10^{10}).

By characterising the global heat transfer we find that in the case of bubbles injected only through one half of the injection section, just as for homogeneous bubble injection, the Nusselt number is nearly independent on the Rayleigh number and increases with increasing gas volume fraction (see Figure 2.5). However, the heat transfer enhancement is more prominent with inhomogeneously injected bubbles when compared to the same gas volume fraction and same range of Ra_H of homogeneous injection, provided $\alpha < 4\%$ (see Figure 2.6). This finding can be explained by the multiple mixing mechanisms present in the setup, once a gradient of gas volume fraction is imposed. Namely, besides the bubble induced turbulence (BIT), the large-scale circulation of the liquid phase induced by inhomogeneous bubble injection leads to the occurrence of a shear layer between the fluid region injected with bubbles and its opposite side. As previously observed by Alméras *et al.* (2016) [43] and Alméras *et al.* (2018) [44] for $\alpha < 3.5\%$, the different superimposed mixing mechanisms lead to enhancement of mixing, which results in up to 1.5 times larger heat transport as compared to homogeneous bubble injection (see Figure 2.7).

Although the measurements of the velocity in the bulk show comparable profiles for hot wall and cold wall injections (see Figure 2.8), the findings on global heat transfer indicate that the injection close to the hot wall induces stronger heat transfer enhancement for gas volume fraction lower than a critical value of 1.4% (see Figures 2.5 and 2.6). At $\alpha \geq 1.4\%$ we observe bubble-rich region near the non-injecting wall which promotes effective mixing near the thermal boundary layer at the wall. As a consequence the difference in the result on heat transport enhancement for the cases of hot wall and cold wall injection at $\alpha \geq 1.4\%$ is diminished. For $\alpha < 1.4\%$ non-injection wall is not covered by bubbles, which means that in this range of α the co-current flow of the liquid directed from the hot wall to the cold wall aids large-scale circulation and the heat transport enhancement.

For $\alpha > 4\%$ the inhomogeneous injection causes lower heat transport enhancement than the homogeneous one. We visually observe that with increasing gas volume fraction the instability of the bubble stream increases as well as the contribution of the shear-induced turbulence (SIT). The velocity measurements show that the large-scale circulation gets stronger with increasing α as well (see Figure 2.9). Therefore the competition between BIT, SIT and the advection reduces the heat transport enhancement.

Lastly we comment on the generality of the obtained results on the heat transfer enhancement. When determining the generality of the results on the scaling of the Nusselt number with the gas volume fraction for lower studied gas

volume fraction, one has to take into account the governing mixing mechanism in a inhomogeneous bubble column which depends on the aspect ratio (height over width) of the column and the size of the bubbles. If the bubble induced turbulence is the limiting mixing mechanism we expect the scaling of the Nusselt number to be the same, namely $Nu \propto \alpha^{0.45}$. On the other hand, a significant change in the bubble size would affect the flow patterns as well. Experimentally it is challenging to generate bubbles of significantly different sizes (in this study it is varied only from ~ 1.8 mm to ~ 2.8 mm), and it is difficult to predict how would the scaling be affected by it. We expect that the evolution of Nusselt number with the Rayleigh number is also general. If the size of injected bubbles is comparable to the thickness of the thermal boundary layers (the thickness of the thermal boundary layer in the studied range of Ra_H in the single phase case is estimated to be of order of few millimeters (see Gvozdić *et al.* (2018) [37]) and if the bubbles are injected close to the wall so that they perturb these boundary layers we expect that Nu does not depend on Ra_H. Unexplored effect of the changes in bubble sizes and the complexity of the interaction between different mixing mechanisms call for future investigations on this topic.

Acknowledgments

Try before you die.

Gert-Wim Bruggert

3

Combining heat transport, high-Reynolds bubbly flows and incident turbulence: Twente Mass and Heat Transfer Water Tunnel [1]

Abstract

A new vertical water tunnel with global temperature control and the possibility for bubble and local heat & mass injection has been designed and constructed. The new facility offers the possibility to accurately study heat and mass transfer in turbulent multiphase flow (gas volume fraction up to 8%) with a Reynolds-number range from 1.5×10^4 to 3×10^5 in the case of water at room temperature. The tunnel is made of high-grade stainless steel permitting the use of salt solutions in excess of 15% mass fraction. The

---

tunnel has a volume of 300 L. The tunnel has three interchangeable measurement sections of 1 m height but with different cross sections (0.3×0.04 m^2, 0.3×0.06 m^2, 0.3×0.08 m^2). The glass vertical measurement sections allow for optical access to the flow, enabling techniques such as laser Doppler anemometry, particle image velocimetry, particle tracking velocimetry, and laser-induced fluorescent imaging. Local sensors can be introduced from the top and can be traversed using a built-in traverse system, allowing for e.g. local temperature, hot-wire, or local phase measurements. Combined with simultaneous velocity measurements, the local heat flux in single phase and two phase turbulent flows can thus be studied quantitatvely and precisely.

3.1 Introduction

Bubbles injected in turbulent flows are widely used in industrial processes to enhance mixing of the continuous phase and consequently the overall heat and mass transfer [7,73,74]. In practical applications two phase flows are preferred for example for highly exothermic processes where heat removal restricts the reactor's performance or for processes where the rate of mass transfer between a gas and a liquid is limited by the diffusion of a solute in the liquid [75]. Another benefit of injection of bubbles is that no additional moving mechanical parts [76] are needed for enhanced mixing which leads to relatively high reliability, and low maintenance and operating costs. Furthermore, bubble columns [77] are easier to use at higher temperatures and pressures when shaft sealing may be difficult [78].

The wide range of applications of bubbly flows has led to many studies on understanding the influence of bubble injection on heat and mass transfer in different configurations [78–80]. While the focus of application-oriented studies is to formulate empirical correlations for the net heat and mass transfer coefficients, fundamental research focuses on measuring and characterising the local flow statistics which leads to physical insight behind the observed correlations. In particular, recent studies in turbulent bubbly flows have investigated a variety of aspects such as: (i) bubble size and velocity distributions [55,81], (ii) global heat and mass transport measurements [56,81,82], (iii) computational studies with ideal boundary conditions [54,57], (iv) liquid velocity and temperature profile [37,45,55], (v) homogeneous and inhomogeneous bubble injection [37,45,49], and (vi) natural and forced convection [49–54].

In systems of natural convection with bubble injection, mixing is provided by large scale circulations driven by density differences in the liquid and bubbles. Within such a system, studies have shown that the bubble size has a major effect on the overall heat transfer [55]. However, there have been only a few studies on forced convective heat transfer in bubbly flows [51,54,83], where, in addition to buoyancy driven circulation, bubble wakes and their interplay provide an additional mixing mechanism. In systems of forced convection, experiments and numerical simulations have primarily focused on understanding the influence of bubble accumulation and deformability on the global mixing properties. Experimental setups (e.g. Ref. [83]) are generally limited by Reynolds number ($O(10^2)$). Industrial systems involving heat and mass transfer with forced convection, i.e. mean liquid velocity (for e.g. heat exchangers) reach much higher Reynolds numbers $O(10^3 - 10^5)$ and beyond. Fundamental stud-

ies on the interaction between the turbulence in the carrier fluid, heat transfer and the dispersed bubbles at such high Reynolds numbers are currently lacking. The objective of our work is to fill this gap. In this paper we will describe a facility which is built to tackle various unresolved questions related to heat transfer in turbulent bubbly flow. The Twente Mass and Heat Transfer Water Tunnel will be used to: (i) quantitatively characterize the global heat transfer of a turbulent flow with and without gas bubble injection; (ii) correlate and understand the local heat flux with the local liquid velocity and temperature fluctuations in the bubbly turbulent flow; (iii) explore and understand the dependence of the heat transfer on the control parameters, such as the gas concentration, bubble size, and the Taylor–Reynolds number of the flow.

Another unexplored aspect of heat transport in bubbly flow is the influence of salt in the continuous phase which is highly relevant in certain industrial applications. For example, chlorate processes in chemical industry use brine (high molarity NaCl solution) as the continuous phase and the interaction of bubbles with turbulence and heat transfer in such systems is very different from bubbles in turbulence without salt. Dissolved salt greatly changes the interfacial properties of the bubbles thus leading to different forces between bubbles and thus different collision characteristics. Even a small concentration of salt dissolved in a bubbly flow can thus significantly change the properties of the bubbles which may lead to drastic changes in the overall flow properties [84]. In order to study such flows and understand the influence of salt (in particular NaCl) on the overall heat and mass transfer, we have built our setup specifically from corrosion-resistant stainless steel. In particular, we aim to: (i) understand the effect of the salt concentration on the surface properties of bubbles and the resulting change of coalescence and breakup of them, and (ii): to quantify the resulting dependence of the global and local heat transport on salt concentration.

Apart from the possibility of heat transfer investigation, also mass transfer measurements can be performed in the new vertical tunnel. The study of the transport of microparticles in turbulent bubbly flow may shed light on finding the optimal parameters for the mixing of particles in a flow with for example catalytic particles, thereby ultimately maximising the overall efficiency of the chemical reactions in a chemical reactor. Thus, we aim to find the transport mechanism of a scalar field (e.g. the concentration field of the catalytic microparticles) in a turbulent bubbly flow.

3.2 System description

The Twente Mass and Heat Transfer Water Tunnel (TMHT for short, see Figs. 5.1 and 3.2) is a recirculating vertical water tunnel for the study of heat and mass transfer in turbulent multiphase flows for both global and local quantities. We first list the main features:

- The tunnel has an internal volume of 300 L.
- It is constructed out of marine-grade AISI316 stainless steel permitting the use of salt solutions in excess of 15% mass fraction.
- An 80 m^3/h capacity propeller pump drives the flow upwards in the measurement section from around 0.05 m/s up to 1 m/s.
- Up to 10 kW of heating power can be added into the flow by means of heater cartridges.
- A 12.5 kW chiller removes the added heat further downstream and allows for global temperature control of the measurement liquid within 20 mK long-term stability at statistically stationary conditions, see 3.3b.
- There are three interchangeable measurement sections of each 1 m in length and of different cross sections, where the width × depth are either 0.3×0.04 m^2, 0.3×0.06 m^2, or 0.3×0.08 m^2.
- Using water at 21°C and a flow velocity range covering 0.05 m/s to 1 m/s in the measurement section results in a Reynolds number range of Re $= 1.5 \times 10^4$ to 3×10^5, where Re $= UW/\nu$ with U the mean flow velocity, W the width of the measurement section, and ν the kinematic viscosity of the liquid.
- Three of the four walls of each measurement section are made of glass (front, back, and one side) in order to gain optical access to the flow allowing techniques such as high-speed imaging, laser-Doppler anemometry, particle image velocimetry, particle tracking velocimetry and laser-induced fluorescent imaging. The fourth wall has several portholes where probes that measure local flow properties can be inserted.
- In the case of heat transfer studies, the tunnel is intended to operate at statistically stationary conditions with the tunnel liquid temperature around the ambient lab temperature to ensure minimal heat flux through the walls.
- Millimetric bubbles can be injected into the flow by 140 exchangeable capillaries. The gas volume fraction inside the measurement section can be measured electronically and can go up to 8%, depending on the flow conditions.

- An active turbulent grid consisting of agitator flaps that rapidly rotate inside the flow agitates the turbulence inside the measurement section to achieve high turbulent intensity levels.
- A computer–controlled two–axis traversing frame allows for positioning sensors inside of the measurement section in order to obtain local quantities, such as the local temperature by using thermistors with a few mK resolution, or the local gas volume fraction by using the optical fiber probe technique [69].
- The local heat flux inside the flow can be measured by simultaneously acquiring local velocity with laser-Doppler anemometry and local temperature with a thermistor.

In the next sections we will describe the TMHT facility in more detail.

3.2.1   Overview

We now give a quick walk-through of all the major components of the tunnel, see 5.1 for a schematic picture and 3.2a for a photo and 3.2b for the coordinates system we have adopted. Starting from the pump, the flow is expanded from a circular cross-section to a larger rectangular area by the diffuser that has two laterally adjustable vanes inside to help steer the flow sideways. The flow then enters the bend and is guided by three corner–turning vanes to facilitate uniformity in the downstream flow velocity profile.

A Pt100 temperature probe measures the bulk '*inlet*' liquid temperature. 140 exchangeable capillaries (detailed in 5.1e) can inject bubbles into the flow near the bottom of this vertical tunnel section. Two modular sections follow that can be interchanged with each other. These are the section containing the heater cartridges (detailed in 5.1d) and the section with the active turbulent grid (detailed in 5.1c). A contraction placed downstream of these sections prevents the flow separation; it contracts the flow over its width (x-direction) and depth (y-direction).

Three interchangeable measurement sections of different cross sections can be installed. Their width and depth are either 0.3×0.04 m^2, 0.3×0.06 m^2, or 0.3×0.08 m^2, each with a matching contraction of height 0.25 m (detailed in 5.1b). All those measurement sections are 1 m tall and their front, back and one of the sides are made of glass. The remaining sidewall is of stainless steel and has equidistant portholes for inserting probes or injecting dye and a wet/wet differential pressure transducer is attached to two of these portholes to monitor the gas volume fraction. The top part of the tunnel directly

above the measurement section is open and this can be used to insert a long probe holder, with e.g. a thermistor attached to its end, down into the measurement section. The pole is attached to a computer–controlled two-axis traversing frame (not shown), allowing for automated positioning over the x and z-directions. The y-direction can be traversed manually by a positioning stage. At the top of the measurement section the flow goes through a bend after which we find another Pt100 temperature probe to register the bulk '*outlet*' liquid temperature. Another Pt100 probe on the outside of the tunnel monitors the ambient air temperature of the lab. The flow then enters the settling vessel where bubbles can rise up to the surface or where salt can be mixed into the liquid. Going downwards from the vessel the flow is sped up by a funnel to pass through an electromagnetic flow rate meter. Lastly, all heat that was added by the heater cartridges can be removed again by the pipe heat exchanger which is fed with coolant from a chiller, after which the flow enters the pump again.

3.2.2 Flow control and adjustment

The flow in the tunnel is driven by a custom close-coupled axial flow propeller pump (Herborner Pumpenfabrik, Uniblock P 125-201/0074) fully cast from marine-grade AISI316 stainless steel to allow the use of saline solution. The capacity is 80 m^3/h at a maximum power of 0.75 kW and 1500 rpm. The three-phase electric motor of the pump is controlled by a digital frequency inverter (Herborner Pumpenfabrik, PED).

Directly after the pump is a rubber compensator to accommodate for thermal expansion of the tunnel. A diffuser with a circular inlet with a diameter of 136 mm expands the flow to a rectangular outlet of 452×146 mm^2. Inside the diffuser are two adjustable lateral vanes to help spread the flow sideways. The next bend directs the flow upwards. Inside the bend are three adjustable corner turning vanes that guide the flow and help increase flow velocity uniformity after the bend.

An electromagnetic flow meter (ABB, ProcessMaster FEP311) with a bore 65 mm measures the volumetric flow rate over its nominal range of 2.4 m^3/hour to 120 m^3/hour. According to the manual the measurement accuracy is better than 1% if the flow velocity through the meter is larger than 0.2 m/s, which is the reason for choosing this specific bore diameter. The flow is sped up by a funnel with an inclination angle of 8° before entering the meter.

The flow rate reported by the flow meter is continuously read out by an Arduino M0 Pro microcontroller board over a 4–20 mA current loop. A tuned

proportional-integral controller programmed into the Arduino feeds back to
the propeller rotation rate of the tunnel pump over another 4–20 mA current
loop to ensure a stable flow rate and velocity over time within 1% of the
setpoint, see 3.3e and 3.3f.

3.2.3   Temperature control and heat injection

Heat can be injected into the flow by twelve cylindrical heater cartridges (Wat-
low, Firerod J5F-15004) placed 300 mm below the measurement section and
sticking perpendicular to the flow direction through the front and back tunnel
walls, see 5.1d. Each heater cartridge has a diameter of 12.7 mm and a heated
zone of 110 mm long as measured from its tip inside the tunnel, indicated
by red. The end of the heated zone matches the start of the interior tunnel
wall. Each heater is thermally insulated from the wall by a Teflon (PTFE)
feed-through, indicated by yellow. A J-type thermocouple with an accuracy
of ± 2.2 K, for the absolute temperature, is embedded inside of each heater.
Because the location of the thermocouple is not guaranteed to be perfectly
centred and a strong temperature gradient is to be expected in the interior
of the heater cartridge when powered and placed in a flow, the thermocouple
temperature readings are only to be used as a rough indication of the heater
temperature. Hence, they are solely used for over-temperature protection.
The heaters are rated for temperatures in excess of $250°C$, but will be limited
by the over-temperature protection to a maximum of $95°C$ to prevent local
boiling.

The heaters are operated by controlling the supply power. Each heater can
provide 1160 W of heat at a maximum of 120 V. They are powered by three
independently programmable DC power supplies (Keysight, N8741A), each
providing up to 3.3 kW at 300 V and 11 A. Either a single heater is connected
to a single power supply, or multiple heaters are connected in series to a
single power supply, and any combination of this depending on the needs of
the experiment. The programming accuracy of the power supplies is 150 mV
and 22 mA, and the measurement accuracy is 300 mV and 33 mA. A tuned
proportional-integral controller running on a computer regulates the power
supply output voltage in order to tune the power output, resulting in an
accuracy of the set power of ± 0.3 W with a settling time of below 10 s. The
power is stable within 0.15 W regardless of the setpoint, see 3.3c and 3.3d.

The bulk temperature of the liquid inside the tunnel is measured at two loca-
tions using two Pt100 temperature probes with a 1/10 DIN accuracy cor-
responding to ± 30 mK (Pico Technology, PT-104 data logger with SE012

probes). One probe labelled '*inlet*' is upstream of the heaters at the location of the bubble injectors and protrudes 100 mm into the flow, see 5.1a. The other probe labelled '*outlet*' is downstream of the measurement section and in front of the settling vessel. A third Pt100 probe labelled '*ambient*' measures the ambient lab air temperature.

Cooling of the tunnel liquid is taken care of by a pipe heat exchanger, manufactured on request by Geurts International, located just in front of the tunnel pump intake. Twenty-two marine-grade AISI316 stainless steel pipes of 500 mm long and with diameters of 22 mm through which the tunnel liquid is flowing, are embedded in an outer jacket through which cooling water is flowing. The pipe heat exchanger is designed to remove up to 10 kW of heat. The temperature of the cooling water is regulated by a 12.5 kW capacity air-cooled recirculating chiller (Thermo Scientific, ThermoFlex 15000 P5) with a listed temperature stability of ± 0.1 K.

We will now show a typical example of settling times and temperature stability. Starting with a quiescent water-filled tunnel at room temperature, it takes up to 2.5 hours to settle to a statistically stationary state, from the moment of setting the flow rate to 21.6 m^3/h (equivalent to a velocity of 0.5 m/s in the measurement section #1), the global heat input to 2.6 kW and the setpoint of the chiller at 19°C. After this settling time, we report a long-term stability of the tunnel liquid temperature of less than ± 10 mK for a duration of over 2 hours, see 3.3.

3.2.4 Local temperature measurements

High precision and local temperature measurements can be made with thermistors. We use thermistors from TE Connectivity (Measurement Specialties G22K7MCD419) with a glass bead of diameter $d = 0.38$ mm and a listed response time of 30 ms in liquids. The temperature response time can also be estimated by considering the temperature inside the glass bead, the temperature 'skin thickness' is given by $\delta = \sqrt{\alpha t}$. For a penetration of $\delta = 0.4d$ we find $t = 29$ ms, which is in accordance with the listed temperature response. All thermistors are calibrated against the '*inlet*' Pt100 probe with a 1/10 DIN accuracy, corresponding to ± 30 mK (Pico Technology, PT-104 data logger with SE012 probe) inside of a large copper body placed in a temperature bath with a 5 mK temperature stability (PolyScience, PD15R-30), resulting in a calibration accuracy of ± 30 mK and a 5 mK resolution.

Temperature time series can be acquired by using a dual-phase lock-in amplifier (Stanford Research, SR830) in combination with a balanced Wheatstone

bridge of which one arm is a single thermistor. A digital acquisition card (National Instruments, PCI-6221) logs the amplifier's output voltage to a file on the computer. Multiple thermistors can be logged during a measurement by a digital multimeter (Keysight, 34972A) installed with a reed-relay multiplexer board (Keysight, 34902A) that will scan sequentially over all the thermistor resistance values with a listed scan rate of up to 250 channels per second.

3.2.5 Traverse

Accurately positioning thermistors, optical fibers or other probes inside of the measurement section and automatically scanning over multiple grid points is made possible by a custom-built two-axis traversing frame located above the tunnel. The traverse consists of two linear actuators (Parker, HMRB15SBD0-1800 and HMRB11SBD0-1000), powered by two servomotors (Parker, SMHA60451 and SMH60301) and digitally operated by two controllers (Parker, Compax3). The traverse can travel over the full width (x-direction) and full height (z-direction) of the measurement section. A probe holder is attached to the traverse carriage and descents into the measurement section from an opening in the top of the tunnel. The carriage can be positioned with an accuracy of ± 0.1 mm. The third axis (depth, y-direction) can be traversed over manually by using the micro-stage that is in between the traverse carriage and the traverse pole.

3.2.6 Bubble injection and gas volume fraction

Bubbles can be injected into the flow by the pressurised air lines that are fed through the wall of the tunnel located underneath the heater cartridges. The lines are pressurised at 8 bars and connected to five rows of twenty-eight Luer lock fittings, see 5.1a and 5.1e. The standardised Luer lock allows for a wide variety of needles/capillaries to be installed and easily replaced (e.g. Nordson precision stainless steel dispensing tips), ranging from inner diameters of 0.2 mm to 2 mm. The resulting size of the bubbles detaching from the capillaries may be influenced by the local velocity and shear of the surrounding liquid, surfactants, air flow rate, and the geometry of the tip of the capillaries. Each of the five rows can be opened or closed individually by computer controlled piston valves. A digital mass flow controller (Bronkhorst, F-111AC-50K-AAD-22-V) drives air through all five rows at up to 44 litres per minute.
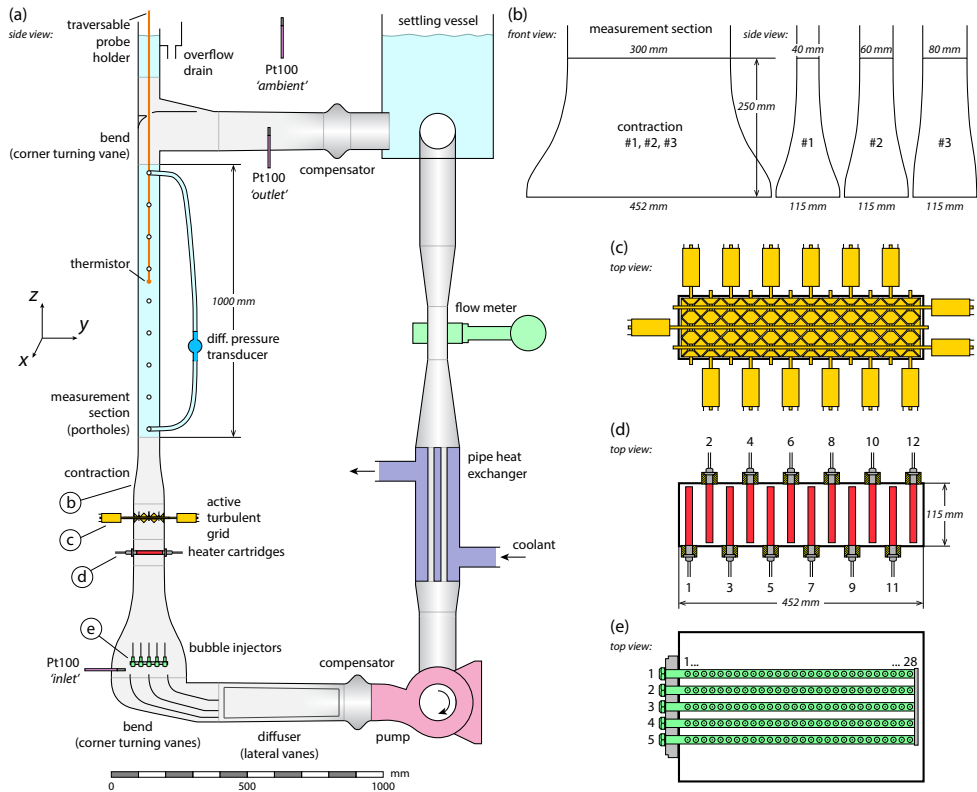
Figure 3.1: Schematic of the Twente Mass and Heat Transfer Water Tunnel (TMHT). x, y, and z are the spanwise, wall-normal, and streamwise directions, respectively, where each of the measurement sections has dimensions W (width), D (depth), and L (length) in the x, y, and z directions. (a) A side view cross-section of the tunnel showing the major components. (b) The front and side profiles of the three exchangeable measurement sections and their respective contractions. (c) A top view of the active turbulent grid showing the fifteen independently rotating rods with agitator flaps attached to them, here all in their horizontal position for displaying purposes. (d) The twelve cylindrical heater cartridges in red and the thermal insulation in yellow. (e) Bubble injection provided by five rows of each twenty-eight exchangeable capillaries. The rows can be opened and closed independently from each other. See Sec. 3.2.1 for a walk-through description.

Figure 3.2:   (a) The Twente Mass and Heat Transfer Water Tunnel (TMHT) in the front (from bottom to top): the heaters, active grid and the measurement section. In the back (from top to bottom): settling vessel, flow meter, the heat exchanger and the pump.   (b) Sketch of the coordinate system and the dimensions of the measurement section.
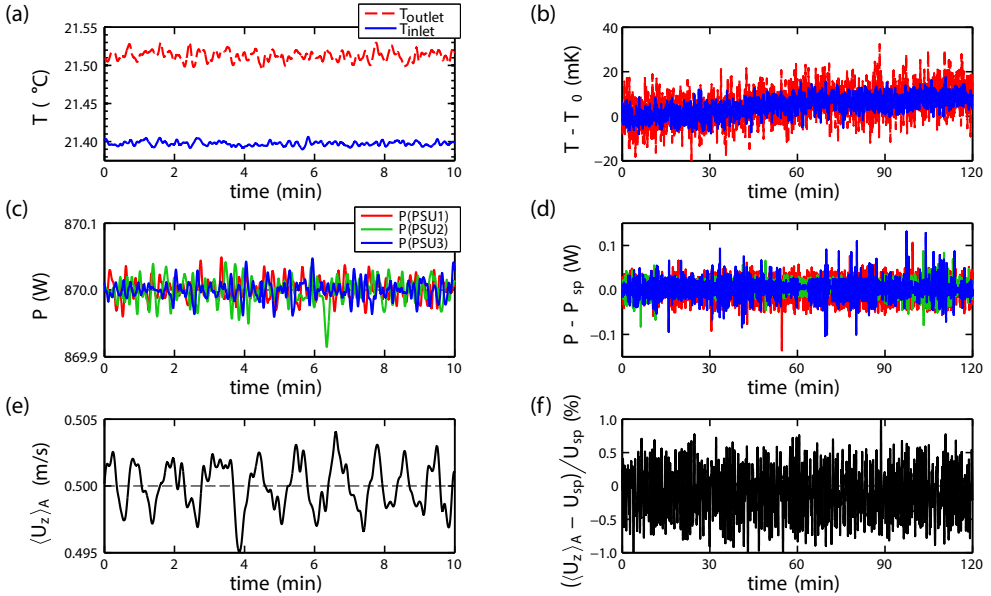
Figure 3.3: Typical timeseries of the main global tunnel quantities after having settled to statistically stationary conditions, demonstrating the short-term fluctuations in (a), (c) and (e) and the long-term 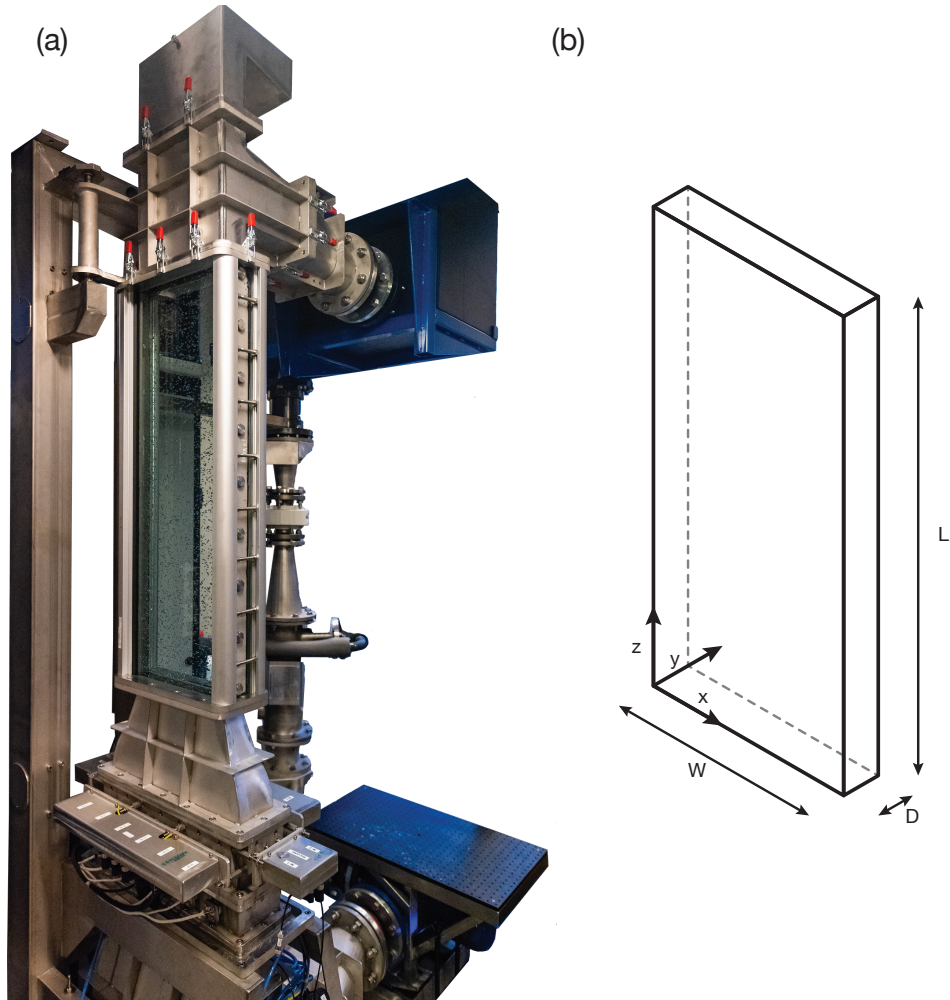stability in (b), (d) and (f). This specific case was at a set tunnel flow velocity of $U_{sp} = 0.5$ m/s using measurement section #1 (subscript sp stand for setpoint), a chiller setpoint of 19°C and a set heating power of 3×870 W = 2610 W divided over heaters 1 to 6. Heaters 1 and 2 were connected in series to power supply PSU1, likewise 3 and 4 to PSU2 and 5 and 6 to PSU3. This caused the heaters to operate at an internal temperature of near 90°C. (a) Temperatures T of the tunnel inlet (solid blue) and outlet (dashed red). (b) The same data as the left panel, but with the starting temperature T_0 subtracted. The temperature drift is below 20 mK over 120 minutes. (c) Heating power P provided by power supplies PSU1 (red), PSU2 (green) and PSU3 (blue). (d) The same data as the left panel, but with the setpoint of the power P_{sp} subtracted. The power is stable within 0.15 W regardless of the setpoint. (e) Instantaneous streamwise flow velocity inside the measurement section $\langle U_z \rangle_A$ averaged over its cross-sectional area A (measured using the flow meter). The dashed line indicates the setpoint. (f) The same data as the left panel, but renormalized with the flow velocity setpoint U_{sp}. The flow velocity is stable within 1% of the setpoint without drift over 120 minutes.

Figure 3.4:   System control diagram. The tunnel filling system and water level monitoring running on Arduino #2 are not discussed in this work and are mentioned for completeness.

The global gas volume fraction over the full height of the measurement section is monitored by a wet/wet differential pressure 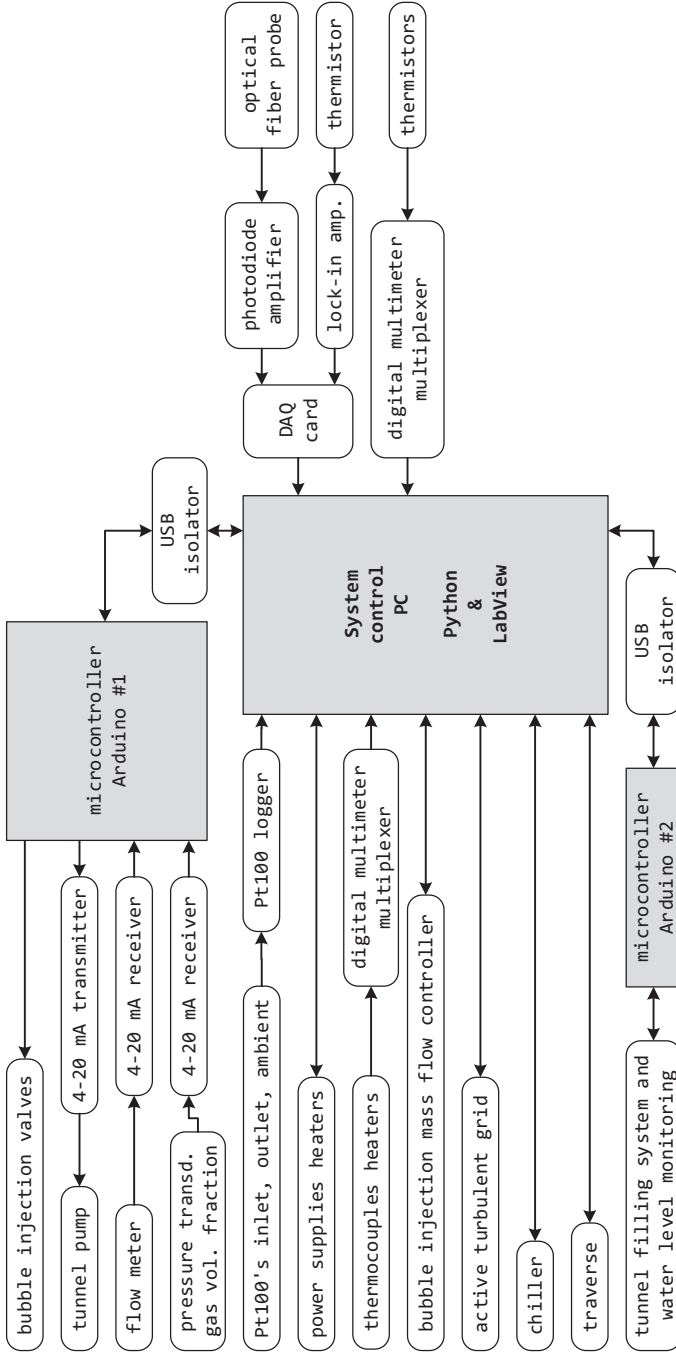transducer (Omega, PXM4091-70HDWUI). The pressure transducer is connected to two portholes, with a distance of $\Delta L = 0.96$ m in height apart, at the side of the measurement section. Each of these portholes has just a narrow channel of 1.0 mm in diameter that connects to the tunnel's internal volume. This ensures that no air will enter the lines from the portholes towards the pressure transducer and that they are always filled with liquid. The resulting difference in static pressure between these lines and the liquid column inside the measurement section translates into the relation $\alpha = \Delta P / (g\rho_l \Delta L)$, where α is the global gas volume fraction over the measurement section, ΔP is the measured pressure difference, g the local acceleration of gravity, ρ_l the density of the liquid and ΔL the distance in height between the portholes. We report a constant measurement accuracy in α of $\pm 0.2\%$, given already in units of the gas volume fraction percentage. Injecting 36 l/min of air through the bubble injection capillaries, we can achieve a maximum of $\alpha = 7.8 \pm 0.2\%$ when the tunnel pump is switched off, and e.g. $\alpha = 5.3 \pm 0.2\%$ at a flow velocity of 0.5 m/s inside measurement section #1. The local gas volume fraction, bubble size and bubble velocity statistics can be obtained by the optical fiber probe technique. For details on this experimental technique and signal processing we refer to Cartellier [69] and van Gils *et al.* [85].

3.2.7   Active turbulent grid

The active turbulent grid consists of fifteen independently-rotating rods with agitator flaps attached to them that stir up the liquid flowing past, see 5.1a and 5.1c. It resembles the grid described in paragraph §3.3.1 of Poorte and Biesheuvel [86], albeit with modern DC-motors (Maxon, DCX32L GB KL 24V) and controllers (Beckhoff, EL7332) and with only 15 rods instead of 24 because of the smaller cross-sectional area of the tunnel. There are several forcing protocols that can be used to drive the rods independently at varying rotation speeds and direction for varying periods of time. The study over the different protocols by Poorte and Biesheuvel [86] revealed that the *double-random asynchronous mode* protocol is the most favourable, as this protocol does not lead to periodicities in the turbulent power spectrum directly downstream of the grid. Hence, this protocol (P0238) is the standard we use in our studies. In short, it varies the rotation speed of a single rod and the duration of that rotation by randomly choosing values from the intervals $[-\Omega_m, \Omega_m]$ and $[50, 90]$ ms, respectively. A control parameter called '*grid speed factor*'

GSF will rescale the value of Ω_m, such that the amount of agitation can be tailored. For example, the nominal value of Ω_m at a grid speed factor of 0.5 corresponds to 18 Hz.

3.2.8   System control

The system control of the TMHT facility is controlled by two programmable multifunction microcontroller boards in conjunction with a PC, see 3.4 for a simplified diagram. The boards used are two Arduino M0 Pro which are powered by a SAMD21 microcontroller unit from Atmel, featuring a 32-bit ARM Cortex M0 core.

One major source of electrical noise is carried by the lab facility electrical ground. Inductive spikes induced by e.g. motors or switching relays can travel over the ground leads and can interfere with the sensitive microcontrollers. To prevent ground loops, ground noise, or inductive spikes from reaching the sensitive microcontrollers, one has to float the microcontroller board with respect to the lab facility ground potential. We do this by powering the microcontrollers using a noise-suppressing power supply (Traco Power, TCL 120-112) whose output is left floating with respect to ground. That means that ground-referenced peripheral devices cannot be connected to the Arduino directly, lest we loose the floating ground reference. Hence, all USB connections from the microcontrollers to the PC are galvanically isolated by USB isolators (Olimex, USB-ISO). All peripheral digital sensors and actuators are connected to the microcontrollers with opto-couplers in between.

All analog signals from and to the microcontrollers (i.e. set pump speed, flow meter and read pressure transducer) transmit over 4–20 mA current loops, which are inherently insensitive to electrical noise in contrast to using voltage as a data carrier. The 4–20 mA current transmitter and receivers used are, respectively MIKROE-1296 T Click and MIKROE-1387 R Click from MikroElektronika. The remaining peripheral devices (i.e. the Pt100 data logger, programmable power supplies, digital multimeter multiplexers, mass flow controller, active turbulent grid, chiller and traverse controllers) are directly connected to the PC.

The main control program is running in Python 3.6 on the PC and handles all device input/output communication including the microcontrollers, with the exception of the active turbulent grid which is running on LabView from National Instruments. The main program has a graphical user interface to provide control, monitoring, and data logging of the TMHT facility, whose global quantities are logged at a rate of 10 Hz. The Python libraries that

Figure 3.5: Normalised (a) streamwise U_z and (b) spanwise U_x velocity profile along the width of the setup at half-height obtained from PIV measurements for different mean flow rates $\langle U_z \rangle_A$ and constant speed of the active grid (the active grid is running at $GSF = 0.5$). U_b is the streamwise velocity in the bulk, calculated by averaging the measured velocity over the width $x/W = 0.25$ to $x/W = 0.75$.

have been written to provide multithreaded communication with the specific laboratory devices including the Arduino microcontrollers are made available under the MIT open-source license and can be found at the GitHub repository [87].

3.3 Examples of flow and temperature measurements

3.3.1 Velocity profile measurements

The transparent measurement section of the THMT allows for the measurements of the local velocity using a variety of optical techniques including particle image velocimetry (PIV), laser Doppler anemometry (LDA), and particle tracking velocimetry (PTV), which could even be performed simultaneously if needed. As a first step in demonstrating the robustness and consistency of the setup, we measure the liquid velocity using two experimental techniques: LDA in backscatter mode and PIV in measurement section #1 (width × depth: 0.3×0.04 m^2). For LDA measurements the flow is seeded with polyamid seeding particles (diameter 5 μm, density 1050 kg/m^3). The LDA system used consists of DopplerPower DPSS (diode–pumped solid–state) laser and a Dantec burst spectrum analyser (BSA). For PIV we seed the flow with fluorescent
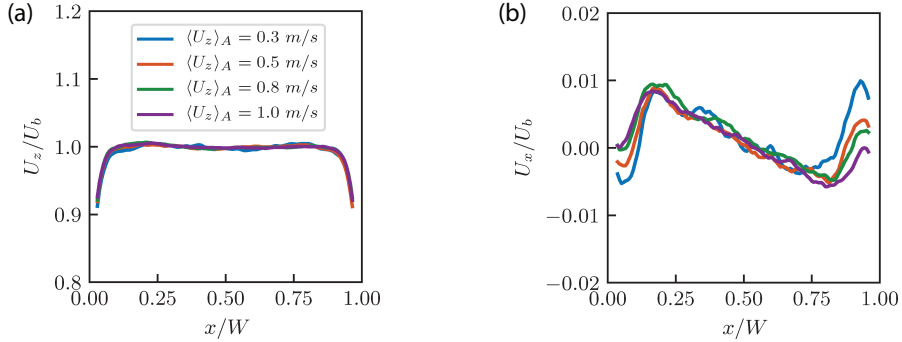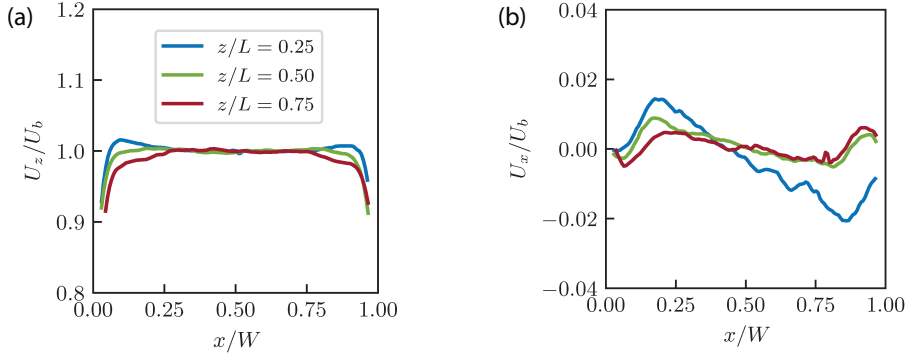
Figure 3.6:   Normalised (a) streamwise U_z and (b) spanwise U_x velocity profile along the width of the setup obtained from PIV measurements at different heights for mean flow rate of $\langle U_z \rangle_A = 0.5$ m/s and constant speed of the active grid $GSF = 0.5$. U_b is the streamwise velocity in the bulk at each height, calculated by averaging the measured velocity over the width $x/W = 0.25$ to $x/W = 0.75$.
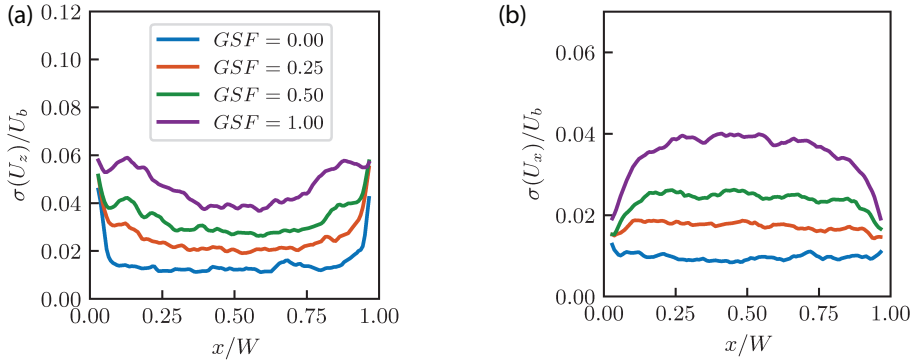
Figure 3.7:   Turbulence intensity in (a) streamwise and (b) spanwise direction along the width of the measurement section at half-height obtained from PIV measurements for $\langle U_z \rangle_A = 0.5$ m/s and varying speed of rotation of the active grid (varying the value of the grid speed factor (GSF)). $GSF = 0$ corresponds to the measurement with the active grid switched off, while for $GSF = 1$ rods are rotating at a maximum speed. $\sigma(U_z)$ is the standard deviation of the streamwise velocity, while $\sigma(U_x)$ is the standard deviation of the spanwise velocity.
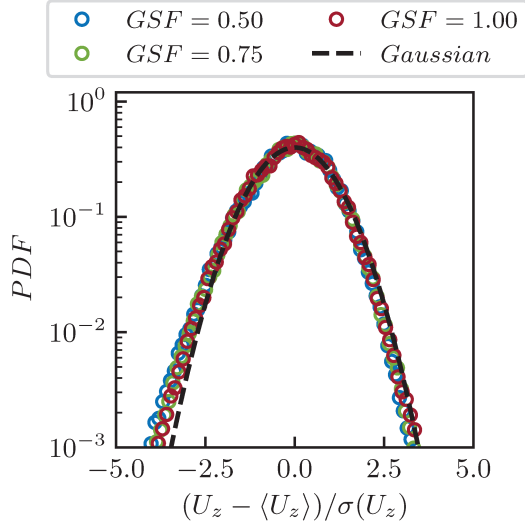
Figure 3.8: Probability density function of the streamwise velocity for $\langle U_z \rangle_A = 0.5$ m/s and different values of the grid speed factor, obtained at $x/W = 0.5$, $y/D = 0.5$, $z/L = 0.5$ using LDA. Gaussian with zero mean and unit variance is added for reference.
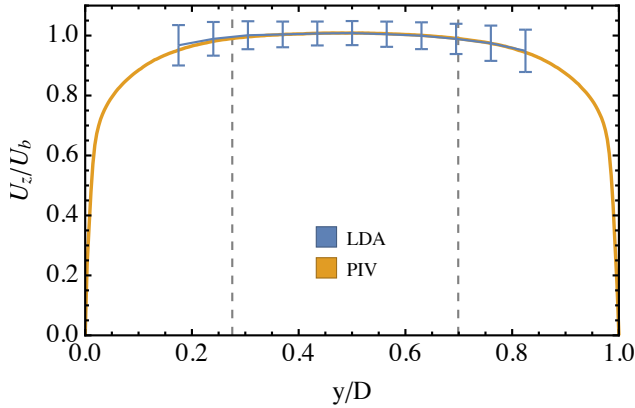
Figure 3.9: LDA-scan and PIV measurement of the vertical velocity along the depth of the setup at half-height performed for $\langle U_z \rangle_A = 0.5$ m/s and $GSF = 0.5$. The bars for the LDA correspond to ± 1 standard deviation of the velocity. Dashed lines present δ_{99} for both boundary layers.
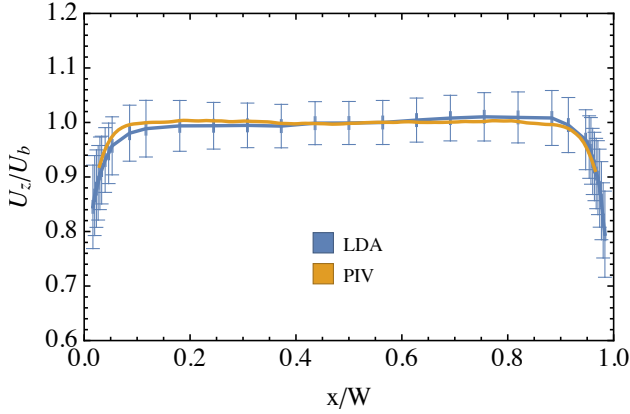
Figure 3.10:   Scan of the vertical velocity along the width of the setup at half-height performed using LDA and PIV for $\langle U_z \rangle_A = 0.5$ m/s and $GSF = 0$. The bars corresponds to ± 1 standard deviation of the velocity. The bars correspond to ± 1 standard deviation of the velocity.

tracer particles (diameter 50 μm). We use a high speed laser (Litron LDY-303HE) with a cylindrical lens to generate a sheet of light passing through the centre of the glass side-wall of the measurement section ($y/D = 0.5$). A double-frame camera (PCO Imager sCMOS) at 20 fps was used to obtain the velocity field. All the velocity profiles obtained using PIV presented in this section are calculated by averaging the velocity over several heights, covering ± 5 cm around the noted height.

In figure 3.5 we plot the normalised mean profile of the streamwise and spanwise velocity obtained from PIV measurements for different mean flow rates, namely 0.3 m/s, 0.5 m/s, 0.8 m/s, and 1.0 m/s, for a constant active grid speed factor of 0.5. We find that the variation of the mean horizontal and vertical velocity is negligible in the bulk of the setup, namely not more than $\pm 1.5\%$ from the mean streamwise velocity. In figure 3.5b we see that the spanwise velocity has a positive and negative peak, which is a signature of the contraction section placed downstream of the measurement section.

Next, we look at the velocity profiles for $\langle U_z \rangle_A = 0.5$ m/s and $GSF = 0.5$ at different heights, namely at $z/L = 0.25$, $z/L = 0.5$ and $z/L = 0.75$. In figure 3.6a we see that the streamwise velocity remains constant (within $\pm 2\%$) along the width at different heights. By scanning the velocity at different heights we observe that the influence of the contraction on the spanwise velocity reduces as the height increases, although its amplitude is only of order of 1% of the

streamwise component (see Figure 3.6b).

In figure 3.7 we plot the turbulence intensity measured using PIV at half-height for $\langle U_z \rangle_A = 0.5$ m/s and study the influence of the active grid on the velocity statistics. By varying the grid speed factor (GSF) from 0 to 1, it is easily observed that the active grid has a strong influence on the velocity fluctuations. For a grid speed factor (GSF) equal to zero, the active grid is switched off, and the rods are placed in such a way that the flaps are open, forming a passive grid instead. In this case we observe the weakest velocity fluctuations. As the GSF increases the fluctuations increase up to 3 times, and for each of the cases the velocity fluctuations remain nearly constant along the width in the bulk. In Figure 3.8 we show the probability density function of the streamwise velocity obtained from LDA measurements for different GSF at the centre of the setup ($x/W = 0.5$, $y/D = 0.5$, $z/L = 0.5$) at mean flow rate of 0.5 m/s. We observe that for all the settings of the active grid the distribution of the vertical velocity nearly follows a normal distribution, with a skewness of around 0.2 and a kurtosis of around 3.25 for all cases.

Furthermore, we examine the homogeneity in the wall-normal direction by measuring the vertical velocity along the depth of the setup at $z/L = 0.5$, $\langle U_z \rangle_A = 0.5$ m/s and $GSF = 0.5$ using LDA and PIV measurement. Results presented in Figure 3.9 demonstrate that the velocity is nearly constant in the wall-normal direction as well, with variations of only around $\pm 2\%$ from $y/D = 0.2$ to $y/D = 0.8$. Furthermore, we identify the boundary layer thicknesses by the δ_{99} criterium, and find that $\delta_{99} = 0.28D$ on the left and $\delta_{99} = 0.30D$ on the right. Leaving a large center flow of $\approx 0.4D$ outside the boundary layers.

Lastly, we compare PIV and LDA measurements of the streamwise velocity profiles in 3.10. We find very good overlap within 1–2%. Note that these were not measured simultaneously but on different moments, which could explain the slight difference between them. The advantage of the PIV measurements is that an entire field is measured at once, rather than measuring point-by-point (LDA). The downside is the difficulty of using PIV in two-phase flows, which is possible with LDA for low volume fractions α. Another advantage of LDA over PIV is the processing requirements are orders of magnitude less for LDA measurements as compared to PIV measurements. LDA also easily offers very high data-rates, which can be tricky for PIV due to the requirements of lasers and cameras.
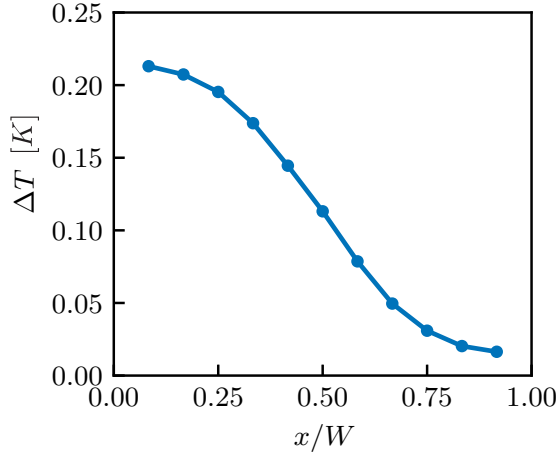
Figure 3.11:   Temperature profile at half height in the case of heating of the left half $x/W = 0$ to $x/W = 0.5$ of the setup. Here $\Delta T = T - T_{inlet}$, where T_{inlet} is the inlet temperature measured before the heaters, and T is the temperature measured by a thermistor in the measurement section.

3.3.2   Local temperature measurements

Here we examine the influence of heating of one half of the heating section on the temperature profile in the measurement section of dimensions width $\times$ depth $= 0.3 \times 0.04$ m^2, with the mean liquid flow of 0.5 m/s and the grid speed factor of 0.5. In this specific configuration six heaters (out of twelve total) which are placed in the left half ($x/W \leq 0.5$) of the heating section have been supplied by a constant power of 870 W each. The thermistor for the temperature measurements is inserted to the measurement section from the sidewall of the section and traversed over the width at half height. The measurements are logged at 2 Hz by a digital multimeter over 2 hours after statistically steady state is achieved. Figure 3.11 shows temperature profile obtained in such a way, where heating was introduced in the heating section $x/W \leq 0.5$. Here $\Delta T = T_{inlet} - T$ is the difference between temperature measured before the heaters T_{inlet} and the temperature measured in the bulk in the measurement section T. We observe decrease in ΔT from $x/W = 0$ to $x/W = 1$ as a consequence of heating of only one half of the section.

After passing the heated section, warm and cold volume of liquid mix, resulting in different temperature signals in the measurement section at $x/W = 0.25$, $x/W = 0.5$ and $x/W = 0.75$ (see Figure 3.12a)). This is also reflected on
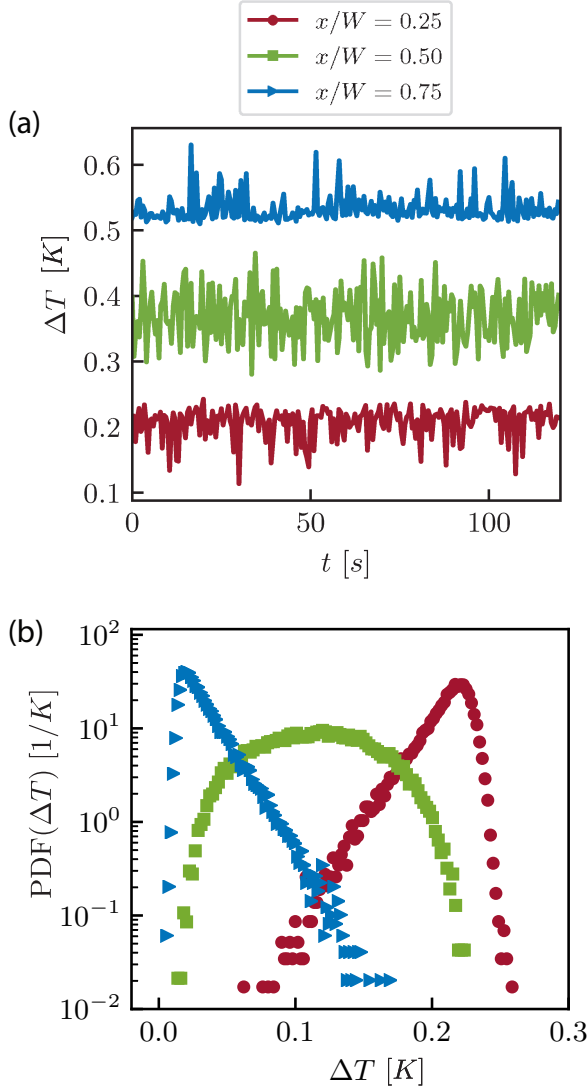
Figure 3.12: (a) Temperature series measured at different locations: $x/W = 0.25$ above the heated area, $x/W = 0.50$ in the centre of the setup and $x/W = 0.75$ above the non-heated area. Note that for the signals at $x/W = 0.50$ and $x/W = 0.75$ offsets of 0.25 K and 0.50 K, respectively, are applied, for clarity of reading the figure. (b) Probability density function of the temperature at different locations of the setup: $x/W = 0.25$ above the heated area, $x/W = 0.50$ in the centre of the setup and $x/W = 0.75$ above the non-heated area.

the probability density function shown in figure 3.12b). Namely, negative skewness is observed for the signal at $x/W = 0.25$ due to non-heated liquid penetrating to the opposite side of the section. In the center $(x/W = 0.5)$, where the mixing between cold and warm part of the bulk is the most intense, the signal is not skewed (skewness = 0), i.e. positive and negative fluctuations are equally represented. Again at $x/W = 0.75$ warm liquid parcels penetrate the cold part of the bulk, yielding a positively skewed PDF.

3.3.3 Combined velocity and temperature measurements

To measure the local heat flux we need to simultaneously measure the temperature and local velocity at the same position in the flow. We measure the local temperature using a thermistor that is connected to one arm of a Wheatstone bridge so that very small variations of the resistance of the thermistor can be measured. We utilize a lock-in amplifier (SRS SR830) in order to reduce noise. We place the thermistor in the middle of the measurement section. We position the measurement volume of our LDA configuration just upstream (≈ 0.5 mm of the thermistor. We synchronize the two systems and for a flow velocity of $\langle U_z \rangle_A = 0.5$, an active grid speed factor $GSF = 0.5$, and heat injection by heaters 1–6 with a total of 2.25 kW, we measured the local temperature and the flow velocity, see figure 3.13. We find that the horizontal velocity v_x and the temperature fluctuations $(T' = T - \langle T \rangle)$ are strongly correlated with a Pearson correlation coefficient of $\rho_{v_x,T'} \approx 0.37$, while we find that the vertical velocity and the temperature are not correlated at all $\rho_{v_z,T'} \approx 0.00$. This results in a positively skewed temperature probability density function for $\tilde{J}_x$ with broad thick tails (kurtosis $K = 7.5$) but not for $\tilde{J}_z$, where we find a platykurtic distribution ($K = 2.6$), akin to the distribution of the temperature itself.

3.3.4 Dispersion of a passive scalar in a turbulent bubbly flow

The TMHT offers the possibility of studying the mixing of a passive scalar in turbulent bubbly flow. The primary advantage of this setup over, for example, the Twente Water Tunnel [88] is that in this setup we can easily achieve gas volume fractions higher than 1%. For the purpose of studying mixing of a low-diffusive dye induced by a swarm of high Reynolds number bubbles rising within a turbulent flow we inject a fluorescent dye (Fluorescein sodium) in the tunnel with the measurement section #2 (width $\times$ depth $= 0.3 \times 0.06$ m^2). The dye injector (diameter 2 mm) is placed in the middle of the cross-section
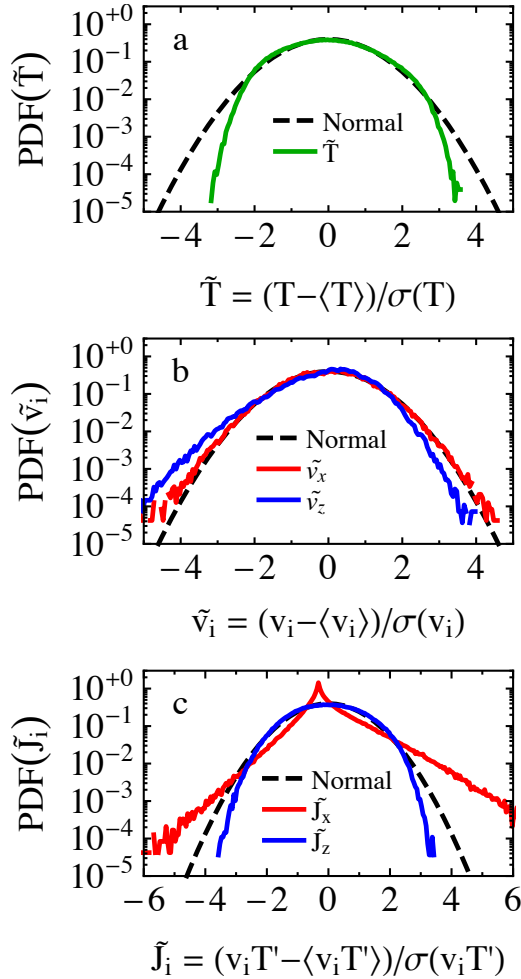
Figure 3.13:   Combined velocity and temperature measurements at the middle of the tunnel ($x/W = y/D = z/L = 0.5$) with mean liquid velocity $\langle U_z \rangle_A = 0.5$ m/s, the active grid speed factor $GSF = 0.5$ and the total heating power 2.25 kW for heaters 1–6. (a) Standardized (zero mean, unit variance) probability density function of the temperature. For reference we have added a normal distribution with zero mean and unit variance as a black dashed line. (b) Standardized probability density function of the velocities $\tilde{v}_i = (v_i - \langle v_i \rangle)/\sigma(v_i)$, where $i = x$ is the horizontal direction and $i = z$ is the vertical direction. (c) Standardized probability density function of the product of the velocity and the temperature fluctuations ($T' = T - \langle T \rangle$), which can be interpreted as a local convective heat flux.

20 cm away from the bottom of the measurement section. The injection is performed over 60 seconds at a flow rate matching the mean liquid velocity in the tunnel (~ 30 cm/s). The images of the flow are taken 10 second after the start of the injection, using two synchronized and vertically aligned cameras (Imager sCMOS, Lavision) with 105 mm macro lenses and optical band-pass filters (450–650 nm).

In figure 3.14a, we show an instantaneous snapshot of the fluorescent dye being advected and diffused in the presence of a bubbly turbulent flow. Using a time–series of such snapshots, we measure the mean intensity profiles of the fluorescent light I across the width of the setup at different heights; profiles for a few selected heights are shown in figure 3.14b. The profiles are symmetric due to the homogeneity of the flow in the horizontal direction. Additionally, we find that the profiles are nearly normally distributed, suggesting that the spreading of the dye in the horizontal dimension is dominated by diffusion. The objective of future studies is to obtain the horizontal diffusion coefficient by measuring concentration of the dye by means of quantitative laser induced fluorescence. For further details on this experimental technique we refer to Alméras *et al.* [35].
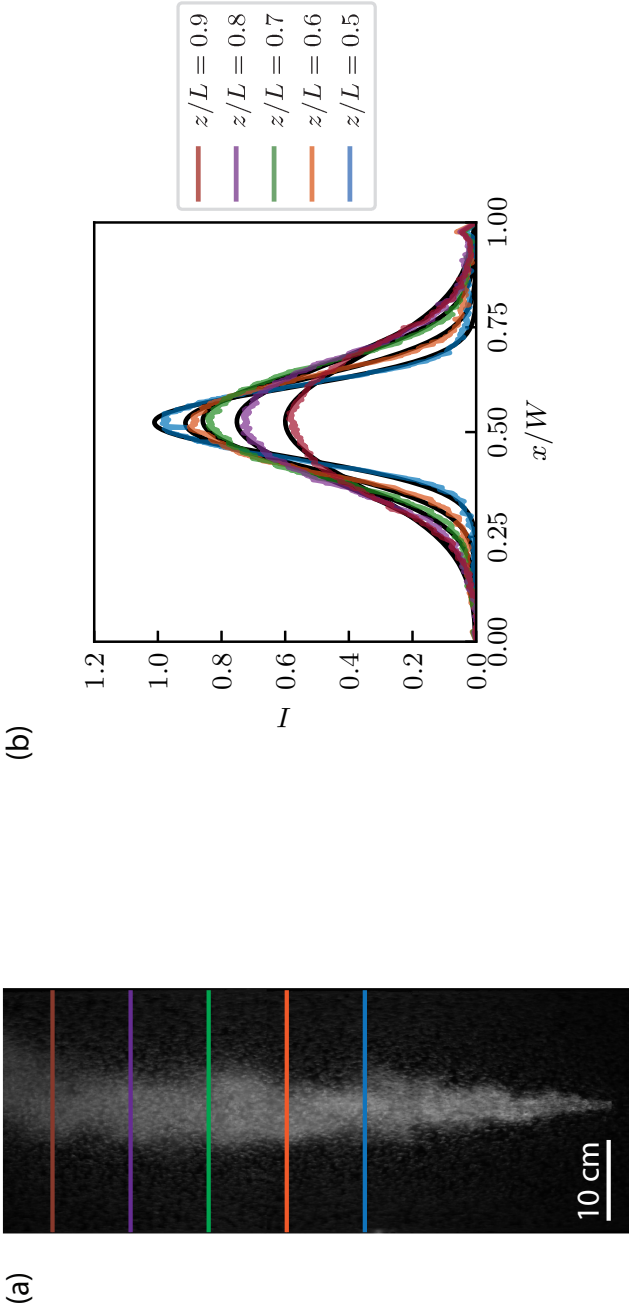
Figure 3.14: Dispersion of a fluorescent dye in a bubbly turbulent flow with $\langle U_z \rangle_A = 0.30$ m/s. (a) Instantaneous snapshot of the flow taken at an arbitrary time showing the spatial distribution of the fluoresced light. (b) Time averaged light intensity profiles across the width of the setup at different heights (in colour) and corresponding Gaussian fits.

3.3.5   Salt

As discussed in the section 5.1, the TMHT also allows the possibility to study the dynamics of bubbles injected in brine (salt solution). We perform preliminary tests by varying the mean liquid flow rate, gas flow rate, and the concentration of salt (NaCl) in the brine solution with a constant grid speed factor $GSF = 0.4$, while using the measurement section #2. In figure 3.15, we show snapshots for the different cases. Images were taken using a Photron SA1 camera at 1000 frames per second.

We visually observe a big difference in the flow regimes as we increase the salt concentration of the solution from $c_m = 0\%$ to $c_m = 12\%$ (mass fraction). The effect is more pronounced when the gas flow rate is higher, which may be due to presence of more smaller bubbles caused by the increase in surface tension by the addition of salt. This also leads to a reduction in the deformability of the bubbles and consequently to a change in the dynamics of the system.

By means of image processing, we measure the bubble diameter for the cases of mean liquid velocity 0.15 m/s and 0.25 m/s and gas flow rate of 5 l/min for varying salt concentrations. In figures 3.16a and 3.16b we show sample images from two different simple image processing algorithms for edge detection implemented using Matlab. For cases with low concentration of salt ($c_m \leq 1.3\%$) we identify contours of objects as well as boundaries of holes inside these objects (see Figure 3.16a). The criterium used to identify bubbles is that the area of the outermost object is 1.3 times greater than the area of the object completely enclosed by it. For the case of high salt concentration $c_m = 12\%$, for which more spherical bubbles are present, bubbles are selected by identifying round objects under the condition that the bubbles are in focus (see Figure 3.16b). Each method detects at least 1300 bubbles for each of the examined cases. The distributions of the equivalent bubble diameter for 4 concentrations and 2 flow speeds is shown in 3.16c. Note that the bubble size is determined from images taken from the side which causes a large spread in the volume-determination as the information of the depth is lacking and the shape of the bubble constantly changes as the bubble deforms while rising. We find that a small increase of the concentration of salt from $c_m = 0\%$ to $c_m = 1.3\%$ significantly decreases the average bubble diameter. Further increasing the salt concentration from $c_m = 1.3\%$ to $c_m = 12\%$ seems to have hardly any influence on the average bubble diameter. For each examined salt concentration, an increase in the mean liquid flow rate resulted in almost no change in the average bubble diameter. Future studies in this setup will be dedicated to studying the effect of salt on the dynamics of the system and the

$\langle U_z \rangle_A$	0.15 *m/s*	0.25 *m/s*	0.25 *m/s*	0.15 *m/s*
$\dot{V}_g$	5 *l/min*	5 *l/min*	35 *l/min*	35 *l/min*
c_m				
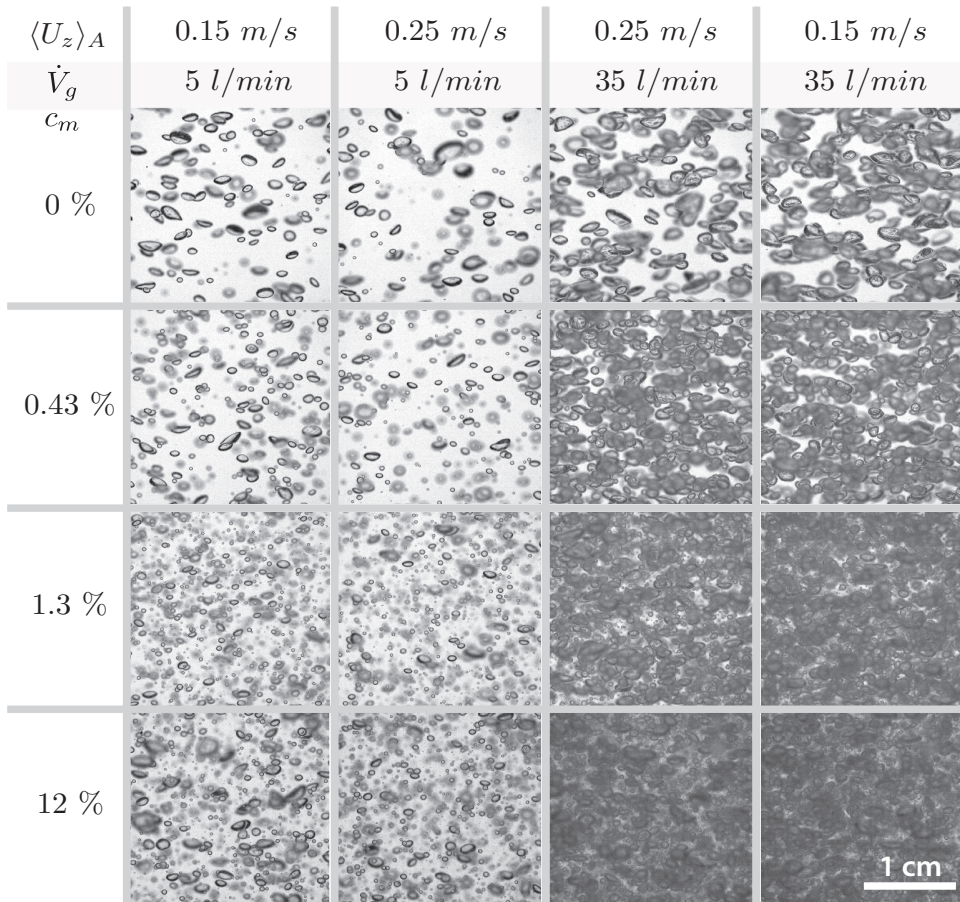
Figure 3.15: Snapshots of the flow in the TMHT with the addition of increasing salt concentration (from top to bottom), for various water flows and gas flow rates. $\langle U_z \rangle_A$ is the mean liquid streamwise velocity, $\dot{V}_g$ is the gas flow rate, c_m is the mass fraction of salt in the solution.
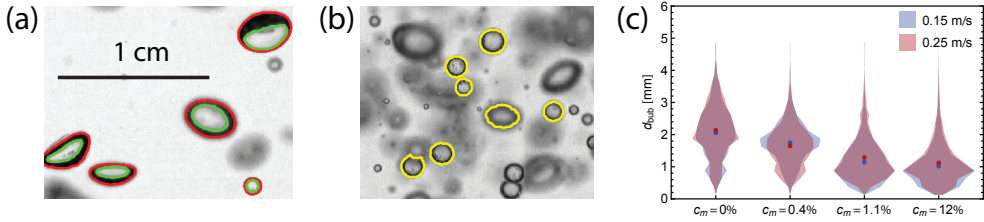
Figure 3.16:   (a) Zoom of a snapshot for the case of mean liquid velocity $\langle U_z \rangle_A = 0.15$ m/s, gas flow rate $\dot{V} = 5$ l/min and $c_m = 0\%$, showing bubbles identified as pairs of objects; (b) Zoom of a snapshot for the case of $\langle U_z \rangle_A = 0.15$ m/s, gas flow rate $\dot{V} = 5$ l/min and $c_m = 12\%$, showing bubbles identified as round objects; (c) Distribution of the bubble diameter for $\langle U_z \rangle_A = 0.15$ m/s and $\langle U_z \rangle_A = 0.25$ m/s for varying salt concentrations. The mean values of the diameter are indicated using points.

coupling of heat transport with the salt concentration.

3.4   Summary and outlook

A new experimental facility the Twente Mass and Heat Transfer Water Tunnel (TMHT) has been built. This facility has global temperature control, bubble injection and local heat/mass injection and offers the possibility to study heat and mass transfer in turbulent multiphase flow. The tunnel is made of high-grade stainless steel permitting the use of salt solutions in excess of 15% mass fraction, besides water. The total tunnel volume is 300 L. Three interchangeable measurement sections of 1 m height but of different cross sections (0.3×0.04 m^2, 0.3×0.06 m^2, 0.3×0.08 m^2) span a Reynolds-number range from 1.5×10^4 to 3×10^5 in the case of water at room temperature. The glass vertical measurement sections allow for optical access to the flow, enabling techniques such as laser Doppler anemometry, particle image velocimetry, particle tracking velocimetry, and laser-induced fluorescent imaging. Thermistors mounted on a built-in traverse provide local temperature information at a few milli-Kelvin accuracy. Combined with simultaneous local velocity measurements, the local heat flux in single phase and two phase turbulent flow can be studied. We demonstrated long term and short term stability of the power of the heaters and the cooler, of the inlet and outlet temperature of the tunnel, and the mean flow rate. PIV and LDA measurements were performed for a variety of flow conditions to show that homogeneity of the flow is satisfying. Preliminary

temperature measurements in single phase flow and measurements with salt and dye injection in two phase flows were performed as well.

Acknowledgments

More is different. [89]
      P. W. Anderson

4

The emergence of bubble-induced scaling in passive scalar spectra in turbulent bubbly flows [1]

Abstract

The statistics of turbulent fluctuations are strongly modified by the injection of large bubbles. While this is well known and well analyzed for the velocity fluctuations, little is known on the fluctuation of a passive scalar under such conditions. Here we uncover the thermal spectral scaling behavior of a turbulent multiphase thermal mixing layer. By injecting a swarm of large bubbles ($\mathrm{Re}_{\mathrm{bub}} = \mathcal{O}(10^2)$), we trigger the development of a -3 spectral scaling, replacing the classical -5/3 scaling of the single phase flow case. For bubbly flows, the -5/3 scaling still observed at large scales is followed by a steeper slope and becomes even steeper with increasing gas volume fractions α. The -3 scaling coincides with the typical energy spectral scaling for the velocity fluctuations in high Reynolds number bubbly flow. We also identify the transition from the -5/3 scaling to the -3 scaling.

4.1   Introduction

In turbulent flows, one searches for universality in the velocity and temperature fluctuations.. According to the Kolmogorov–Obukhov–Corrsin theory [13–15], the universal scaling of the scalar spectra $E_\theta(k) \propto k^{-5/3}$ in the inertial-convective range for high enough Reynolds and Péclet number, where k is the wavenumber and θ is a scalar [2]. Different scaling behaviours can emerge if more physical complexity is added. In this work, we include a swarm of large rising bubbles to the liquid flow [3, 7, 90]. Large rising bubbles are defined as having a bubble Reynolds number $\mathrm{Re_{bub}} = V_r d / \nu = \mathcal{O}(10^2)$, where V_r is the mean bubble rise velocity relative to the carrier liquid, d is the mean area equivalent bubble diameter and ν is kinematic viscosity of the ambient liquid. For the velocity fluctuation (energy) spectra $E_u(k)$, the bubbles lead to the emergence of $E_u(k) \propto k^{-3}$ scaling, being first observed and theoretically addressed in Lance and Bataille [21]. They argued that in a statistical steady state, the k^{-3} scaling can be achieved in the spectral space by balancing the viscous dissipation and the spectral production due to the rising bubbles [21]. It was also reviewed in Ref. [7] that the k^{-3} scaling can result from spatial and temporal velocity fluctuations in homogeneous bubbly flow. As reviewed in Ref. [7] and the recent DNS work [91], this scaling is robust and is observed for a homogeneous bubble swarm for a wide range of parameters: $10 \leq \mathrm{Re_{bub}} \leq 1000$ and $1 \leq \mathrm{We} \leq 4$ where We is the Weber number. In contrast, point particle simulations do not show k^{-3} scaling [25], because the wakes behind the bubbles are crucial for the emergence of a -3 scaling (in both frequency or wavenumber space) [7].

While there are abundant studies on the energy spectra in high-Re bubbly flow, the study of scalar spectra in such flow is limited. Ref. [41] investigated the time-resolved concentration fluctuations of a passive fluorescent dye (passive scalar) in a confined bubbly thin cell in which the scalar spectral scaling f^{-3} is observed, where f is the frequency. For the three-dimensional case, Ref. [37] investigated the scalar spectra in a bubbly column in a vertical convection setup, but they were not able to resolve the frequencies related to the -3 scaling of the energy spectra in bubble-induced turbulence [37].

In the present work, by utilizing a fast-response temperature probe, we are able to capture the gradual change of *passive scalar* spectral scalings for increasing α in high-Re bubbly flow superposed in a turbulent thermal mixing layer.

Apart from investigating the scaling behaviour itself, also the onset scale of the -3 scaling is of interest because it may be related to the physical origin of

the -3 subrange of the scalar spectra. The onset scale of the -3 subrange for energy spectra is still not yet exactly identified in general [7]. We report the transition scales to -3 scaling for passive scalar spectra as a function of α to open the discussion that may ultimately help to understand the -3 subrange in both the energy and scalar spectra in high-Re bubbly flow.

4.2 Experimental setup and methods

We utilize the Twente Mass and Heat Transfer Tunnel [92] which can produce active-grid generated turbulent vertical channel flow, inject rising bubbles and heat the liquid in a controlled manner. A turbulent thermal mixing layer [93] with liquid mean flow velocity of approximately 0.5 m/s is produced. A sketch of the setup is shown in Fig. 4.3a in the Appendix. The global gas volume fraction α in the measurement section is measured by a differential pressure transducer of which the two ends are connected to the top and bottom of the measurement section. A fast-response transducer (Amphenol Advanced Sensors type FP07, response time 7 ms in water) is placed into the middle of the measurement section in order to measure the temperature. An AC bridge with with a sinusoidal frequency 1.301 kHz drives the thermistor in order to reduce electric noises, in which the bridge potential is measured by a lockin amplifier (Zurich Instrument MFLI). A tempearture-control water bath (PolyTemp PD15R-30) with the temperature stability ± 0.005 K is used for calibrating the thermistor. By fitting the temperature-resistance characteristic equation proposed by Steinhart and Hart [94] over a short range of temperature of interest (in which the terms are kept only up to the first order to avoid over-fitting), the thermistor has an accuracy of 20 mK. The typical large-scale temperature difference from the heated side to the non-heated side at the mid-height of the measurement section is about 0.2K (see Fig. 5.4 in Chapter 5). For the velocity measurements, we employ constant temperature anemometry (CTA) using a hot film sensor (Dantec 55R11, 70 μm diameter with 2 μm nickel coating, 1.3 mm long and up to 30 kHz frequency response) in the middle of the tunnel. We note that since a CTA measurement requires negligible temperature variation of the flow, the velocity is measured when the heaters are idle. The velocity statistics are not influenced by the temperature because the flow is practically a forced convection (see also the discussion in the next paragraph). The working-liquid is decalcified tap water at around 22.7°C (Prandtl number $Pr = \nu/\kappa = 6.5$, where ν and κ are the kinematic viscosity and thermal diffusivity of water, respectively) and the bubbles are

created by regular air through needles (see Fig. 4.3a in the Appendix). The rising bubbles provide additional stirring to the liquid.

We first explored the parameter space by increasing α from 0.0% to 5.2%. Let λ_u and λ_θ be the Taylor-microscale of the velocity and the temperature, respectively [12]. For the single phase turbulent thermal mixing layer, the Taylor Reynolds number is $\mathrm{Re}_{\lambda_u} = u_0' \lambda_u / \nu = 130$ and the Péclet numbers based on both microscales are $\mathrm{Pe}_{\lambda_u} = u_0' \lambda_u / \kappa = 870$ and $\mathrm{Pe}_{\lambda_\theta} = u_0' \lambda_\theta / \kappa = 520$ [12]. Re_{λ_u} is the typical Reynolds number that is used for characterising the inertial effect when compared to viscous effect for grid-turbulence (freely decaying turbulence) [9], unlike other bounded turbulent flows which use the length of the size domain as the length scale. Extending this notion to scalar field in grid-turbulence, to compare the inertial effect to the diffusive effect of the scalar, we use the Péclet number that based on the microscales. One traditional choice of such microscale is λ_u [95] but recent numerical simulations uncover that the small-scale anisotropy of the scalar field depends on the Péclet number based on λ_θ [12]. For the millimetric bubble sizes and velocities, the bubbles are detected by a circular Hough transform and tracked (see Table 4.1 in the Appendix). $\mathrm{Re}_{\mathrm{bub}}$ decreases from 480 ($\alpha = 0.6\%$) to 220 ($\alpha = 4.7\%$). The method of calculating the spectra of the velocity and temperature fluctuations for two-phase flows is discussed in Appendix 4.A. Let the height of the measurement section be h. The temperature difference across $\pm 0.25h$ from the mid-height of the measurement section is less than 0.05K. To idenifiy whether the flow is a forced convection or whether the scalar is simply advected passively, we consider the relative importance of the buoyancy force (parallel to the streamwise direction) to the inertial force, which is the ratio of Grashof number Gr and the square of the Reynolds number $\mathrm{Re}_{0.5h}^2$ [38] that is based on the vertical distance between $\pm 0.25h$ from the middle of the measurement section, the temperature difference across such height $\Delta_{0.5h}$ and the mean liquid velocity U. This gives $\mathrm{Gr}/\mathrm{Re}_{0.5h}^2 = 0.5hg\beta\Delta_{0.5h}/U^2 \leq \mathcal{O}(10^{-3})$, where g and β are the gravitational constant and volumetric expansion coefficient of water, respectively. Putting in the numbers, we find $\mathrm{Gr}/\mathrm{Re}_{0.5h}^2 \lesssim 10^{-3}$ implies that the temperature can be seen as passive scalar under these flow conditions.

4.3 The energy and scalar spectra

As the scalar in the present study is advected passively by the liquid velocity, the corresponding energy spectra first need to be examined in order to understand the passive scalar spectra. In Fig. 4.1, we show the power spectra

normalized by their corresponding variance, denoted as $P_i(f)$, where $i = u$ and $i = \theta$ corresponds to the normalized energy and scalar power spectra, respectively for different α. The energy spectra for single-phase shows a limited inertial range. However, whenever $\alpha > 0$, a pronounced -3 scaling is observed with the presence of an energy 'bump' just before this -3 scaling when α is large enough, which is consistent with [30]. We find that such -3 scaling occurs roughly between 100 Hz to 1000 Hz and has a higher energy content than the single-phase in the same frequency range. The physical mechanism of such small-scale enhanced velocity fluctuations is attributed to bubble-induced agitations, in which the velocity fluctuation production due to the bubbles is directly dissipated by viscosity [7, 21, 46].

Next we examine the passive scalar (temperature fluctuations) spectra. A scaling of -5/3 for 1 Hz $\leq f \leq$ 15 Hz is observed for the single-phase scalar spectrum. The phenomenon that a developed inertial range is observed in a passive scalar spectrum but not in the corresponding energy spectrum due to limited Reynolds number is also recorded in [96]. Moreover, as opposed to the relative high frequency (small-scale) fluctuation enhancement in the energy spectra, the scalar spectra show relative high frequency (small-scale) diminution when α increases from zero. The -5/3 scaling is followed by a steeper slope when α increases but such change of scaling is gradual and approximately saturated to the scaling of -3 for high enough α ($\alpha \approx 4.7\%$) around $f = \mathcal{O}(10\text{Hz})$. The main differences between the energy and the passive scalar spectra are that the rising bubbles produce additional fluctuations in the former but diminish the fluctuations in the latter; the emergence of the -3 scaling is abrupt in the former but gradual in the latter; and the -3 scaling occurs at $\mathcal{O}(100\text{Hz})$ for the former but $\mathcal{O}(10\text{Hz})$ for the latter.

Clearly, there are difference(s) in the physical mechanisms that lead to the same -3 scaling for the energy and passive scalar spectra. We first clarify the physical and mathematical background before speculating on the emergence of the -3 scaling in the scalar spectra.

The main commonalities and differences of the physical settings of the velocity and temperature fields are as follows. One common aspect is that along the measurement section, both the viscosity and diffusivity reduce the velocity and temperature fluctuations, respectively. On the other hand, the mean velocity field is homogeneous in the bulk of the measurement section while the temperature field has a large-scale nonlinear mean temperature gradient. The high-Re bubbles have viscous boundary layers at the air-water interface but there is negligible temperature difference between the bubbles and the liquid
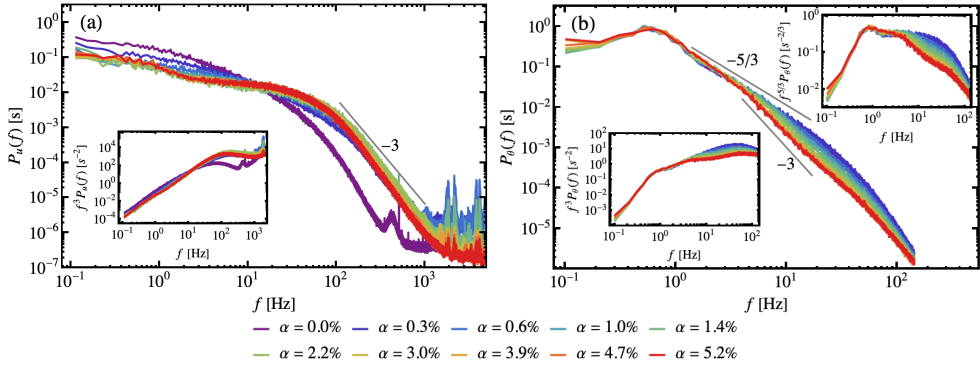
Figure 4.1:   (color) $P_i(f)$, the power spectra normalised by their respective variance of (a) the velocity fluctuations ($P_u(f)$) and of (b) the temperature fluctuations ($P_\theta(f)$) for α from 0 % (purple) to 5.2% (red). The compensated spectra $f^3 P_i(f)$ are the insets located at the bottom-left corner for both (a) and (b) while $f^{5/3} P_\theta(f)$ is located at the top-right corner of (b). The scalar spectra are cut at the limit of 143 Hz, corresponding to the highest resolved frequency of the thermistor.

phase, thus no thermal boundary layers are formed at the air-water interface. The viscous boundary layers transport momentum to the liquid phase at the scale related to bubbles, producing velocity agitations. The absence of thermal boundary layers implies no heat transport is present at the scale related to bubbles. To conclude, the only source of scalar fluctuations is from the mean temperature gradient while the source of velocity fluctuations is from bubble agitations.

Mathematically, for the spectral behavior of the passive scalar, one can consider the general spectral equation for the three dimensional scalar spectra $E_\theta(k,t)$ derived from the advection-diffusion equation [2] which as well-known of course neglects viscous heating,

$$\frac{\partial}{\partial t} E_\theta(k,t) + 2\kappa k^2 E_\theta(k,t) = T_\theta(k,t) + \Pi_\theta(k,t), \qquad (4.1)$$

where t is the time; T_θ and Π_θ are the local net transfer and the production at wave-number k respectively. One can employ Taylor's frozen-flow hypothesis to transform from the frequency domain to the wavenumber domain. In the present case, for increasing α, the single-phase -5/3 scaling of the spectrum gradually transitions to a -3 scaling at higher k (or f).

With the above discussed physical settings and scaling behaviors, we now speculate on the physical mechanisms on the -3 scaling of the scalar spectra in bubbly flows. As the -5/3 range is considered to be the inertial range where there is negligible net local transfer, negligible production and neglected diffusivity (and viscosity) effect (e.g. [9]), the scalar production due to the mean temperature gradient occurs at a smaller frequency than the -5/3 frequency range (lower than 1 Hz). Since the production due to the presence of bubbles is negligible as discussed previously, we speculate that $\Pi_\theta \approx 0$ at the scalar -3 subrange. Furthermore, we speculate that the rising bubbles enhance the mixing of temperature by homogenizing the temperature with increasing α at the scale related to the bubbles, and thus we observe a faster drop (steeper slope) in the passive scalar spectra. When α *is large enough*, the smoothing of temperature inhomogeneity due to the bubbles is so strong that the fluctuations are *directly dissipated by the molecular thermal diffusivity* which causes the saturation of the scaling. In accordance with Eq. 4.1, when the said situation happens, we speculate $T_\theta = T_\theta(\epsilon_\theta, k)$, where ϵ_θ is the scalar fluctuation dissipation rate. From dimensional analysis, we find $T_\theta \propto \epsilon_\theta k^{-1}$. In statistical stationary state, rearranging the terms we obtain $E_\theta \propto k^{-3}$ scaling [2].

4.4 Transition frequencies from -5/3 to -3 scaling

The onset frequencies of -3 scaling in the scalar spectra are now examined. For large enough α, each spectrum exhibits a rough -5/3 scaling before the -3 scaling, see Fig. 4.2a for examples. We identify the onset frequency by the a generalised Batchelor parametrisation (first used in Ref. [97] for the second order structure function) which can capture a transition from one scaling to another,

$$P_\theta(f) = \frac{(f/f_L)^{\zeta_b}}{[1 + (f/f_d)^2]^{\frac{\zeta_b - \zeta_a}{2}}} \qquad (4.2)$$

where f_L is a fitting parameter which can be interpreted as some small frequency scale and influencing the height of fit, and f_d is another fitting parameter which is the transition frequency from the scaling f^{ζ_b} (before) to f^{ζ_a} (after) with scaling exponents ζ_b and ζ_a. One can verify that by taking logarithmic derivatives on $P_\theta(f)$, $f \ll f_d$ leads to ζ_b while $f \gg f_d$ leads to ζ_a, see

---

[2]Derivation similar to Ref. [21] but they neglect the net local transfer term and perform dimensional analysis on the velocity fluctuation production due to the bubbles instead.
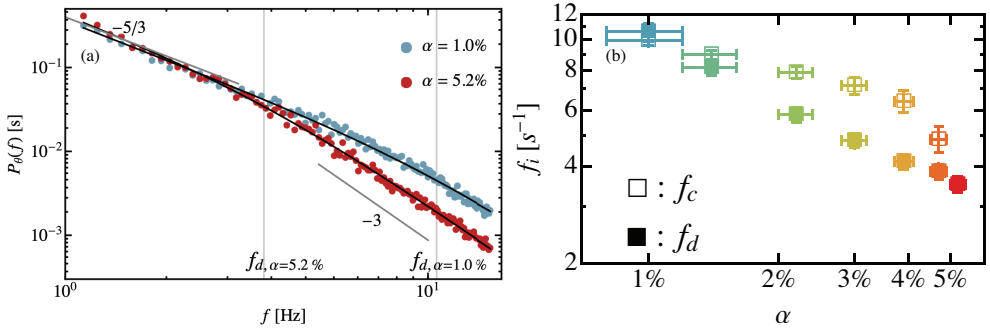
Figure 4.2: (Color) (a) The power spectral densities $P(f)$ of the temperature fluctuation from the measurements (dots) and the corresponding fits (generalised Batchelor parametrization, Eq. 4.2) in logarithmic scale for the gas volume fractions $\alpha = 1.0\%$ and $\alpha = 5.2\%$ at the frequency range of 1.2 Hz to 15 Hz (color scale same as Fig. 4.1. The two grey sloped straight lines with labels '-5/3' and '-3' indicate the scaling behaviours of the two limits. The vertical grey straight lines labeled by f_d indicate the fitted transition frequency for the two cases. (b) The comparison between f_c (open symbols, Eq. 4.3) versus α and f_d (solid symbols) versus α. The error bars of the α are the absolute errors quoted from [92] while the error bars of f_d and f_c are the 95% confidence level from the Batchelor parametrization fitting.

Fig. 4.2a. The power spectra at the frequencies near the scaling crossover are fitted using the generalised Batchelor parametrisation (Eq. 4.2). We select $\zeta_b = -5/3$ (scaling before) and $\zeta_a = -3$ (scaling after) in Eq. 4.2 as these scaling have been observed in experiments and explained theoretically. By inspection of the local logarithmic slope of the thermal spectra (see Appendix), the range that covers most of the -5/3 and -3 scaling for fitting is from 1.2 Hz to 15 Hz for the highest gas volume fraction case ($\alpha = 5.2\%$). The above fitting settings are applied to the cases which $\alpha \geq 1.0\%$ since for lower α the transition frequencies resulted from the fits are either outside the fitting range or very close to the boundary of the fitting range. The technical details of the fitting can be found in the Appendix. The fits for $\alpha = 1.0\%$ and $\alpha = 5.2\%$ are shown in Fig. 4.2a. It shows qualitatively nice fits for $\alpha = 1.0\%$, even though this does not exhibit a developed -3 scaling. We note that this fit ($\alpha = 1.0\%$) assumes a developed -3 scaling outside the fitting range, though from Fig. 4.1b it does not appear to be present. The figure also shows $\alpha = 5.2\%$ is qualita-

tively close to -3 scaling after the transition and the transition frequency f_d is smaller for higher α.

Fig. 4.2b shows the transition frequency f_d obtained from the Batchelor parameterisation as a function of α for $\alpha \geq 1.0\%$. A decreasing trend of f_d with increasing α is found.

Currently there is no prediction for the onset frequencies f_d of the bubble-induced subrange for the passive scalar spectra. However, there is a candidate of the onset frequency of the -3 scaling in the *energy spectra*, which is proportional to V_r/d, where V_r is the mean relative (to the liquid phase) rise velocity of the bubbles and d is the mean area equivalent diameter of the bubbles [30]. This frequency is given by $f_{\mathrm{bub}} \equiv V_r/\lambda_{\mathrm{bub}} \equiv C_D V_r/d$ [30], where C_D is the drag coefficient of the bubbles, and $\lambda_{\mathrm{bub}} \equiv d/C_D$ is a candidate of the onset scale for the -3 scaling in the energy spectra in the wavenumber space [7, 27], see also Eq. 1.23 in the Introduction in page 14. Apart from f_{bub}, there are also several frequency scales that are proportional to V_r/d, which roughly locate a 'bump' in the energy spectra just before the -3 scaling for high enough α (summarised in Ref. [30]), see also Eq. 1.24 in the Introduction in page 14. It is desirable to know whether the transition frequencies for the passive scalars' case also scales with V_r/d.

One frequency that is proportional to V_r/d and that locates a 'bump' in the energy spectra just before the -3 scaling for high enough α is given by [24, 30],

$$f_c = 0.14 V_r/d. \tag{4.3}$$

f_c and f_d as a function of α are plotted on logarithmic scale in Fig. 4.2 for comparison. However, since -3 scaling has not developed for low α and thus the validity of f_d for low α is questionable, we can only conclude that both have decreasing trends and f_c is bigger than f_d in our parameter regime, and they possibly have different scaling exponents.

4.5   Conclusion

To conclude, when a swarm of high-Reynolds number bubbles are injected into a turbulent thermal mixing layer ($0.3\% \leq \alpha \leq 5.2\%$), the scalar spectra that originally have a -5/3 scaling are followed by a steeper -3 slope for larger α. As opposed to the energy spectra, which abruptly developed a -3 scaling with the enhancement of the small-scale content for non-zero α, the change of spectral scaling for passive scalar spectra is gradual by diminishing the small-scale content when α increases. While the -3 scaling at $\mathcal{O}(100\mathrm{Hz})$ of the energy

spectra is attributed to the balance of the production of velocity fluctuations due to bubbles and the molecular viscous dissipation, we speculate that the physical mechanism of the steeper spectral slope in the passive scalar spectra is due to enhanced mixing of bubbles that promotes the homogenization of small-scale temperature differences. The scaling saturates to -3 at around 4 Hz to 15 Hz when the smoothing of temperature fluctuations is so strong such that the local net transfer of the spectral fluctuation is directly diffused by molecular diffusivity. The transition frequency f_d from the -5/3 to -3 scaling in the scalar spectra are fitted by the generalised Batchelor parametrisation and found to monotonically decrease with increasing α.

4.6   Outlook

Finally, note that the above speculation on the -3 scaling mechanism for a scalar spectrum requires diffusivity to be important. This means that the inverse of scalar diffusive time scale needs to be around the onset frequency of -3 subrange. A direct verification on the speculation may be done by the investigation on the diffusive, spectral transfer budgets of the spectral content of scalar fluctuations at the -3 subrange that can be analysed by direct numerical simulations similar to [91]. Another future investigation is to predict the critical α that leads to the saturation of the -3 scaling in passive scalar spectra for a general turbulent bubbly thermal mixing layer (for different incident turbulent intensities, mean temperature gradient forcing and high-Re bubble properties).

4.A   Method of calculating the energy and scalar spectra in two-phase flow

The hot-film voltage E_{hf} is measured over time. We remove parts of the signal where bubbles interact with the sensor by the means of threshold method on the time derivative of the measured voltage across the hot-film, which was also used in other literature [30,32,98]. By inspection of dE_{hf}/dt over time, a fixed threshold $|dE_{hf}/dt| > 500\text{V s}^{-1}$ is used to detect the moments when bubbles are at the probe.

Apart from the threshold on the slope of the rising and falling signal due to the bubble collisions, we also set the minimal successive bubble collision time (5 ms) in order to make sure that the entire bubble interaction events are captured. We check the latter threshold by examining the distributions of the

$\alpha(\%)$	d (mm)	V_{bub} (m s^{-1})	f_d (Hz)	f_L (Hz)
*0.3 ± 0.2	2.4 ± 0.5	0.68 ± 0.14	25 ± 4	0.50 ± 0.01
0.6 ± 0.2	2.5 ± 0.5	0.70 ± 0.13	15 ± 1	0.53 ± 0.01
1.0 ± 0.2	2.5 ± 0.5	0.68 ± 0.11	10.6 ± 0.7	0.54 ± 0.01
1.4 ± 0.2	2.6 ± 0.6	0.67 ± 0.11	8.1 ± 0.5	0.55 ± 0.01
2.2 ± 0.2	2.6 ± 0.6	0.64 ± 0.11	5.8 ± 0.3	0.58 ± 0.02
3.0 ± 0.2	2.5 ± 0.4	0.62 ± 0.11	4.8 ± 0.3	0.57 ± 0.02
3.9 ± 0.2	2.5 ± 0.4	0.60 ± 0.11	4.1 ± 0.2	0.60 ± 0.02
4.7 ± 0.2	2.6 ± 0.5	0.59 ± 0.11	3.9 ± 0.2	0.59 ± 0.02
5.2 ± 0.2	/	/	3.5 ± 0.2	0.61 ± 0.02

Table 4.1: A summary of the bubble area equivalent diameter d, the mean bubble rise velocity V_{bub}, the best fitted parameters f_d and f_c (Eq. 4.2) with different gas volume fraction ($0.3\% \leq \alpha \leq 4.7\%$). The bubble sizes and velocity are obtained by image analysis (see Sec. 4.2). The uncertainty of α is quoted from [92] while the uncertainties of the bubble diameters and the rise velocities are the corresponding standard deviations. The errors of f_L and f_d are the 95% confidence level obtained from the fitting. *Note that $\alpha = 0.3\%$ case has a bimodal distribution of the bubble diameter and the velocity (not shown).

bubble residence time and any unphysical bumps present in the energy spectra due to many unphysically short bubble collisions.

To calculate the velocity power spectra, we use Bartlett Method [99] with linear interpolations between the 'gaps' of the liquid phase velocity over time for each α. Each partition segment (20 sec) cover at least one turnover time by inspecting the auto-correlation function of the signal.

Linear interpolation between the gaps of the liquid signal to calculate the power spectra was also used in [30, 41]. The discussion on the effects of using linear interpolation can be found in [32, 41].

Next the computation of the scalar spectra is considered. We did not create gaps of the temperature time series to distinguish gas or liquid phase as will be discussed and reasoned in Sec. 5.2.3 of Chapter 5. The Bartlett method [99] is applied to continuous temperature signal with no gaps even in two-phase flow for each α. Each partition segment (10 sec) cover at least one turnover time by inspecting the auto-correlation function of the signal.

4.B   Local logarithmic slope of the scalar spectra

The local logarithmic slope $\xi(f)$ of the scalar power spectra normalised by its variance $P_\theta(f)$ is given by

$$\xi(f) = \frac{d \log_{10} P_\theta(f)}{d \log_{10} f}. \tag{4.4}$$

To estimate the local logarithmic slope at different frequency, for each spectrum, a moving fit of a straight line in logarithmic space (centred at a frequency with a window size one-fourth decade of the frequency) is employed in order to obtain a local logarithmic slope at that frequency. The results of $\xi(f)$ for different α are shown in Fig. 4.3b. In the figure, we see that at around 1.2 Hz, -5/3 scaling starts to develop for also while the -3 scaling ends at around 15 Hz. Therefore, 1.2 Hz to 15 Hz is a reasonable range that covers the transition from -5/3 to -3 scaling for the highest gas volume fraction case $\alpha = 5.2\%$.

4.C   The fitting methods of the Batchelor parametrisation and the results

To fit a spectrum, we weight each data point by its uncertainty of which the standard error of the mean is used. The whole time series is partitioned into segments of which each covers at least one turnover time of the signal. We average over only the spectra that are computed from every other segment such that the segments being averaged are uncorrelated, and thus also obtain the standard errors of the mean.

From the results of the previous section, the frequency range 1.2 Hz to 15 Hz is used for fitting the mean spectra for each α. The Levenberg-Marquardt method is used for fitting the data points with the Batchelor parameterisation in log-space (Eq. 2 in the main text where $\zeta_b = -5/3$ and $\zeta_a = -3$) while weighting individual data point by its standard error of the mean. Accordingly, the statistical errors of the fitted parameters (f_L and f_d in Eq. 4.2) such as the confidence level in log-space are obtained. The results are tabulated in Table 4.1. From the table, we see that the fitted transition frequencies for $\alpha < 1.0\%$ is either outside or near the boundary of the fitting frequency range. Therefore we do not perform the transition frequency analysis for $\alpha < 1.0\%$.
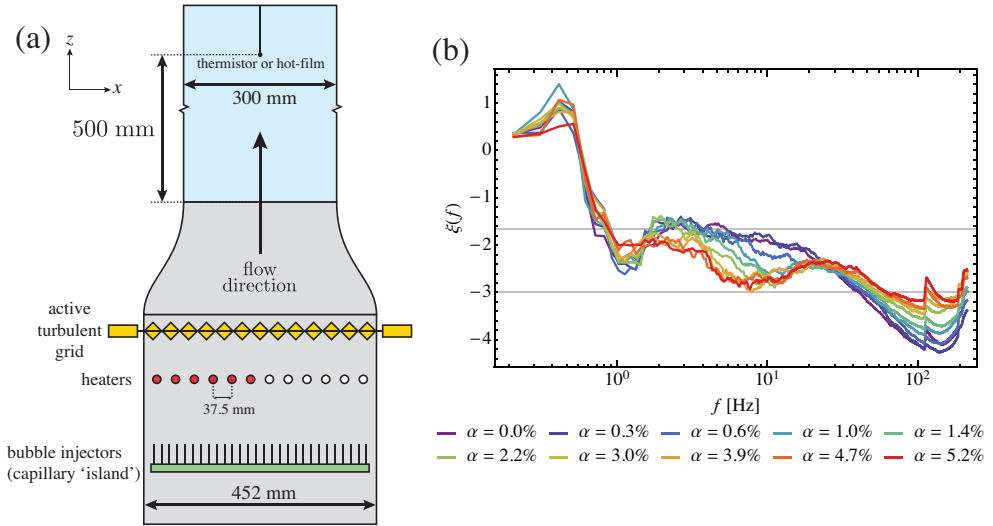
Figure 4.3: (color) (a) The schematics of the experimental setup used in the current study. There are 12 heaters in the setup in which half of them are supplied with a fixed total power of 2250W (red) and the other half are switched off, producing a turbulent thermal mixing layer. Each heating cartridge (Watlow, Firerod J5F-15004) has a diameter of 12.7 mm. The center-to-center distance between two consecutive heaters is 37.5 mm. The measurement section (blue area) has a height of 1.00 m, a width of 0.3 m and is 0.04 m thick. (b) The local scaling exponent $\xi(f)$ (defined by Eq. 4.4) of $P_\theta(f)$ over an interval of more than three decades for different gas volume fractions α. Two grey horizontal lines indicates the the slopes -5/3 and -3. The details of obtaining the local slope is described in the Appendix 4.B.

欲誠其意者，先致其知，致知在
格物[a]。

《禮記・大學》[Liji: Da Xue,
also known as Liji: The Great
Learning]

_____

[a]Translation from James
Legge: "Wishing to be sin-
cere in their thoughts, they
first extended to the utmost
their knowledge. Such exten-
sion of knowledge lay in the
investigation of things. " [100].

5

Integral-Scale and Small-Scale Passive Scalar Statistics in Turbulent Bubbly Flows[1]

Abstract

The integral statistics and small-scale statistics of a turbulent bubbly thermal mixing layer were studied. The mean upward liquid velocity was fixed at 0.5 m/s while the gas volume fraction α was varied from 0% to 4.7%. For the integral statistics, we investigated the mean profiles, the standard deviation profiles and the probability density functions (PDFs) of the velocity and the temperature for $0\% \leq \alpha \leq 4.7\%$. The velocity variance increased with α. In contrast, the temperature variance showed marginal decrease when α increased. The contributions of the temperature variance included the mean temperature gradient and the turbulent heat flux which were both in general not monotonically increasing functions of α. For velocity PDFs, they showed exponential tails for $\alpha > 0\%$, which is a signature of the contributions of bubble-induced turbulence. For the standardised temperature PDFs, the kurtosis had insignificant change from $\alpha = 0\%$ and 0.6% (sub-Gaussian kurtosis).

_____

[1]To be submitted with the authors **On-Yu Dung**, Pim Waasdorp, Chao Sun, Detlef Lohse, Sander G. Huisman

However, the kurtosis increased significantly when α increased from 0.6% to 1.0%, though it was still sub-Gaussian. The temperature PDFs had insignificant change within three temperature standard deviations for $\alpha \geq 1.0\%$. This implies that rising bubbles promoted more extreme values of the temperature fluctuation when normalised by its standard deviation. After that, we investigated the small-scale statistics of the temperature increments for $\alpha = 0\%$ and $\alpha = 4.7\%$, in which –3 scaling has been developed in the latter case, see Chapter 4. The PDFs of the standardised temperature increments were studied. The kurtosis of such increments was larger for $\alpha = 4.7\%$, implying that the intermittency was enhanced when rising bubbles were injected. It was attributed to the enhanced mixing due to the rising bubbles, which smoothened the small amplitude, small-scale temperature fluctuations , leaving only the large fluctuations of the temperature. The scaling properties of the moments of the absolute value of the temperature increments were investigated using extended self-similarity (ESS) analysis. We denote the scaling exponent of the p-th order moment against the second order moment as $\beta(p, 2)$. When rising bubbles were injected, there was only marginal increase of such exponent up to $p = 5$. Moreover, $\beta(p, 2)$ resembled that for the boiling Rayleigh-Bénard convection (point bubbles simulations) reported in Lakkaraju *et al.*, Journal of Fluid Mechanics **745**, 1–24 (2014) and were higher than other single-phase cases summarised in Gylfason *et al.*, Physics of Fluids **16**, 4012–4019 (2004).

5.1   Introduction

Turbulent bubbly flows are turbulent flows in which there are fast-moving, finite size bubbles [3,7,90]. Scalar fields in such turbulent bubbly flows have both practical relevance and are of interest from a fundamental point of view. Industrial examples include large-scale chemical plants that make use of bubbles to enhance the mixing of temperature or reactants in a turbulent flow. Engineering communities have investigated the large-scale, integral-scale properties such as heat transport, scalar probability density functions (PDFs), scalar variance, fluxes, etc. because of the industrial relevance. Physicists have focused on possible universality in such flows by looking at the small-scales and the internal structures of the scalar field. In fact, both the large-scales and the small-scales are coupled together and their interplay is crucial for a full understanding of the physical problem [101]. Practically, Large Eddy Simulations (LES), which have a lower computational cost than Direct Numerical Simulations (DNS), also must model the small-scales of the turbulent flows, reflecting that the knowledge of small-scale in turbulent flows is essential [101]. Fundamentally, the emergence of the universal scaling of the velocity fluctuation spectra $E_u(k) \propto k^{-3}$ (see e.g. Ref. [7,90]) and the passive scalar spectra $E_\theta \propto k^{-3}$ [41] (see also Chapter 4), where k is the wavenumber, u is a velocity field, and θ is a passive scalar field, in high-Reynolds bubbly swarms leads us to further investigate the fine structure in turbulent bubbly flows.

Previous work on the integral-scale properties of the scalar fields in bubbly flows ranges from experimental [35, 37, 45, 48, 53, 78], theoretical [52, 78] and computational [54, 102, 103] research. Notably, for theoretical and experimental work, a heat transfer equation was derived to predict the dependence of Nusselt number on the control parameters of the flow [78]. The eddy diffusivity of the turbulent liquid phase was decomposed into a turbulent contribution independent of the bubble agitations and an additional agitations due to bubbles [52, 53]. The mean temperature profile in vertical upward bubbly flows with forced convection was predicted [52, 53]. For DNS, rising bubble swarms were simulated in a background liquid mean flow in vertical channels with heated side walls [54]; while the simulations of bubble swarms without forcing any mean flow but with fixed temperature difference at the side walls were performed in Ref. [102]. Moreover, DNS of a rising light droplet swarm, where the droplets had half the density of the ambient liquid, in a vertical convection setup revealed the influence of light droplets on heat transport [103]. Experimentally, the heat transfer enhancement was investigated in homoge-

neous bubbly column superposed in a vertical convection setup [37] and it was extended to inhomogeneous bubbly flows [45]. By using dye as the passive scalar, the effective diffusivity of a passive scalar in bubbly flow without and with incident turbulence were investigated in Refs. [35] and [48], respectively.

Although the above-mentioned research focused on the scalar fluxes, global profiles and heat transport, the discussion on the modification of the scalar PDF due the presence of the bubbles is presently lacking. The bubbles especially modify the tails of the PDF which can be important in some practical concerns such as mixing, combustion and the spread of toxic pollutants [4,101]. Apart from that, the PDF formulations on turbulent reaction problems also concern the scalar PDF [104,105], which serves as an essential tool for describing a mixing problem [4]. There has been a long controversy of non-Gaussian or Gaussian scalar PDF in single-phase turbulence (see the introduction in Ref. [106] and the reviews by Refs. [6,101]). Moreover, two-phase turbulent flows are omnipresent both in nature and industries. Therefore the modification of the scalar PDF due to high-Reynolds bubbles is of interest for investigation.

Limited research has been performed on the small-scale statistics of the scalar fields in bubbly flows. Point vapour bubbles in boiling Rayleigh-Benard convection were simulated, showing that the intermittency is reduced by the vapour bubbles [107] while enhanced intermittency is observed with vapour bubbles in a thermal convection using Lattice-Boltzmann method for simulation [108]. However, the intermittency for the case of mechanical mixing of high-Reynolds bubbles that has wake-induced agitation on the liquid phase with negligible heat exchange with the ambient fluid and the scalar being passive, has not yet been studied. Time-resolved concentration fields in a bubbly swarm in a confined cell were obtained in Ref. [41], showing a -3 scaling range in the passive scalar spectra but does not further investigate its internal structure and is limited to two dimensions [41].

Investigating the small-scale statistics may also help us to obtain a better understanding of the emergence of the bubble-induced scaling in the bubble-induced subrange of passive scalar spectra. Chapter 4 includes experiments of a turbulent bubbly thermal mixing layer and shows that the logarithmic slope in the passive scalar spectra at the small-scale (high frequency range) becomes steeper and then saturates to -3 for increasing gas volume fraction α. The above results show that, as opposed to the velocity fluctuation spectra having small-scale enhancement due to bubbles, the small-scale spectral amplitude diminishes for passive scalar spectra. It is then important to study the small-

scale statistics in order to understand such emergent phenomenon due to the presence of high-Reynolds bubble swarms.

In this chapter, we investigate the integral-scale properties of the scalar field in turbulent bubbly thermal mixing layer and the small-scale characteristics and we will show that the bubbles enhance the mixing at the small-scales and enhance the intermittency. Sec. 5.2 presents the experimental setup and the experimental methods for the characterisation of the gas phase (high-speed imaging), for measuring the liquid velocities (Laser Doppler Anemometry), and liquid temperatures (fast-response thermistor). For the experimental results and discussion, the integral-scale quantities (Sec. 5.3) are first discussed, followed by the small-scale statistics (Sec. 5.4).

The current work presents the global velocity and scalar variance profile changes due to increasing gas volume fraction α (Sec. 5.3.1), and also shows the effect of α on the velocity and scalar p.d.f (Sec. 5.3.3). The change of temperature variance for increasing α is discussed in Sec. 5.3.2. After that, the small-scale properties of the passive scalar are investigated. The PDFs of the temperature increments for $\alpha = 0$ and $\alpha = 4.7\%$ are compared at different scales (Sec. 5.4.1), followed by their skewness that indicate anisotropy and the kurtosis that quantifies the tails of said PDFs (Sec. 5.4.2), showing the enhancement of intermittency due to the presences of bubble swarms. Next, the scaling behaviour of the temperature structure functions are investigated by an extended self-similarity (ESS) analysis [109] (Sec. 5.4.3). This analysis investigates the scaling behavior of the structure function of the order p versus the second order structure function, in which the exponent is denoted as $\beta(p, 2)$. These are compared between the cases of having bubbles ($\alpha = 4.7\%$) and no bubbles, and with other fluid dynamics geometries (Sec. 4.6).

5.2 Description of the experiments

5.2.1 Experimental facility

We utilise the Twente Mass and Heat Transfer Tunnel (TMHT) which is a vertical upward water channel that can heat up the fluid, inject rising bubbles, and produce an active-grid generated turbulent flow in a controlled manner [92]. A schematic of the experimental setup is shown in Fig. 5.1. The flow is in upward direction, against gravity. The working-liquid is decalcified tap water at atmospheric pressure. From the bottom, the water first passes the capillary needles that inject bubbles, followed by the heating cartridges which were
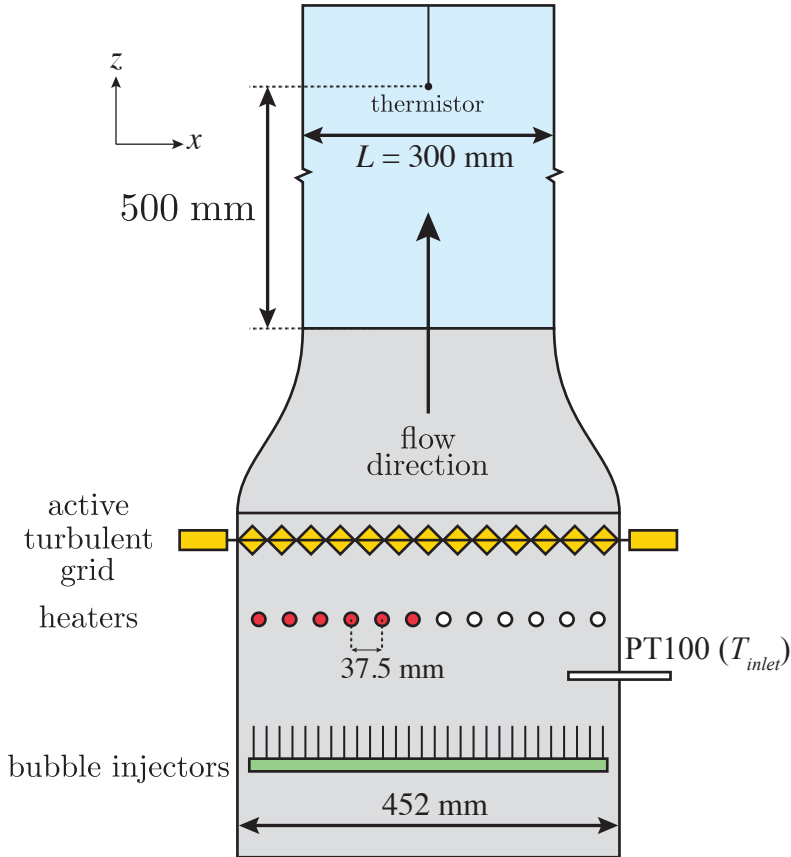
Figure 5.1: Schematics of the experimental setup, Twente Mass and Heat Transfer Tunnel (TMHT). The dimensions of the measurement section has width $\times$ length $\times$ height $= (40 \times 300 \times 990)$ mm. There are twelve heaters; here half of them are switched on (red) and the other half off. A Pt100 thermocouple measures the temperature T_{inlet} of the incoming liquid before it is heated up by the heaters. Each heating cartridge (Watlow, Firerod J5F-15004) has a diameter of 12.7 mm. The center-to-center distance between two consecutive heaters is 37.5 mm.

positioned across the transverse direction, and after that passing through the active turbulent grid and finally into the measurement section. By applying a fixed total power of 2250 W to half of the heating cartridges on one side while letting the other half being idle, a temperature step is produced, being mixed when the water goes upward. After the measurement section, a heat exchanger cools the water before it is recirculated, achieving a statistically stationary state for the whole setup. Each heating cartridge (Watlow, Firerod J5F-15004) has a diameter 12.7 mm. The center-to-center distance between two consecutive heaters is 37.5 mm. The tunnel temperature is monitored by a PT100 thermocouple that measures the temperature T_{inlet} of the incoming liquid before it is heated up again by the heaters. For single-phase, such flow is called a turbulent thermal mixing layer [110]. When rising bubbles are present in the flow, we therefore have a turbulent bubbly thermal mixing layer. The bulk temperature of the water is kept at around 22.7°C (Prandtl number $Pr = 6.5$), close to the ambient environment temperature to reduce the environmental heat exchange.

5.2.2   Instrumentation for the gas-phase characterisation

We inject regular air into the channel to create gas bubbles that serve as mechanical stirring of the liquid velocity field. The global gas volume fraction α is measured by a differential pressure transducer of which two ends are connected to the bottom and the top of the measurement section [92]. One note has to be added here for approximating α. The differential pressure transducer also detects the hydrodynamic pressure difference. Therefore in order to measure the pressure difference due to the presence of voids in the measurement section, we first record the hydrodynamic pressure difference without the bubbles and then with the bubbles for the same liquid mean flow. The liquid mean flow is estimated by the liquid volume flow rate divided by the cross-sectional area of the measurement section. Hence when α is non-zero, the cross-sectional area in the measurement section is actually smaller, thereby underestimating the mean liquid flow speed at the measurement section (by a factor of $1/(1-\alpha)$ if we assume the bubble columns does not change its cross-sectional area in the measurement section). A different liquid mean flow can lead to a different hydrodynamic pressure contribution to the differential pressure transducer. For small gas volume fractions ($\alpha < 5\%$), we neglect this effect and assume that the liquid mean speed is approximately the same when α is non-zero.

For measuring the bubble rise velocities, we use the Photron mini AX camera

with a frame rate of 1000 Hz to image the bubbles. The circular Hough transform is used to detect the bubbles and size the bubbles.

5.2.3　Instrumentation for the liquid-phase velocity and temperature characterisation

For the characterisation of the single-phase upward liquid velocity, both constant temperature anemometry (CTA) and laser-Doppler anemometry (LDA) are used. We use LDA to characterise the two-phase liquid velocities in the transverse and streamwise direction. The CTA system utilised a hot-film probe with the model type Dantec 55R11 (Dantec 55R11, 70 μm diameter with 2 μm nickel coating, 1.3 mm long and up to 30 kHz frequency response) and the LDA system is a backscatter model (Dantec).

The open measurement section allows us to traverse the thermistor inside the measurement section and measure the temperature at different positions. The thermistor is the Amphenol Advanced Sensors FP07 model which has a response time of 7 ms in water. The thermistor is driven by an AC bridge in which the bridge potential is measured by a lockin amplifier (Zurich Instrument MFLI). The temperature was oversampled in order to avoid aliasing effects. Therefore, when performing any time series analysis, a digital finite-impulse low-pass filter (which has linear phase change) at the response frequency is used. The thermistor calibrations are performed in a temperature-control water bath (PolyTemp PD15R-30) with a temperature stability $\pm$0.005 K. Although the thermistor model used for Chapter 4 and Chapter 5 are the same, the thermistors are subject to manufacturing differences or electronic differences due to soldering. The uncertainty of the thermistor in Chapter 5 is lower, which is 0.01 K, obtained by fitting the temperature-resistance characteristic equation proposed by Steinhart and Hart [94] over a short range of the temperature of interest (in which the terms are kept only up to the first order to avoid over-fitting).

The temperature's upstream of the measurement section (see Fig. 5.1) are measured by a Pt100 temperature probe with a 1/10 DIN accuracy, $\pm$30 mK (Pico Technology, PT104 data logger with SE012 probes) [92].

One might worry that the signal response of the thermistor spikes when it encounters a bubble collision since it is well-known that spikes are measured for hot-film anemometry when a bubble hits the film which causes a huge change of heat transfer at the liquid-air interface [111]. However, the measuring principles of a thermistor and a hot-film are different. The former has its own characteristic resistance-temperature curve while the latter makes use of the

heat carried away by the fluid when the fluid move across the film. When a bubble impinges the hot-film, due to the large change of heat capacity from liquid to air, there will be a large change of heat transfer, inducing an abrupt change of the hot-film voltage. On the other hand, for a general situation, if a bubble impinges the thermistor, the thermistor will only measure the temperature at the interface and the air inside. The temperature of the air, however, is very close to the ambient water and the probe-bubble interaction is shorter than (though comparable to) the thermistor response time (bubble residence time is smaller than 5 ms, estimated by using bubble rising speed and the bubble diameter). To further illustrate this, we put an optical fibre at around 1.5 mm distance next to the thermistor and simultaneously perform the temperature measurement and liquid-gas phase indication measurement. By sending light in the optical fibre and receiving the light signal coming back from the tip, one can detect the change of refractive index in time at the tip. The result is shown in Fig.5.2. From the illustration, it can be seen that the bubble residence time at the optical fibre is smaller or comparable to the response time of the thermistor. Cutting out the signals that the bubbles collide with the optical fibre (near the thermistor) will have negligible effect on the temperature time series. Therefore in the following analysis the signals measured by the thermistor are not cut even when the gas volume fraction is non-zero.

5.2.4 Measurement conditions: single phase turbulent characterisation

The liquid mean flow is fixed approximately at 0.5 m/s (a note on this approximation was discussed in Sec. 5.2.2) and the active grid rotation speed is also kept constant as half of its full speed. The relevant flow parameters are tabulated in Table 5.1 and their definitions are as follows.

For the velocity field characterisation, we use LDA and CTA to measure the upward liquid velocity fluctuations at the middle of the tunnel. Let u_z be the vertical velocity. The standard deviation of the velocity $\sigma(u_z)$ is measured by LDA, where $\sigma(.)$ denotes the standard deviation. When using CTA, Taylor's frozen-flow hypothesis is used for transforming time coordinates into vertical spatial coordinates. CTA measurements are used for calculating the longitudinal second order structure function $D_{LL}(r)$ in single-phase flow, where r is the spatial distance between two points, enabling us to estimate the viscous dissipation rate ϵ by using the velocity two-third law $D_{LL} = C_2(\epsilon r)^{2/3}$ which is valid at the inertial range, assuming isotropy and where $C_2 = 2.0$
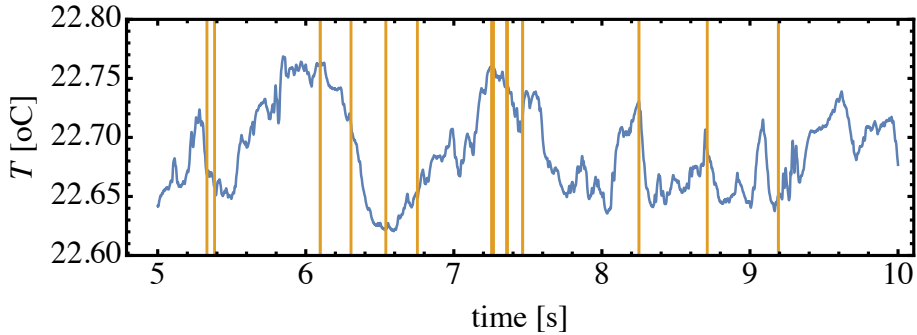
Figure 5.2: The time series of the temperature measured by the thermistor (blue) and the time series of the liquid-gas phase indicator function (yellow) measured by a optical fibre where the tip is around 1.5 mm next to the thermistor ($\alpha = 1.4\%$). The bubble residence time at the optical fibre is very small that a full bubble-collision event can be hardly seen. The bubble residence time is comparable to the response time of the thermistor. The bubble collisions have negligible effect on the temperature signal at that short residence time.

is an universal constant [9]. Then we can calculate the Kolmogorov length scale $\eta = (\nu^3/\epsilon)^{1/4}$ and the dissipation time scale $\tau_\eta = (\nu/\epsilon)^{1/2}$, where ν is the kinematic viscosity of the working liquid. Moreover, we estimate the Taylor-microscale $\lambda_u = 15\nu(2k/3)/\epsilon$ and the Taylor-Reynolds number $Re_{\lambda_u} = (2k/3)^{1/2}\lambda_u/\nu = 130$, where $k = 3\sigma(u_z)/2$ is the average turbulent kinetic energy, by assuming isotropy. To estimate the velocity integral length scale L_u, we use $\epsilon = C_\epsilon u_0'^3/L_u$, where $C_\epsilon = 0.9$ [112, 113].

For the scalar field characterisation, the temperature fluctuations are measured by a thermistor. We note that the mean horizontal temperature profile is nonlinear and can be characterised by an error function [93, 114–117] (see Fig.5.4a). Therefore, for symmetry reasons, we characterise the scalar field at the middle of the measurement section which is the middle of the thermal mixing layer. First, for the scalar dissipation rate ϵ_θ, we similarly use the temperature (scalar) two-third law $D_{\theta\theta}(r) = C_\theta'\epsilon_\theta\epsilon^{-1/3}r^{2/3}$ which is valid at the inertial-convective subrange [2], where $D_{\theta\theta}$ is the second order structure function of the scalar fluctuation and $C_\theta' \approx 0.25^{-1}C_\theta$ [2] with $C_\theta \sim 0.5$ is the Obukhov-Corrsin constant [95, 101], which assumes isotropy. It is well-known that passive scalar fields are not isotropic at small scales when there is a large-scale mean temperature gradient [101] but for the order of esti-

mation of ϵ_θ we assume isotropy. Second, we estimate the scalar microscale $\lambda_\theta = \sqrt{6\kappa\langle T'^2\rangle/\epsilon_\theta}$, which also assumes isotropy. Third, motivated by recent work [12] that shows the Péclet number based on the scalar microscale can characterise the degree of small-scale anisotropy of passive scalar fluctuations, we also calculate such Péclet number $Pe_{\lambda_\theta} = u'_0\lambda_\theta/\kappa$, where κ is the thermal diffusivity of the working liquid. The commonly used Péclet number based on the Taylor microscale of the velocity $Pe_{\lambda_u} = u'_0\lambda_u/\kappa$ is also calculated [95]. For the length scale of the scalar dissipation, since $Pr = 6.5 > 1$, we use the Batchelor scale to characterise the smallest scale of the passive scalar field which is given by $\eta_\theta = \eta Pr^{-1/2}$ [2]. For the integral length scale of the scalar fluctuations, intuitively it is of the order of the size of the thermal mixing layer. For a single-phase thermal-mixing layer, the mean temperature profile follows a self-similar shape that can be characterised by an error function [93, 117]. Therefore, quantitatively we first fit the mean temperature profile (with an offset of the mean temperature at the coldest position) $\tilde{T}(x)$ by the function

$$\tilde{T}(x) = \frac{\Delta T}{2}\text{erfc}\left(\frac{x - x_c}{L_\theta/2}\right), \tag{5.1}$$

where x_c is the x-coordinate at the center of the measurement section, $\text{erfc}(x)$ is the complementary error function; and ΔT and $L_\theta/2$ are the fitting parameters which describe the asymptotic value of the mean profile and the characteristic length of the thermal mixing layer, respectively. For the quality of the fit, see Fig. 5.3. L_θ is then defined as the integral length scale of the scalar fluctuations. The results are summarised in Table 5.1.

For the temperature spectra and the energy (velocity fluctuation) spectra for both single- and two-phase flows that have the same measurement conditions as in this article, we refer to Chapter 4. We note that the inertial range of the energy spectra is limited but the inertial-convective subrange in the thermal spectra has a wider frequency range (see Fig. 4.1 in page 86). The inertial-range in the energy spectra for non-zero gas volume fraction is covered by the energy injections due to bubbles (see Chapter 4), meaning that we cannot estimate the viscous dissipation rate by the velocity two-third law. The probability density functions of the velocity field and the temperature will be discussed in Sec. 5.3.3.

5.2.5 Measurement conditions: Bubble properties

The global gas volume fraction α is increased from 0% to 4.7% while the liquid mean flow is kept approximately at 0.5 m/s.
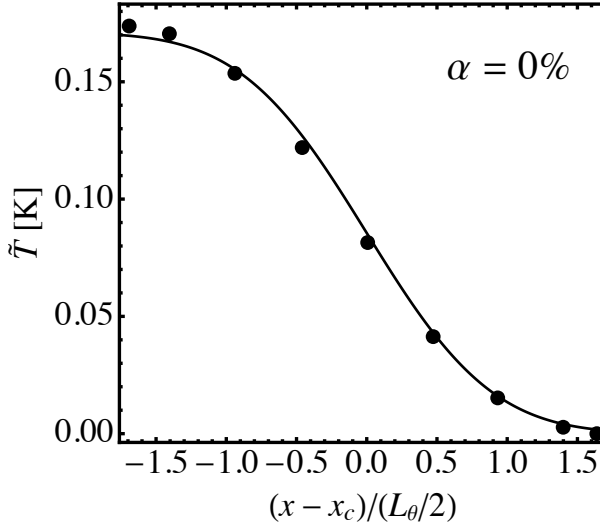
Figure 5.3: The mean temperature profile $\tilde{T}$ versus $\frac{x-x_c}{L_\theta/2}$ for $\alpha = 0\%$ and the corresponding fit using Eq. (5.1) (solid black line), where $\tilde{T} \equiv \langle T - T_{\mathrm{inlet}} \rangle - \langle T - T_{\mathrm{inlet}} \rangle|_{x/L=0.9}$, T_{inlet} is the temperature measured of the incoming liquid before being heated up by the heaters, $x_c = L/2$ is the x-coordinate of the middle of the tunnel, and L_θ is one the fitting parameter that measures the width of the thermal mixing layer (Eq. (5.1)).

η (mm)	τ_η (ms)	η_θ (mm)	λ_u (mm)	λ_θ (mm)
0.22	49	0.085	4.9	2.1
Re_{λ_u}	Pe_{λ_u}	Pe_{λ_θ}	L_u (m)	L_θ (m)
130	870	520	0.04	0.15

Table 5.1: Relevant turbulent flow parameters of the single-phase turbulent thermal mixing layer in the current study ($\alpha = 0\%$, mean liquid flow speed = 0.5 m/s). For the definitions of the parameters, see Sec. 5.2.4.

$\alpha(\%)$	d (mm)	V_r (m s^{-1})	Re$_{bub}$
0.6 ± 0.2	2.5 ± 0.5	0.19 ± 0.13	480
1.0 ± 0.2	2.5 ± 0.5	0.18 ± 0.11	450
1.4 ± 0.2	2.6 ± 0.6	0.16 ± 0.11	420
2.2 ± 0.2	2.6 ± 0.6	0.15 ± 0.11	380
3.0 ± 0.2	2.5 ± 0.4	0.13 ± 0.11	320
3.9 ± 0.2	2.5 ± 0.4	0.12 ± 0.11	290
4.7 ± 0.2	2.6 ± 0.5	0.09 ± 0.11	220

Table 5.2: A summary of the bubble area equivalent diameter d, the mean bubble rise velocity V_r with different gas volume fraction ($0.6\% \leq \alpha \leq 4.7\%$). The uncertainty of α is quoted from [92] while the uncertainties of the bubble diameters and the rise velocities are the corresponding standard deviations.

The mean relative rise velocity V_r versus α, the average bubble equivalent diameter d and the bubble Reynolds number Re$_{bub} = V_r d/\nu$ for different α are tabulated in Table 5.2. V_r decreases from 0.19 m/s to 0.09 m/s when α increases from 0.6% to 4.7%.

The mean bubble diameter $d = 2.5$mm has negligible change when α increases. However, other research, which also make use of capillary needles to inject bubbles, indicates that the bubble diameter increases with α. This includes a homogeneous bubbly flow in quiescent liquid [81] and a rising bubbly flow with a background upward liquid flow which is weakly turbulent [118]. Bubble swarms with a background upward liquid flow that is strongly turbulent are investigated in Ref. [30,46] by using the Twente Water Tunnel, and the authors of that paper find also a small increase of d with α but the investigated range of α is limited ($\alpha < 1\%$). It is not clear why the bubble sizes are constant in our case. The active turbulent grid in our setup has a similar design but with different aspect ratio and has a smaller overall size than the Twente Water Tunnel [30, 46]. It is also reported in Ref. [30, 46] that the fragmentation of bubbles caused by the active grid leads to smaller bubble sizes for high liquid mean flow. In our case, possibly the rotating speed of the active turbulent grid is too high that it cuts the bigger bubbles into smaller bubbles with sizes similar to lower α.

On the other hand, the trend that the bubble rise velocity decreases when α increases is consistent with the well-known hinderance effect because of the entrainment of liquid by bubbles that generates a downward flow between the

bubbles (see the review [7]). But since the incident turbulence is not weak, there are interactions between the bubbles and the ambient turbulence, leading to complex dependence of the bubble rise velocities of other flow parameters. It is different from the case of homogeneous bubbly flows in a quiescent liquid which has empirical expressions of the bubble rise velocity versus α (see section Sec. 3 of [27]).

The experimental results are divided into two main sections, namely integral-scale statistics (mean profile, standard deviation profile, temperature variance and the PDFs) as a function of α and small-scale statistics (statistics of temperature increments and the scaling properties of their moments) for $\alpha = 0\%$ and 4.7%. All the measurements are performed at mid-height of the measurement section.

5.3   Integral-scale Statistics

When rising bubbles are injected into a turbulent thermal mixing layer, the global velocity and temperature mean profile generally change. The change of the mean temperature profile may also change the standard deviation profile of the temperature because the mean temperature gradient changes (discussed below).

5.3.1   Mean and Standard Deviation Profile of the Velocity and the Temperature

Fig. 5.4 shows the time averages and standard deviations of the vertical velocity u_z and the temperature T as a function of transverse- (x) direction at the mid-height of the measurement section for different α. $T - T_{inlet}$ is studied for the global profile instead of T because the room temperature can change the bulk tunnel temperature over time, but the liquid temperature increased by the heating are in a statistical stable state.

First the mean vertical velocity $\langle u_z \rangle$ profile is discussed. For $\alpha < 2.2\%$, the velocity profile is relatively flat for $0.1 < x/L < 0.9$ but when α increases further, the liquid flow at the sides ($x/L < 0.15$ and $x/L > 0.85$) goes faster than the bulk ($0.15 < x/L < 0.85$). This is because the bubble injectors have a longer length than the measurement section. Due to the contraction section just below the measurement section, the rising bubble streams at the sides are contracted and generate faster flow at the sides. Moreover, there is an overall decrease of liquid speed at the bulk. As mentioned in Sec. 5.2.2, we
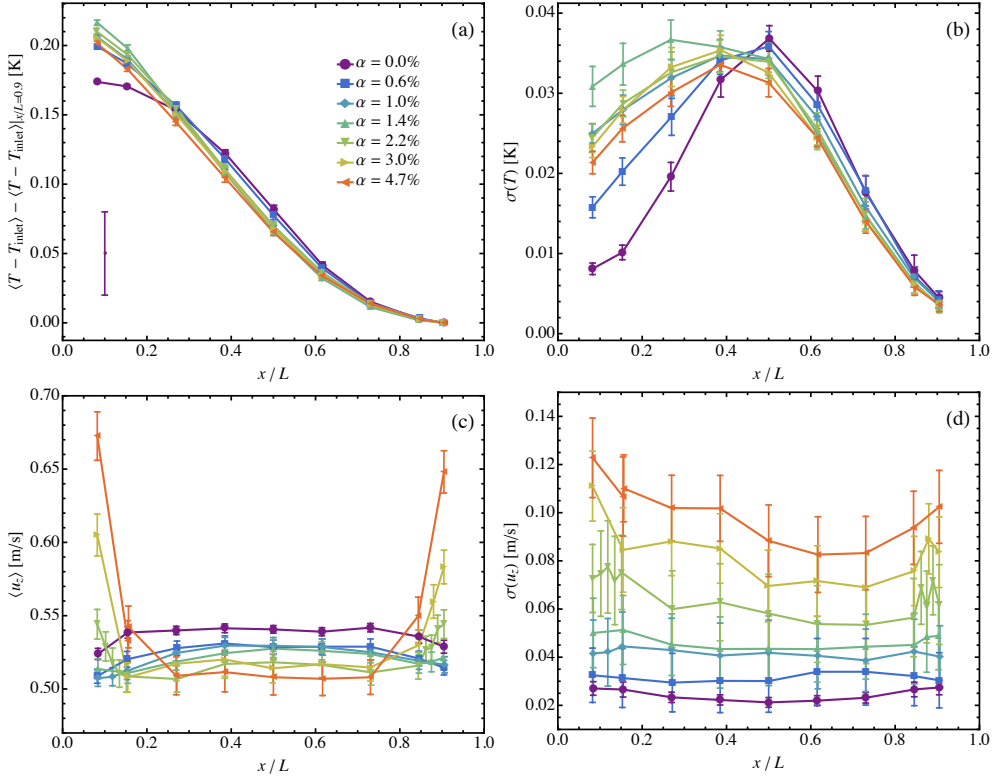
Figure 5.4: The measurements for different gas volume fraction α took place along the transverse- (x) direction at the mid-height of the measurement section which has tunnel width L. The legends are in (a). The error bars at each data point represents the statistical uncertainty 68% confidence interval. (a) The sample mean of the temperature T with an offset of the temperature T_{inlet} of the water before being heated up by the heaters as a function of transverse coordinate x/L. The purple error bar ± 0.03 K at the left bottom corner stems from the absolute uncertainty of the PT100 probe that measures T_{inlet}. (b) The sample standard deviation of $T - T_{inlet}$ versus x/L. (c) The same mean of velocity $\langle u_z \rangle$ as a function of x/L. (d) The sample standard deviation $\sigma(u_z)$ of the vertical velocity versus x/L.

approximately fix the liquid mean flow by maintaining a constant liquid volume flux. The liquid vertical velocity is decreased to compensate the increase of velocity at the sides to keep the overall liquid volume flux being constant when α increases.

The standard deviation of the vertical liquid velocity u_z (denoted as $\sigma(u_z)$) is monotonically increasing with α and the $\sigma(u_z)$ profile is relatively flat across x/L as compared to the u_z profile even though there are faster liquid flow near the side walls when α increases. This monotonic increase is attributed to the increasing effect of bubble-induced agitations as a result of the presence of the randomly distributed bubbles and the induced wakes behind them [7]. The $\sigma(u_z)$ profiles are relatively flat as compared to the $\langle u_z \rangle$ profiles which have large mean velocity gradients at the side walls, suggesting that the agitations of the liquid is dominated by bubble-induced agitations over the shear turbulence induced from the side wall.

Next, the $\langle T - T_{\text{inlet}} \rangle$ horizontal temperature profile is discussed. For single-phase, there is an anti-symmetric profile where the point of inflection is at the mid-length of the tunnel. However, when rising bubbles are injected, this point of inflexion shifts to the left (to the hot side). We note that there is no strict left-right symmetry from the middle of the tunnel. The hot side have heaters at a higher temperature than the incoming flow, inducing heat wakes behind them. The cold side, however, have idle heaters which do not produce any 'cold' wakes behind them. There are also gaps in between the heaters which allows for some unheated fluid passing through the gaps at the hot side while all the fluid at the cold side remains unheated. Moreover, the mean temperature gradient has a marginally small decrease at the point of inflection when rising bubbles are injected, suggesting that the bubbles enhance the overall mixing between the hot side and the cold side which leads to a smaller temperature gradient (but not the overall temperature difference).

For the standard deviation profile of T (denoted as $\sigma(T)$, see Fig. 5.4), the rising bubbles shifted the peak position of the maximum standard deviation to the hot side. There is a marginally small decrease of amplitude when compared to the single-phase case as opposed to the almost monotonic increase of vertical and horizontal velocities variance with increasing α (see Fig. 5.4d and Fig. 5.5).

The interpretation of the shape of the standard deviation of $T - T_{inlet}$ profile is elaborated as follows. Since the temperature in a forced convection is a passive scalar, it has no dynamic effect of the velocity field. Intuitively, from an Eulerian perspective, one contribution of the temperature fluctuation is from the

eddies that bring the temperature from the hot side and from the cold side to the center which gives rise to temperature fluctuations. Therefore, if the mean temperature gradient is large, the same characteristic velocity fluctuation will give a larger temperature fluctuation. Moreover, if the correlation between the velocity fluctuations and temperature fluctuations is non-zero, larger velocity fluctuations also lead to stronger temperature fluctuations. Thus, the peak of the standard deviation profile should occur at the location where the combined contributions of the mean temperature gradient and the correlation between the velocity fluctuations and the temperature fluctuations is maximum. The position of the largest mean temperature gradient approximately coincide with the peak position of $\sigma(T)$ (except $\alpha = 1.4\%$), suggesting that the main contribution to the temperature fluctuations may be the magnitude of the mean temperature gradient.

To conclude, the effect of bubbles on the global profile of the first and second order moments for the temperature and velocity are illustrated. The velocity statistics are homogeneous at the bulk ($0.25 < x/L < 0.75$), regardless whether bubbles are injected or not. When bubbles are injected, the temperature profile are no longer anti-symmetric about the center of the tunnel (the point of inflection shifts towards the hot side, and correspondingly, the peak of the standard deviation profile shifts from the middle of the tunnel towards the hot side.

5.3.2 Velocity and temperature variance

As one can also see from Fig. 5.5, the horizontal and vertical velocities variance normalised by those for single-phase flow at the middle of the tunnel almost monotonically increases with α, but the normalised temperature variance (at the profile peak positions) shows a small decrease instead. In fact, a decrease of temperature variance is also observed in turbulent bubbly flows in a vertical channel with side walls being heated when α increased from zero [54]. While the bubble-induced agitation is the main source of velocity variance, the non-increasing trend of temperature variance suggests that the source of temperature variance may be different. As mentioned in the discussion on the standard deviation profile of $T - T_{\text{inlet}}$, the contributions are the amplitude of the mean temperature gradient and the correlation between the velocity and temperature fluctuations.

Indeed, the production mechanisms of the velocity fluctuation and the temperature fluctuation injections are different within our experimental settings. There is a large-scale temperature gradient across the tunnel length L but
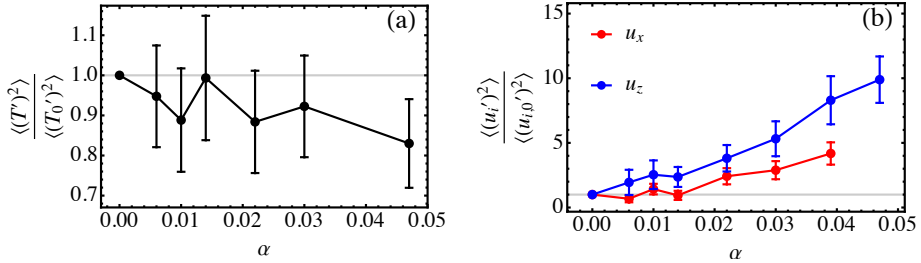
Figure 5.5: (a) The temperature variance $\langle T'^2 \rangle$ at the standard deviation peak position at mid-height (see Fig.5.4), normalised by the single phase temperature variance $\langle T_0'^2 \rangle$ as a function of the gas volume fraction α. (b) The velocity variance $\langle u_i'^2 \rangle$, normalised by the single-phase variance $\langle u_{i,0}'^2 \rangle$ at $x/L = 0.5$ and mid-height as a function of α, where $i = x$ or z. The grey horizontal line corresponds to an ordinate value of 1. Note that the temperature variance shows only a small decrease with respect to α as opposed to the considerable change of the velocity variances with respect to α. The error bar for each point in both (a) and (b) are the propagated errors derived from the statistical uncertainties (68% confidence level) of the individual variances.

there is no large-scale velocity gradient at the bulk of the measurement section (away from the wall). Moreover, there is a hydrodynamic pressure gradient that drives the liquid flow but there is no scalar-analogy to this hydrodynamic pressure gradient. Apart from that, there are viscous boundary layers at the bubble-liquid interface that transfer extra momentum to the liquid, while the temperature gradient across the bubble-liquid interface is negligible, thus no thermal boundary layers are formed to produce additional temperature fluctuations. Therefore, the interfacial at the bubble interface is approximately zero.

It may be helpful to consider the balance equation of the passive scalar variance $\langle T'^2 \rangle$ for incompressible Navier-Stokes flow, see e.g. [119]. As discussed in Sec. 5.2.2, since the residence time of bubbles at the thermistor is marginally smaller than the response time of the thermistor, we do not perform any phase averages on the temperature signal. Moreover, we neglect the bubble contributions at the bubble-liquid interface. Therefore, we use the general single-phase balance equation which can be derived from the advection-diffusion

equation [2, 119],

$$\frac{\partial\langle T'^2\rangle}{\partial t}+\langle\mathbf{u}\rangle\cdot\nabla\langle T'^2\rangle = -2\langle\mathbf{u}'T'\rangle\cdot\nabla\langle T\rangle+\nabla\cdot\left(-\langle\mathbf{u}'T'^2\rangle + \kappa\nabla\langle T'^2\rangle\right)-2\kappa\langle(\nabla T')^2\rangle,$$
(5.2)

where κ is the thermal diffusivity of water and the superscript prime denotes the fluctuating quantity deviating from the time ensemble averages $\langle.\rangle$ over the liquid phase ($x' = x - \langle x\rangle$). The L.H.S. of Eq. (5.2) is the material derivative of $\langle T'^2\rangle$. On the R.H.S. of Eq. (5.2), the first term describes the production due to the coupling of the turbulent scalar flux and the mean temperature gradient; the second term describes the local net fluxes from the scalar variance that includes the turbulent flux and the diffusive flux; while the last term is the scalar dissipation rate.

The flow is statistically stationary and unidirectional. The mean temperature gradient is predominantly in the horizontal (x) direction and the turbulent scalar variance flux is dominant over the diffusive scalar variance flux. Therefore, by using boundary-layer approximation in a turbulent thermal mixing layer, Eq. (5.2) can be simplified into [114–117, 120]

$$\langle u_z\rangle\frac{\partial\langle T'^2\rangle}{\partial z} = -2\langle u_x'T'\rangle\frac{\partial\langle T\rangle}{\partial x} - \frac{\partial}{\partial x}\langle u_x'T'^2\rangle - 2\epsilon_\theta,$$
(5.3)

where $\epsilon_\theta \equiv \kappa\langle(\nabla T')^2\rangle$ is the scalar fluctuation dissipation rate. The turbulent heat flux and the turbulent scalar variance flux are extra unknowns. In order to proceed further, one can model on the turbulent heat flux $\langle u_x'T'\rangle$ by using the eddy diffusivity hypothesis (see e.g. [9, 20]), which is given by

$$-\langle u_x'T'\rangle \equiv \kappa_{t,xx}\frac{\partial\langle T\rangle}{\partial x},$$
(5.4)

where $\kappa_{t,xx}$ is the eddy thermal diffusivity that depends on spacial coordinates, where $\kappa_{t,xx}$ depends on the flow conditions and is not universal. Similarly, the turbulent scalar variance $-\langle u_x'T'^2\rangle$ can be modelled by considering the 'lumps' of scalar variance being convected by the turbulent fluctuations, being proportional to the gradient of the scalar variance flux [114], which is given by

$$-\langle u_x'T'^2\rangle \equiv K_{xx}\frac{\partial\langle T'^2\rangle}{\partial x},$$
(5.5)

where K_{xx} depends on spatial coordinates. Substitute Eqs. (5.4) and (5.5)

into Eq. (5.3), rearranging terms, we have,

$$2\kappa_{t,xx}\left(\frac{\partial\langle T\rangle}{\partial x}\right)^2 = \langle u_z\rangle\frac{\partial\langle T'^2\rangle}{\partial z} - K_{xx}\frac{\partial^2\langle T'^2\rangle}{\partial x^2} + 2\epsilon_\theta. \qquad (5.6)$$

Therefore, the $\langle T'^2\rangle$ horizontal profile, the production due to the coupling between the turbulent heat flux and the mean temperature gradient is balanced by the decay of the temperature variance along the z-direction, the turbulent diffusion of the temperature variance and the scalar fluctuation dissipation rate. Now we shall evaluate the balance equation Eq. (5.6) with the above models at the *peak position* x_{peak} of the temperature standard deviation profile. For the turbulent diffusion of the temperature variance, the curvature $\partial^2\langle T'^2\rangle/\partial x^2|_{x=x_{\text{peak}}} < 0$, as shown in Fig. 5.4b. This implies that, at $x = x_{\text{peak}}$, the temperature variance is diffusing out instead of diffusing in. Therefore, the only contribution to the temperature variance is the production term at $x = x_{\text{peak}}$. If the production is higher, we expect the temperature variance is also higher.

First, from Fig. 5.4, when rising bubbles are injected, the mean temperature gradient $|\partial\langle T\rangle/\partial x|$ decreased marginally.

Second, for the eddy diffusivity, there are experimental results in turbulent bubbly flows that show that it does not necessarily increases with α [48]. For turbulent bubbly flows, fluorescent dye mixing experiments suggested that the mixing of passive scalar in turbulent bubbly flow is an effectively diffusive process with an effective diffusivity D_{xx} [48], in the same x-direction we are considering. The authors of Ref. [48] found that D_{xx} does not increase with α for high incident turbulent intensity. Applying this result to our study, $\kappa_{t,xx}$ does not always increase with α, implying that the turbulent heat flux also does not necessarily increase with α. But we note that in general D_{xx} depends on the Péclet number [40]. An comparison of the results from the fluorescent dye to temperature in water may not be valid since the Péclet number between these two cases are different by a factor of the ratio of their diffusivities, which is given by $\kappa/\kappa_{dye} = \mathcal{O}(100)$ where κ_{dye} is the diffusivity of the fluorescent dye that Ref. [48] used. Nonetheless, we just want to illustrate that $\kappa_{t,xx}$ does not always increase with α for passive scalar in bubbly flows.

Combining the above two contributions, the decreased mean temperature gradient and the non-monotonic dependence of turbulent scalar flux on α, one can conclude that there is no strict implication that increasing α will lead to an increase of the passive scalar variance.

To summarise this subsection, we have analysed the contributions of the temperature fluctuations in a turbulent bubbly thermal mixing layer, which in-

cludes the mean temperature gradient and the turbulent heat flux (the correlation between temperature and velocity fluctuation). Since these two contributions are not enhanced by increasing α in our case, the temperature variance does not increase with α. While the velocity variance increases with α because of increasing contributions from the bubble-induced agitations, the temperature variance does not increase with α.

5.3.3 The probability density functions of velocity and temperature fluctuations

As mentioned in Sec. 5.1, the shape of a scalar PDF is important both practically and fundamentally. The modification of the scalar PDF due to high-Reynolds bubbles as a function of gas volume fraction α are discussed below. First, note that the scalar PDFs at different positions differ in a single-phase thermal mixing layer [92, 115, 121], of which a qualitative explanation is as follows. Just as in the discussion in section Sec. 5.3.1, the temperature fluctuation may be thought of as originating from fluid particles coming from the neighbouring hotter and colder regions (mainly in the horizontal direction) since the temperature field is practically a passive scalar. Then if the horizontal velocity fluctuation has no preferred direction, there is similar chance of fluid particles coming from the same distance away from the location that we are interested in. At the bulk, the horizontal velocity statistics are homogeneous (see Fig. 5.4) and we also expect there is negligible skewness in the horizontal velocity fluctuations even with bubbles [7] (see also Fig. 5.6b). However, since the mean temperature gradient is nonlinear, in general the increases of the mean temperature at the hotter side with some distance away from the interested position is different from the decrease of the mean temperature at the colder side with the same distance away, except at the point of inflection of the mean temperature profile. Therefore, at the position which is *not* the point of inflection, there is a higher chance of getting a hotter (colder) temperature at the point of interest since there is a larger increase (decrease) of mean temperature at direction of the hotter (colder) side. This leads to an asymmetric PDF with skewness being negative (positive) when the mean temperature gradient is decreasing (increasing), except at the point of inflection. Finally, for the mathematical forms of the PDF of the temperature (scalar) at different positions in a single-phase turbulent thermal mixing layer, we refer to Ref. [121] and the references therein. The exact mathematical forms are not important here and we just want to stress that the PDF of a thermal mixing layer differs at different positions.
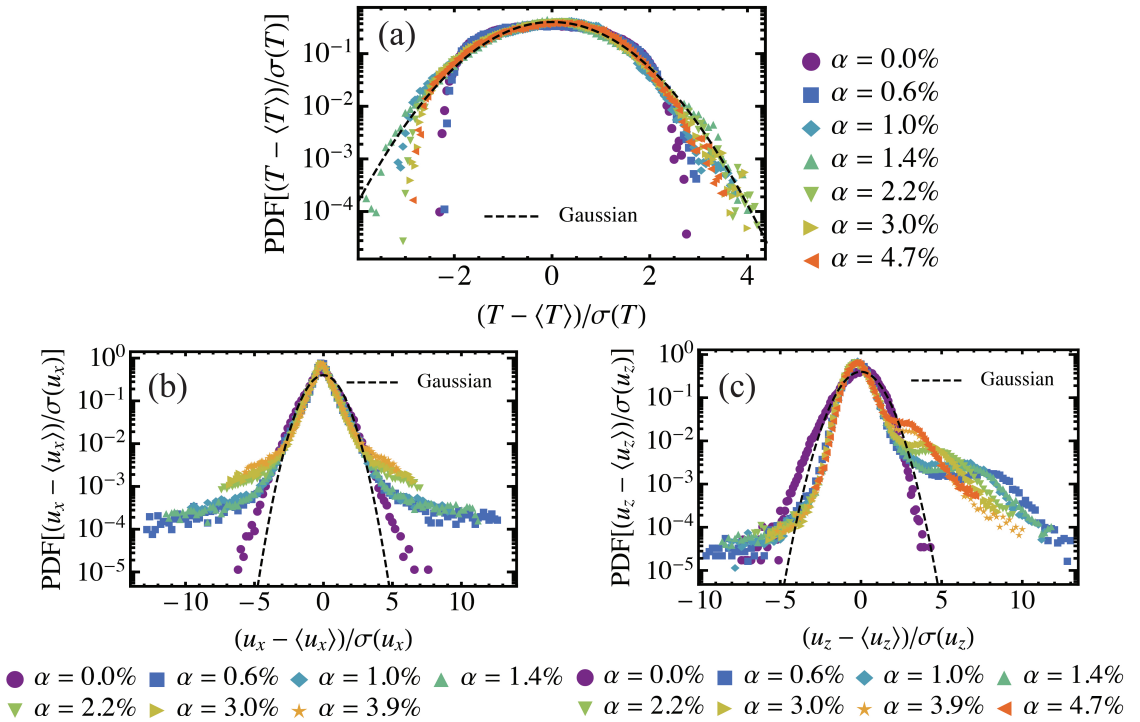
Figure 5.6: The log-linear probability density functions (PDFs) of (a) the standardised temperature (T) at the peak position of the standard deviation profile in Fig.5.4, (b) the standardised horizontal velocity (u_x) at $x/L = 0.5$ (middle of the tunnel) and (c) the standardised vertical velocity (u_z) at $x/L = 0.5$ (middle of the tunnel), for $0\% \leq \alpha \leq 4.7\%$. The dashed lines are Gaussian distribution with zero mean and unit variance for comparison.

As one can already see that the mean temperature profile changes when bubbles are injected (see Fig. 5.4a), to make meaningful comparisons of the temperature PDF with different α, we only compare the temperature PDF at the point of inflection of the mean temperature profile (which coincides with the peak position of the standard deviation profile, see Fig. 5.4). The horizontal and vertical velocity PDFs measured by LDA are also presented for comparisons. The results are plotted as standardised PDFs, as shown in Fig. 5.6.

For the single-phase case, it is the classic thermal turbulent mixing layer, having a sub-Gaussian shape of the scalar PDF, being consistent with the

results mentioned in Ref. [122, 123], that made use of thermal mixing layer experiments in Ref. [117]. On the other hand, the single-phase vertical velocity u_z PDF has a tiny deviation from the symmetric Gaussian distribution, having the skewness being equal -0.4. But for the horizontal velocity u_x it has a symmetric PDF but deviates from Gaussian distribution when $|u_x - \langle u_x \rangle| \gtrsim 3\sigma(u_x)$.

When rising bubbles are injected, the velocity PDFs are dominated by the effect of bubble-induced agitations. From Fig. 5.6b, each of the horizontal velocity PDFs is symmetric, first having a steep self-similar exponential decay and then with a smaller exponential decay which initiates at smaller $|u_x|$ for higher α, which are the signatures of bubble-induced agitations, being consistent with other high-Reynolds bubbly flow experiments summarised in the review Ref. [7]. For the vertical velocity PDFs (Fig. 5.6c), they are asymmetric, and the negative fluctuations exhibit a self-similar double-exponential decay (a steep exponential decay followed by a smaller exponential decay), which is again the signature of bubble-induced agitations. But for the positive vertical velocity fluctuations, there is a second peak for each PDF when $\alpha > 0$. The physical origin of this second peak is unknown. One possibility is that this peak is the most probable bubble rise velocity since tracer particles may stick on the bubble surface when the bubbles are rising. The decreasing relative distance between the two peaks of each of the vertical velocity PDF when α increases may then be consistent with the trend that the relative rise bubble velocity decreases as α increases (Table 5.2). Regardless, before the second peak, the vertical fluctuation exhibits also a self-similar decay, being consistent with other high-Reynolds bubbly flow experimental results summarised in [7].

After the characterisation of the velocity PDFs for non-zero α, the corresponding scalar (temperature) PDFs are now discussed. When α increases from 0% to 0.6%, there is little change of the PDFs. However, when α further increases from 0.6%, the kurtosis increases as reflected by the tails of the probability density functions. Since the current measurements cannot resolve the tails for $T - \langle T \rangle$ for more than three standard deviations, it is inconclusive to tell the differences at the tails for higher α. However, one can still distinguish the PDF for $\alpha \leq 0.6\%$ as sub-Gaussian and $\alpha > 0.6\%$ has a significant larger kurtosis. In the small-scale statistics section (Sec. 5.4), the PDFs of the temperature increments at the largest scale for $\alpha = 4.7\%$ are resolved up to 4 standard deviations and was closer to Gaussian than that of $\alpha = 0\%$. This means that in a thermal mixing layer with fixed power provided to the heaters, there are

more extreme values of temperature when normalised by its standard deviation when bubbles are injected, suggesting the engineers or scientists may have to be aware of any chemical reactions that may/may not happen more probably.

For single-phase turbulence, as mentioned in section Sec. 5.1, there has been a long debate on under what situation the scalar PDF will be Gaussian or non-Gaussian. The recent review by Ref. [6] provides a short summary on this issue and, deducing from Ref. [124], suggests that the ratio L_u/L_T, where L_u and L_T are the length scales at which the velocity and temperature fluctuations are respectively introduced, may play a role in determining the shape of the scalar PDF to be Gaussian or exponential. However, in the single-phase turbulent thermal mixing layer, it is even sub-Gaussian at the middle of the mixing layer. It is still not clear whether the above insight can be applied to thermal mixing layer.

To conclude this subsection, we obtain high quality PDFs of the velocity fluctuations that exhibit double exponential decays which are the signatures of bubble-induced agitations [7]. The temperature PDFs at the peak standard deviations (Fig. 5.4b) for different α are compared, showing that the kurtosis of the temperature PDF is similar for $\alpha = 0\%$ and 0.6%. However, the kurtosis of the temperature PDF is significantly increased when α increases from 0.6% to 1.0%, though they are still sub-Gaussian. When α is increased further, there are insignificant changes of the shapes of the temperature PDFs for $|T - \langle T \rangle| < 3\sigma(T)$. A practical message can be drawn is that the bubbles promote more extreme values of the temperature when normalised by its standard deviations, leading to practical considerations on any reactions can be more/less probable.

5.4   Small-scale Statistics

To study the structure of a passive scalar in turbulent bubbly flows, one can study the statistics of the temperature difference between two instants measured at the middle of the measurement section, which is given by

$$\Delta_\tau T \equiv T(t + \tau) - T(t), \tag{5.7}$$

where τ is the time difference. By using Taylor's frozen flow hypothesis [9], the time coordinates can be transformed into spatial coordinates by $t = -z'/U$, where z' is the vertical coordinate and U is the liquid mean vertical velocity measured by LDA at the middle of the tunnel. The minus sign stems

from the coordinate system, in which upward is positive, meaning that the measurements in the future are the temperature at the lower height from the mid-height of the measurement section. The time difference can then also be transformed as $\tau = -z/U$, where z is the vertical distance between two points in space. In spatial coordinates, the temperature difference is given by

$$\Delta_z T \equiv T(\mathbf{x} - z\mathbf{e_z}) - T(\mathbf{x}), \tag{5.8}$$

where $\mathbf{x}$ is the spatial coordinates in the measurement section, $\mathbf{e_z}$ is a unit vector pointing upward along the z-direction. Thus, the statistics of $\Delta_z T$ reflects the structure of the temperature at the spatial scale z. Such statistics are the moments of $\Delta_z T$ which are also called structure functions. The p-th order moments or temperature structure functions $R_p(z)$ are defined as

$$R_p(z) \equiv \langle (\Delta_z T)^p \rangle, \tag{5.9}$$

where averaging is over time here. The Kolmogorov-Obukhov-Corrsin (KOC) theory [13–15] predicts that when the Reynolds number and Péclet number are much larger than unity, there exists a so-called 'inertial-convective subrange' [2] where the diffusivity and viscosity can be neglected, in which, by dimensional analysis,

$$R_p(z) \propto z^{p/3}, \qquad \text{(KOC theory)} \tag{5.10}$$

meaning that all the normalised moments $R_p/R_2^{p/2}$ are constants. However, it is well-known that Eq. (5.10) does not hold for all p (see e.g. Ref. [101]). Extending the notions of the deviations of Kolmogorov's theory for the velocity structure functions (see e.g. Ref. [125]), it signifies the breakdown of scale invariance [126, 127] and the scaling becomes *anomalous* (see e.g. Ref. [101, 125, 127, 128]). If a power law for R_p still exists in the inertial-convective subrange, we have

$$R_p(z) \propto z^{\zeta_p} \tag{5.11}$$

where ζ_p is the scaling exponent of the p-th order temperature structure function. By extending the notion of intermittency for the velocity structure functions (e.g. [125, 129, 130]), the *intermittency correction* for the scalar field is defined as $\delta\zeta_p \equiv \zeta_p - p/3$. There is a *stronger intermittency* if the deviation is larger [128], modulus-wise.

Such deviation can also be reflected in the tails (the extreme events) in the probability density function (PDF) of $\Delta_z T/\sigma(\Delta_z T)$ being more significant

when z decreases [128], since it implies that $R_p/R_2^{p/2}$ increases rather than being constant when z decreases. Larger tails in the PDF signifies stronger deviation of the KOC theory, and therefore stronger intermittency.

It is then of interest to also investigate whether introducing rising bubbles will enhance the intermittency or not.

In the current study on small-scale statistics, we only compared the cases $\alpha = 0\%$ and $\alpha = 4.7\%$. A –3 scaling in the thermal spectra was observed in the latter (see Fig. 4.1 in Chapter 4). We measured the temperature at the locations where the corresponding standard deviation profile is approximately maximum (see Fig. 5.4b). At such locations, the temperature PDF is approximately symmetric (see Fig. 5.6a). For $\alpha = 0\%$, we measured 9.7×10^6 data points; while for $\alpha = 4.7\%$, we measured 3.56×10^6 data points. The liquid mean vertical velocity for $\alpha = 0\%$ and $\alpha = 4.7\%$ are 0.52 m/s and 0.50 m/s respectively, which are only slightly different (see also Fig. 5.4). We assumed the Kolmogorov length scale η is the same for the two cases. The Taylor-hypothesis is used [9], and therefore the smallest resolved time scale τ_{res} (the response time of the thermistor) can be transformed into the the smallest resolved spatial scale z_{res} by $\tau_{\mathrm{res}} = z_{\mathrm{res}}/U$, yielding is $z_{\mathrm{res}} = 19\eta$.

5.4.1 Probability density function of the temperature increments

As mentioned before, the intermittency effect in turbulence can be investigated by studying the PDF of $\Delta_z T$ as function z.

Fig. 5.7a–d compares the PDFs of the *standardised* temperature increments $\Delta_z T/\sigma(\Delta_z T)$, where $\sigma(.)$ is the sample standard deviation, for $\alpha = 0\%$ and $\alpha = 4.7\%$ for z from $\mathcal{O}(10\eta)$ to $\mathcal{O}(10^4\eta)$. It shows that for the smallest resolved scale $z = \mathcal{O}(10\eta)$, the tails of the PDF of $\Delta_z T$ for $\alpha = 4.7\%$ extends up to 10 standard deviations, which are larger than those for $\alpha = 0\%$ that only extends up to 8 standard deviations. When $z = \mathcal{O}(100\eta)$, both $\alpha = 0\%$ and $\alpha = 4.7\%$ cases have distributions close to Gaussian. When the scale grows even further the PDF of $\alpha = 0\%$ becomes sub-Gaussian but that of $\alpha = 4.7\%$ stays close to Gaussian (only slightly sub-Gaussian). The shape of the PDF of $\Delta_z T/\sigma(\Delta_z T)$ at the largest scale is consistent with the PDF of the temperature itself (see Fig. 5.6). The tails of the PDF of $\Delta_z T/\sigma(\Delta_z T)$ being larger for $\alpha = 4.7\%$ implies that the rising bubbles enhances the intermittency in a turbulent thermal mixing layer.

Figs. 5.7e and f show the PDFs of $\Delta_z T/\sigma(\Delta_z T)$ for different z/η for $\alpha = 0\%$ and $\alpha = 4.7\%$ respectively, providing a clear view of how the shape of the
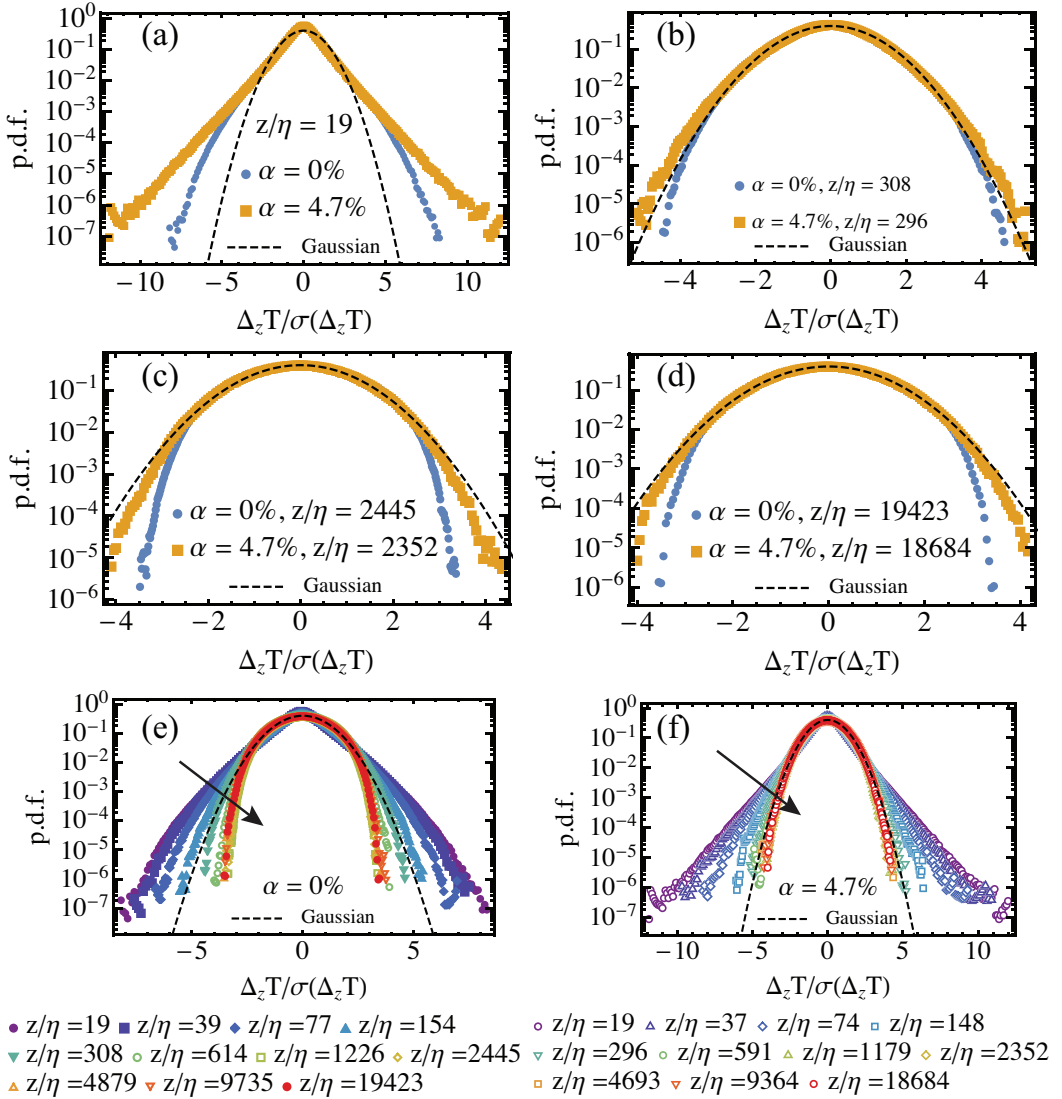
Figure 5.7: (a) to (d): The probability density functions (p.d.f.) of the standardised temperature increments $\Delta_z T/\sigma(\Delta_z T)$, where $\sigma(.)$ is the sample standard deviation, for $\alpha = 0\%$ and $\alpha = 4.7\%$ at z from $\mathcal{O}(10\eta)$ to $\mathcal{O}(10^4\eta)$. (e) and (f): The p.d.f. of $\Delta_z T/\sigma(\Delta_z T)$ for different z/η for $\alpha = 0\%$ and $\alpha = 4.7\%$ respectively. The p.d.f. for the smallest scale is purple and for the largest scale is red. The arrows show the p.d.f. when the scale z becomes larger.
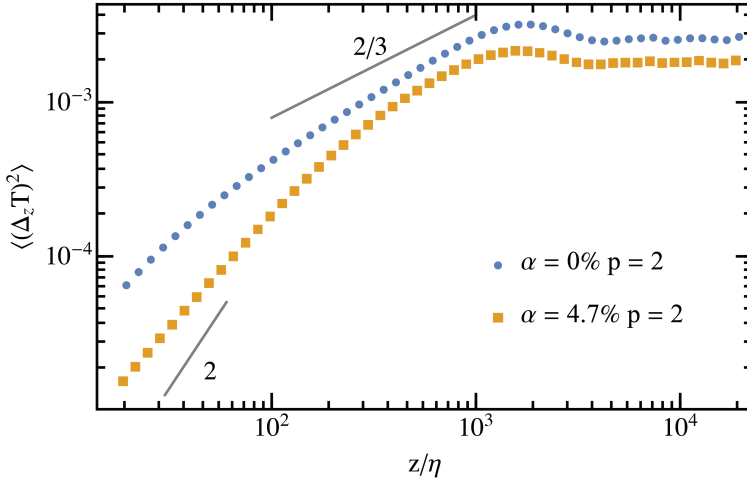
Figure 5.8: The variance of the temperature increment or the second order temperature structure function, $\langle(\Delta_z T)^2\rangle$ versus z/η, for $\alpha = 0\%$ and 4.7%, where η is the Kolmogorov length scale for $\alpha = 0\%$. A straight line with the slope of 2 that represents the scaling in the viscous subrange is plotted for comparison [2]. Another straight line with the slope 2/3 derived from the KOC theory [13–15] is also plotted for comparison. The smallest resolved scale is $z/\eta = 19$.

PDFs changes from highly non-Gaussian that has large tails to sub-Gaussian ($\alpha = 0\%$) or to slightly sub-Gaussian ($\alpha = 4.7\%$).
We stress that Fig. 5.7 are plotted the PDFs of the *standardised* temperature increments $\Delta_z T/\sigma(\Delta_z T)$, which does not reflect the variance of the temperature increments. In Chapter 4, we mentioned that there is enhanced mixing at the small-scale due to the rising bubbles. Indeed the variance of $\Delta_z T$ are smaller when bubbles are injected, as shown in Fig. 5.8.

5.4.2 The skewness and the kurtosis of the temperature increments

It is well-known that the local isotropy assumption in passive scalar turbulence does not always hold [67,101,125]. One test of the local isotropy is to check the skewness of the temperature. The larger the deviation of skewness from zero, the larger the anisotropy. In particular, for an unidirectional, isotropic grid
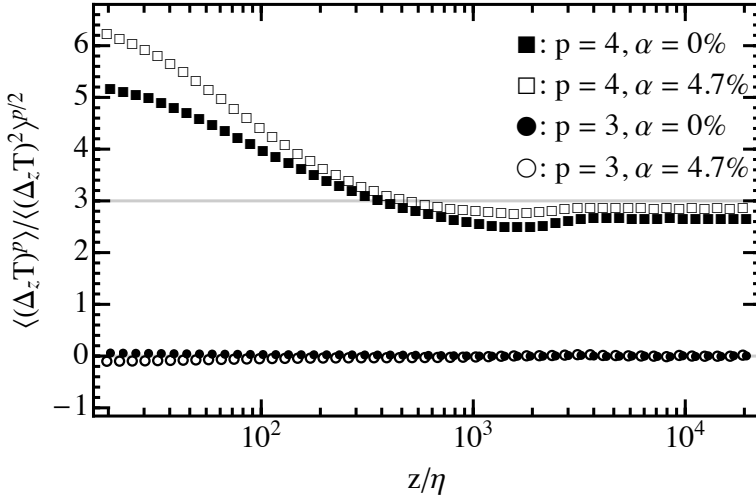
Figure 5.9: The normalised third and fourth order structure function of the temperature increments $\langle(\Delta_z T)^p\rangle/\langle(\Delta_z T)^2\rangle^{p/2}$ versus z/η ($p = 4, \alpha = 0\%$: solid square; $p = 4, \alpha = 4.7\%$: hollow square; $p = 3, \alpha = 0\%$: disk; $p = 3, \alpha = 0\%$: circle).

turbulence with a mean temperature gradient, the skewness of the temperature gradient is above unity when the gradient is *parallel* to the mean temperature gradient [131, 132]. However, the skewness of the temperature gradient is below 0.1 when it is *perpendicular* to the mean temperature gradient [132]. Our measurements employed Taylor-hypothesis which can only investigate the temperature increment in the streamwise-direction (i.e. perpendicular to the mean temperature gradient), which we expect to be close to zero for the single-phase case at small scales. However, the up-down symmetry will be further broken by the rising bubbles due to the presence of the wakes behind the bubbles, meaning that the skewness may become non-zero. Furthermore, we also provide a quantification of the tails of the PDFs of $\Delta_z T$, which is the kurtosis as a function of z.

Fig. 5.9 shows the normalised third (skewness) and fourth (kurtosis) order moments, that is $R_3/R_2^{3/2}$ and R_4/R_2^2. It shows that both $\alpha = 0\%$ and 4.7% have skewness very close to zero. Thus there is only a small effect of bubbles on the anisotropy of small-scale fluctuations. For the kurtosis, the single-phase case has a kurtosis always smaller than the $\alpha = 4.7\%$ case, showing the
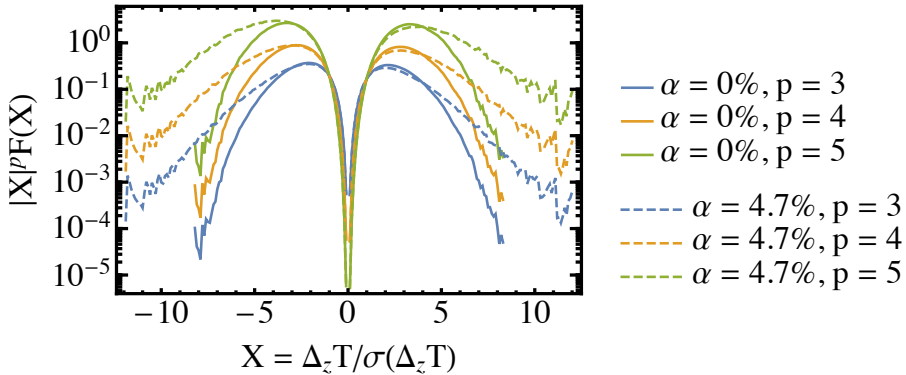
Figure 5.10: Convergence tests of the moments of the absolute value of the temperature increments: $|X|^p F(X)$ vs X, where $X = \Delta_z T / \sigma(\Delta_z T)$ and $z/\eta = 19$, for $p = 3, 4$ and 5 with $\alpha = 0\%$ (solid lines) and 4.7% (dashed lines) in semi-log scale.

enhanced intermittency due to the presence of rising bubbles.

5.4.3 Temperature structure functions and the analysis by using extended self-similarity

The odd moments of $\Delta_z T$ have slower convergence than the even moments because they consider both the positive and negative values of $\Delta_z T$. Moreover, when one extracts the scaling exponents for the velocity structure functions through extended self-similarity (ESS) method [109, 133], it is argued and found that the odd moments of the *absolute value* of the velocity increments should be used instead [130]. Therefore, we investigate the moments of the *absolute value* of $\Delta_z T$, which are given by,

$$R_p^* \equiv \langle |\Delta_z T|^p \rangle, \tag{5.12}$$

where p is the order of the moment. If a power law scaling exists in the inertial-convective range, we write $R_p^* \sim z^{\zeta_p^*}$, where ζ_p^* is the corresponding scaling exponents of the p-th order moments of $|\Delta_z T|$. We note that the scaling properties for R_p^* and R_p may not be the same (see. e.g. [134]).

In order to check the convergence of the statistics of R_p^*, we compute the integrand of the following integral,

$$R_p^*(z) = \int_\infty^\infty F(\Delta_z T) |\Delta_z T|^p d(\Delta_z T), \tag{5.13}$$

where $F(\Delta_z T)$ is the PDF of $\Delta_z T$. $R_p^*(z)$ is converged if the integrand drops fast enough for sufficiently large $|\Delta_z T|$ [135]. From the PDFs of $\Delta_z T/\sigma(\Delta_z T)$ shown in Fig. 5.7, we see that the tails of the PDF become larger for smaller scale, meaning that the PDF requires more data points to have the statistics to converged. Therefore if the structure function converges at the smallest resolved scale, it will be also converged at the larger scales. Moreover, the higher the order of the moments, the tails of the PDF will be enlarged, meaning that more data points are needed in order to achieve convergence. If a high order moment converges, the moments of the lower orders will also converge. Fig. 5.10 plots the integrands $|X|^p F(X)$, where $X = \Delta_z T/\sigma(\Delta_z T)$ and $z/\eta = 19$, for $p = 3, 4$ and 5 with $\alpha = 0\%$ and 4.7% in semi-log scale. It shows the fast drops of the integrands (the tails drop more than 1 decade from the peaks of the integrand), meaning that the structure functions converge up to order 5 with the smallest resolution of $z/\eta = 19$.

Fig. 5.11 shows $R_p^*(z) = \langle|\Delta_z T|^p\rangle/b_2^{p/2}$ versus z/η, where $b_2 = R_2^*(z_{min})$ and $z_{min} = 19\eta$, for $\alpha = 0\%$ and 4.7% with $p = 1$ to 5. For $\alpha = 4.7\%$, it is difficult to observe a power law scaling for $R_p^*(z)$ (see also Fig. 5.12 for the local logarithmic exponent of $R_2^*(z)$). Nonetheless, we can still apply the ESS analysis by investigating the *relative* scaling exponents, if they exist, which are defined as

$$R_p^* \sim (R_2^*)^{\beta(p,2)} \tag{5.14}$$

where $\beta(p,2)$ is the *relative scaling exponent* of the order p over order 2 (see e.g. Ref. [133]). The notion 'relative scaling exponents' were used in several literature [136–139] while some other works called it 'normalized scaling exponents' [140–142]. To distinguish from the scaling exponents ζ_p or ζ_p^* of a structure function (Eq. 5.11), we use $\beta(p,2)$ and call it 'relative scaling exponents'. If there is a power law scaling in z at some range, for example the inertial-convective subrange, such that $R_p^* \propto z^{\zeta_p^*}$, then $\beta(p,2) = \zeta_p^*/\zeta_2^*$.

Fig. 5.13a plots $R_p^*(z)/b_2^{p/2}$ versus R_2^*/b_2 for $p = 1$ to 5. It shows that the rising bubbles ($\alpha = 4.7\%$) extended the range of the scaling as compared to the single phase case when R_2^* is normalized by $b_2 = R_p^*(z_{min})$. Moreover, from the logarithmic slopes of the plots, $\beta(p,2)$ only shows tiny differences between single-phase flow and multiphase flow for p up to 5. Quantitatively, by fitting the data points in log-log scale, we found the slopes with error bars and they are tabulated in Table 5.3. The table shows that the relative exponents $\beta(p,2)$ are only marginally larger when rising bubbles were introduced (start to have difference at the third significant figure). The difference of the relative scaling
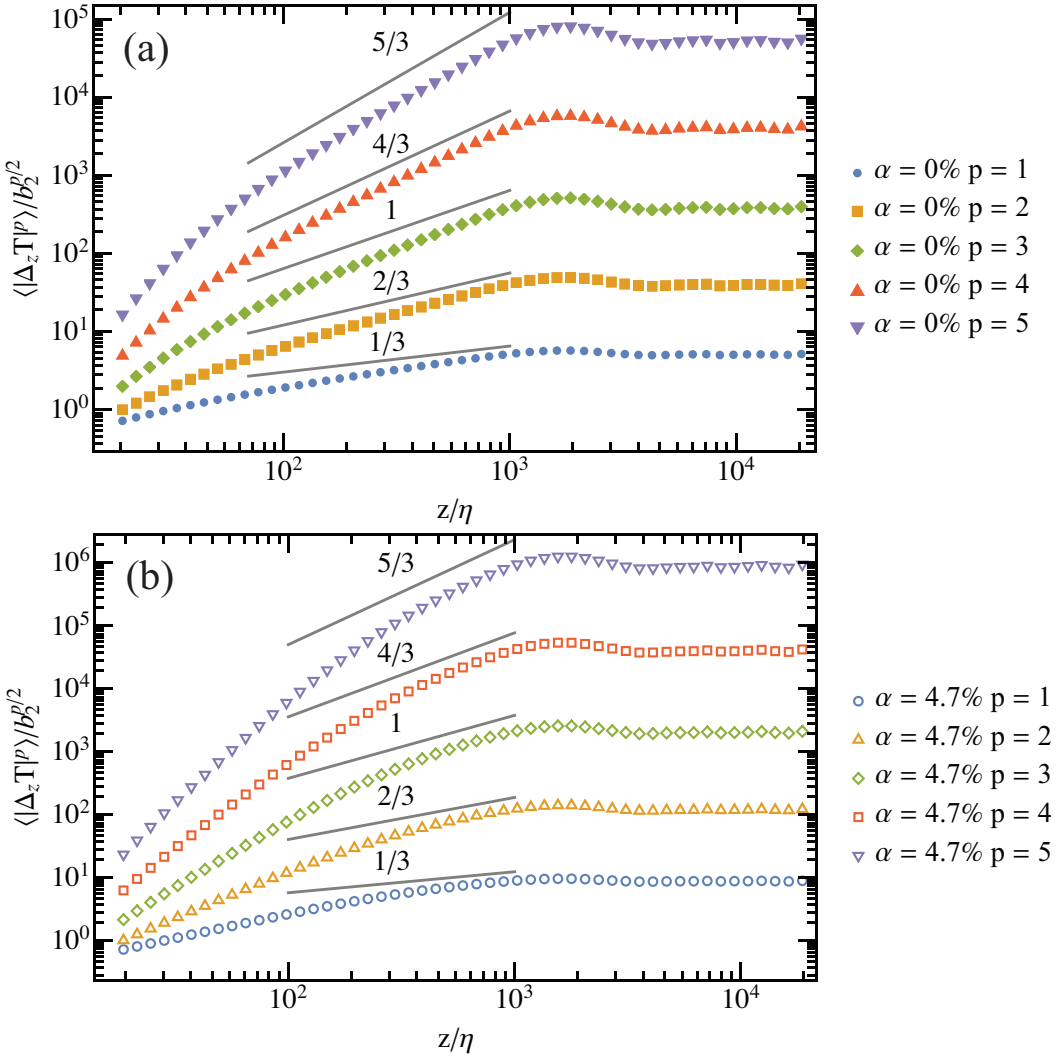
Figure 5.11: $\langle |\Delta_z T|^p \rangle / b_2^{p/2}$ versus z/η, where $\langle |\Delta_z T|^p \rangle \equiv R_p^*(z)$ is the p-th order moment of the absolute value of the temperature increment, $b_2 \equiv R_p^*(z_{min})$, $z_{min} = 19\eta$ and η is the Kolmogorov length scale for the single-phase case, for (a) $\alpha = 0\%$ and (b) 4.7%. Straight lines with the slopes $p/3$ derived from the KOC theory [13–15] are plotted for comparison.
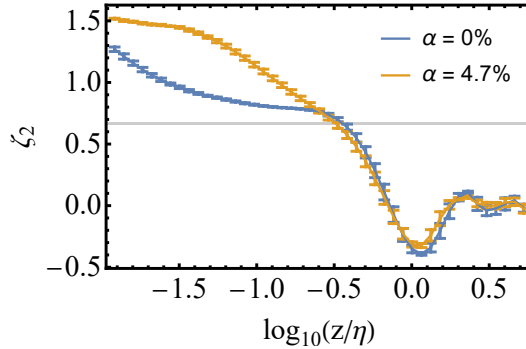
Figure 5.12: The local logarithmic exponent ζ_2 (computed for every 0.25 decade) for the second order moments of $\langle |\Delta_z T|^p$ versus z/η for $\alpha = 0\%$ and 4.7%. The horizontal grey line indicates the 2/3 logarithmic slope. The error bars are the standard errors of the logarithmic slopes when a fit is applied.

exponents between having bubbles or not increases when p goes higher up to $p = 5$. For $p > 6$ we do not obtain enough data points to have converged statistics so it is unknown whether such difference will continue to increase. The comparison of the relative exponents with other scalar turbulence systems will be discussed in the next section.

Furthermore, to demonstrate the intermittency effect that can be hidden in the ESS plots because the exponents at one subrange (e.g. viscous subrange) and at another (e.g. inertial-convective subrange) may only marginally differ from each other, we compensated the ESS plots by $[R_2^*(z)]^{p/2}$ [130], as shown in Fig. 5.13b. The logarithmic slopes of these plots will then be $\beta(p, 2) - \frac{p}{2}$ for some scaling range if it exist. The compensated ESS plots (Fig. 5.13b) demonstrate that the scaling is not perfect for the whole range (not perfect straight lines).

5.4.4 Discussion on the intermittency and relative scaling exponents

We only analysed the relative scaling exponents $\beta(p, 2)$ but not the scaling exponents ζ_p^* because there is no range that shows a clear scaling in the original structure functions for $\alpha = 4.7\%$ (see Fig. 5.11 and 5.12). As the strength of intermittency relies on the deviation of the scaling exponents of the structure functions but not the relative scaling exponents $\beta(p, 2) = \zeta_p/\zeta_2$, we cannot conclude whether the intermittency is stronger or not by just investigating the
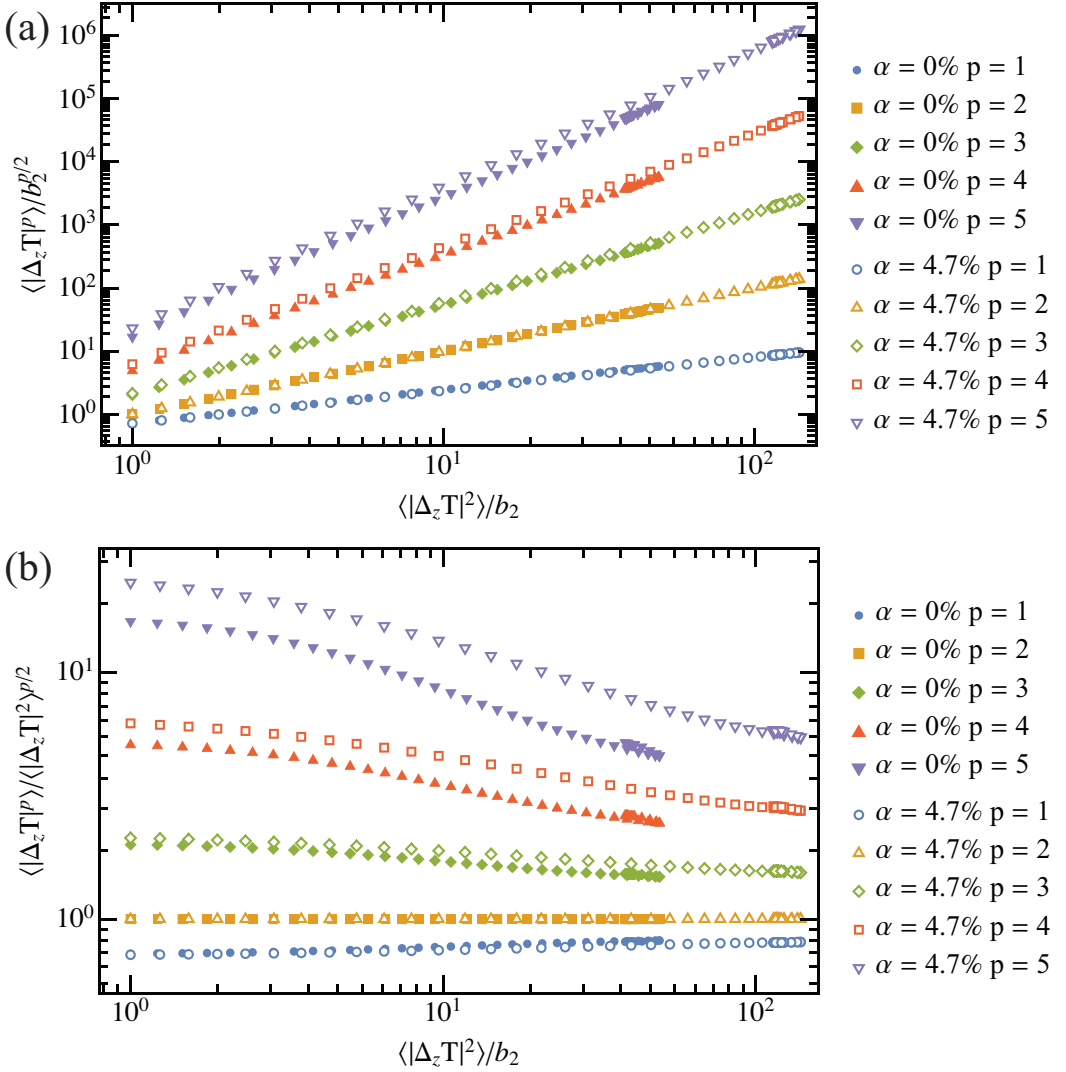
Figure 5.13: (a) Extended self-similarity (ESS) analysis for temperature increments: $\langle|\Delta_z T|^p\rangle/b_2^{p/2}$ versus $\langle|\Delta_z T|^2\rangle/b_2$ for $\alpha = 0\%$ (filled markers) and 4.7% (open markers) and $p = 1$ to 5. For the slopes of the plots, see Table 5.3. (b) The corresponding compensated ESS plots: $\langle|\Delta_z T|^p\rangle/\langle|\Delta_z T|^2\rangle^{p/2}$ versus $\langle|\Delta_z T|^2\rangle/b_2$.

Cases	$\beta(1,2)$	$\beta(3,2)$	$\beta(4,2)$	$\beta(5,2)$
$\alpha = 0.\%$, ML	0.535 ± 0.002	1.414 ± 0.004	1.79 ± 0.01	2.14 ± 0.02
$\alpha = 4.7\%$, ML	0.526 ± 0.001	1.428 ± 0.002	1.820 ± 0.006	2.18 ± 0.01
Standard RBC [107]	–	1.363	1.651	1.874
Boiling RBC* [107]	–	1.420	1.782	2.122

Table 5.3: The relative exponents $\beta(p,2)$ obtained by performing the extended self-similarity (ESS) analysis from the relation $R_p^* = R_2^{*\beta(p,2)}$ for $p = 1, 3, 4$ and 5 for different scalar turbulence settings: ML corresponds to mixing layer (the current study) and RBC corresponds to turbulent Rayleigh-Benard convection in which * corresponds to boiling point-bubbles simulations [107]. The uncertainties are the 99.7% of confidence level that are obtained from the fitting. By definition, $\beta(2,2) = 1$.

relative scaling exponents unless ζ_2 are similar (from Fig. 5.12, ζ_2 is different between $\alpha = 0\%$ and $\alpha = 4.7\%$). Nonetheless, we can still compare the *relative* scaling exponents $\beta(p,2)$ in our study with other scalar turbulence systems since it may be within a more general universality class of scalar turbulence. Even the scaling exponents for the *velocity* structure functions are different for 3D homogeneous and isotropic turbulence, turbulent Rayleigh-Bénard convection and magnetohydrodynamic (MHD) turbulence, the *relative* scaling exponents are still very similar [143]. Therefore, it is still of interest to compare the relative exponents of the scalar structure functions in our current study with and without bubbles and also with other scalar turbulence systems.

There are models which predict the values of scaling exponents for the velocity structure functions, such as the β model, the log-normal model, the multifractal model and the She-Leveque (SL) model (see e.g. Ref. [126]). The SL model [144] is extended in Ref. [145] to passive scalar by considering a hierarchical structure of R_p^* and using the notion of the geometry of 'the most intermittent structures' to understand the scaling exponents [145]. The model in Ref. [145] (in short, RCBC model) stated that, after normalizing the scaling exponents ζ_p by ζ_2,

$$\frac{\zeta_n}{\zeta_2} = \frac{\Delta_\infty}{\zeta_2}n + \frac{C}{\zeta_2}(1 - \tilde{\alpha}^n), \qquad (5.15)$$

where

$$\frac{C}{\zeta_2} = \frac{\zeta_1/\zeta_2}{1-\tilde{\alpha}} - \frac{1-(1+\tilde{\alpha})(\zeta_1/\zeta_2)}{(1-\tilde{\alpha})^2}, \tag{5.16}$$

$$\frac{\Delta_\infty}{\zeta_2} = \frac{1-(1+\tilde{\alpha})(\zeta_1/\zeta_2)}{1-\tilde{\alpha}}, \tag{5.17}$$

and C is the codimension of the most intermittent structure [144] and $\tilde{\alpha}$ is a fitting parameter. For example, in the passive scalar turbulence study (wind tunnel with no mean temperature gradient) in [145] (in short, RCBC96), they obtained $\tilde{\alpha} = 0.63$, $C = 0.8 \pm 0.1$ and $\Delta_\infty = 0.06 \pm 0.02$, implying the dimension of the structures is 2.2 ± 0.1 which is close to 2, representing some convoluted sheets instead of the filaments as in the velocity field described in Ref. [144]. However, if we only investigate the relative exponents (ζ_p/ζ_2) and ζ_2 is not known, even though we obtained $\tilde{\alpha}$ through fitting the data points, we can only calculate C/ζ_2 but not C itself. Therefore, one still cannot obtain the geometric property of the most intermittent structures in the current study, meaning that the RCBC model is not helpful for improving our physical understanding in our study. However, even though their model is not helpful for the physical understanding, we can still use their experimental results that are captured by their model for comparisons.

After discussing the models that will be helpful for comparing the scaling properties, we compare the relative scaling exponents $\beta(p, 2)$ (or ζ_p/ζ_2) with other systems (standard and boiling turbulent Rayleigh-Bénard (RB) convection, in short LTD14 [107] and heat wake experiments RCBC96) and theoretical models (KOC theory, SL model). For LTD14, we directly use the data in Table 2 and 3 of Ref. [107]. We compare our results with the RCBC model with the original values found in their passive scalar results [145] but we do not fit our own data using their model. We again note that the SL model only models the exponents for the velocity structure functions. The RB simulations in Ref. [107] not only reproduced the scaling exponents result of RCBC96 on passive scalar, but also reproduced the numerical results of Ref. [146] on passive scalar and the experimental results in Ref. [147] on the scaling exponents in the bulk of the turbulent RB convection cell. However, when the difference of $\beta(p, 2)$ between LTD41 and RCBC96 is significant when $p > 3$. The comparison of the relative scaling exponents $\beta(p, 2)$ are plotted in Fig. 5.14 and tabulated in Table 5.3. We discuss the intermittency and the comparison of the relative scaling exponents in the next section.
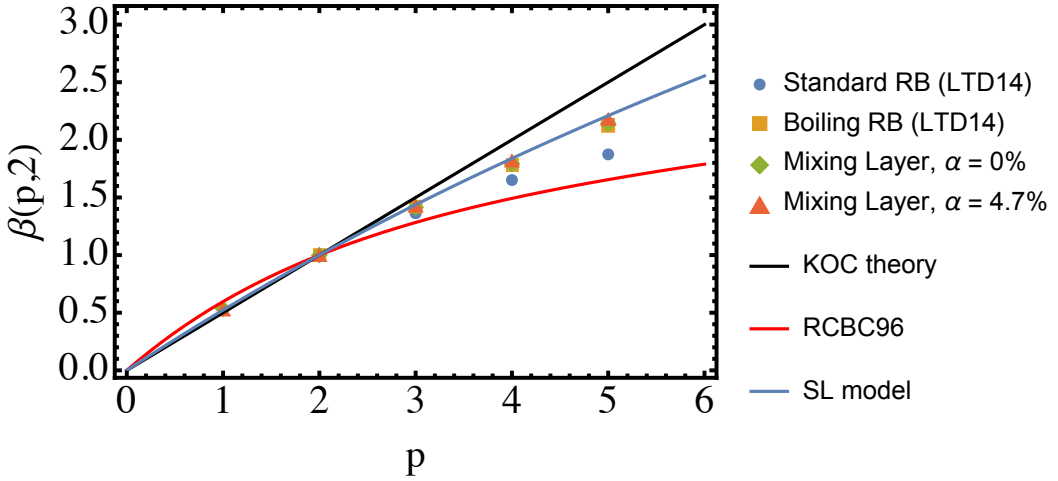
Figure 5.14: The relative scaling exponents $\beta(p,2)$ (or ζ_p/ζ_2) of the temperature structure functions (absolute temperature increment) R_p^*. The legends with 'Mixing layer' refer to the current study. The data on standard and boiling RB are from LTD41 [107]. Other data are KOC theory [13–15], She-Leveque Model (SL model) [144] and RCBC96 [145].

With or without rising bubbles: enhanced intermittency but marginal increase of the relative exponents

Although the local exponent ζ_2 differs significantly between the two cases before reaching the largest scale, see Fig. 5.12, we found that the relative scaling exponents $\beta(p,2)$ only shows a marginally increase when bubbles are introduced, see Fig. 5.13 and Table 5.3. The PDFs of the temperature increments show larger tails when bubbles are introduced (Fig. 5.7), quantified by the kurtosis (Fig. 5.9), indicating the increase of intermittency when bubbles are introduced. Therefore, while the intermittency is enhanced, the relative exponents only increased slightly when bubbles are introduced.

To qualitatively understand the increase of intermittency, a section of the time series of the temperature fluctuations T' for $\alpha = 0\%$ and 4.7% are plotted in Fig. 5.15. For $\alpha = 0\%$, there are small-scale rapid fluctuations at small amplitude ('ramps') and some sudden jumps of temperature ('cliffs') (for the notion of ramp-cliff structure, see e.g. Ref. [6, 101, 128]). On the other hand, the small-amplitude rapid fluctuations are smoothened when $\alpha = 4.7\%$. This implies that the rising bubbles enhanced the mixing of the temperature field
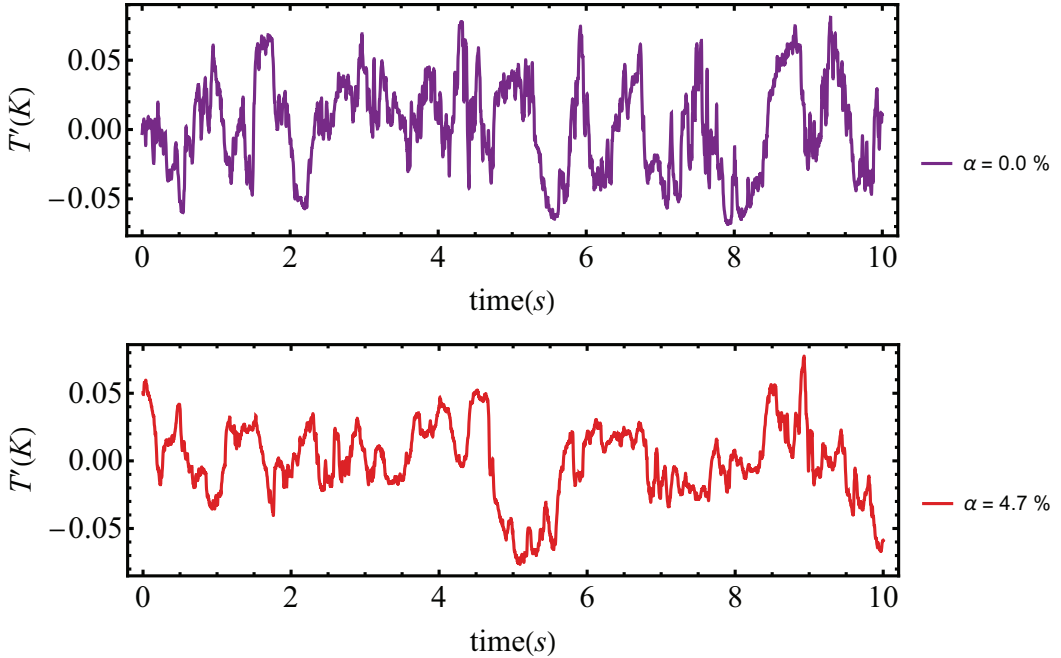
Figure 5.15: The time series of the temperature fluctuations T' for $\alpha = 0\%$ (above) and 4.7% (below) in a turbulent thermal mixing layer, measured at the peak position of the temperature standard deviation profile for the liquid mean flow speed $= 0.5$ m/s. For the global temperature profiles, see Fig. 5.4a.

at the small-scale that have small amplitude, leaving predominantly the large, sudden temperature changes (cliffs). Therefore, the large temperature increments contributes more in the PDFs of temperature increments (see Fig. 5.7), thus the intermittency is enhanced when bubbles are introduced.

Comparison with other scalar turbulence systems

From Table 5.3, the values of $\beta(p, 2)$ for $p = 3, 4$ and 5 for both $\alpha = 0\%$ and 4.7% in the current study are similar to the boiling turbulent Rayleigh-Bénard (RB) convection simulation case [107] (the first two significant figures being the same except for $\alpha = 4.7\%$ in our study starts to have a change at the second significant figure after rounding up). We now state the similarities and differences between our system and the boiling RB simulations. For the possible similarities, we have an imperfection of the experimental setting that a

tiny amount of finite size vapour bubbles (those very small ones cannot be seen by eye) were produced due to overheating heaters in the long measurements for small-scale statistics (not for the integral-scale statistics analysis in Sec. 5.3). However, the comparably much larger amount of gas bubbles most likely makes the effect of the vapour bubbles negligible. Still, the relative scaling exponents for $\alpha = 4.7\%$ in our study are quite similar to the boiling RB case for $p < 6$, which may imply that both the vapour bubbles and gas bubbles can lead to similar relative scaling exponents. For the differences between our system with the boiling RB case, the latter simulates the vapour bubbles by point particles while we have gas bubbles with finite size that have negligible latent heat transfer and produce significant wakes. Moreover, we have forced convection while the boiling RB with point-bubble simulations is a mixed convection. The difference of the relative scaling exponents $\beta(p, 2)$ between our study with the boiling RBC becomes larger when p increases from $p = 3$ to $p = 5$ though only marginal. By just analysing $p < 6$, it is difficult to tell whether such difference will increase when $p > 5$. Nonetheless, such difference is very small as compared to the significant difference with the relative scaling exponents of the standard RBC. It is not clear why $\beta(p, 2)$ for the current study is similar to the point-bubble boiling RB simulations in Ref. [107].

From Fig. 5.14, the difference of $\beta(p, 2)$ of our study with the passive scalar measurements for heated wake without mean temperature gradient (RCBC96) is even bigger. One may wonder whether the presence of mean temperature gradient will change the relative exponent significantly. However, Ref. [142] shows that even for a wind tunnel experiments with *constant* mean temperature gradient, the relative scaling exponents does not have significant change as compared to RCBC96 up to $p = 6$ [145]. Our experiments were thermal mixing layers which had nonlinear mean temperature gradient. It is not clear whether the big difference of the relative scaling exponents (at the second significant figure) are due to the shape of the mean temperature gradient, due to the imperfection of the experiments (having small vapour bubbles for $\alpha = 0\%$) or some other unknown factors. The difference of the constant or step-like mean temperature gradient is that the former may seem to have unbounded temperature while the step-like mixing layer is bounded by two extreme hottest and the coldest temperatures, which can be also reflected by the difference in the shapes of the PDFs of the temperature at the middle of tunnel. Mixing layers have a PDF with a sub-Gaussian kurtosis 2.3 in the current study while the constant mean temperature gradient case has an exponential PDF. Finally, the values of $\beta(p, 2)$ for both $\alpha = 0\%$ and 4.7% in our study are higher than that

in all other single-phase experiments summarised in Fig. 10 in Ref. [142]. In short, the relative scaling exponents $\beta(p, 2)$ in our current study are all higher than other single-phase scalar turbulence mentioned above and the reason is to be further investigated.

To conclude, the relative scaling exponents in turbulent thermal mixing layer in our study, no matter having large amount of gas bubbles ($\alpha = 4.7\%$) or not ($\alpha = 0\%$), are similar to the boiling RB case (LTD14 [107]) and higher than most of the other popular single-phase scalar turbulence experiments (summarised in Ref. [142]). While the relative scaling exponents are still lower than that deduced from KOC theory, the reason of such high relative scaling exponents for a turbulent thermal mixing layer is to be further investigated.

5.5   Conclusion and outlook

In this chapter, the integral-scale and small-scale statistics of the passive scalar in turbulent bubbly mixing layer for the gas volume fraction $\alpha = 0\%$ to 4.7% were investigated. For the integral-scales, when α increases, we find that the temperature variance does not increase, as opposed to the velocity variance that increases with α. This is because the source of temperature fluctuations includes the coupling of the turbulent heat flux and the mean temperature gradient which are both not monotonically increasing functions of α. The probability density function (PDF) of the standardised temperature and velocity fluctuations were examined. When bubbles were introduced, the standardised velocity PDF shows exponential tails, signifying the contributions of bubble-induced agitations [7]. For the PDFs of the standardised temperature at the peak location of standard deviation (which are approximately symmetric), when α increases from 0% to 0.6%, there is insignificant change and the PDFs have sub-Gaussian kurtosis. A significant change of the kurtosis occurs when α increases from 0.6% to 1.0%, but they still have sub-Gaussian kurtosis. Within three standard deviations of the temperature, the shapes of the PDFs are similar for $1.0\% \leq \alpha \leq 4.7\%$.

Next, the small-scale statistics were investigated for $\alpha = 0\%$ and 4.7%. For $\alpha = 4.7\%$, The PDFs of the standardised temperature increments at small-scale were shown to have larger tails, signifying the enhanced intermittency due to the presence of rising bubbles. The scaling properties of the temperature structure functions (of the *absolute* value of the temperature increments) were investigated using extended self-similarity (ESS) analysis, in which the p-th order structure function were plotted against the second order structure

function. $\beta(p,2)$, up to $p = 5$, shows only marginal increase when bubbles are injected. Our results were also compared with other physical systems. Our $\beta(p,2)$ resembles those found in boiling Rayleigh-Bénard convection [107], but are significantly higher than all of the other single-phase scalar turbulence systems summarised in Ref. [142]. The fundamental reason of such high relative exponents is to be further investigated. Thus, while the rising bubbles enhanced intermittency by enhancing the mixing of the small-scale, small-amplitude fluctuations (leaving only the large, rapid change of temperature), the relative exponents of the temperature structure functions have only marginal increase when compared to the single phase case.

Our integral-statistics lack the investigation of turbulent heat flux. Therefore, future research should include the systematic investigation of the effective diffusivity of temperature (i.e. to measure the turbulent heat flux and the mean temperature gradient) for different turbulent bubbly flow conditions (different α, bubble sizes, and incident turbulent intensities).

Conclusions

The mixing of scalar fields in bubbly flows are omnipresent in nature and industry. Examples of scalars are the temperature field and the concentration field of micro-particles. In this thesis, to improve our understanding of the mixing mechanisms, we investigated the mixing of temperature in inhomogeneous bubbly flows (Chapter 2), then, with the Twente Mass and Heat Transfer Tunnel (Chapter 3), the mixing in turbulent bubbly flows were also studied (Chapter 4–5).

In Chapter 2, the mixing of the temperature in inhomogeneous bubbly flows was studied. Such flows have three mixing mechanisms, namely bubble-induced agitations (BIA), shear-induced turbulence (SIT) and the transport due to buoyancy-driven large-scale circulation. The interactions between these three mixing mechanisms were investigated by studying the heat transport in inhomogeneous bubbly flows. We measured the heat transport from one vertical hot wall to another cold wall in a rectangular bubble column with millimetric bubbles injected from half of the injection section (near the hot or near the cold wall, see Fig. 2.1, page 35). The Rayleigh number, Ra_H (Eq. 2.1, page 33), was changed from 4.9×10^9 to 2.2×10^{10} and the gas volume fraction α, ranged from 0.4% to 5.1%. A shear-layer was formed between the bubbly column and the other half of the cell which had no injection of bubbles. Moreover, the inhomogeneity of bubbles lead to a large-scale buoyancy-driven flow. First, we found that $\overline{Nu}$, the dimensionless heat transfer rate, is independent of Ra_H and depends only on α, which is the same case for homogeneous bubbly flows, see Fig. 2.5 in page 40. Different mixing regimes were identified. For $\alpha < 4\%$, we found a heat enhancement as compared to the homogeneous bubbly flow case because of the induced shear layer and large-scale recirculation. For $\alpha < 1.4\%$, the empirical power law of the heat transfer as a function of α is similar to that of the homogeneous bubbly flow case, and $\overline{Nu}$ is higher for the bubbles injected near the hot wall. When α increases further, there are more bubbles migrated to the non-injection side, leading to no preferred $\overline{Nu}$ enhancement near the hot wall or cold wall. Moreover, the shear-induced tur-

bulence and large-scale circulation start to compete with BIA. When $\alpha > 4\%$, the bubble column becomes more unstable and SIT is too strong, so does the competition between the three contributions. In this case, the homogeneous injection is more efficient, see Fig. 2.6 in page 41.

To investigate the mixing of scalar fields in turbulent bubbly flows, the Twente Mass and Heat Transfer Tunnel (TMHT) was built (Chapter 3). In this chapter, we demonstrated that, by using TMHT, heat and mass transfer measurements can be performed in a controlled manner. With the optical access through the glass at the measurement section (Fig. 3.2, page 60), laser Doppler anemometry (LDA), particle image velocimetry, particle tracking velocimetry, and laser-induced fluorescence (LIF) imaging can be applied. Temperature measurements with millimetric Kelvin accuracy at different locations can be performed by mounting thermistor(s) on a built-in traverse system at the top of the measurement section, see Fig. 5.1 in page 100. Local heat flux measurements were also performed by simultaneous measurements of the velocity (measured by LDA) and the temperature (measured by a thermistor), see Fig. 3.13 in page 73. Preliminary measurements on LIF (Fig. 3.3.4 in page 75) and the effect of salt on the bubble sizes (Fig. 3.15–3.16, page 77–78) in turbulent bubbly flows were performed.

In Chapter 4, the spectral properties of temperature fluctuations in a turbulent bubbly thermal mixing layer ($0\% \leq \alpha \leq 5.2\%$) were revealed. The development of the -3 scaling is triggered by the rising bubbles. The classical -5/3 scaling is followed by a steeper slope and becomes steeper for increasing α, see Fig. 4.1b in page 86. The slope saturates to -3 when α is large enough. For the velocity fluctuation spectra (energy spectra), similar to other turbulent bubbly flows studies [30, 46], the spectra abruptly develop a -3 scaling for $\alpha \neq 0$ and show enhancement of the small-scale content. In contrast to the energy spectra, when α increases, the thermal spectra gradually changes its slope by diminishing the small-scale content. Moreover, the -3 scaling for the energy and the thermal spectra occurs at different frequency ranges. The former is at $\mathcal{O}(100\text{Hz})$ while the latter is at $\mathcal{O}(10\text{Hz})$. The physical mechanism of the steeper spectral slope in the thermal spectra is speculated to be due to the enhanced mixing of bubbles which enhances the homogenization of small-scale temperature differences. The scaling saturates to -3 when the homogenization is too strong such that the local net transfer of the spectral fluctuation is directly dissipated by molecular diffusivity.

In Chapter 5, we further investigated the effect of rising bubbles on the integral statistics and small-scale statistics of a turbulent bubbly mixing layer

for $0\% \leq \alpha \leq 4.7\%$. The integral statistics includes the global mean profile, the variance and the probability density functions (PDF) of the velocity and temperature, while the small-scale statistics involves the statistics of temperature increments. For the integral-scale statistics, as opposed to the velocity variance which increases with increasing α, there is no increase for temperature variance, see Fig. 5.5 in page 112. It is due to the difference between the sources of the temperature fluctuations and the velocity fluctuations in bubbly flows. There are liquid agitations from the momentum transported to the liquid from the viscous boundary layers at the air-water interface of the bubbles. In contrast, there are no thermal boundary layers at the air-water interface, and the source of the temperature fluctuations includes the coupling of the mean temperature gradient and the turbulent heat flux (Eq. 5.3) which both are not strictly increasing functions of α (see Sec. 5.3.2). Furthermore, we obtained well-resolved velocity PDFs, showing exponential decays for both the vertical u_z and horizontal velocity u_x PDFs, which are the signatures of BIA [7] (except showing a second peak in each u_z PDF for $\alpha \neq 0$), see Fig. 5.6 in page 116. For the temperature PDFs, the rising bubbles promote more extreme values of the temperature fluctuations when normalised by the temperature variance, leading to practical considerations on any reaction. Next, for the small-scale statistics, we focused on the cases $\alpha = 0\%$ and 4.7%. With bubbles, the tails of the PDFs are larger for the temperature increments (Fig. 5.7 in page 121). The kurtosis of the temperature increments is larger when rising bubbles are present (see Fig. 5.9 in 123), implying that the rising bubbles enhance intermittency. The enhanced intermittency is due to the mixing of the bubbles which smoothen the small-scale, small-amplitude fluctuations, leaving only the large, rapid change of temperature fluctuations. Moreover, the scaling properties of the moments of the absolute values of the temperature increments (denoted as R_p^*, where p is the order of the moment) were investigated by extended self-similarity (ESS) [109]. This analysis was performed by investigating the scaling behavior of R_p^* versus R_2^*, in which the exponent was denoted by $\beta(p, 2)$, see Fig. 5.13 in page 128. Up to order $p = 5$, $\beta(p, 2)$ for $\alpha = 0\%$ resembles that for $\alpha = 4.7\%$. We compare our $\beta(p, 2)$ with other scalar turbulence systems. It is found that $\beta(p, 2)$ in boiling Rayleigh-Bénard convection [107] were similar to ours, but all of the other single-phase scalar turbulence systems summarised in Ref. [142] are significantly lower than our $\beta(p, 2)$.

Bibliography

[1] P. W. Anderson, "Science: A 'Dappled World' or a 'Seamless Web'?", Studies in History and Philosophy of Science Part B: Studies in History and Philosophy of Modern Physics **32**, 487–494 (2001).

[2] A. S. Monin and A. Yaglom, *Statistical Fluid Mechanics* (The MIT Press, Cambridge, MA) (1975).

[3] S. Balachandar and J. K. Eaton, "Turbulent Dispersed Multiphase Flow", Annual Review of Fluid Mechanics **42**, 111 133 (2010).

[4] E. Villermaux, "Mixing Versus Stirring", Annual Review of Fluid Mechanics **51** (2019).

[5] R. B. Bird, W. E. Stewart, and E. N. Lightfoot, *Transport Phenomena, Revised Second Edition* (John Wiley Sons, Inc.) (2007).

[6] K. R. Sreenivasan, "Turbulent mixing: A perspective", Proceedings of the National Academy of Sciences 201800463 (2018).

[7] F. Risso, "Agitation, Mixing, and Transfers Induced by Bubbles", Annual Review of Fluid Mechanics **50**, 1–24 (2017).

[8] E. Climent and J. Magnaudet, "Large-Scale Simulations of Bubble-Induced Convection in a Liquid Layer", Physical Review Letters **82**, 4827 4830 (1999).

[9] S. B. Pope, *Turbulent Flows* (Cambridge University Press, Cambridge, England) (2000).

[10] P. Davidson, *Turbulence, An Introduction for Scientists and Engineers, 2nd edition* (Oxford University Press, Oxford) (2015).

[11] F. T. M. Nieuwstadt, B. J. Boersma, and J. Westerweel, *Turbulence, Introduction to Theory and Applications of Turbulent Flows* (Springer International Publishing, Switzerland) (2016).

[12] T. Yasuda, T. Gotoh, T. Watanabe, and I. Saito, "Péclet-number dependence of small-scale anisotropy of passive scalar fluctuations under a uniform mean gradient in isotropic turbulence", Journal of Fluid Mechanics **898**, A4 (2020).

[13] A. N. Kolmogorov, Dokl. Akad. Nauk. SSSR **30**, 301 (1941).

[14] A. M. Obukhov, Izv. Akad. Nauk. SSSR, Geogr. Geofiz. **13**, 58–69 (1949).

[15] S. Corrsin, "On the Spectrum of Isotropic Temperature Fluctuations in an Isotropic Turbulence", Journal of Applied Physics **22**, 469–473 (1951).

[16] M. Bourgoin, "Turbulent pair dispersion as a ballistic cascade phenomenology", Journal of Fluid Mechanics **772**, 678–704 (2015).

[17] G. H. Socolofsky, S.A. Jirka, *CVEN 489-501: Special Topics in Mixing and Transport Processes in the Environment* (Texas AM University) (2005).

[18] G. I. Taylor, "Diffusion by Continuous Movements", Proceedings of the London Mathematical Society **s2-20**, 196–212 (1922).

[19] H. Tennekes and J. L. Lumley, *A First Course in Turbulence* (The MIT Press, Cambridge, Massachusetts, and London, England) (1972).

[20] D. P. Combest, P. A. Ramachandran, and M. P. Dudukovic, "On the Gradient Diffusion Hypothesis and Passive Scalar Transport in Turbulent Flows", Industrial & Engineering Chemistry Research **50**, 8817–8823 (2011).

[21] M. Lance and J. Bataille, "Turbulence in the liquid phase of a uniform bubbly air–water flow", Journal of Fluid Mechanics **222**, 95–118 (1991).

[22] E. Bouche, V. Roig, F. Risso, and A.-M. Billet, "Homogeneous swarm of high-Reynolds-number bubbles rising within a thin gap. Part 2. Liquid dynamics", Journal of Fluid Mechanics **758**, 508–521 (2014).

[23] J. Mercado Martínez, D. Chehata Gómez, D. van Gils, C. Sun, and D. Lohse, "On bubble clustering and energy spectra in pseudo-turbulence", Journal of Fluid Mechanics **650**, 287–306 (2010).

[24] G. Riboux, D. Legendre, and F. Risso, "A model of bubble-induced turbulence based on large-scale wake interactions", Journal of Fluid Mechanics **719**, 362–387 (2013).

[25] I. M. Mazzitelli and D. Lohse, "Evolution of energy in flow driven by rising bubbles", Physical Review E **79**, 066317 (2009).

[26] Z. Amoura, C. Besnaci, F. Risso, and V. Roig, "Velocity fluctuations generated by the flow through a random array of spheres: a model of bubble-induced agitation", Journal of Fluid Mechanics **823**, 592 616 (2017).

[27] G. Riboux, F. Risso, and D. Legendre, "Experimental characterization of the agitation generated by bubbles rising at high Reynolds number", Journal of Fluid Mechanics **643**, 509–539 (2010).

[28] F. Risso, V. Roig, Z. Amoura, G. Riboux, and A.-M. Billet, "Wake attenuation in large Reynolds number dispersed two-phase flows", Philosophical Transactions of the Royal Society A: Mathematical, Physical and Engineering Sciences **366**, 2177–2190 (2008).

[29] P. K. Kundu, I. M. Cohen, and D. R. Dowling, *Fluid Mechanics, Sixth Edition* (Academic Press, Elsevier Inc.) (2016).

[30] E. Alméras, V. Mathai, D. Lohse, and C. Sun, "Experimental investigation of the turbulence induced by a bubble swarm rising within incident turbulence", Journal of Fluid Mechanics **825**, 1091–1112 (2017).

[31] M. Sathe, J. Joshi, and G. Evans, "Characterization of turbulence in rectangular bubble column", Chemical Engineering Science **100**, 52–68 (2013).

[32] J. Rensen, S. Luther, and D. Lohse, "The effect of bubbles on developed turbulence", Journal of Fluid Mechanics **538**, 153–187 (2005).

[33] E. Bouche, S. Cazin, V. Roig, and F. Risso, "Mixing in a swarm of bubbles rising in a confined cell measured by mean of PLIF with two different dyes", Experiments in Fluids **54**, 1552 (2013).

[34] E. Alméras, F. Risso, V. Roig, C. Plais, and F. Augier, "Mixing mechanism in a two-dimensional bubble column", Physical Review Fluids **3**, 074307 (2018).

[35] E. Alméras, F. Risso, V. Roig, S. Cazin, C. Plais, and F. Augier, "Mixing by bubble-induced turbulence", Journal of Fluid Mechanics **776**, 458–474 (2015).

[36] S. Corrsin, "Estimates of the Relations between Eulerian and Lagrangian Scales in Large Reynolds Number Turbulence", Journal of the Atmospheric Sciences **20**, 115–119 (1963).

[37] B. Gvozdić, E. Alméras, V. Mathai, X. Zhu, D. P. M. v. Gils, R. Verzicco, S. G. Huisman, C. Sun, and D. Lohse, "Experimental investigation of heat transport in homogeneous bubbly flow", Journal of Fluid Mechanics **845**, 226–244 (2018).

[38] H. Schlichting and K. Gersten, *Boundary-layer theory* (Springer-Verlag, Berlin, Heidelberg) (2017).

[39] G. Ahlers, S. Grossmann, and D. Lohse, "Heat transfer and large scale dynamics in turbulent Rayleigh-Bénard convection", Reviews of Modern Physics **81**, 503–537 (2009).

[40] A. Loisy, A. Naso, and P. D. M. Spelt, "The effective diffusivity of ordered and freely evolving bubbly suspensions", Journal of Fluid Mechanics **840**, 215 237 (2018).

[41] E. Alméras, S. Cazin, V. Roig, F. Risso, F. Augier, and C. Plais, "Time-resolved measurement of concentration fluctuations in a confined bubbly flow by LIF", International Journal of Multiphase Flow **83**, 153–161 (2016).

[42] F. Risso, "Theoretical model for k^{-3} spectra in dispersed multiphase flows", Physics of Fluids **23**, 011701 (2011).

[43] E. Alméras, C. Plais, F. Euzenat, F. Risso, V. Roig, and F. Augier, "Scalar mixing in bubbly flows: Experimental investigation and diffusivity modelling", Chemical Engineering Science **140**, 114–122 (2016).

[44] E. Alméras, C. Plais, V. Roig, F. Risso, and F. Augier, "Mixing mechanisms in a low-sheared inhomogeneous bubble column", Chemical Engineering Science **186**, 52–61 (2018).

[45] B. Gvozdić, O.-Y. Dung, E. Alméras, D. P. M. van Gils, D. Lohse, S. G. Huisman, and C. Sun, "Experimental investigation of heat transport in

inhomogeneous bubbly flow", Chemical Engineering Science **198**, 260–267 (2019).

[46] V. N. Prakash, J. M. Mercado, L. van Wijngaarden, E. Mancilla, Y. Tagawa, D. Lohse, and C. Sun, "Energy spectra in turbulent bubbly flows", Journal of Fluid Mechanics **791**, 174–190 (2016).

[47] L. van Wijngaarden, "On Pseudo Turbulence", Theoretical and Computational Fluid Dynamics **10**, 449–458 (1998).

[48] E. Alméras, V. Mathai, C. Sun, and D. Lohse, "Mixing induced by a bubble swarm rising through incident turbulence", International Journal of Multiphase Flow **114**, 316–322 (2019).

[49] A. Kitagawa, K. Kosuge, K. Uchida, and Y. Hagiwara, "Heat transfer enhancement for laminar natural convection along a vertical plate due to sub-millimeter-bubble injection", Experiments in Fluids **45**, 473–484 (2008).

[50] A. Kitagawa, K. Uchida, and Y. Hagiwara, "Effects of bubble size on heat transfer enhancement by sub-millimeter bubbles for laminar natural convection along a vertical plate", International Journal of Heat and Fluid Flow **30**, 778–788 (2009).

[51] K. Sekoguchi, M. Nakazatomi, and O. Tanaka, "Forced convective heat transfer in vertical air-water bubble flow", Bulletin of JSME **23**, 1625–1631 (1980).

[52] Y. Sato, M. Sadatomi, and K. Sekoguchi, "Momentum and heat transfer in two-phase bubble flow—I. Theory", International Journal of Multiphase Flow **7**, 167–177 (1981).

[53] Y. Sato, M. Sadatomi, and K. Sekoguchi, "Momentum and heat transfer in two-phase bubble flow—II. A comparison between experimental data and theoretical calculations", International Journal of Multiphase Flow **7**, 179–190 (1981).

[54] S. Dabiri and G. Tryggvason, "Heat transfer in turbulent bubbly flow in vertical channels", Chemical Engineering Science **122**, 106–113 (2015).

[55] A. Kitagawa and Y. Murai, "Natural convection heat transfer from a vertical heated plate in water with microbubble injection", Chemical Engineering Science **99**, 215–224 (2013).

[56] A. T. Tokuhiro and P. S. Lykoudis, "Natural convection heat transfer from a vertical plate—i. Enhancement with gas injection", International Journal of Heat and Mass Transfer **37**, 997–1003 (1994).

[57] N. G. Deen and J. A. M. Kuipers, "Direct numerical simulation of wall-to liquid heat transfer in dispersed gas-liquid two-phase flow using a volume of fluid approach", Chemical Engineering Science **102**, 268–282 (2013).

[58] F. Risso and K. Ellingsen, "Velocity fluctuations in a homogeneous dilute dispersion of high-Reynolds-number rising bubbles", Journal of Fluid Mechanics **453**, 395–410 (2002).

[59] I. Roghair, J. Martinez Mercado, M. van Sint Annaland, H. Kuipers, C. Sun, and D. Lohse, "Energy spectra and bubble velocity distributions in pseudo-turbulence: Numerical simulations vs. experiments", International Journal of Multiphase Flow **37**, 1093–1098 (2011).

[60] J. W. Elder, "Turbulent free convection in a vertical slot", Journal of Fluid Mechanics **23**, 99–111 (1965).

[61] N. C. Markatos and K. A. Pericleous, "Laminar and turbulent natural convection in an enclosed cavity", International Journal of Heat and Mass Transfer **27**, 755–772 (1984).

[62] S. Kimura and A. Bejan, "The boundary layer natural convection regime in a rectangular cavity with uniform heat flux from the side", Journal of Heat Transfer **106**, 98–103 (1984).

[63] A. Belmonte, A. Tilgner, and A. Libchaber, "Temperature and velocity boundary layers in turbulent convection", Physical Review E **50**, 269 (1994).

[64] C. S. Ng, A. Ooi, D. Lohse, and D. Chung, "Vertical natural convection: application of the unifying theory of thermal convection", Journal of Fluid Mechanics **764**, 349–361 (2015).

[65] O. Shishkina and S. Horn, "Thermal convection in inclined cylindrical containers", Journal of Fluid Mechanics **790**, R3 (2016).

[66] C. S. Ng, A. Ooi, D. Lohse, and D. Chung, "Changes in the boundary-layer structure at the edge of the ultimate regime in vertical natural convection", Journal of Fluid Mechanics **825**, 550–572 (2017).

[67] D. Lohse and K.-Q. Xia, "Small-scale properties of turbulent Rayleigh-Bénard convection", Annual Review of Fluid Mechanics **42**, 335–364 (2010).

[68] V. Roig, C. Suzanne, and L. Masbernat, "Experimental investigation of a turbulent bubbly mixing layer", International Journal of Multiphase Flow **24**, 35–54 (1998).

[69] A. Cartellier, "Optical probes for local void fraction measurements: characterization of performance", Review of Scientific Instruments **61**, 874–886 (1990).

[70] R. F. Mudde, J. S. Groen, and H. E. A. van den Akker, "Liquid velocity field in a bubble column: LDA experiments", Chemical Engineering Science **52**, 4217–4224 (1997).

[71] J. S. Groen, R. F. Mudde, and H. E. A. van den Akker, "On the application of LDA to bubbly flow in the wobbling regime", Experiments in Fluids **27**, 435–449 (1999).

[72] C. Vial, R. Laine, S. Poncin, N. Midoux, and G. Wild, "Influence of gas distribution and regime transitions on liquid velocity and turbulence in a 3–D bubble column", Chemical Engineering Science **56**, 1085–1093 (2001).

[73] R. F. Mudde, "Gravity-driven bubbly flows", Annual Review of Fluid Mechanics **37**, 393–423 (2005).

[74] N. Deen, R. Mudde, J. Kuipers, P. Zehner, and M. Kraume, "Bubble columns", Ullmann's Encyclopedia of Industrial Chemistry (2010).

[75] D. Darmana, N. G. Deen, and J. A. M. Kuipers, "Detailed 3d modeling of mass transfer processes in two-phase flows with dynamic interfaces", Chemical Engineering Technology **29**, 1027–1033 (2006).

[76] D. Jain, Y. M. Lau, J. Kuipers, and N. G. Deen, "Discrete bubble modeling for a micro-structured bubble column", Chemical Engineering Science **100**, 496 – 505 (2013), 11th International Conference on Gas-Liquid and Gas-Liquid-Solid Reactor Engineering.

[77] G. Besagni, F. Inzoli, and T. Ziegenhein, "Two-phase bubble columns: A comprehensive review", ChemEngineering **2** (2018).

[78] W.-D. Deckwer, "On the mechanism of heat transfer in bubble column reactors", Chemical Engineering Science **35**, 1341 – 1346 (1980).

[79] J. Heijnen and K. V. Riet, "Mass transfer, mixing and heat transfer phenomena in low viscosity bubble column reactors", The Chemical Engineering Journal **28**, B21 – B42 (1984).

[80] A. A. Kulkarni, "Mass transfer in bubble column reactors: Effect of bubble size distribution", Industrial Engineering Chemistry Research **46**, 2205–2211 (2007).

[81] D. Colombet, D. Legendre, F. Risso, A. Cockx, and P. Guiraud, "Dynamics and mass transfer of rising bubbles in a homogenous swarm at large gas volume fraction", Journal of Fluid Mechanics **763**, 254–285 (2015).

[82] H. Ayed, J. Chahed, and V. Roig, "Hydrodynamics and mass transfer in a turbulent buoyant bubbly shear layer", AIChE journal **53**, 2742–2753 (2007).

[83] A. Kitagawa, K. Kimura, and Y. Hagiwara, "Experimental investigation of water laminar mixed-convection flow with sub-millimeter bubbles in a vertical channel", Experiments in Fluids **48**, 509–519 (2010).

[84] P. T. Nguyen, M. A. Hampton, A. V. Nguyen, and G. R. Birkett, "The influence of gas velocity, salt type and concentration on transition concentration for bubble coalescence inhibition and gas holdup", Chemical Engineering Research and Design **90**, 33–39 (2012).

[85] D. P. M. van Gils, D. Narezo Guzman, C. Sun, and D. Lohse, "The importance of bubble deformability for strong drag reduction in bubbly turbulent Taylor–Couette flow", Journal of Fluid Mechanics **722**, 317–347 (2013).

[86] R. Poorte and A. Biesheuvel, "Experiments on the motion of gas bubbles in turbulence generated by an active grid", Journal of Fluid Mechanics **461**, 127 (2002).

[87] D. P. M. van Gils, University of Twente, "Python library for (multithreaded) communication with laboratory instruments", `https://github.com/Dennis-van-Gils` (2018).

[88] R. Poorte, "On the motion of bubbles in active grid generated turbulent flows", Ph.D. thesis (1998).

[89] P. W. Anderson, "More Is Different", Science **177**, 393–396 (1972).

[90] V. Mathai, D. Lohse, and C. Sun, "Bubbly and Buoyant Particle–Laden Turbulent Flows", Annual Review of Condensed Matter Physics **11**, 529–559 (2020).

[91] V. Pandey, R. Ramadugu, and P. Perlekar, "Liquid velocity fluctuations and energy spectra in three-dimensional buoyancy-driven bubbly flows", Journal of Fluid Mechanics **884**, R6 (2020).

[92] B. Gvozdić, O.-Y. Dung, D. P. M. v. Gils, G.-W. H. Bruggert, E. Alméras, C. Sun, D. Lohse, and S. G. Huisman, "Twente mass and heat transfer water tunnel: Temperature controlled turbulent multiphase channel flow with heat and mass transfer", Review of Scientific Instruments **90**, 075117 (2019).

[93] S. M. de Bruyn Kops and J. J. Riley, "Re-examining the thermal mixing layer with numerical simulations", Physics of Fluids **12**, 185–192 (2000).

[94] J. S. Steinhart and S. R. Hart, "Calibration curves for thermistors", Deep Sea Research and Oceanographic Abstracts **15**, 497–503 (1968).

[95] L. Mydlarski and Z. Warhaft, "Passive scalar statistics in high-Péclet-number grid turbulence", Journal of Fluid Mechanics **358**, 135–175 (1998).

[96] Jayesh, C. Tong, and Z. Warhaft, "On temperature spectra in grid turbulence", Physics of Fluids **6**, 306–312 (1994).

[97] G. K. Batchelor, "Pressure fluctuations in isotropic turbulence", Proceedings of the Cambridge Philosophical Society **47**, 359–374 (1951).

[98] H. H. Bruun, *Hot Wire Anemometry: Principles and Signal Analysis* (Oxford University Press) (1995).

[99] A. V. Oppenheim and R. W. Schafer, *Discrete-Time Signal Processing, Third Edition* (Prentice Hall Press, Upper Saddle River, NJ) (2009).

[100] D. Sturgeon, "Liji: Da xue - chinese text project", URL `https://ctext.org/liji/da-xue`.

[101] Z. Warhaft, "Passive Scalars in Turbulent Flows", Annual Review of Fluid Mechanics **32**, 203–240 (2000).

[102] A. Panda, Y. Weitkamp, A. Rajkotwala, E. Peters, M. Baltussen, and J. Kuipers, "Influence of Gas Fraction on Wall-to-Liquid Heat Transfer in Dense Bubbly Flows", Chemical Engineering Science: X **4**, 100037 (2019).

[103] C. S. Ng, V. Spandan, R. Verzicco, and D. Lohse, "Non-monotonic transport mechanisms in vertical natural convection with dispersed light droplets", Journal of Fluid Mechanics **900**, A34 (2020).

[104] J. C. Hill, "Homogeneous Turbulent Mixing with Chemical Reaction", Annual Review of Fluid Mechanics 1–27 (1976).

[105] S. Pope, "PDF methods for turbulent reactive flows", Progress in Energy and Combustion Science **11**, 119–192 (1985).

[106] M. Ferchichi and S. Tavoularis, "Scalar probability density function and fine structure in uniformly sheared turbulence", Journal of Fluid Mechanics **461**, 155–182 (2002).

[107] R. Lakkaraju, F. Toschi, and D. Lohse, "Bubbling reduces intermittency in turbulent thermal convection", Journal of Fluid Mechanics **745**, 1–24 (2014).

[108] L. Biferale, P. Perlekar, M. Sbragaglia, and F. Toschi, "Convection in Multiphase Fluid Flows Using Lattice Boltzmann Methods", Physical Review Letters **108**, 104502 (2012).

[109] R. Benzi, S. Ciliberto, R. Tripiccione, C. Baudet, F. Massaioli, and S. Succi, "Extended self-similarity in turbulent flows", Physical Review E **48**, R29–R32 (1993).

[110] W. E. Watt and W. D. Bainis, "The Turbulent Mixing Temperature Mixing Layer", Journal of Hydraulic Research **11**, 157–166 (1973).

[111] K. Bremhorst and D. B. Gilmore, "Response of hot wire anemometer probes to a stream of air bubbles in a water flow", Journal of Physics E: Scientific Instruments **9**, 347 (1975).

[112] P. C. Valente and J. C. Vassilicos, "Universal Dissipation Scaling for Nonequilibrium Turbulence", Physical Review Letters **108**, 214503 (2012).

[113] J. C. Vassilicos, "Dissipation in Turbulent Flows", Annual Review of Fluid Mechanics **47**, 1–20 (2015).

[114] P. A. Libby, "Diffusion of heat downstream of a turbulence grid", Acta Astronautica **2**, 867–878 (1975).

[115] J. C. LaRue and P. A. Libby, "Thermal mixing layer downstream of half-heated turbulence grid", Physics of Fluids **24**, 597 (1981).

[116] J. C. LaRue, "Further results on the thermal mixing layer downstream of a turbulence grid", Physics of Fluids **24**, 1927 (1981).

[117] B.-K. Ma and Z. Warhaft, "Some aspects of the thermal mixing layer in grid turbulence", Physics of Fluids **29**, 3114 (1986).

[118] V. Roig and A. Larue de Tournemine, "Measurement of interstitial velocity of homogeneous bubbly flows at low to moderate void fraction", Journal of Fluid Mechanics **572**, 87 110 (2007).

[119] C. Morel, *Mathematical Modeling of Dispersed Two-Phase Flows* (Springer) (2015).

[120] J. L. Lumley, "Evolution of a non-self-preserving thermal mixing layer", Physics of Fluids **29**, 3976 (1986).

[121] S. M. de Bruyn Kops and M. Mortensen, "Conditional mixing statistics in a self-similar scalar mixing layer", Physics of Fluids **17**, 095107 (2005).

[122] Jayesh and Z. Warhaft, "Probability distribution of a passive scalar in grid-generated turbulence", Physical Review Letters **67**, 3503 (1991).

[123] Jayesh and Z. Warhaft, "Probability distribution, conditional dissipation, and transport of passive temperature fluctuations in grid-generated turbulence", Physics of Fluids A: Fluid Dynamics **4**, 2292–2307 (1992).

[124] A. Bourlioux and A. J. Majda, "Elementary models with probability distribution function intermittency for passive scalars with a mean gradient", Physics of Fluids **14**, 881–897 (2002).

[125] K. R. Sreenivasan and R. A. Antonia, "The phenomenology of small-scale turbulence", Annual Review of Fluid Mechanics **29**, 435 472 (1997).

[126] U. Frisch, *Turbulence* (Cambridge University Press, Cambridge) (1995).

[127] G. Falkovich and K. R. Sreenivasan, "Lessons from hydrodynamic turbulence", Physics Today **59**, 43–49 (2006).

[128] B. I. Shraiman and E. D. Siggia, "Scalar turbulence", Nature **405**, 639 (2000).

[129] F. Anselmet, Y. Gagne, E. J. Hopfinger, and R. A. Antonia, "High-order velocity structure functions in turbulent shear flows", Journal of Fluid Mechanics **140**, 63 89 (1984).

[130] S. Grossmann, D. Lohse, and A. Reeh, "Application of extended self-similarity in turbulence", Physical Review E **56**, 5473 (1997).

[131] R. Budwig, S. Tavoularis, and S. Corrsin, "Temperature fluctuations and heat flux in grid-generated isotropic turbulence with streamwise and transverse mean-temperature gradients", Journal of Fluid Mechanics **153**, 441–460 (1985).

[132] C. Tong and Z. Warhaft, "On passive scalar derivative statistics in grid turbulence", Physics of Fluids **6**, 2165–2176 (1994).

[133] G. Ruiz-Chavarria, C. Baudet, and S. Ciliberto, "Extended Self-Similarity of Passive Scalars in Fully Developed Turbulence", Europhysics Letters (EPL) **32**, 319–324 (1995).

[134] G. Stolovitzky and K. R. Sreenivasan, "Scaling of structure functions", Physical Review E **48**, R33–R36 (1993).

[135] F. Belin, P. Tabeling, and H. Willaime, "Exponents of the structure functions in a low temperature helium experiment", Physica D: Nonlinear Phenomena **93**, 52–63 (1996).

[136] E. Leveque and Z.-S. She, "Cascade structures and scaling exponents in a dynamical model of turbulence: Measurements and comparison", Physical Review E **55**, 2789–2799 (1997).

[137] N. Cao, S. Chen, and Z.-S. She, "Scalings and Relative Scalings in the Navier-Stokes Turbulence", Physical Review Letters **76**, 3711–3714 (1996).

[138] A. Attili and F. Bisetti, "Fluctuations of a passive scalar in a turbulent mixing layer", Physical Review E **88**, 033013 (2013).

[139] I. Arad, L. Biferale, I. Mazzitelli, and I. Procaccia, "Disentangling Scaling Properties in Anisotropic and Inhomogeneous Turbulence", Physical Review Letters **82**, 5040–5043 (1999).

[140] F. Toschi, G. Amati, S. Succi, R. Benzi, and R. Piva, "Intermittency and Structure Functions in Channel Flow Turbulence", Physical Review Letters **82**, 5044–5047 (1999).

[141] V. Carbone, L. Sorriso-Valvo, E. Martines, V. Antoni, and P. Veltri, "Intermittency and turbulence in a magnetically confined fusion plasma", Physical Review E **62**, R49–R52 (2000).

[142] A. Gylfason and Z. Warhaft, "On higher order passive scalar structure functions in grid turbulence", Physics of Fluids **16**, 4012–4019 (2004).

[143] R. Benzi, L. Biferale, S. Ciliberto, M. V. Struglia, and R. Tripiccione, "Generalized scaling in fully developed turbulence", Physica D: Nonlinear Phenomena **96**, 162–181 (1996).

[144] Z.-S. She and E. Leveque, "Universal scaling laws in fully developed turbulence", Physical Review Letters **72**, 336–339 (1993).

[145] G. Ruiz-Chavarria, C. Baudet, and S. Ciliberto, "Scaling laws and dissipation scale of a passive scalar in fully developed turbulence", Physica D: Nonlinear Phenomena **99**, 369 380 (1996).

[146] S. Chen and R. H. Kraichnan, "Simulations of a randomly advected passive scalar field", Physics of Fluids **10**, 2867–2884 (1998).

[147] C. Sun, Q. Zhou, and K.-Q. Xia, "Cascades of Velocity and Temperature Fluctuations in Buoyancy-Driven Thermal Turbulence", Physical Review Letters **97**, 144504 (2006).

Summary

The mixing of temperature and substances in dispersed gas-liquid turbulent flows is common in nature and in industries. Large-scale chemical reactors contain chemical reactants (microparticles) mixing in a turbulent environment and heat may be released because of the chemical reactions. To enhance the mixing of heat and reactants, commonly rising bubbles are injected. To understand the physics of the mixing in turbulent bubbly flows, this thesis studied the temperature statistics and heat transport in swarms of rising bubble in a flow with and without incident turbulence.

For a general high-Reynolds bubbly flow without incident turbulence, there are three mixing mechanisms, namely bubble-induced agitations (BIA, from the velocity flucutations induced by bubbles), shear-induced turbulence (SIT, from the velocity flucutations induced due to the nonlinearity in the carrier phase) and the transport due to buoyancy driven recirculation (due to the inhomogeneity of bubble distributions). The heat transport in an inhomogeneous bubbly flow was first studied in Chapter 2. We measured the heat transport from one vertical hot wall to another cold wall in a rectangular bubble column with millimetric bubbles injected from half of the injection section (near the hot or near the cold wall). The Rayleigh number, Ra_H, ranges from 4.9×10^9 to 2.2×10^{10} and the gas volume fraction α, ranges from 0.4% to 5.1%. A shear-layer was formed between the bubbly column and the other half of the cell which had no injection of bubbles. Moreover, the inhomogeneity of bubbles lead to a large-scale buoyancy-driven flow. Different mixing regimes were identified. For $\alpha < 4\%$, there is a heat enhancement as compared to the homogeneous bubbly flow case because of the induced shear-layer and large-scale recirculation. When α increases, SIT and large-scale circulation start to compete with BIA. When $\alpha > 4\%$, the competition between the three contributions is enhanced because the effect of SIT becomes stronger. In this case, the homogeneous injection is more efficient.

To study the effect of incident turbulence, the Twente Mass and Heat Transfer Tunnel (TMHT) was built (Chapter 3). It was demonstrated that temperature

and mass transfer measurements in turbulent bubbly flows are possible in a controlled manner. Measurements on the velocity flow profile, local heat flux at the middle of the tunnel in a single-phase turbulent thermal mixing layer, the spread of a fluorescent dye in a turbulent bubbly flow and the effect of salt concentration on the bubble sizes were reported in Chapter 3.

By using the TMHT, the temperature statistics in a turbulent bubbly thermal mixing layer was studied. Chapter 4 focused on the spectral properties of the temperature fluctuations. The mean liquid speed was fixed at 0.5 m/s and the range $0\% \leq \alpha \leq 5.2\%$ was studied. The Kolmogorov -5/3 law in the temperature frequency spectra was followed by a steeper spectral slope when α increases. It saturated to a -3 scaling when α is large enough. The -3 power law was proposed to be attributed to the enhanced mixing due to bubbles and that the local net spectral transfer of the temperature fluctuations was directly dissipated by diffusivity. We identified the transition frequency f_d from -5/3 to -3 scaling by using a Batchelor type parametrisation.

Chapter 5 continued to study the turbulent bubbly mixing layer by investigating the integral statistics such as the global mean profile, the variance and the probability density functions (pdfs) of the temperature and velocity for $0\% \leq \alpha \leq 4.7\%$. We found that, as opposed to the velocity variance which increases with increasing α, the temperature variance does not increase. This is because the source of temperature fluctuations includes the coupling of the turbulent heat flux and the mean temperature gradient which are both not strictly increasing functions of α. Moreover, from the standardised temperature pdfs, we found that rising bubbles promotes more extreme values of the temperature fluctuation when normalised by its variance. The small-scale statistics, such as the temperature structure functions and the pdfs of the temperature increment that described the structure of scalar bubbly turbulence, were also investigated. Enhanced intermittency due the mixing of bubbles was observed. Furthermore, the scaling properties of the moments of the absolute values of the temperature increments for $\alpha = 0\%$ and 4.7% (where -3 scaling has been developed) were analysed by extended self-similarity (ESS) analysis. This analysis investigated the scaling behavior of the structure function of the order p versus the second order structure function, in which the exponent was denoted as $\beta(p, 2)$. $\beta(p, 2)$ for $\alpha = 0\%$ were similar to that for $\alpha = 4.7\%$ up to order $p = 5$. $\beta(p, 2)$ for both cases were also similar to that for the boiling Rayleigh-Bénard convection (point bubbles simulations) reported in Lakkaraju *et al.*, Journal of Fluid Mechanics **745**, 1–24 (2014) and were higher than other single-phase cases summarised in Gylfason *et al.*, Physics of

Fluids **16**, 4012–4019 (2004).

Samenvatting[2]

Het mengen van temperatuur en stoffen in gemengde gas-vloeistof stromen komt veelvuldig voor in de natuur en industriën. Grootschalige chemische reactoren maken gebruik van chemische reactanten (microdeeltjes) die mengen in een turbulente omgeving, waarbij warmte vrij kan komen door de chemische reacties. Om het mengen van warmte en reactanten te bevorderen, worden over het algemeen gasbellen geïnjecteerd. Om de physische eigenschappen van turbulente stromen met bubbels te begrijpen, zijn in dit proefschrift de statistieken van de temperatuur en warmteoverdracht in vloeistofstromen met zwermen stijgende bellen, met en zonder bijkomstige turbulentie, bestudeerd. Voor een algemene bellenstroom met hoog Reynolds getal, zonder bijkomstige turbulentie, zijn er drie mechanismen voor het mengen te onderscheiden: bubbel-geïnduceerde agitaties (BIA, door de snelheidsfluctuaties veroorzaakt door de aanwezigheid van de bubbels), schuiving-geïnduceerde turbulentie (SIT, door de snelheidsfluctuaties veroorzaakt door de non-lineariteit in de continue fase), en de overdracht door drijfkracht gedreven recirculatie (veroorzaakt door de inhomogeniteit van de bubbelverdeling). Warmteoverdracht in een inhomogene bellenstroom wordt bestudeerd in hoofdstuk 2. We meten de warmteoverdracht van een verwarmde verticale wand naar een onverwarme/koude wand in een rechthoekige bubbelkolom, waar milimetrische bubbels worden geïnjecteerd in de helft van de injectiesectie (aan de warme of koude zijde). Het Rayleigh getal, Ra_H, bevindt zich tussen 4.9×10^9 en 2.2×10^{10}, en de gasvolumefractie, α, bevindt zich tussen 0.4% en 5.1%. Een afschuiflaag wordt gevormd tussen de bellenkolom en de andere helft van de cel waar geen bubbelinjectie plaatsvindt. Bovendien lijdt de inhomogeniteit van de bubbels tot een grootschalige drijfkracht gedreven stroming. Verschillende menggebieden zijn geïdentificeerd. Voor $\alpha < 4\%$ is er een verbetering in de warmteoverdracht vergeleken met homogene bruisende stroming vanwege de geïnduceerde afschuiflaag en grootschalige recirculatie.Wanneer α stijgt zullen de schuiving-geïnduceerde turbulentie en large scale circulatie concurreren met

---

[2]This Dutch summary was translated by Pim Waasdorp.

de BIA. Als $\alpha > 4\%$ wordt de competitie versterkt, omdat het effect van de SIT groter wordt. In dit geval is de homogene injectie efficiënter.

Om het effect van incidentele turbulentie te bestuderen is het Twente Massa- en Warmteoverdracht Waterkanaal (TMHT) ontworpen (hoofdstuk 3). Het is aangetoond dat de temperatuur en massa overdracht metingen in turbulente bellenstromen mogelijk zijn op een gecontroleerde manier. Metingen van het snelheidsprofiel, lokale warmtestroom in het midden van de tunnel in één-fase turbulente thermische menglaag, de spreiding van een fluoriscerende verf in een turbulente bellenstroom en het effect van zoutconcentratie worden beschreven in hoofdstuk 3.

Met behulp van de TMHT zijn temperatuur statistieken in een turbulente thermische menglaag met bellen bestudeerd. Hoofdstuk 4 richt zich op de spectrale eigenschappen van de temperatuurfluctuaties. De gemiddelde vloei-stofsnelheid wordt vastgezet op 0.5 m/s en de invloed van de gasvolumefractie, variërend van $0\% \leq \alpha \leq 5.2\%$, wordt bestudeerd. De Kolmogorov -5/3 scha-lingswet voor de temperatuurfrequentie spectra wordt gevolgd door een steilere helling als α toeneemt. Deze helling verzadigt tot een -3 schaling wanneer α groot genoeg is. Het wordt voorgesteld om de -3 machtsfunctie toe te schrijven aan het verbeterde mengen door de bubbels en dat de locale netto spectrale overdracht van de temperatuurfluctuaties direct wordt gedissipeerd door diffu-siteit. De overdrachtsfrequentie van -5/3 naar -3 is geïdentificeerd met behulp van een Batchelor parametrisatie.

Hoofdstuk 5 gaat door met de studie naar de turbulente menglaag met bellen, door integrale statistieken zoals het globale gemiddelde profiel, de variantie en de waarschijnlijkheidsdichtheidfuncties (pdf) van de temperatuur en snelheid, voor $0\% \leq \alpha \leq 4.7\%$, te bestuderen. In tegenstelling tot de snelheidsvarian-tie, die toeneemt met stijgende α, neemt de temperatuursvariantie niet toe wanneer α stijgt. Dit komt doordat de bron van de temperatuurfluctuaties de koppeling tussen turbulente warmteflux en de gemiddelde temperatuur gra-dient bevat, welke beide niet strict toenemen met toenemende α. Verder kan uit de gestandaardiseerde temperatuur pdf's (genormaliseerd met de varian-tie) afgeleid worden dat stijgende bubbels de aanwezigheid van meer extreme waarden voor de temperatuurfluctuaties bevorderen. De kleinschalige statis-tieken, zoals structuurfuncties voor de temperatuur en de pdf's van de lokale temperatuurstoename die de structuur van de scalaire turbulentie met bellen beschrijven, zijn ook onderzocht. Versterkte intermittentie door het men-gen van de bubbels wordt geobserveerd. De schalingseigenschappen van de momenten van de absolute waarden van de locale temperatuurstoename, voor

$0\% \leq \alpha \leq 4.7\%$, (waar een -3 schaling zich heeft ontwikkeld) zijn geanalyseerd met een uitgebreide zelfgelijkheidsanalyse (ESS). Deze analyse onderzoekt het schalingsgedrag van de structuurfunctie van orde p tegenover de tweede orde structuurfunctie, waar de exponent wordt beschreven als $\beta(p,2)$. $\beta(p,2)$ voor $\alpha = 0\%$ is vergelijkbaar met de waarde van $\beta(p,2)$ voor $\alpha = 4.7\%$ tot een orde van $p = 5$. $\beta(p,2)$ was voor beide gevallen ook vergelijkbaar met de waarde gevonden in kokende Rayleigh-Bénard convectie (punt-bubbel simulaties), beschreven in Lakkaraju *et al.*, Journal of Fluid Mechanics **745**, 1–24 (2014) en was hoger dan andere eenfase gevallen, samengevat in Gylfason *et al.*, Physics of Fluids **16**, 4012–4019 (2004).

Short intro. and summary (Chinese)[3] 簡介 與概要

此論文旨在研究高速氣泡流中溫度的混合過程。

簡介

　　一般而言，「混合」（mixing）是指原本分布不均的「物理量」（如粉末、溫度及顏料等），到最後達致均勻遍佈所有空間的過程[4]。

　　其中，物質與溫度在流體中的混合過程，常見於在日常生活、自然界和工業。以湯裡加入胡椒粉為例，再經過湯匙攪拌，使胡椒粉在湯裡平均分布，即形成混合過程。假設在胡椒粉不會溶入到湯裡及無浮力作用的條件下，此混合過程具有兩種不同輸送模式，一種稱為「擴散作用」（diffusion），另一種為「平流」（advection）或「對流」（convection）[5]。前者是指將胡椒粉放入湯碗中的某處，不加以任何攪動，粉末在靜止的湯裡自由地擴散到四周，利用粉末分布不均所產生的輸送過程；後者是利用湯匙的攪動而引致「液體流動」，利用湯的流動帶動胡椒粉到別處，加快了整個混合過程。故此，混合過程主要有二，一為微觀的「擴散作用」，另一為因「平流」或「對流」所帶動的輸運過程，而且兩者可同時進行。另一方面，溫度在液體的混合過程也是類似的情況。其中涉及因溫差所致的「擴散作用」和受液體帶動的「平流」來輸送熱到另一個地方。

　　這裡進一步說明何謂擴散作用，將有助了解和推廣其知識到湍流中的擴散作用。胡椒粉在液體中「擴散作用」，實際上跟「布朗運動」（Brownian motion）有關，即每粒粉都被更微小的液體分子所碰撞而隨機走動，從而「擴散」開[6]。從宏觀層面來看，液體是靜止的，然而「擴散」現象由微觀層

---

[3]This summary is NOT a direct translation of the English version.

[4]詳見Villermaux E., Mixing Versus Stirring. Annu Rev Fluid Mech. 51 (2019)的文獻回顧。

[5]詳見Bird R. B., Stewart W. E., and Lightfoot E. N., Transport Phenomena (John Wiley Sons, Inc., 2007)。

[6]詳見Bird R. B., Stewart W. E., and Lightfoot E. N., Transport Phenomena (John Wiley Sons, Inc., 2007), pp. 531–532。

面的物理所引致，即每粒粉被更微小的液體分子碰撞。

「混合」現象亦常見於化工業。大型化學反應爐中，局部的物質濃度不均，以及因反應熱造成的局部溫度變化，皆會促使混合過程發生。此外，流體不同的流動形態亦會衍生不同的混合過程。一般而言，大型化學反應爐裡的液體流動速度快，流體進入「湍流」（turbulence）狀態。

湍流，為流體呈現混亂及不規則之態，由流體的速度足夠快或尺度足夠大所產生，常見於日常生活和自然界。例如，水龍頭出水的形態會因流動的速度上升而變得混亂，另外大氣層裡空氣的流動尺度之大也會形成湍流。湍流自身的流動形態，也影響著混合的方式。如果我們在湍流中放入粉末，其流體混亂的流動也能帶動粉末混亂地走動（即「平流」的混合方式）。正如在微觀層面因液體分子所碰撞而隨機走動所引致的「擴散作用」般，但湍流所引致的粉末的隨機走動，則在宏觀的層面上（由液體帶動），擴散的速度更快[7]。重申一次，那些粉末在湍流的擴散，是由於液體在宏觀層面的混亂流動所帶動（平流）所致，並非在微觀層面的液體分子所碰撞而生。因湍流或水的擾動所引致的擴散作用，稱之為「亂流擴散」，其擴散速度比起微觀的擴散作用所引致的擴散速度一般都快很多[8]。

化學反應爐中，除了本身的湍流現象外（稱之為「背景湍流」），一般會注入「氣泡」（gas bubbles），以增加其反應物與溫度的混合效率。氣泡的密度比液體低，故此會因浮力往上升，每個氣泡都能額外攪動其周圍液體，從而增加其混合效率。一群氣泡的流動為「氣泡流」（bubbly flow）。而量化「氣泡流」密度的物理量為「氣泡體積分數」（gas volume fraction），簡稱為α。簡言之，一個固定的空間裡，α越大，被氣泡所佔據有空間則越大。

「氣泡流」可以分為三種，第一種為「均勻分布氣泡流」（homogeneous bubbly flows），即α在空間均勻地分布[9]，現實中並不常見；第二種為「非均勻分布氣泡流」（inhomogeneous bubbly flows），即α在空間裡分布不均[10]，現實中較為常見；而第三種為「湍急氣泡流」（turbulent bubbly flows），即在有「背景湍流」中的「氣泡流」[11]，常見於大型化學反應爐。在「湍急氣泡流」中，氣泡的攪動影響著背景湍流本身，而背景湍流也能影響氣泡的運動，可見兩者相互影響[12]。

然而，目前物理研究對於廣義的「氣泡流」中的混合方式仍欠缺全面的理解。有鑑於此，此論文集中研究在

---

[7]詳見Bourgoin M., Turbulent pair dispersion as a ballistic cascade phenomenology. J. Fluid Mech. 772:678–704 (2019) 中的簡介。

[8]詳見Davidson P.A., Turbulence, An Introduction for Scientists and Engineers, 2nd edition (Oxford University Press, Oxford, 2016), pp. 252–263。

[9]Risso F., Agitation, Mixing, and Transfers Induced by Bubbles. Annu. Rev. Fluid Mech. 50(1):1–24 (2017)。

[10]同上。其參考資料稱之為Heterogeneous bubble column。

[11]同上。

[12]同上。

（一）無「背景湍流」的「非均勻分布氣泡流」、或

（二）「背景湍流」中的氣泡流，即「湍急氣泡流」之情況下，溫度如何混合。

　　此論文以統計學的方式來描述湍流現象，以考慮湍流是不規則而且有急劇的變化。例如，考慮其速度和溫度的平均數，而非考慮每一刻瞬間的速度和溫度。原因在於平均數的變化相較每一刻瞬間的變化為低。本論文組織架構分為五章，茲將各章之主要內容扼要敘述如下：

第一章

　　此論文的英文簡介。

第二章[13]

　　此章主要研究在「非均勻分布氣泡流」中注入越來越多的氣泡時，其傳熱的效率有何變化，以了解其混合過程。實驗過程中，先在一個長方體的容器裝滿了水，一邊垂直的壁面加熱，另一邊（對面）的壁面則冷卻。容器的底部有大量的針孔用以注入氣泡，但為了製造「非均勻分布氣泡流」的實驗效果，實驗只用了一半的針孔來注氣泡（靠近熱壁面或冷壁面），另一半則不用。因此，容器的一半有氣泡流而另一半則沒有。顯然熱會從熱壁面通過中間的水和氣泡，傳到另一端的冷壁面。熱量由溫度高的一方輸送至溫度低的一方，是為一種混合過程。而其量化其傳熱效益的物理量，是為「努塞爾特數」（Nusselt number, Nu），定義為：總傳熱量（total heat flux）與只有「擴散作用」時的傳熱量（diffusive heat flux）之比[14]。

　　要確切了解物質或溫度在流體中的混合過程，此研究先探討其流態和擾動（agitate）水的模式。原因在於，水如何流動和被攪動會影響熱輸送的方式，進一步決定其混合過程。首先，每一氣泡的上升速度快，這時就好像水沖向一個球體時其後面會產生的旋渦，在每個氣泡後面產生了尾流（wake）。這些尾流擾動著水。這些純粹由氣泡流所引致的水的速度擾動稱之為「氣泡誘發擾動」（bubble-induced agitations, BIA）[15]。接著，有氣泡流的一邊會因為氣泡的上升帶動水向上升，然而水的高度和體積有限，在沒有氣泡的一方，水被帶動向下，形成「大尺度環流」（large-scale recirculation）[16]。在容器中間部分，水移動的方向有大尺度的改變（由有氣

---

[13]文章發布為Gvozdić B. *et al.*, Experimental investigation of heat transport in inhomogeneous bubbly flow. Chem Eng Sci. 198:260–267 (2019)。

[14]詳見Bird R. B., Stewart W. E., and Lightfoot E. N., Transport Phenomena (John Wiley Sons, Inc., 2007)。

[15]Risso F., Agitation, Mixing, and Transfers Induced by Bubbles. Annu. Rev. Fluid Mech. 50(1):1–24 (2017)。

[16]同上。

泡流的一方為向上，到沒有氣泡的一方為向下）。這個水速大幅度改變的區域稱之為「剪切層」(shear-layer)。「剪切層」會因為其大尺度的水速度之改變，而產生水流速度脈動（velocity fluctuations）。脈動，即為起伏變化。此外，水的大尺度環流的速度夠快，也能產生上述的湍流。此「剪切層」所生之擾動加上其水的大尺度流動所形成的湍流，稱之為「剪切誘發擾動」(shear-induced turbulence, SIT)[17]。

簡言之，水的擾動或攪動模式一共分為三種，第一種為「氣泡誘發擾動」；第二種為「剪切誘發擾動」[18]。這些水的擾動，正如簡介中所描述的「亂流擴散」般，以其特有的擾動方式導致溫度的擴散。故此，這兩種擾動模式同時也是兩種混合的模式。第三種的則是先前提及的「大尺度環流」[19]，因環流直接帶動了其溫度從熱的一方到冷的一方。

以上三種的混合模式有助理解 α 對傳熱效率的影響。此研究發現，當 α 改變，主導的混合模式也會隨之變化，進而影響傳熱效率。總括而言，α 上升時，本來只佔容器一半的氣泡流慢慢因頂部水面的限制致使氣泡走到容器的另一半。當 α 少於4%時，相比起「均勻分布氣泡流」的傳熱效率（Nu）更高。原因在於，當比較「均勻分布氣泡流」和「非均勻分布氣泡流」時，後者有了「剪切誘發擾動」和「大尺度環流」的幫助，為水產生更多的速度擾動以及在大尺度上輸送熱到冷壁面。當 α 高於4%之時，「剪切誘發擾動」變得很強，但同時開始與本身已存在的「氣泡誘發擾動」和「大尺度環流」競爭。此時傳熱效率（Nu）則開始比「平均分布氣泡流」時低。

第三章[20]

此章主要説明能夠同時創造「背景湍流」和「氣泡流」（即「湍急氣泡流」）的實驗設備。此設備的中文名稱可翻譯為「屯特傳質傳熱水洞」（Twente Mass and Heat Transfer Water Tunnel, TMHT）。此設備能不斷泵水，能調控水的速度以及湍流的力度，與此同時能為流動的水加熱和冷卻。此章描述了該實驗儀器的操作，包括：量度溫度和速度的方法，放入螢光染料來做關於傳質的實驗，以及水中鹽對氣泡大小之影響。

第四章

此章主要研究溫度在「湍急氣泡流」混合時所呈現的「功率譜」（power spectrum）。

---

[17]同上。
[18]同上。
[19]同上。
[20]文章發布為Gvozdić B. *et al.*, Twente mass and heat transfer water tunnel: Temperature controlled turbulent multiphase channel flow with heat and mass transfer. Rev Sci Instrum. 90(7):075117 (2019)。

　　此研究利用「屯特傳質傳熱水洞」來同時泵水、注入上升的氣泡流及製造「溫度混合層」（thermal mixing layer）。「溫度混合層」，即是將一半被泵的水加熱，致使一方往上流的水比另一方同時往上流的水有著更高的溫度，令水向上流時溫度會傳向較冷的一方，換句話說這是由一個階躍的溫度分布進而混合的過程。實驗裡溫度在湍流中時有變化，變化因湍流的帶動而急速和劇烈，而且變化時大時小，時快時慢。本研究希望能檢視其溫度在不同時間尺度的變化有多大，例如：會否有大量急速的小變化，或會否有相對慢的大變化。科學研究中，常用頻率來表示不同的時間尺度。數學描述中，其中一種能夠量化在不同頻率的變化大小的物理量，叫作「頻率功率譜」（frequency power spectrum）。

　　故此，此章探究了α由0%上升到4.7%時，「湍急氣泡流」中「溫度混合層」的溫度功率譜變化。在此「湍急氣泡流」中的「溫度混合層」的中間位置，此研究量度了其溫度隨時間的變化(即溫度的時間序列)。接著，將此溫度的時間序列進行了傅里葉變換(Fourier transform)，從而計算出其溫度的頻率功率譜。實驗過程中發現，一旦注入了足夠多的氣泡時，其溫度的頻率功率譜除了呈現經典的柯爾莫哥洛夫–5/3冪定律[21]（Kolmogorov –5/3 power law）之外，還呈現了–3冪定律（–3 power law）[22]。此–3冪定律，也能從高速氣泡流中的速度功率譜中找到[23]。溫度頻率功率譜出現了–3冪定律，可能由於氣泡加強了溫度的混合效率，使其溫度的脈動在頻譜空間的傳遞過程中，直接因為液體分子引致的擴散作用而消散。

第五章

　　此章進一步探究「湍急氣泡流」裡「溫度混合層」中的統計量。統計量的分析有「積分尺度」（integral-scale）和「小尺度」（small-scale）之分。兩者區別在於前者將所有尺度的變化和數值一拼加入統計學分析，而後者側重於某尺度的變化和數值作統計學之分析。

　　「積分尺度」的統計量包括：平均溫度和平均速度在空間的分布、溫度和速度的標準差[24]（standard deviation）在空間的分布、溫度和速度的機率

---

[21]冪定律的例子：若函數$P(f)$的表達公式為$P(f) = f^{-5/3}$，那麼我們稱之為–5/3的冪定律。

[22]其湍流中的溫度理論為Kolmogorov-Obukhov-Corrsin (KOC) theory (Kolmogorov, A. N., Dokl. Akad. Nauk. SSSR **30**, 301 (1941); Obukhov, A. M., Izv. Akad. Nauk. SSSR, Geogr. Geofiz. **13**, 58–69 (1949); Corrsin, S. On the spectrum of isotropic temperature fluctuations in an isotropic turbulence, Journal of Applied Physics **22**, 469–473 (1951))。

[23]詳見Risso F., Agitation, Mixing, and Transfers Induced by Bubbles. Annu. Rev. Fluid Mech. 50(1):1–24 (2017)的文獻回顧。

[24]此統計量量度一組數據的離散程度。物理層面上，標準差能顯示其數據的起伏幅度有多大。如果溫度的標準差越大，則溫度圍繞著其平均數的起伏幅度也越大。

密度函數[25]（probability density functions, PDFs）、以及溫度和速度隨α上升時的方差[26]（variance）變化。其中主要結果如下：

一）水流的速度脈動幅度[27]會隨氣泡密度越多而變得越大[28]，溫度脈動幅度則不然。脈動幅度能使用「方差」統計量來表示。由於溫度方差空間分布不均，所以此研究選取其方差峰值位置，以比較在不同α時的溫度方差變化。此研究發現溫度的方差沒有隨α上升。原因在於，雖然氣泡的速度與水的速度有顯著的分別，但是氣泡的溫度則與水的溫度相若。前者能透過尾流攪動著水，但後者卻沒有從氣泡傳熱到水裡。為此，此研究分析了溫度擾動的來源。其來源有兩種，第一種為速度脈動與溫度脈動的相關值（即亂流熱通量，turbulent heat flux）；另一種為平均溫度的梯度[29]（mean temperature gradient）的絕對數值。兩者都建基於水的擾動能帶動溫度運動（平流）的物理現象。上述第一種來源指，如果水的速度脈動和溫度的脈動的關聯越大，水的脈動越強時溫度的脈動也越強。而第二種來源指，當某點平均溫度的梯度（斜度）越大，即某點鄰近的溫度差越大時，周邊的水帶來的溫度的脈動幅度也越大。最後，我們指出這兩種來源不一定隨α上升而上升。故此，溫度的脈動不一定隨α上升。

二）在溫度標準差（或方差）分布的峰值位置，標準化溫度（standardised temperature）在有氣泡的情況下有更多的極端數值。標準化溫度即溫度減去其平均值後再除以其標準差。其PDF在由$\alpha = 0.6\%$升至1.0%時，其PDF的峰度[30]（kurtosis）顯著增加。不過隨後α再增加時，PDF沒有明顯的改變。實際用途上，更多極端（標準化）溫度或會促使更多或更少化學反應。

繼探究「積分尺度」的統計量以及分析其物理意義之後，此研究分析了「小尺度」的物理。第四章介紹的功率譜能讓我們分析各頻率大小的起伏幅度的分布。而此章則利用另一種物理量來表達不同尺度的起伏幅度。此物理量為「兩點溫度差異」（temperature increment）。其中在空間兩點的距離代表了其考慮溫度變化的尺度。若兩點距離越少，其溫度差所考慮的尺度則越小。

首先，此研究發現，如同標準化溫度所得的結果，氣泡所致之混合能

---

[25]簡言之，即不同數值的溫度和速度的出現率分布。類似「直方圖」（histogram）但其直方圖的面積為一。

[26]即標準差的平方。

[27]即水速的起伏幅度。

[28]原因在於有更多的氣泡在攪動著液體，詳見Risso F., Agitation, Mixing, and Transfers Induced by Bubbles. Annu. Rev. Fluid Mech. 50(1):1–24 (2017)的文獻回顧以及Alméras E. *et al.*, Experimental investigation of the turbulence induced by a bubble swarm rising within incident turbulence. J Fluid Mech. 825:1091–1112 (2017)的實驗結果。

[29]即平均溫度在空間的斜度。簡言之為溫度差除以長度。

[30]此統計量為用作量化其PDF的「尾巴」大小，越大的PDF「尾巴」指其分布有更多的極端數值。

促使標準化的「兩點溫度差異」更多的極端數值。利用湍流學術用語來形容此情況，氣泡促進了更大的「陣發混沌」（intermittency）[31]。我們分別在α為0%以及4.7%的設定下，計算了標準化的「兩點溫度差異」後，在兩點距離不同（即在不同尺度）的情況下的PDF。這裡提及一下，在α為4.7%的情況下，-3冪定律已經出現了（詳見第四章）。此研究發現，無論在任何尺度，α為4.7%時的PDF有著更大的峰度，即其尾跡比α為=0%時的PDF更大。故此，氣泡所致之混合，促使標準化的「兩點溫度差異」有更多的極端數值。

接著，統計學上除了平均數和方差（即標準差的平方）這些統計量之外，還有更高階的統計量，這些統計量叫作「矩」（moments）。第一和第二階的「矩」分別是上述的平均數和方差。討論「小尺度」的物理時，此研究考慮了「兩點溫度差異」的「矩」，在湍流學術界裡稱為溫度的「結構函數」（structure functions）。因為「矩」有不同階級，所以根據定義「結構函數」也有不同階級。顧名思義，這函數能透過溫度在空間不同尺度的差異之統計量，來反映其湍流的結構。不過，計算結構函數時，我們其實考慮了「兩點溫度差異」的絕對值的矩。此研究分析了第p階結構函數相對於第二階結構函數的冪律關係（power relation），即「延伸自相似」（extended self-similarity）[32]分析。其指數被定義為$\beta(p,2)$。在p少於六的情況下，我們發現α為0%時的$\beta(p,2)$與α為4.7%時的$\beta(p,2)$相似，沒有明顯的分別。此研究亦比較其他湍流系統的$\beta(p,2)$。例如，點蒸氣泡(point vapour bubbles)在湍急瑞利–貝納德對流（turbulent Rayleigh-Bénard convection）的電腦模擬（Lakkaraju *et al.*, Journal of Fluid Mechanics **745**, 1–24 (2014)）所獲得的$\beta(p,2)$與此研究所獲得的相近。另一方面，Gylfason *et al.*, Physics of Fluids **16**, 4012–4019 (2004)所匯報的沒有氣泡的湍流系統裡，此研究的$\beta(p,2)$比它們的高。以上實驗結果的物理解釋有待研究。

結語和展望

此論文探究了（一）無「背景湍流」的「非均勻分布氣泡流」和（二）「背景湍流」中的氣泡流，即「湍急氣泡流」的情況下，溫度如何混合。用另一種說法，此論文研究了「氣泡誘發擾動」和「剪切誘發擾動」[33]的相互作用下所產生的混合作用。「非均勻分布氣泡流」和「湍急氣泡流」其實也受上述兩種擾動影響[34]。根據上述第一章概要對「剪切誘發擾動」的定義，

---

[31]Shraiman B. I., Siggia E. D., Scalar turbulence. Nature. 405(6787):639 (2000)。

[32]Benzi R. *et al.*, Extended self-similarity in turbulent flows. Phys Rev E. 48(1):R29–32 (1993)。

[33]「氣泡誘發擾動」和「剪切誘發擾動」的解釋詳見Risso F., Agitation, Mixing, and Transfers Induced by Bubbles. Annu. Rev. Fluid Mech. 50(1):1–24 (2017)。

[34]同上。

只要包含大尺度的水流所產生的湍流，那就是「剪切誘發擾動」[35]。故此，「湍急氣泡流」除了因為氣泡流動而受「氣泡誘發擾動」的影響之外，其「背景湍流」也為「剪切誘發擾動」所影響[36]。

　　上述簡介提及了一般情況下氣泡能提升混合效率。此論文分別在「非均勻分布氣泡流」和「湍急氣泡流」中的傳熱問題上，展現了氣泡如何提升混合效率。「非均勻分布氣泡流」方面，α少於4.0%時，「剪切誘發擾動」和「大尺度環流」幫助了傳熱，促進了溫度的混合。而「湍急氣泡流」中的「溫度混合層」實驗展現了氣泡促進小尺度溫度擾動的混合。此論文更提出當此小尺度的混合足夠強的時候，溫度的脈動在頻譜空間的傳遞時直接在擴散作用中消散，從而推導出–3冪定律。而且，氣泡促進了急速（即小尺度）而小幅度溫度的混合而只留下大幅度的變化，也符合溫度的總起伏幅度（標準差）沒有因氣泡多了而上升，並因此得出氣泡誘發更大的「陣發混沌」的結論。

　　溫度湍流的結構方面，此研究探究溫度的結構函數時，以「延伸自相似」[37]的方法分析第p階結構函數相對於第二階結構函數的冪關係。由此發現了其指數$\beta(p,2)$在α為0%時與α為4.7%時沒有顯著的分別，也發現與在另一個點蒸氣泡–湍急瑞利–貝納德對流的電腦模擬中的$\beta(p,2)$相似，但相較其他之前匯報沒有氣泡的湍流系統所獲得的$\beta(p,2)$為低。以上實驗結果的物理解釋尚待研究。

　　雖然我們已經探究了「非均勻分布氣泡流」和「湍急氣泡流」的混合過程，但仍有很多尚待研究之處。首先，「非均勻分布氣泡流」方面，此論文還未探討氣泡大小如何影響傳熱[38]。接著，「湍急氣泡流」方面，此論文只研究了平均溫度梯度非零的情況，尚未探討欠缺平均溫度梯度時的情況。其中研究問題包括：溫度頻功率譜能否同樣地展示–3冪定律？溫度的PDF會如何改變？另一方面，三維的「均勻分布氣泡流」中的溫度頻功率譜又能否呈現–3冪定律？理論上α超過什麼數值，溫度頻功率譜才會出現–3冪定律？哪一個物理頻率開始呈視–3冪定律？最後，第五章提及亂流熱通量不一定因氣泡增加而上升。然而，此論文並未量度其「湍急氣泡流」中「溫度混合層」的亂流熱通量。這涉及到在氣泡流裡同時測量液體的溫度和速度，仍有待將來進一步的實驗研究。

---

[35]同上。

[36]同上。

[37]Benzi R. *et al.*, Extended self-similarity in turbulent flows. Phys Rev E. 48(1):R29–32 (1993)。

[38]Gvozdić B. *et al.*, Experimental investigation of heat transport in inhomogeneous bubbly flow. Chem Eng Sci. 198:260–267 (2019)。

飲水思源[a]。

Acknowledgements

My turbulence journey dated back to the summer in 2014. Thanks to the connection of my current supervisor, Chao, with the university (CUHK) where I was doing my Bachelor study, I was able to participate a summer exchange programme (SURE) organised by Prof. M.C. Chu. It allowed me to do summer research in this wonderful research group, Physics of Fluids group (PoF). In PoF, I met Detlef, Chao and my daily supervisors at that time, Sander and Roeland. I am grateful to have them be my supervisors for my exchange programme. Sander and Roeland are very helpful daily supervisors. Whenever we have technical problems on the Taylor-Couette, they help solving it together, allowing me to focus on pressing the buttons and performing data analysis. This led to fruitful research outcomes, which I think are crucial to my entrance to pursue a PhD in PoF later. Moreover, the exchange experience opened my view on the work-life style in the Netherlands, which I appreciate a lot. Thank you, Chao, Prof. Chu and Detlef, for providing me the opportunity to do research in PoF when I was still an undergraduate student. Thank you, Sander and Roeland for guiding me and helping me to produce nice research results together during my exchange programme in 2014.

I am grateful that Detlef offered me a PhD position in PoF. PoF is a wonderful, large group. During the four years of my PhD, PoF gave me the exposure of different fields in fluid mechanics, from nano-bubbles, micro-bubbles, larger bubbles, droplets, capillary phenomena, elasticity, granular materials, solid-water impact, to large-scale turbulence. The opportunities to attend external workshops and conferences also expanded my knowledge in Physics and

Physics of Fluids. Apart from that, I enjoyed the joyful and good relationships between colleagues in PoF, from which a lot of good memories were created. Certainly I cannot forget to thank a NWO-funded program, **Multiscale Catalytic Energy Conversion (MCEC)**, which provided the funding for my PhD, gave me the exposure to some chemistry research and the opportunity to make friends with the MCEC colleagues.

I would also like to thank the **University of Twente**. It is a beautiful campus and has good facilities. It is where I also met other friends apart from PoF in Enschede.

Supervisor and collaborators

Detlef, thank you for being my promotor and supervisor. Thanks for building a lot of connections from other research groups to the group. It can be useful to PhDs and Postdocs in the sense that we can collaborate, make use of the expertise from each other and learn from each other. Maintaining such a big group is not easy. Thanks for that. I am amazed by your curiosity of many different topics. Like some of the interviews you mentioned, you 'see no difference between fundamental and applied research', though it may be a privilege of working on fluid mechanics. Thanks for showing how you stay curious on problems which inspire us to not to constrain ourselves only to certain topics. One of the probably famous quotes from Detlef is, '...you should have known this...' It means that if we do not know this, we'd better know it because it is highly related to the research! Thanks for saying that!

Joanita, whenever we have administrative problems that we cannot solve by ourselves, you help us solving them efficiently. Thanks also for organising the PoF Christmas dinner every year, initiating writing cards for the PoFers who have a new family member, etc. Thank you for taking care of the group. Without you, we cannot focus on our research. Your willingless to help, positive attitude and supreme efficiency entitles you to be the best secretary or group manager we can ever find. Thank you, Joanita.

Chao, thanks for being my co-supervisor. As mentioned before, because of your connection with CUHK, I was able to come to PoF to do an exchange programme and then because of that I could even pursue a PhD here. I am very grateful about that. Although when I came to PoF for my PhD, you had already moved to Tsinghua University, we still meet online nearly weekly. Your experience and advice on the experimental and some general turbulence topics are helpful. Furthermore, you remind me to beware of some academic things that we should do or should not do. Lastly, thanks for helping me to

ask **Cheng Wang** for reviewing my summary in Chinese. Therefore, I also would like to thank **Cheng Wang** for the review and the comments especially on the technical terms in Chinese! Thank you, Chao.

Sander, like Chao and Detlef, we know each other since the summer in 2014. You were my daily supervisor during my exchange programme in 2014 and also later from September 2017 till now. I am very grateful that you helped me a lot of experimental problems and providing many helps on data analysis. When you were still a PhD student and I was still a Bachelor student, I enjoyed our interactions a lot already, not only during work but also after work. We went to Texel island together with Vamsi, Kike and some other people, and to some parties in Enschede. I could feel the PoF family atmosphere and the PoF friendliness already at that time. Now back to the time for my PhD. As you also mentioned in your acknowledgement in your PhD thesis, you encountered Chao as your daily supervisor who was very encouraging on your experimental research. I can feel that you may inherit this attitude. As a PhD student, I encountered experimental, technical, research difficulties which made me feel devastated sometimes. But your passion and willingless of solving and helping the others to solve experimental and data analysis problems, definitely helped me feel better. Your positiveness were also shown during the meetings. All these helped us to keep a positive attitude to face the difficulties. Reflecting upon your attitude and also how some others saying why some people are more effective, it may be because they embrace challenges and are willing to solve the problems and do not give up easily [39]. Thanks for creating a positive peer group, Sander. A great mentor can influence his/her pupils which promotes their growth to become successful scientists or researchers [40]. It may be not just because of the knowledge the mentor passed on (as the pupils normally work on some other fields later as well), but more importantly those ways of doing research and the attitudes that the pupil felt and internalised which also promotes new ideas. I am not saying I am a great scientist or researcher now but your attitude definitely inspired me. It holds even though our backgrounds and ways of thinking differ. Apart from attitude, I also learnt something from your research taste. One way of doing research is first deal with the fundamentals, constructing a big picture, filling the gaps and proceed. But I can feel that your taste of choosing the research topics can be adventurous like 'find something interesting so let's try it out'. For example, mayonnaise

---

[39]See e.g. the book 'Mindset' by Dr. Carol Dweck.

[40]See also the recent study, Ma Y, Mukherjee S, Uzzi B. 2020. 'Mentorship and protégé success in STEM fields'. Proc National Acad Sci. 117(25):14077–83.

turbulence and ice turbulence, not shying away from those complex flows which may be extremely difficult to model. Certainly I can be just ignorant that they can be modelled easily and to make use of the full potential of the advanced setups, the complications are suitable. But these choices of topics opened my eyes. Also, Thanks for always answering me emails quickly. Lastly, in the final time of writing my thesis, thank you very much for checking my manuscripts. I learnt a lot from your comments. Thank you, Sander.

Bert, thank you for being one of my committee members. Thank you for bringing some salt and help performing some preliminary measurements with the newly built setup TMHT. Also thank you for inviting me to the IPP-FOM meetings. I also learnt a lot from these meetings.

Dr. Maike Baltussen and Prof. Hans Kuipers, thanks for the discussions and organisations for possible collaborations between your group and PoF, in order to exchange knowledge and expertise. I learnt a lot from the discussions. Maike, also thanks for the bubbly flow lectures in MCEC and in a JMBC course in Twente. I learnt more about bubbly flows and simulating bubbly flows from you.

Dennis (Dr. van Gils), thank you for making the wonderful setup (Twente Mass and Heat Transfer Tunnel, TMHT) and helping us to solve many technical problems. We interacted a lot not only because I am the main user of your lovely creation TMHT, but also I am a 'question PhD' who asked for helps many times. To me, you are more than a technician and the guardian (safety officer) of PoF. You taught me a lot of practical experimental techniques during my PhD, like soldering and eliminating electric noises, basic ensemble of different parts to make a probe or anything, and so on. When I faced a problem, you also encourage me to think by myself first. It is because the related skills have been taught previously and I eventually cannot rely on the technicians too much or otherwise it prevents me to become an independent experimentalist. I remember a lot of the time when we worked together in the water tunnel lab to solve problems like eliminating electric noises, replacing some heaters and so on. Without you, the experiments in this thesis would not be possible. Thank you, Dennis.

Gert-Wim, Martin and Bas, thank you for the technical support and the fun conversations in the technician office.

Gert-Wim, thank you for letting me to bother you many times in your office (sorry!) because I looked for help many times. I am honoured to work with the legendary technician who can design and make anything. Thanks for sharing also your life and your hobbies to us. Your farm and your house are amazing.

I love our 'Dutch' conversations with you and Martin. You taught me some funny Dutch, thank you!

Martin, jaja, thank you for teaching me how to be a good ninja. Your practical skills and experience on solving practical, technical problems of our setups are supreme. You trained me to become a ninja and I hope I will not disappoint you in the future.

Bas, I am honoured to get your help before your retirement. Thank you for ordering stuff and solving our computer-related problems. You are efficient in solving them. Enjoy the life after your retirement.

Biljana, thank you for being a close working colleague in the first two years of my PhD. When I started my PhD I was not sure what exactly I would do for my PhD. After some time I was suggested to collaborate with you, focusing on heat and mass transfer in bubbly flows. It was my pleasure to work with you and thanks for guiding me to work on the experimental setups and for the discussions we had. I enjoyed the conversations with you about different topics and the times when we worked together in the lab. Your suggestions on academic parts and on my presentations are helpful. Thank you, Biljana.

Varghese, thank you for working with me when I first started my PhD and taught me some experimental techniques. Especially you taught me how to perform a fluorescence dye experiment in the big water tunnel, so that I can apply it to the small water tunnel. Thanks a lot. All the best for your academic career.

Elise, thank you for some discussions on the subjects of bubbly flows and suggesting some literature on laser-induced fluorescence. I regret not building my bubbly flows knowledge sooner so that we can have more fruitful discussions and learn more from you while you were still in PoF. Without Elise, Biljana, Dennis and Gert-Wim, the idea of building the TMHT setup would not be applied and I would not be able to use this setup for my thesis. Your research work helped me a lot on my understanding and provided me some directions for my PhD research. Thank you, Elise.

Pim W, thank you for being my close working colleague in the last one and half years of my PhD and translating the summary into Dutch. We met each other in the Elasticity course already before you started your PhD. We interacted physically often before the pandemic started. Luckily we managed to work together in the lab when the pandemic was not serious in the lab. I enjoyed the conversations with you about different things, like music, Dutch culture and so on. Thank you for also listening to me explaining things. I am a person who likes to talk a lot. 'Teaching' helps consolidating one's knowledge.

Thank you for being my listener sometimes. I wish you have a fruitful PhD. Thank you, Pim.

Timothy and Jack, thank you for working with me for some preliminary results using the TMHT setup. **Jack**, thank you for your preliminary data analysis on heat flux. Hope you have a fruitful career after your Bachelor study. **Timothy**, unfortunately we encountered a rusty setup and we had to clean it together. I am grateful that you helped. It is good to have you in Enschede and thanks for the Cantonese conversations. I wish you have a fruitful PhD in PoF in the coming four years.

Bo, thanks for doing a Master thesis with us. It was my pleasure to work with you and see how our projects can be continued with another research student. You are motivated and willing to learn. I appreciate that. Keep it up and good luck for the rest of your Master thesis.

I would also like to thank the Bachelor students who work with me, **Bas and Hein-Dirk**. Both of you performed preliminary experiments with the newly built setup at that time. You learnt how to work on a thesis project and I also learnt and gained experience on how to supervise students. It was my pleasure to work with both of you. All the best for your future career.

During the pandemic, thanks for showing up in the **regular weekly meetings**, Luuk, Pim B, Pim W, Yoan, Bo, Morgan, Sander and Chao. At least we can still be connected online these days. Thanks for the discussions and I learnt a lot from all of you.

Seminar organisers

I also want to thank the seminar organisers which composed of French colleagues (**Guillaume, Elise, Maxime, Anaïs, Pierre and Mathieu**). My knowledge and exposure to different topics are built bit by bit over time with the seminars. Merci boku!

Other PoF staff members

For the teaching of fluid mechanics, I would like to thank **Guillaume, Richard, Hanneke, Dennis, Alvaro, Jacco, Devaraj, Michel and Detlef**. I have taken courses on the physics of fluids with all of you, which helped me to build a foundation of the knowledge of fluid mechanics (and granular material, elasticity) in general.

Jacco, in addition to the above formal master courses, I would like to also thank you for giving the visco-elasticity lectures which covered some theo-

retical formulations which I enjoyed a lot. Although I am mainly working on experiments for my PhD, I am deeply interested in the theoretical side as well. So I am happy to talk to you since sometimes you shared some 'theoretician jokes' with me.

Leen, thanks for the discussion on bubbly flows with me. There were times when we discussed by writing on the board in your office. Moreover, you introduced the cookies from Speciaal Jagers (now called Bakkerij Nollen) to us when you celebrated your birthday to us. The cookies were very good. It was fun and my pleasure to talk to you.

Guillaume, we somehow know each other already when I did my exchange in PoF in 2014. For the Physics of Bubbles course, I learnt quite some knowledge from you and Michel because of the project. Thank you for answering my questions. Thanks for inviting me to your house for a barbecue party. I am glad that you can stay here to continue your academic career for the tenure track. All the best.

Alvaro, thanks for organising some journal clubs, being quite active in the PoF group and sharing what constitutes to a good fluid mechanics video!

Michel, thanks for the Physics of Bubbles course project. I learnt a lot from this project. Moreover, thanks for lending me a book about electronics!

Devaraj, Hi Devaraj! Thanks for being positive to us and for the nice, short chats at the coffee corner. Devaraj, you always show a huge positiveness which makes us feel positive. Thank you!

Richard, thanks for some chats and interactions on turbulence topics. Thanks for showing us your wind farm research in a seminar. All the best with your research!

Dominik, thanks for being active to join the Waaier lunch group and thanks for the conversations about your kids, haha! Thanks for sharing your research on some spectral analysis in turbulent Rayleigh-Bénard convection in one seminar. It is my pleasure to know you and I enjoyed the time we held some beer and have some conversations. I wish you all the best for your research!

Andrea, thanks for a JMBC dispersed two-phase flow lecture in Twente in 2018 and the discussions we had when you visited PoF. You have very sharp observations and opinions. Thanks a lot.

Roberto, thank you also for a JMBC dispersed two-phase flow lecture in Twente in 2018. Thank you for being one of the committee members.

MCEC colleagues

During the MCEC meetings, apart from the presentations, there are also some social activities organised by our MCEC colleagues and representatives from each university. Thank you.

Anne-Eva, thanks for being the manager of MCEC and maintain the working of the group during the pandemic.

Ivan, Renée and Alessia, thanks for being the UT representatives for MCEC. Thank you also for the conversations during our MCEC meetings and when we met in UT.

Maxim, in the early times Biljana and I were collaborating with you on the numerical simulations part. For every MCEC event, it was nice to talk to you. Thanks for also showing me your research while I visited Eindhoven. All the best for your career in scientific computing.

Miquel, thanks for the conversations for every MCEC event and when we saw each other in UT. Also thanks for showing me and my girlfriend where you used to hang around in Barcelona. You are very kind person. It is my pleasure to know you. I wish you all the best for your academic career.

ME214C

Of course I have to thank my dear ME214C officemates, **Adeline, Misha, Myrthe, Carola, Pim W and Ambre**. Our office is known to be the most diverse office, haha. It has a time when everyone is working on a different topics in different scales, even different nationalities and equal relative proportions of ladies and gentlemen. Laughing moments occurred from time to time and sometimes Alvaro in the next office came by to check what happened!

Adeline, thanks for introducing bouldering to me, though I did not continue to do that (sorry!). Thank you for the super cute card that has a picture of your baby.

Misha, you are my best Russian officemate. Your kindness and laugh I will never forget. Thanks for being my groupmate for the first MCEC school and the experimental techniques course. Wish you all the best for your career!

Carola, you are a very kind person who would check on the others from time to time and are willing to know more what is happening to the others. I really appreciate that. I enjoyed our conversations a lot. Thanks for also sharing some interesting knowledge with us, like some knowledge about animals and sometimes some categorisation of some fruits or plants. I learnt a lot from you. Wish you all the best for the rest of your PhD.

Myrthe, I will never miss the time you eat carrots next to me. Thanks for organising the BATA and the conversations about different things like PhD life, life in general or any other things in our office. It was my pleasure to talk to you and to share some of our PhD experience.

Ambre, it is unfortunate that you started your Postdoc at the beginning of the pandemic but at least we still have some conversations during lunch. I enjoyed our conversations and thanks for the interactions. Also thanks for increasing the number of French people in the ME214 corner! All the best for your Postdoc in PoF.

Thank you, ME214C, for holding many of my books in one place. Thanks Gert-Wim to build another bookself to hold these books.

Lunch and dinner groups

I enjoyed the lunch Waaier group a lot before the pandemic. Although I was not doing this every working day, when it was around 10 mins before 12 pm, I used to ask people for lunch at each office, since my office is at the end of the corridor of the 2nd floor of Meander. In the early times of my PhD, it may have only 8 people or less. Over time the lunch group is getting bigger and bigger and we need more than two tables to accommodate every one. Thanks for everyone who joined the Waaier lunch group and I treasured the conversations with all of you. To name a few, **Dominik, Carola, Álvaro, José, Misha, Youssef, Vatsal, Marvin, Pierre, Alex, Yanshen, Ricardo, Jessica, Anja, Farzan, Vanshu, Pim W, Robert, Minkush, Diana, Pablo, Udo, Sarah, CS, Yoan, Sander, Minkush, Dennis (v.G.), Dennis (crossfit), Anaïs, Mathieu, Mazi, Walter, Ivan, Rodrigo,** ...

So indeed I should also thank Waaier to provide me lunch and even dinner. I also thank those who joined the **Waaier dinner group** with me sometimes, for example **Pieter, Alex, Ricardo, Yanshen and Vanshu.**

Talking about lunch, I should also thank **Cindy, CS**'s wife for making the wonderful, delicious lunchboxes to us. I am going to miss that.

Dutch colleagues

PoF is a very culturally diverse group.

Dutch colleagues certainly are the majority. Sorry I am not naming all of you here since there are too many. All of you are very friendly and willing to share your Dutch culture and some funny Dutch language with us. Dank je wel!

Maaike, thank you for organising the BATA and accepting my oranges. I enjoyed our conversations. Thanks for the interactions in PoF, in APS and in Physics in Veldhoven. Also thanks for joining to try out some restaurants together with other PoFers. All the best for the rest of your PhD.

Dennis (crossfit), thank you for organising many activities in PoF, including BATA and the group outing. You are very cool and kind. A lot of jokes and laugh we shared. May the Force be with you, always. Thank you Dennis.

Dr. Pim Bullee, hii. The trips with you and othe PoFers to Udine and Trieste were great. I enjoyed also a lot for the Nantahala trip with other PoFers. The conversations with you on the ground floor in the water tunnel lab were joyful and fun. I would like to also thank you and Bob in the other group for helping me to make coatings of two thermistors. You are a cool guy and thanks for the interactions. All the best for your Postdoc in Norway.

Martin Klein, thanks for the interactions we had. Thanks for also answering some questions about some master courses at the beginning of my PhD.

Michiel (Hack), you are sitting next to my office and I used to letting you go through the ME214 door. I enjoyed our chats in PoF and in Nantahala. Thanks for the interactions. Wish you all the best for the rest of your PhD.

Martin Essink, we did several master courses together. Thanks for the conversations and interactions we had. Also thanks for introducing me another way to get coffee from the coffee machine, which is mixing chocolate milk with coffee!

Luuk, thanks for sharing your knowledge and a Mathematica code with me. Also thanks for the interactions and interesting chats we had. Wish you all the best for your PhD and wish that your korfball skills keep improving!

Charlotte, thanks for some interactions and conversations about your TA work and so on. It is good to know how students are willing to learn though there has been a pandemic. Good job for your TA work and all the best for the rest of your PhD.

Martin Assen, thank you for our interactions, which happened more often before the pandemic. Good memories in Nantahala, BATA and some parties. All the best for the rest of your PhD.

Simon, thank you for the conversations in the water tunnel lab. Thanks for listening to me on sharing some bubbly flows knowledge. Good luck with your PhD.

Daniel, thank you for the chats and interactions in PoF and being active also in the Whatsapp/Signal group. Your information and answers to our questions are useful and interesting. All the best for the rest of your PhD.

Tim, before the pandemic we used to see each other sometimes in the ME214 corner. Thanks for the chats and random conversations.

Ruben, we met back in 2014. I enjoyed our conversations about your hiking. Thank you for the interactions.

Dr. Michiel van Limbeek, thanks for the interactions already back to 2014. 'What's happening?' ME201 sometimes became like a cafe with music because of you. Nice chats and wish you all the best for your academic career.

Liz, your office is also next to me and we sometimes had conversations with each other. The conversations were fun. Thanks for asking me my opinion on your thesis cover. All the best for your career.

French colleagues

I would like to thank again the French colleagues in our group (Guillaume, Adeline, Elise, Maxime, Anaïs, Pierre, Mathieu and Ambre) for sharing their French culture to us. I think the French language sound very interesting and thanks for teaching me some French! Merci boku!

Maxime, you were sitting next to my office. Thanks for checking on me sometimes when I stayed late in PoF (in fact same to you!). I enjoyed our conversations.

Anaïs, since you were working in the lab next to the water tunnel lab, I can pass by from time to time and see you working with your experiments. Thanks for sharing your excitement with your experiments. The inverse Leidenforst effect is super cool (used very cool liquid nitrogen)!

Pierre, thanks for teaching a lot of French word to me. Bonjour Pierre, je m'appelle baguette. Thanks to Mathieu, I know how to say Tonton Pierre to you (hope you don't mind!). Again, thanks for organising the seminars. It is fun to talk to you and thanks for you infusing some Frenchness to me!

Mathieu, thanks for organising the seminars and once explaining to me about mixing in your office. It is very helpful! I love the conversations with you. It seems that you can come up with some interesting stories every time we talked!

Spanish colleagues

I would also like to thank the Spanish colleagues (José, Álvaro Moreno Soto, Pablo and visitors Gonzalo, Irene and Patricia). Thanks for sharing your Spanish culture to us. It is fun to talk to all of you!

José, you are a kind person and I can always feel your happiness all the time. We have been to the MCEC schools together and some parties. It is my pleasure to know you and wish you all the best in the Netherlands.

Álvaro M.S., your reactions to many different things are great. I enjoy talking to you! With you, our Waaier lunch group never runs out of topics. Thanks! All the best for your career back to Spain.

Pablo, thanks for showing the city Toledo to me and my girlfriend when we visited Madrid. It was a very nice experience. I enjoyed our conversations and the times when we hang out together to have dinner. Your ALRIGHT production of editing Misha's movie is amazing, probably the best edit I have ever seen. Thanks to you, I am deeply influenced by your ALRIGHT. AAL-RIGHTTT!

Gonzalo and Irene, thank you for the talks and the interactions we have in PoF. I enjoyed the time we went to the Tankstation together and talked about different things.

Patricia, thank you for sharing your Spanish culture to us. Thanks for some interest in Chinese culture. I enjoyed our conversations and learnt a lot about Spain from you!

German colleagues

In fact at the beginning of my PhD, there were not many German colleagues (Alex, Christian). Later Kristen, Borge, Carola, Anja, Marvin, Sarah, Dominik and Robert joined PoF. Thanks for bringing some German culture to us. In particular, Alex (and Dennis van Gils) organised the traditional German drinks Feuerzangenbowle for two years. Thanks for that!

Alex, we started our PhD at a similar time. It is my pleasure to know you. The trips we go to Venice, Udine and Trieste were amazing. I learnt some table manners and tips of choosing good local restaurants in Italy from you. You also taught me some German and Italian. I appreciate that. As we are both PhD students, we both have our own ups and downs and thanks for sharing them with each other. Wish you all the best for your future career back in Germany!

Anja, thanks for inviting us to Lukas' and your birthday party in your German house. It was a very good party and I enjoyed a lot of the conversations in there! Thank you for being kind and friendly to us and acted as Biljana for her PhD movie even when you just started your PhD! You performance was amazing!

Marvin, thanks for smiling to me all the time. It is my pleasure to talk to

you. We can easily talk when we see each other. Thanks for sharing your hobbies and so on. All the best for your PhD.

Robert, thanks for inviting me to your housewarming party! It was fun! You mentioned that people from Hamburg are friendly inside once they know each other a bit longer, and I guess I can see that from you! Thanks for being friendly to me!

Sarah, thanks for joining the Waaier lunch group and the conversations we had. Good luck with your Postdoc in PoF.

Kristen, thanks for the conversations in PoF. Thanks for sharing your work in PoF and also in the drop tower. They are very cool.

Borge, I also enjoyed our interactions and chats. Thank you.

Indian colleagues

For our Indian friends (Utkarsh, Srinidhi, Nakul, Minkush, Charu, Vatsal, Pallav, Lijun, Yogesh, Vanshu, Srinath, Shantanu, Varghese, Vamsi, Anupam, Uddalok), thanks for also sharing some Indian culture to us. Thanks for sharing Indian candies and food to us sometimes (like candies at 3pm). I enjoyed talking to all of you and to learn some Indian words from you. Namaste!

Vamsi, like Sander and Kike, we met each other already back in 2014. Thanks for the fun we shared back to the time in 2014. We have parties together, dancing. Thanks for inviting me to the Oktoberfest in Gronau, from which I went to that festival every year. Also the farewell party in your apartment. It was super fun. It is my pleasure to know you and I wish you all the best for your future career.

Nakul, we started at the same time so sometimes we share our PhD experience to each other. You are a fun guy to talk to. Thank you for the interactions.

Yogesh, we are late workers in PoF sometimes. So having you in PoF lately making me feel less lonely. Thanks for that and in fact I wish that you do not have to work that late. All the best for your PhD!

Vatsal, thank you for showing your enthusiasm on fluid mechanics, showing that you really love the subject. You also like the history of fluid mechanics. Thanks for sharing it to us to enhance our history knowledge. Your happiness and positiveness are encouraging. Keep them like this and all the best for your PhD.

Charu, thank you the interactions we had. I enjoyed our conversations, for example during the housewarming party in Robert's house. Theoreticians in PoF are scarce. Since I also would like to be a theoretician, I would like to

thank you for your presence in PoF, maybe to make me feel that I am not so lonely, haha!

Minkush, thank you for the interactions we have, during lunch and other times. I appreciate that you strive for working on theories, later getting a cum laude for your master thesis and you managed to pursue a PhD with Jacco. I can see you grow over time. If you continue like this, strive to improve yourself, not shying away of asking questions, embracing new challenges to learn new things, you can be a very good theoretician (or if you are very good already, then I'd replace it with very very good, never end). Keep going and good luck for the rest of your PhD.

Srinath, I enjoyed our conversations and interactions. All the best for your PhD.

Lijun, thanks for the chats and introducing me about your home when we first met in the group outing. All the best for the rest of your PhD.

Uddalok, we interacted a lot during lunch. Thanks for sharing your Indian culture and the discussion of Indian food. I appreciate that you join Kangoo jump with us at least once. You hold your promise. It is a pity that the pandemic prevents us to talk to each other more physically. Good luck for the rest of your Postdoc.

Pallav, thanks for the interactions we have. We interact a bit more when you use ME201. Good luck with the rest of your Postdoc here.

Shantanu, the prince of India, thank you for coming to PoF and pursue your PhD. It is my pleasure to talk to you.

Anupam, in the first two years of my PhD, you were probably the only theoretician among the PhDs and Postdocs I know. Thank you for answering some of my theoretical questions and also some helps related to Advanced Fluid Mechanics. All the best for your academic career.

Chinese colleagues

Yantao, it is my pleasure to know you. You are kind and cool person. It is coincident that when you moved out from Enschede, my housemates and I were moving in into a new apartment. Thanks for selling us your household stuff when you moved out.

Yanshen, thanks for joining the Waaier dinner group and thanks for staying late in PoF so that I did not feel so lonely (but of course I wish you go home earlier!). Thank you for the chats and interactions.

Steven, thanks for talking in Cantonese with me (haha!) We know each other long ago when I worked on a summer project with Xie Yichao. I wish you all

the best for your future career.

Huanshu, thanks for providing me and Misha an experimental project to work on for the experimental technique course. Also thanks for the conversations we have! Your basketball skill is supreme. Thanks for playing basketball with me and Ivan and the others.

Jiaming, thanks for the conversations though they are not many. You always smiled to me, thanks for that! I wish you all the best in your career.

Yuliang, you were sitting next to me when you first(?) visit our group. I enjoyed our conversations. Good luck with you research.

Binglin and Xiaolai, thank you for the interactions. Binglin you smiled to us all the time. Thank you for being so polite to us. Wish you all the best for the rest of your PhD.

Rui, thanks for being a student in Advanced Fluid Mechanics. All the best with your PhD!

Yaxing, we started at the same date. Thank you for the intereactions we had in PoF. Good luck with your academic career.

Shuai, thanks for the conversations we had during some dinner in Waaier and in PoF. Thanks for sharing your research results using boundary-integral methods. They are cool!

Haorun, thank you for showing your simulations using phase-field methods. Your seminar was very interesting!

Luoqin, thanks for the interactions we had, for example in Jessica's house-warming party. Thanks for sharing your wind farm research!

Morgan, thanks for sharing your research updates in the regular meeting. Your seminar about your PhD work was cool and interesting. Good luck for the rest of your Postdoc.

Latin American colleagues

Thanks for sharing your Latin American culture to us. It is my pleasure to talk to and interact with all of you.

Ricardo, we interacted a lot in PoF. Thanks for being my friend who discussed things and hanged out together. Thanks for being a company for going to Waaier at night and also to Kangoo jump. Thanks for listening to what I learnt which consolidates my knowledge. I enjoyed a lot of our conversations and discussions, from which I also learnt a lot. You also taught me some Spanish. I also thank you for learning some Cantonese in return, like saying how the words before we eat. Thanks a lot and wish you all the best for the rest of your PhD.

Rodrigo, thank you for all the interactions we had. You are a cool person. We have a lot of fun when we have conversations. Thanks for always checking on me when we see each other. I am grateful that you invited me to your parties. Wish you all the best with your career in Netherlands.

Diana, thanks for being active in PoF and in the Whatsapp/Signal PoF group. You established the Beer group for us, tightening the relationships between PoFers, thank you. I enjoyed the conversations with you and thanks for sharing your PhD experience, even though there were ups and downs. Thanks for sharing and reminding us some practical information and also asking questions so to have more communications between PoF members. All the best for the rest of your PhD and your future career.

Bernardo, it is unfortunate that you started your PhD when the pandemic just started. So we can only have limited chats. But all the best for your PhD.

Kike, we knew each other back to the summer in 2014. I am very grateful that you shared a lot of fun with me and invite me to parties. It was a unforgettable experience to go to the Texel island. I will never forget your friendliness to the others. All the best.

Loreto and Leo, thanks for inviting me to join some parties, dinner and celebrations. I enjoyed the Oktoberfest parties in Gronau every year with both of you! The parties and so on were super fun. Wish you two all the best.

Olinka, thanks for the conversations and interactions in PoF. Thanks for some Mexican candies and they were very nice. All the best for the rest of your PhD and your future career.

Edger, thanks for the interactions in PoF. Sometimes we had chats at the coffee machine. All the best for the rest of your PhD.

Other PoF colleagues

Youssef, it is my pleasure to know you. Thank you for helping me to type a email to a French institute. Thank you the talks and the conversations. Also once you help me to order some nice Lebanese food in a Lebanese restaurants. I enjoyed the time with you and the others for going out for dinner (Japanese and Labanese). All the best for the rest of your PhD.

CS, thank you for bring lunchboxes to us with Cindy. I enjoyed our interesting conversations a lot, in particular in a workshop in Udine. You are a smart and sharp person (because you worked hard for it). Thanks for the interactions we had in PoF and thanks for joining the lunch Waaier group. It is my pleasure to know you. Good luck for your future career.

Jessica, thanks for being active in PoF. Thanks for organising some small activities and a group outing (unfortunately there is a time crash with the JMBC group meeting in MARIN in which some of us were there). For example, the lovely Christmas tree and some Christmas decoration in PoF. The Secret Santa was fun. Thanks for inviting us to your housewarming party. Also thanks for the conversations and sharing your experience and thoughts with us. People come and people leave. Certainly we are also part of it and it seems to be sad sometimes; but thanks for the contributions while you are still in PoF. I wish you all the best for the rest of you PhD.

Dawid, I first saw you in PoF and then somehow I heard your name from Miguel but not sure who that guys was. At some point we talked to each other and things got clear. It was fun to talk to you, like sharing some culture, headphones stuff and learn some Polish. I enjoyed our interactions. All the best for the rest of your PhD.

The Guillaume's PhD students gang (group), **Nathan, Ali and Saeed**. You guys are funny and thanks for the joy you shared to me. Thanks for asking me smile, **Saeed**. All the best for your PhDs and wish your friendship and laugh can sustain.

Nayoung, thank you for some chats in PoF. Thanks for letting me practice my very poor Korean language with you. Good luck with you Postdoc in PoF.

Çayan, we have limited interactions since you started your PhD during the pandemic. But thanks for teaching me how to pronounce your name. It is fun to learn to pronounce some words in a language I am not familiar with. All the best for your PhD.

Ahmed, thanks for the chats about introducing your setup to me and about yourself. I enjoyed knowing different culture and some work that has been happening in PoF. All the best for your PhD.

I would also like to thank the current Iranian colleagues (**Ali, Farzan, Hadi**). You guys are very funny and friendly. It seems that every time seeing any of you are laughing somehow. Saalem, che khabar?

Mazi, I enjoyed the time with you and other PoFers in the JMBC course in Udine. We travelled to Trieste together with some other PoFers which was a nice trip. Thanks for the interactions in PoF. I could learn things from you in our conversations, thank you. Moreover, thanks for volunteering in Tankstation and serving food for us.

Ivan, thanks for inviting me to play basketball with you and the others. Also thanks for a lot of conversations in PoF and during lunch in Waaier. With you, we never ran out of topics. All the best back in Croatia.

ME24/7

Another office that I should also thank is ME24/7. There was a lot of fun whenever I came to your office. For a short time, Kike was there. For a long time, **Pieter, Utkarsh, Jelle and Srinidhi** were there. I did not work in this office but I came to this office sometimes when people are laughing and talking and discussing. The joy and jokes and a lot stuff happen in this office. There is a lot of memories in ME24/7.

Jelle, our bromantic stories dated back in the summer in 2015 in Hong Kong, when I just finished my summer project with Keqing and you just started your internship in Keqing's group. I remember we talked to each other sometimes on the ground floor of the science center. You are a very nice, kind person. You are willing to help people and listen to other people's thoughts with patience. We share a lot of laughing moments in ME247 and also in the water tunnel lab. Also thanks for buying the Oktoberfest tickets to us and kind of make sure we go back safely from Gronau. You are a great man. I am glad and grateful to know you. Thank you for being my good friend, Jelle.

Pieter, (Hi Pieter, how are you?) indeed, we interact a lot in the first one and half years of your PhD. We lived together and went to Waaier together at that time. You are a very sharp, mature person and have many insightful ideas and opinions. I admired a lot on your efficiency and organised way of doing things. Every time I talked to you it seems that I got some inspirations from you. Thanks for being my friend and the fruitful discussions we had. I will definitely visit you again in Delft. All the best for your future career.

Utkarsh, we somehow share a lot of similarities in our background. We studied physics and started doing our PhD in the same month. We lived on campus at the beginning and later we lived together in the same apartment until now. As you also said, I also enjoyed a lot on the discussion one day at home next to the whiteboard. It seems that we also share similar interests in those things we discussed. All the best also after your Postdoc in PoF.

Srinidhi, I remember one time you bring me and Ricardo to enjoy Indian food in the Light of India, in which you discuss some India culture and history. Thanks for sharing them to me. I enjoyed the time we had each other. Soon you will also defend your thesis. I wish you all the best for your defense and also after your PhD.

Outside PoF

Miguel, thanks for being my friend. I enjoyed a lot of our interactions and conversations. They are fun! I got to know more about Mexico from you. Thanks for inviting me to your house for gatherings. I enjoyed the parties and drinks with you. And thanks for checking on me from time to time. You are a good, caring friend.

Myles, thanks for the conversations and the interactions in Meander, and also during the drinks and gatherings. It is my pleasure to talk to you. Thanks for sharing your life and also listening to mine. Also thanks for accepting my invitation to get a cake for my birthday and have some drinks and dinner (e.g. the small Turkish place) together! I wish you all the best for your future career.

Ainoa, thanks to Mafer I get to know you and Myles. Thank you for the joy you brought and the conversations we had. Also thanks for accepting my invitation to get a cake for my birthday and have some drinks with the others. All the best for the rest of your PhD!

Mehri, it is fun to talk to you. You are always laughing. Also thanks to Mafer I get to know you. Thanks for inviting me and others to your house to enjoy your Iranian cusine. The food you cooked a very delicious. Thanks a lot! All the best for the rest of your PhD!

Tao Yin, we met each other back in 2014. Thanks a lot of helping me to adapt to the life in Enschede when I first arrived. Thanks for taking me to travel to the north of the Netherlands do some visiting together. One day we also went to Germany. When I started my PhD, you almost finish yours. Now you are working in the Netherlands for some time already. Thanks for the interactions we had and I wish you all the best for your career!

Sports and food

Thank you **Kangoo jump and the instructors** for offering me such a nice sport to do before the pandemic. Thank you for the nice music and the training of my legs. It is unfortunate that the pandemic started and I cannot continue. Thank you, **Jumbo (珍寶)**, a Chinese-Indonesian take-away restaurant near the university. Thank you for providing me food for these four years whenever the Waaier did not open and I was at the university (e.g. weekends). Sometimes you offered soup and so on, which are very good and brings me memories of the soup back in Hong Kong.

Thank you, **De Lange Muur (長城)**, another Chinese take-away restaurant near my place. Thank you providing me food in the last few months during the pandemic. Without your food, I have to spend more time on cooking. Thank you!

'PoF house'

After living on campus for 10 months, I moved to an apartment with Pieter, Yibo and Utkarsh. Mafer also lived here and now Yoan. It is my pleasure to live with all of you. It has been fun. Sometimes we watched a movie and so on. Thank you for accompanying and keeping the house as fine. Thanks Pieter and Utkarsh for taking care of the bills and split them among us. Later when the pandemic came, thank you, Yibo, Utkarsh and Yoan for letting me occupy most of the space for the desk in the living room. I am grateful that you guys are tolerant to me.

Yibo, you are a very very kind person. You are happy and you are friendly to me and to all of us. Thank you for making a dinner to us when we just moved in. Your cooking skills are good. Thank you for asking us about whether we need anything from time to time. All the best for the rest of your PhD.

Yoan, you are also a very very kind person. You help keeping the house fine. Thanks a lot about that. You are also tolerant to us, thank you. Your cooking skills improved over time, as I could see. Also thanks for answering me questions. I enjoyed our conversations about some turbulence stuff at the board and many other things. I enjoyed also the trip together to Milan and Udine. Lastly thanks for giving comments on my Chinese summary. All the best for the rest of your PhD.

Mafer, thanks for cooking some Venezuelan food to us. The food was very good. I enjoyed our conversations and interactions. You taught me quite some Spanish, thanks a lot. Thanks a lot for inviting us for drinks and for hanging out with other friends. Thanks for introducing more friends to me. All the best for the rest of your study and wish you have a very good career.

Teachers in CUHK

Prof. M. C. Chu (Dr. Chu), thank you first of all for organising the Summer Undergraduate Research Exchange (SURE) programme. Otherwise, I would not have the opportunity to come to this group and later even pursue a PhD. I guess I still inherit your 'sor power'. Probably it is a characteristic of CUHK graduates.

Prof. Keqing Xia and Dr. Yichao Xie, thank you for providing me the opportunity to work with you for a summer. It is a pleasure to work with you for a summer project and I learnt a lot from the weekly group meetings. The experience of working with you also help me to pursue a PhD with Prof. Sun and Prof. Lohse. Thank you very much.

Prof. Emily S.C. Ching, thank you for supervising me for my Bachelor thesis. I learnt a lot from you when we worked on boundary layers in Rayleigh-Bénard convection, consolidating my knowledge to pursue a PhD in turbulence. Learning how to do theoretical research with you was my pleasure. Also thank you for teaching a mathematical physics course and Quantum Mechanics I. You taught the subjects well and clearly. Thank you very much.

Prof. P. M. Hui, thank you for your teaching during my Bachelor studies. Your emphasis on 'think like a physicist' still inspires me to ask myself many times, what are the physical implications that can be drawn from these phenomena? Your passion of teaching also inspired me. Thanks a lot.

Prof. C.F. Lo and Prof. P.T. Leung, thank you for teaching us some mathematical techniques for physics, which consolidates my knowledge that helps me to learn more advanced subjects during my PhD.

Prof. S.K. Goh, thanks for teaching us Solid-state Physics in my last year undergraduate studies, from also an experimentalist perspective. Your passion of teaching also inspired me.

Dr. Karen Lee and Prof. Amos Tai, thank you for the friendship and teaching me Continuum Mechanics in CUHK. It is my pleasure to know you two and thanks for the dinner at your home some time ago. Karen, I still owe you a meal for helping me for the grammatical check for my motivation letters. Thanks!

Secondary school teachers

Everything has a process. My pursue of being a physicist and building the foundation of how to learn began in my high school years.

Teacher Kelvin, you are my class teacher and my Mathematics teacher except in grade 8 and 9. You influenced me a lot on how to learn and on a good learning attitude. You taught us to integrate what we learn and understand them as a whole (融匯貫通) and teaches us the habit of doing extensions from what we learn (推廣). Moreover, you taught us to open our hearts and embrace the knowledge when learning (放開懷抱) so that we can learn it effectively. To check whether we learnt the things you suggested us to present them using our own language, encouraging us to teach others. You also showed us

an anime to show how a person who loves one subject, works hard and never stops improving himself/herself to reach a higher and higher regime (追求更高境界). I am really grateful to what you taught me.

Teacher Eric, thanks for teaching me Physics in high school. I am a 'question student' who asked quite some questions after classes. Thanks for being patient to answer my questions in high school so that my Physics knowledge get consolidated over time. I am grateful to your teaching and patience.

Teacher Daniel, you taught me Physics in grade 9 only but you also did not avoid answering me physics questions. Apart from Teacher Eric, I also came to you to ask you physics questions. How you try to respond to my answer inspired me because sometimes you mentioned you will think about it first, making me also to think about the logic carefully. Thank you, teacher Daniel.

Teacher Benjamin, thanks for taught me English in grade 9 and grade 11. More importantly, you suggested good literature to us to read. They are very useful and enjoyable. I asked you once whether I needed to be good in English in order to study English literature. You replied to me saying that my English will be good if I study English literature. This actually can be extended to other subjects. Thanks a lot for introducing this beautiful subject to me and I even studied that in high school. The recent book you suggested me to read last year is 'Mindet' by Dr. Carol Dweck. It is very inspiring book. I hope I have read it at the start of my PhD so I can grow even more. Thank you, Teacher Ben.

Teacher Henry, thanks for being my teacher for the Liberal Studies subject. Again, the knowledge itself may not be the most important thing that I learnt from you. What I learnt from you is that you searched a large amount of sources for us for discussion. This made me not to shy away from browsing a lot of literature in order to obtain the background of what we would like to investigate. Certainly later in the university, there are also chances to do the same thing. However, you inspired me already back in high school.

Thesis cover

Prof. A. Celani and Prof. M. Vergassola, Thank you for your permission on using the design of Fig. 1 in the publication Celani A., Vergassola M. 2001. Phys. Rev. Lett. **86**(3):424. It is a beautiful figure and is relevant to my research.

Mr. Wong Shing Kit. 誠傑，謝謝你幫我設計這畢業論文的封面。這封面設計得非常好，同事看了都讚好，我也很喜歡。無論如何，我還欠你一頓飯！

Family 家人

多謝家人一直以來的支持和養育。沒有家人的供書教學，我不能攻讀學士學位，進而攻讀博士學位。

作為獨子的我離開了家這麼久，辛苦了爸爸媽媽，因為你們一定很想念我。我也想念大家。

家人一直以來都給予我很大的自由，我想買什麼書媽媽都會買給我，讓我自由地探索、成長和學習。我家中的起居飲食，一直以來得到媽媽的照顧，致使我能健康地成長，有力氣和精力地做我想做的事。

一路以來很感激爸爸做家庭的經濟支柱。爸爸不時都要應酬，加重身體的負擔，但是為的是讓家人住得好、食得好和我有更好的教育。

感謝媽媽做家務、照顧，在家互相體諒對方，致使一家和和氣氣。

謝謝自小時候的照顧和教育。雖然不懂什麼學校的知識，但仍能督促我在小學時的學習。小時候頑皮，但你給我的教訓讓我知道做什麼是危險的。

爸爸在家庭幫助不少，媽媽也維持著這美好的家庭，使我不用太憂心的追求自己的目標。感謝你們。

最後，感謝祖先一直的保祐，謝謝家人定期為神臺裝香、拜祭祖先。

My partner 伴侶

安琪，謝謝你一直以來的支持和鼓勵。從攻讀博士學位開始，我們就分隔兩地，只在假期時相互探望和一起旅行，故此一直以來都辛苦你了。感激一直以來的交流和溝通，彼此分享生活的點滴、遇到的難題、種種喜怒哀樂、對將來的投想以及對過去的反思等不同的話題，大部分時間在精神和心靈上彼此陪伴著。

讀博士時只能在假期時見面。我們的相簿滿滿的都是一起旅遊的照片。從一六年聖誕到波士頓和紐約遊，直到二零年聖誕到馬德里和巴塞隆拿遊玩，一起走到不同的國度和城市，感受當地的文化、享受異地的美食、欣賞不同建築風格，這些已成為我們寶貴的回憶，也讓我在忙碌的博士生涯裡喘息一下。

讀博士的四、五年以來，彼此見證住我們的成長。從讀書、研究、工作、待人接物、見識各方面，我們都互相分享經驗、互相給予意見，令大家都變得更成熟。

最後，謝謝你對我的中文概要給予意見，使之行文更流暢和更合乎正式的寫法。

謝謝你，安琪。